SAPIENZA
UNIVERSITÀ DI ROMA

ICRANet

International Relativistic Astrophysics Program Ph.D.
IRAP Ph.D.

Accretion in Compact Stars:

Hypercritical accretion in the Induced Gravitational Collapse and the post-merger evolution of white dwarfs mergers.

PhD Student
Laura Marcela Becerra Bayona

Supervisors
Dr. Jorge Rueda

Sapienza University of Rome
Academic Year 2013-2017

Abstract

The Induced Gravitational Collapse (IGC) paradigm points to a binary origin for the long-duration gamma-ray burst (GRBs) associated with supernovae (SN). In this one, a carbon-oxygen core ($\mathrm{CO_{core}}$) explodes in a Type Ib/c SN in presence of a close neutron star (NS) companion. The SN triggers an hypercritical accretion into the NS and depending on the initial binary parameters, two outcomes are possible. In a first scenario, also referred as binary-driven hypernova (BdHNe), the binary is enough tight, so the accretion rate onto NS can be as high as 0.1 $M_\odot$ s^{-1}, the NS reaches its critical mass, and collapses to a black hole (BH), emitting a GRB with $E_{\mathrm{iso}} > 10^{52}$ erg. A second scenario can happen for binary systems with larger binary separations, then the hypercritical accretion onto the NS is not sufficient to induce its gravitational collapse, giving place to a x-ray flash (XRF) with energy $E_{\mathrm{iso}} < 10^{52}$ erg.

The first part of this thesis focus on the hypercritical accretion process in the IGC paradigm. We constructed an analytical framework based on the Bondi-Hoyle accretion formalism, in order to identify the separatrix of systems in which a BH is formed and the ones where there is no BH formation and characterize the observational signatures of the BdHNe and the XRF systems. We show that the material entering into the Bondi-Hoyle region possesses sufficient angular momentum to circularize around the NS, forming a disk-like structure. We estimate the maximum orbital period, P_{max}, as a function of the NS initial mass, up to which the NS companion can reach by hypercritical accretion the critical mass for gravitational collapse leading to BH formation. We find that XRFs and BdHNe are produced in binaries with $P > P_{\mathrm{max}}$ and $P < P_{\mathrm{max}}$, respectively. One of the most important results is that the presence of the NS produce large asymmetries in the SN ejecta around the orbital plane that lead observational signatures in the SN emission as well as in the afterglow of long GRBs. We also studied the hydrodynamics within the accretion flow. We find that the temperature developed near the NS surface is around $1 - 10$ MeV, hence electron–positron annihilation into neutrinos becomes the main cooling channel leading to accretion rates of $10^{-9} - 10^{-1}$ $M_\odot$ s^{-1} and neutrino luminosities of $10^{43} - 10^{52}$ erg s^{-1}. Additionally, 3D numerical simulations of the IGC paradigm are performed with the smoothed particle hydrodynamics (SPH) technique. The fate of the binary system is explored for a wide parameter space including different $\mathrm{CO_{core}}$ masses, orbital periods and SN explosion geometry and energies. We determine whether the star gravitational collapse is possible and assess if the binary holds gravitationally bound or it becomes unbound by the SN explosion.

The second part of this thesis is about the evolution of postmergers remnants of white dwarfs binary systems. The simulations of coalescence between white dwarfs have shown that the final result consists of a central remnant made of the undisturbed primary star. The secondary star is totally disrupted and about half of the material is accreted by the primary, forming a hot corona surrounding it, and the rest of the material forms a rapidly rotating Keplerian disk, since little mass is ejected from the system during the coalescence process. In this thesis the evolution of metastable, magnetized super-Chandrasekhar white dwarfs formed in the aftermath of the merger of close binary systems has been modeled taking into account the magnetic torques acting on the star, accretion from the Keplerian disk, the threading of the magnetic field lines through the disk, as well as the thermal evolution of the white dwarf core. We explore the binary parameters that lead the white dwarf central remnant to evolve toward the gravitational collapse forming a neutron star or toward explosive carbon ignition leading to a type Ia supernova.

Introduction

Accretion processes release energy efficiently while matter falls into the gravitational field of a compact massive object. A simple order of magnitude estimation of this energy can be made calculating the change in the gravitational potential energy of a mass m falling onto the surface of a body of mass M and radius R. Then, the energy that potentially can be released is: $\Delta E_{\rm acc} = GMm/R$, i.e the more compact is the accreting object, the accretion is more efficient. For instance, a white dwarf (WD) with $M \sim M_\odot$ and $R \sim 10^9$ cm can release $\Delta E_{\rm acc} \approx 10^{17}$ erg per each gram of matter accreted while a neutron star (NS) with the same mass and $R \sim 10$ km will release $\Delta E_{\rm acc} \approx 10^{20}$ erg per each gram of matter accreted.

Accretion plays an important role in many astrophysical scenarios, e.g. protoplanetary disks, circumstellar disks of dense gas surrounding newly formed stars [5], interacting close binaries where a compact star accretes matter from its companion either via stellar wind or Roche-lobe overflow (e.g. X-ray binaries [67], cataclysmic variables (CV) form by a WD and a normal star [143]), active galactic nuclei (AGN), supermassive black holes ($> 10^6\, M_\odot$) in the centre of galaxies accreting from hot disks [152]. The work done along the time of my PhD and presented in this thesis is centered on the accretion into compact object in two specific scenarios: the hypercritical accretion onto a NS inside the framework of the induced gravitational collapse (IGC) scenario [see, e.g., 90, 227, 231]; and the disk accretion onto a magnetized WD as the remnant configuration of WDs binaries mergers in the double degenerate model for SN type Ia progenitors [124, 304].

The IGC paradigm was formulated to explain the connection between gamma ray bursts (GRBs) and supernovae (SN). GRBs are the brightest explosions in the universe with isotropic luminosities between $10^{47} - 10^{54}$ erg s^{-1}. Since its first detection in the late 1960s by the Vella Satellites [146], many efforts have been made in order to enrich the understanding of these phenomena. The theory has advanced with the new knowledge given by the observations. To mention some examples, with BATSE, as part of the Compton Gamma-ray Observatory (CGRO) launched in 1991, was evidenced that GRBs follow an isotropic distribution in the sky [173]; Beppo-SAX, put in orbit in 1996, detected the first GRB afterglow, making possible to determined their cosmological origin in star formation regions of galaxies [180, 294].

The relation between GRBs and SNs events was considered first with the detection of GRB 980425 associated with a broad line type Ic supenova, SN 1998bw [95], and the first truly solid evidence came with the detection of GRB 030329 ($z = 0.1685$ [105]) with SN 2003dh [172]. However, the SN-GRB connection has been also supported by the observation of a SN-like bump in the optical GRB afterglow, e.g. of GRB 980326 [25] and GRB 970228

[223]. Further clear spectroscopic evidences of GRB-SN connection have been found in the cases of GRB 031203 [270, 278], GRB 060218 [38, 271], GRB 100316D [35, 47, 251], GRB 120422A [9, 174], and GRB 130427A [175, 295, 315], all at relatively low redshifts ($z \lesssim 0.3$). Due to observational constraints, photometric identification of Type Ibc SNe is reasonable possible up to $z \lesssim 1.2$. To date, 46 GRB-SN associations have been confirmed on spectroscopic and/or photometric grounds [40, 151].

Many models have been proposed as progenitors of long GRBs. The most popular among the scientific community are the *magnetar* [292] and the *collapsar* models [167, 310]. In the former, the energy source for GRBs comes from the spin down of a newly formed highly magnetized rotating NS with an initial period of about one millisecond [179]. While in the latter, the iron core of a rapidly rotating massive star ($M > 20\,M_\odot$) collapses to a black hole (BH), either directly or during the accretion phase that follows the core collapse, and an accretion disk is formed around it. Three possible mechanisms have been proposed to explain the GRB emission in the *collapsar* scenario: (a) neutrino/anti-neutrino ($\nu\bar{\nu}$) annihilation along the rotational axis may drive a jet [62, 192, 214, 310]; (b) magnetic instabilities in the disk [23, 219]; and (c) magnetohydrodynamic (MHD) extraction of the BH rotational energy [24, 157, 185].

As was said above, the first part of this thesis is focused on the IGC model, introduced as an alternative progenitor of the subfamily of GRBs with energies $E_{\rm iso} \gtrsim 10^{52}$ erg associated with type Ic SN [90, 227, 231]. Within this paradigm, the SN explosion and the GRB occur in the following time sequence taking place in a binary system composed by a carbon–oxygen core ($\rm CO_{core}$) and a NS companion: (1) collapse and explosion of the $\rm CO_{core}$; (2) hypercritical accretion onto the NS that reaches the critical mass; (3) NS gravitational collapse to a BH; (4) emission of the GRB. This sequence occurs on short timescales of ~ 100 seconds in the source rest-frame, and it has been verified for several systems, that have called binary-driven hypernovae (BdHNe), with cosmological redshift from $z < 1$[210], all the way up to one of the farthest sources, GRB 090423, at $z = 8.2$ [241]. Recently, the model has been extended to include a second scenario where the hypercritical accretion onto the NS is not sufficient to induce its gravitational collapse. This scenario corresponds to the progenitors of a second subfamily of GRBs, the X-Ray flashes (XRFs) with $E_{\rm iso} \lesssim 10^{52}$ erg [246].

In Chapter 1, in order to model the hypercritical accretion phase in the IGC scenario and keep control on the parameter variation of the initial binary system, an analytical framework based on the Bondi-Hoyle accretion formalism is constructed. This formulation takes into account the angular momentum carried by the SN ejecta, and eventually might transfer to the NS during the accretion process. A detailed computation of the time evolution of both the mass and angular momentum of the accreting NS is given, showing that the NS (1) reaches either the mass-shedding limit or the secular axisymmetric instability in a few seconds depending on its initial mass, (2) reaches a maximum dimensionless angular momentum value, $[cJ/GM^2]_{\rm max} \approx 0.7$, and (3) can support less angular momentum than the one transported by SN ejecta, $L_{\rm acc} > J_{\rm NS,max}$, hence there is an angular momentum excess that necessarily leads to jetted emission.

In Chapter 2 is made a characterization of the initial binary system that gives BdHNe events and produces NS-BH binary, from the system giving XRF events in which the final product is a new NS binary. This is done through the computation of the maximum orbital period, $P_{\rm max}$ (having fixed the other system parameters, i,e. NS initial mass, $\rm CO_{core}$ progenitor and SN outermost velocity) up to which the induced gravitational collapse of the NS to a BH by accretion can occur. Possible evolutionary scenario leading to the IGC in-state binary systems ($\rm CO_{core}$-NS) and the disruption of the final out-state systems are also discussed.

During the hypercritical accretion on the NS, the neutrino emission at the based of the NS surface dominates the cooling and allows the NS to increase its mass. Chapter 3 is dedicated to the study of the hydrodynamics inside the NS accretion region. For accretion rate between $10^{-2} - 10^{-4}$ $M_\odot$ s^{-1}, the range of temperature and density developed on the NS surface are such that the e^+e^--pair annihilation becomes the dominant channel for the neutrino emission, reaching luminosities up to 10^{52} erg s^{-1} and mean neutrino energies of the order of 20 MeV. These make the XRFs and the BdHNe astrophysical laboratories for MeV-neutrino physics additional to core-collapse SN. In Chapter 3 is also discussed the main features of the neutrino oscillation phenomenology from the bottom of the accretion zone, where the neutrinos are created, until their escape to the outer space, i.e. outside the Bondi-Hoyle region.

Chapter 4 focuses on the observational characteristics of the long GRBs and their theoretical origin in the context of the IGC paradigm. To contrast with observation, the expected luminosities during the hypercritical accretion process are calculated. Additionally, we show that the accreting NS produces asymmetries on the SN ejecta around the orbital plane. In the case of XRFs, these asymmetries can influence the SN emission both in X-rays and in the optical; and in the case of BdHNe, can be associated with the origin of the early X-ray flares on the GRBs afterglow.

Up to this point, the study of the hypercritical accretion process in the IGC scenario has been done following an analytical prescription based on the Bondi-Hoyle formalism. However, due to the particular characteristics of the IGC scenario, e.g. its high time-variable nature, the implementation of full hydrodynamical simulations of this process becomes a necessity in order to validate the analytical estimations. In Chapter 5, the first 3D hydrodynamics simulations of the IGC scenario are presented. These simulation were done using the Smooth Particles Hydrodynamics (SPH) technique as developed in the SNSPH code [89]. The simulations start from the moment that the SN shock front reaches the $\rm CO_{core}$ external radius. In order to determine whether the star collapse is possible, a wide range of initial conditions for the binary system was covered, i.e. the $\rm CO_{core}$ progenitors, the binary initial separation and SN total energy and geometry have been varied. For all the simulation, we follow the evolution of the SN ejecta, including their morphological structure, subjected to the gravitational field of both the new NS (νNS), formed at the center of the SN, and the one of the NS companion. Additionally, we also follow the evolution of the binary parameters (e.g. the binary separation, period, eccentricity) and compute the accretion rate of the SN ejecta onto the NS companion as well as onto the νNS from SN matter fallback. We evaluate, for selected nuclear equations-of-state of NSs, if the accretion process leads the NSs either to the mass-shedding limit, or to the secular axisymmetric instability for gravitational collapse to a BH, or to a more massive, fast rotating, but stable NS. We assess if the binary holds gravitationally bound or it becomes unbound by the SN explosion, hence we explore the space of initial binary and SN explosion parameters leading to the formation of νNS-NS or νNS-BH binaries. The consequences of our results for the IGC model of GRBs are also discussed.

In the last Chapter, we jump to the second topic of this thesis, the accretion on a WD. The evolution of the remnant of the merger of two white dwarfs is still an open problem. Furthermore, few studies have addressed the case in which the remnant is a magnetic white dwarf with a mass larger than the Chandrasekhar limiting mass. Angular momentum losses might bring the remnant of the merger to the physical conditions suitable for developing a thermonuclear explosion. Alternatively, the remnant may be prone to gravitational or rotational instabilities, depending on the initial conditions reached after the coalescence. Dipole magnetic braking is one of the mechanisms that can drive such losses of angular momentum. However, the timescale on which these losses occur depend on several parameters, like the strength of the magnetic field. In addition, the coalescence leaves a surrounding Keplerian disk that can be accreted by the newly formed white dwarf. In Chapter 6, we compute the post-merger evolution of a super-Chandrasekhar magnetized white dwarf taking into account all the relevant physical processes. These include magnetic torques acting on the star, accretion from the Keplerian disk, the threading of the magnetic field lines through the disk, as well as the thermal evolution of the white dwarf core. We find that the central remnant can reach the conditions suitable to develop a thermonuclear explosion before other instabilities (such as the inverse beta-decay instability or the secular axisymmetric instability) are reached, which would instead lead to gravitational collapse of the magnetized remnant.

List of publications

Articles published

- **L. Becerra**, F. Cipolleta, C.L. Fryer, J. A. Rueda and R. Ruffini. *Angular Role in the Hypercritical Accretion of Binary-Driven Hypernova*, ApJ, 812: 100 (2015). Chapters 1 and 2

- **L. Becerra**, C. L. Blanco, C.L. Fryer, J. A. Rueda, and R. Ruffini. *On the Induced Gravitational Collapse Scenario of Gamma-ray Burst Associated with Supernovae.* ApJ 833: 107 (2016). Chapters 1, 2, 3 and 4

- R. Ruffini, J. A. Rueda, M. Muccino, G. B. Pisani, Y. Wang, **L. Becerra**, M. Kovacevic, F. G. Oliveira, Y. Aimuratov, C. L. Bianco and R. Moradi. *On the Classification of GRBs and Their Occurrence Rates.* , ApJ 832: 136 (2016). Chapter 4

- J. A. Rueda, Y. Aimuratov, U. B. de Almeida, **L. Becerra**, C. L. Bianco, C. Cherubini, S. Filippi, M. Karlica, M. Kovacevic, J. D. M. Fuksman, R. Moradi, M. Muccino, A. V Penacchioni, G. B. Pisani, D. Primorac, R. Ruffini, N. Sahakyan, S. Shakeri, Y. Wang. *The binary systems associated with short and long gamma-ray* *bursts and their detectability.* IJMPD 26 (2017)

- R. Ruffini, Y. Wang, Y. Aimuratov, U. Barres de Almeida, **L. Becerra**, C. L. Bianco, Y. C. Chen, M. Karlica, M. Kovacevic, J. D. Melon Fuksman, R. Moradi, M. Muccino, A. V. Penacchioni, G. B. Pisani, D. Primorac, J. A. Rueda,G. V. Vereshchagin, and S. S. Xue. *Early X-ray Flares in GRBs.* , ApJ 852: 53 (2018). Chapter 4

- J. D. Uribe, **L. Becerra**, M. M. Guzzo, F. Rossi-Torres, J. A. Rueda and R. Ruffini. *Neutrino oscillations within the induced gravitational collapse paradigm of long gamma-ray bursts.* ApJ 852: 120 (2018) Chapter 3

- **L. Becerra**, J. A. Rueda, P. Loren-Aguilar and E. García-Berro. *The Spin Evolution of Fast-Rotating, Magnetized Super-Chandrasekhar White Dwarfs in the Aftermath of White Dwarf Mergers.* To be published in ApJ. Chapter 6

Articles submitted or in preparation

- R. Ruffini, Y. Aimuratov, **L. Becerra**, C. L. Bianco, Y. Chen, M. Karlica, M. Kovacevic, J. Fuksman, R. Moradi, M. Muccino, G. Pisani, D. Primorac, J. Rueda and Y. Wang. *On the nature of prompt emission, x and gamma ray flares and extended thermal emission in GRB 151027A.* `arXiv: 1712.05001`. Submitted to ApJ. Chapter 4.

- R. Ruffini, J. Rodriguez, M. Mucciono, J. A. Rueda, Y. Aimuratov, U. Barres de Almeida, **L. Becerra**, C. L. BiancoG. C. Cherunini, S. Filippi, D. Gizzi, M. Kovacevic, R. Moradi, F. G. Oliveira, B. Pisani, Y. Wang. *On the rate and on the gravitational wave emission of short and long grbs.* `arXiv: 1602.03545`. Sumitted to Apj.

- **L.Becerra**, C. Ellinger, C.L. Fryer, J. A. Rueda and R. Ruffini. *SPH simulations of the induced gravitational collapse scenario of long gamma-ray bursts associated with supernovae.* Submitted to ApJ (2018) Chapter 5

Proceedings

- L. Becerra, et. al.*Hypercritical Accretion, Induced Gravitational Collapse and Binary-Driven Hypernova*, Swift 10th anniversary conference proceedings. La Sapienza University, Rome, Italy (2014).
  `PoS(SWIFT 10)171, https://pos.sissa.it/233/171/pdf`

- L. Becerra, et. al. *Black holes, neutron stars and supernova within the induced gravitational collapse paradigm for GRBs*, Proceeding of the Second ICRANet Cèsar Lattes meeting: Supernovae, neutron stars and black holes, AIP Conf. Proc. vol. 1693, 02002. Rio de Janeiro, Brasil (2015).

- L. Becerra, J. A. Rueda, P. Loren-Aguilar and E. García-Berro. *Induced compression by angular momentum losses in fast-rotating magnetized super-Chandraskehar dwarfs*, Proceeding of the Fourteenth Marcel Grossmann Metting (MG14), World Scientific, Singapore, 2017: pp. 4291-4296. La Sapienza University, Rome, Italy (2015)
  `https://doi.org/10.1142/9789813226609_0575`

- L. Becerra, F. Cipolletta, C. Fryer, J. A. Rueda, and R. Ruffini. *Angular momentum role in the Hypercritical accretion of Binary-Driven Hypernova*, Proceeding of the Fourteenth Marcel Grossmann Meeting (MG14), World Scientific, Singapore, 2017: pp. 2953-2956. La Sapienza University, Rome, Italy (2015).
  `https://doi.org/10.1142/9789813226609_0370`

- L.Becerra, C. L. Blanco, C.L. Fryer, J. A. Rueda, and R. Ruffini. *Hypercritical Accretion in the Induced Gravitational Collapse.* RMxAA, 49:83. XV Latin American Regional IAU Meeting, Cartagena, Colombia (2016)

- L. Becerra, F. Cipolletta, C. Fryer, J. A. Rueda, and R. Ruffini. *On the Induced Gravitational Collapse.* Joint International Conference of ICGAC-XIII and IK-15 on Gravitation, Astrophysics and Cosmology. EPJ Web of Conferences, Volume 168. Ewha Womans University, Seoul, Korea (2017)
  `https://doi.org/10.1051/epjconf/201816802005`

Abbreviations

BdHNe	Binary Driven Hypernova
BH	Black Hole
$CO_{\rm core}$	Carbon-oxygen core
EOS	Equation of state
GRB	Gamma ray burst
IGC	Induced Gravitational Collapse
NS	Neutron star
νNS	New neutron star
SPH	Smooth particle hydrodynamics
SN	Supernova
WD	White Dwarf
XRF	X-ray flash
ZAMS	Zero age main sequence

Contents

1. The Induced Gravitational Collapse

1.1. Introduction

Recently, Ruffini et al. [246] proposed a binary nature for the progenitors of both long and short GRBs. The first five chapters of this thesis focus on long GRBs associated with supernovae. For such systems the *induced gravitational collapse* (IGC) paradigm [see, e.g., 90, 137, 227, 231, 240] indicates as progenitor a binary system composed of a carbon-oxygen core ($\mathrm{CO_{core}}$) and a neutron-star (NS) in a tight orbit. Such a binary system emerged first as a necessity for the explanation of a set of observational features of long GRBs associated with type Ic supernovae [227]. Besides, it also appears in the final stages of a well defined evolutionary path which includes the presence of interacting binaries responsible for the formation of stripped-envelope stars such as $\mathrm{CO_{cores}}$ leading to type Ic supernovae [14, 88, 227].

The core-collapse of the $\mathrm{CO_{core}}$ produces a supernova (SN) explosion ejecting material that triggers an accretion process onto the binary neutron-star companion. It was advanced in Ruffini et al. [246] the existence of two classes of long GRBs depending on whether or not a black-hole (BH) is formed in the hypercritical accretion process onto the NS (see Chapter 4 for more detailed description):

- First, there is the subclass of binary-driven hypernovae (BdHNe) [BdHNe, see 242, and references therein], long GRBs with isotropic energy $E_{\mathrm{iso}} \gtrsim 10^{52}$ erg and rest-frame spectral peak energy $0.2 \lesssim E_{\mathrm{p,i}} \lesssim 2$ MeV. Their prompt emission lasts up to ~ 100 s and it is at times preceded by an X-ray emission in the 0.3–10 keV band lasting up to 50 s and characterized by a thermal and a power-law component (i.e. Episode 1 in GRB 090618 in [137]). For all BdHNe at $z \lesssim 1$, an optical supernova with luminosity similar to the one of supernova 1998bw [95] has been observed after 10–15 days in the cosmological rest-frame [see, e.g., 175]. It has been proposed that this class of GRBs occurs when the NS reaches its critical mass through the above accretion process and forms a BH. This GRB subclass occurs in compact binaries with orbital periods as short as $P \sim 5$ min or binary separations $a \lesssim 10^{11}$ cm [90].

- Second, there is the subclass of X-ray flashes (XRFs), long GRBs with isotropic energies in the range $E_{\mathrm{iso}} \approx 10^{47}$–$10^{52}$ erg; spectral peak energies $E_{\mathrm{p,i}} \approx 4$–$200$ keV [2, 243, 246]. Their prompt emission phase lasts $\sim 10^2$–10^4 s and it is generally characterized by a spectrum composed by a thermal component (with radii 10^{10}–10^{12} cm and temperatures 0.1–2 keV, 38) and power-law component. For all XRFs at $z \lesssim 1$, an optical supernova with luminosity similar to the one of supernova 2010bh [35], has been observed after 10–15 days in the cosmological rest-frame. These sources have been associated within the IGC paradigm to binaries of a $\mathrm{CO}_{\mathrm{core}}$ core and an NS in which there is no BH formation: when the accretion is not sufficient to bring the NS to reach the critical mass. This occurs in binaries with orbital periods longer than $P \sim 5$ min or binary separations $a \gtrsim 10^{11}$ cm [14, 246].

It is clear that the observational properties of the IGC binaries are sensitive to the binary parameters which can change the fate of the system. The first estimates of the accretion rate and the possible fate of the accreting NS in an IGC binary were presented in Rueda & Ruffini [227]. To obtain an analytic expression of the accretion rate, such first simple model assumed: (1) a pre-SN homogeneous density profile; (2) an homologous expansion of the density; (3) constant mass of the NS ($\approx 1.4\ M_\odot$) and the supernova ejecta (≈ 4–$8\ M_\odot$). The first application of this model was presented in Izzo et al. [137] for the explanation of the Episode 1 of GRB 090618.

More recently, Fryer et al. [90] performed the first more realistic numerical simulations of the IGC by using more detailed SN explosions coupled to hypercritical accretion models from previous simulations of supernova fallback [79, 83]. The core-collapse of the $\mathrm{CO}_{\mathrm{core}}$ producing the SN Ic was simulated in order to calculate realistic profiles for the density and expanding velocity of the supernova ejecta. The hydrodynamic evolution of the material falling into the accretion region of the NS was there followed numerically up to the surface of the NS. The accretion in these systems can proceed at very high rates that exceed by several orders of magnitude the Eddington limit due to the fact that the photons are trapped in the accreting material and the accretion energy is lost through neutrino emission [see 90, and references therein for additional details].

Although all the above works have already shown that indeed the SN can induce, by accretion, the gravitational collapse of the NS to a BH, there is still the need of exploring systematically the entire, physically plausible, space of parameters of these systems, as well as to characterize them observationally. Following this line of ideas, in this chapter, we're going to formulated an analytical approach base on the Bondi-Hoyle accretion formalism for the IGC scenario. Contrary to the previous works that assume an spherical symmetry approximation of the hypercritical accretion process, here we introduced the effects that the angular momentum carried by the SN, and eventually transferred to the NS during the accretion process could have on the evolution and final fate of the system.

This chapter is organized as follows: In Section 1.2 we present the framework of the hypercritical accretion of the SN ejecta onto the NS: we compute the Bondi-Hoyle accretion rate and estimate the angular momentum transported by the part of the SN ejecta that enters into the gravitational capture region (Bondi-Hoyle surface) of the NS (Section 1.2.1). Additionally, we show that the material entering into the Bondi-Hoyle region possesses sufficient angular momentum to circularize around the NS, forming a disk-like structure (Section 1.2.2). In Section 1.2.3, we extend the Bondi-Hoyle formalism in order to introduce first an asymmetric SN expansion and then, consider an initial elliptic binary orbit. In Section 1.3 we give details on the computation of the time evolution of both the mass and angular momentum of the accreting NS. The accretion process is assumed to occur from an inner disk radius given by the most bound circular orbit around a rotating NS or by the NS equatorial radius. We show that, depending upon the initial mass of the NS and the efficiency of the angular momentum transport, the NS might reach either the mass-shedding limit or the secular axisymmetric instability in a short time. In Section 1.4, we calculate the mass and angular momentum flux of the SN ejecta that cross the NS capture surface. Finally, in Section 1.5, we summarize the results of this chapter and, in addition, show that the total angular momentum transported by the SN ejecta is larger than the maximum angular momentum supported by a maximally rotating NS. Therefore, we advance the possibility that such an excess of angular momentum constitutes a channel for the formation of jetted emission during the hyperaccretion process of BdHNe leading to possible observable non-thermal high-energy emission. In this last section, we also give some perspective for future work.

1.2. Hypercritical accretion induced by the supernova

The accretion rate of the SN ejecta onto the NS can be estimated via the Bondi-Hoyle accretion formula [27, 28, 121]:

$$\dot{M}_B(t) \;=\; \pi\rho_{\rm ej}R_{\rm cap}^2\sqrt{v_{\rm rel}^2+c_{\rm s,ej}^2}, \tag{1.1}$$

where $R_{\rm cap}$ is the gravitational capture radius of the NS

$$R_{\rm cap}(t)=\frac{2GM_{\rm NS}(t)}{v_{\rm rel}^2+c_{\rm s,ej}^2}, \tag{1.2}$$

Here $\rho_{\rm ej}$ and $c_{\rm s,ej}$ are the density and the sound speed of the ejecta, $M_{\rm NS}$ the NS mass, $\vec{v}_{\rm rel}=\vec{v}_{\rm ej}-\vec{v}_{\rm orb}$, the velocity of the ejecta as seen from an observer at the NS, and G is the gravitational constant. The orbital velocity is $v_{\rm orb}=\sqrt{GM/a}$, where $M=M_{\rm NS}+M_{\rm CO}$ is the total binary mass, $M_{\rm CO}=M_{\rm env}+M_{\rm Fe}$ the total mass of the $\rm CO_{core}$ which is given by the envelope mass $M_{\rm env}$ and the central iron core mass $M_{\rm Fe}=1.5\ M_\odot$. The latter is the mass of the new neutron-star formed in the core-collapse supernova process, hereafter indicated as νNS and its mass $M_{\nu\rm NS}$, i.e. we adopt $M_{\nu\rm NS}=M_{\rm Fe}=1.5\ M_\odot$ in agreement with the range of masses predicted under the convective supernova paradigm [82].

In order to integrate equation (1.1) and simulate the hypercritical accretion onto the NS, we need to implement a model for the SN explosion from which we determine the velocity and the density of the ejecta near the capture region of the NS. We shall adopt for such a scope an homologous expansion of the SN ejecta, i.e. the velocity is proportional to the radius:

$$v_{\rm ej}(r,t)=n\,\frac{r}{t}. \tag{1.3}$$

Table 1.1.: Properties of the pre-supernova $\mathrm{CO}_{\mathrm{cores}}$

Progenitor M_{ZAMS} ($M_\odot$)	ρ_{core} (10^8 g cm^{-3})	R_{core} (10^7 cm)	M_{env} ($M_\odot$)	$R_{0_{\mathrm{star}}}$ (10^9 cm)	m
15	3.31	5.01	2.079	4.49	2.771
20	3.02	7.59	3.89	4.86	2.946
30	3.08	8.32	7.94	7.65	2.801

NOTE — $\mathrm{CO}_{\mathrm{cores}}$ obtained for the low-metallicity ZAMS progenitors with $M_{\mathrm{ZAMS}} = 15$, 20, and 30 $M_\odot$ in . The central iron core is assumed to have a mass $M_{\mathrm{Fe}} = 1.5\ M_\odot$, which will be the mass of the νNS, denoted here as $M_{\nu\mathrm{NS}}$, formed out of the supernova process.

Thus, the outermost layer of the ejecta, which we denote hereafter as R_{star}, evolves as:

$$R_{\mathrm{star}}(t) = R_{0_{\mathrm{star}}} \left(\frac{t}{t_0}\right)^n , \tag{1.4}$$

where $t_0 = nR_{0_{\mathrm{star}}}/v_{0_{\mathrm{star}}} > 0$, being $v_{0_{\mathrm{star}}}$ the velocity of the outermost layer and n is the so-called *expansion parameter* whose value depends on the hydrodynamical evolution of the ejecta and the circumstellar material, i.e., $n = 1$ corresponds to a free expansion, $n > 1$ an accelerated expansion, and $n < 1$ a decelerated one.

The condition of homologous expansion give us the density profile evolution [see 53, for details]:

$$\rho_{\mathrm{ej}}(X, t) = \rho_{\mathrm{ej}}(X, t_0)\frac{M_{\mathrm{env}}(t)}{M_{\mathrm{env}}(t_0)}\left(\frac{R_{0_{\mathrm{star}}}}{R_{\mathrm{star}}(t)}\right)^3 , \quad \text{with} \quad X \equiv \frac{r}{R_{\mathrm{star}}}, \tag{1.5}$$

where $M_{\mathrm{env}}(t)$ is the mass expelled from the $\mathrm{CO}_{\mathrm{core}}$ in the SN explosion, and hence available to be accreted by the NS, and $\rho_{\mathrm{ej}}(X, t_0)$ is the density profile of the outermost layers of the $\mathrm{CO}_{\mathrm{core}}$ (i.e., the pre-supernova profile). The CO envelope of such pre-supernova configurations can be well approximated by a power law [see Figure 2 in 90]:

$$\rho_{\mathrm{ej}}(r, t_0) = \rho^0_{\mathrm{ej}} = \rho_{\mathrm{core}} \left(\frac{R_{\mathrm{core}}}{r}\right)^m , \quad \text{for} \quad R_{\mathrm{core}} < r \leq R_{0_{\mathrm{star}}}, \tag{1.6}$$

In Table 1.1 has been shown the properties of the $\mathrm{CO}_{\mathrm{core}}$ produced by low-metallicity progenitors with initial zero-age main sequence (ZAMS) masses of $M_{\mathrm{ZAMS}} = 15$, 20, and 30 $M_\odot$ using the Kepler stellar evolution code [312]. In order to take into account the finite size of the envelope, we modify the above density profile by introducing boundaries to the SN ejecta through density cut-offs at the outermost and innermost layers of the ejecta, namely:

$$\rho^0_{\mathrm{ej}} = \hat{\rho}_{\mathrm{core}} \ln\left(\frac{r}{\hat{R}_{\mathrm{core}}}\right)\left(\frac{R_{\mathrm{star}}}{r} - 1\right)^m , \tag{1.7}$$

where $\hat{R}_{\mathrm{core}} < r < R_{\mathrm{star}}$. The condition that the modified profile has the same ejecta mass with respect to the unmodified power-law profile implies $\hat{R}_{\mathrm{core}} < R_{\mathrm{core}}$. Figure 1.1 shows the pre-supernova density profile described by equations (1.6) and (1.7) for the $\mathrm{CO}_{\mathrm{core}}$ $M_{\mathrm{ZAMS}} = 30\ M_\odot$. For this progenitor we have $\hat{R}_{\mathrm{core}} = 0.31\ R_{\mathrm{core}}$ and $\hat{\rho}_{\mathrm{core}} = 567.67$ g cm^{-3}.

Introducing the homologous expansion for the description of the evolution of the SN

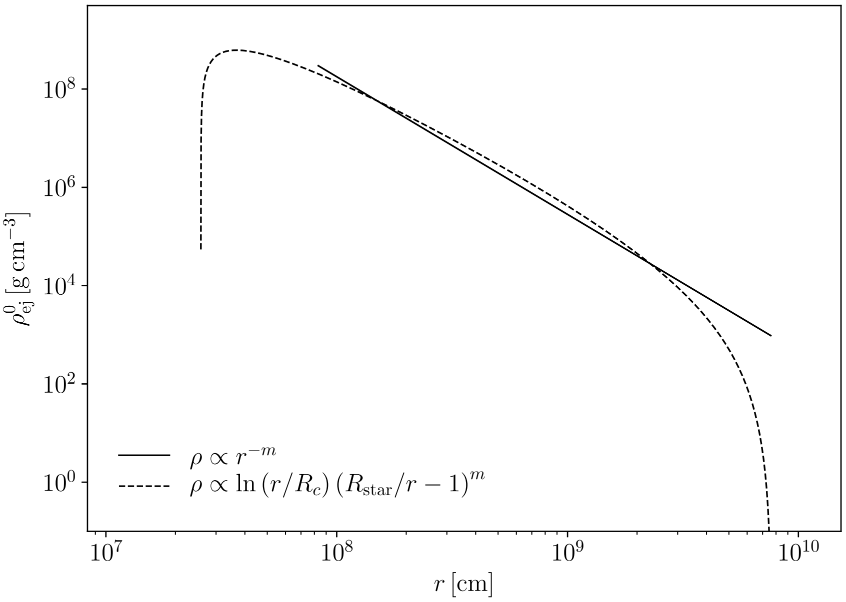

Figure 1.1: Pre-supernova density profile produced by the $M_{\rm ZAMS} = 30\ M_\odot$ progenitor of Table 1.1. We compare and contrast the power-law density profile (solid curve) with a modified profile (dashed curve) with density cut-offs at the outermost and innermost ejecta layers following equations (1.6) and (1.7). The two profiles have the same envelope mass.

ejecta, equation (1.1) becomes:

$$\frac{\dot{\mu}_B(\tau)}{(1-\chi\mu_B(\tau))M_{\rm NS}^2} = \frac{\tau^{(m-3)n}}{\hat{r}^m}\ln\left(\frac{\hat{r}}{\hat{r}_c\tau^n}\right)\frac{(\hat{r}_s-\hat{r}\tau^{-n})^m}{[1+\eta\hat{r}/\tau^2]^{3/2}}, \tag{1.8}$$

where

$$\tau \equiv \frac{t}{t_0}, \quad \mu_B(\tau) \equiv \frac{M_B(\tau)}{\Sigma_B}, \quad \hat{r} \equiv 1-\frac{R_{\rm cap}}{a}, \tag{1.9}$$

and the parameters χ, Σ_B and η depend on the properties of the binary system before the SN explosion:

$$\Sigma_B = \frac{4\pi\hat{\rho}_c G^2 M_\odot^2 t_0}{v_{\rm orb}^3}, \quad \chi = \frac{\Sigma_B}{M_{\rm env}^0}, \quad \eta = \left(\frac{n\,a}{t_0 v_{\rm orb}}\right)^2, \tag{1.10}$$

where $M^0_{\rm env} \equiv M_{\rm env}(t=t_0) = M_{\rm env}(\tau=1)$.

1.2.1. Angular Momentum Transport by the supernova ejecta

Now, we are in a position to give an estimate of the angular momentum transported by the SN material to the NS during the IGC process. In doing so, we “extrapolate” the results of Shapiro & Lightman [261] and Wang [297] for the accretion process from stellar wind in a binary system. Due to the motion of the material and the orbital motion of NS, see Figure 1.2, the material falls radially with a velocity $v_{\rm rel}$ making an angle φ with respect to the line that joins the stars centers of the binary (so, $\sin\varphi = v_{\rm orb}/v_{\rm rel}$). Introducing Cartesian coordinates (y, z) in the plane perpendicular to $\vec{v}_{\rm rel}(a)$, and putting the origin on the NS position, the angular momentum per unit time that crosses a surface element $dydz$ is:

$$d^2\dot{L}_{\rm acc} = \rho_{\rm ej}(y,z)v_{\rm rel}(y,z)^2 y\,dydz. \tag{1.11}$$

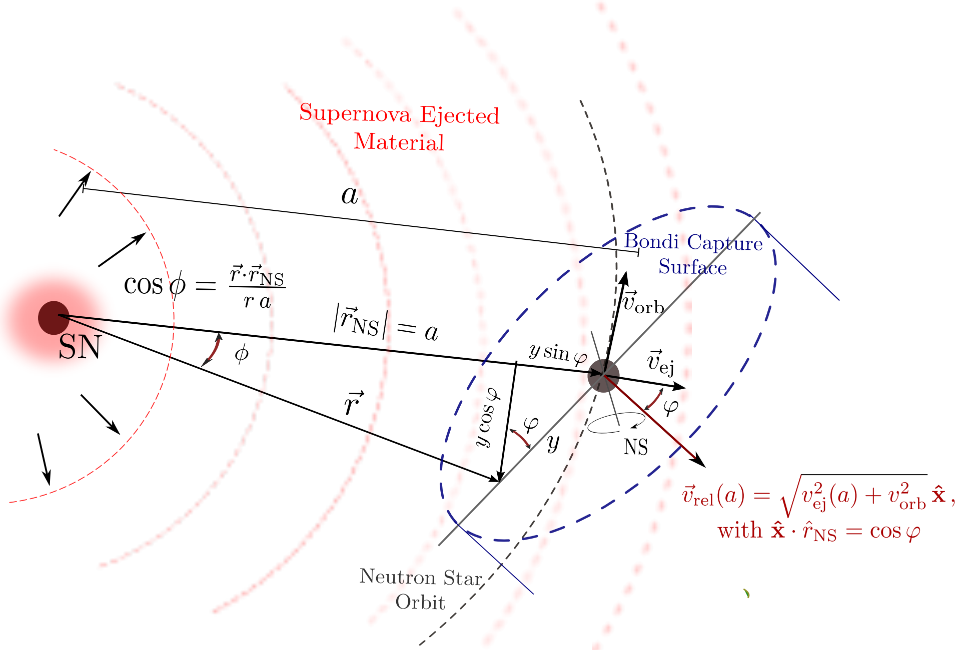

Figure 1.2: Scheme of the IGC scenario: the $\mathrm{CO}_{\rm core}$ undergoes SN explosion and then the NS accretes part of the SN ejecta.

To first order in y, $\rho_{\rm ej}$ and $v_{\rm rel}$ can be written as:

$$\rho_{\rm ej}(y) \simeq \rho_{\rm ej}(a)(1+\epsilon_\rho y)\ , \qquad \text{and} \qquad v_{\rm rel}(y) \simeq v_{\rm rel}(a)(1+\epsilon_\nu y), \tag{1.12}$$

and equation (1.11) becomes

$$d^2\dot{L}_{\rm acc} = \rho_{\rm ej}(a)v_{\rm rel}^2(a)\left[y + (\epsilon_\rho + 2\epsilon_\nu)y^2\right]\, dydz. \tag{1.13}$$

Integrating over the area of the circle delimited by the capture radius

$$y^2 + z^2 = R_{\rm cap}^2 = \left(\frac{2GM_{\rm NS}}{v_{\rm rel}^2(a,t)}\right)^2 (1 - 4\epsilon_\nu y)\,, \tag{1.14}$$

where we have applied $c_{\rm s,ej} \ll v_{\rm ej}$, we obtain the angular momentum per unit time of the ejecta material falling into the gravitational attraction region of the NS

$$\dot{L}_{\rm acc} = \frac{\pi}{2}\left(\frac{1}{2}\epsilon_\rho - 3\epsilon_\nu\right)\rho_{\rm ej}(a,t)v_{\rm rel}^2(a,t)R_{\rm cap}^4(a,t). \tag{1.15}$$

Now, we have to evaluate the terms ϵ_ρ and ϵ_ν of equation (1.15). Following Anzer et al. [4], we start expanding $\rho_{\rm ej}(r)$ and $v_{\rm ej}(r)$ in Taylor series around the binary separation distance, $r = a$:

$$\rho_{\rm ej}(r,t) \approx \rho_{\rm ej}(a,t)\left(1 + \frac{1}{\rho_{ej}(a,t)}\left.\frac{\partial\rho_{\rm ej}}{\partial r}\right|_{(a,t)}\delta r\right)\,, \tag{1.16}$$

$$v_{\rm ej}(r,t) \approx v_{\rm ej}(a,t)\left(1 + \frac{1}{v_{\rm ej}(a,t)}\left.\frac{\partial v_{\rm ej}}{\partial r}\right|_{(a,t)}\delta r\right)\,, \tag{1.17}$$

where we assumed $\delta r = |\vec{r} - \vec{r}_{\rm NS}| \ll 1$, keeping only the first order terms. For the SN material, the continuity equation implies $\dot{\rho}_{\rm ej} = -\vec{\nabla} \cdot (\rho_{\rm ej}\, \vec{v}_{\rm ej})$, and therefore we obtain

$$\epsilon_\rho = \left(\frac{\rho'_{\rm ej}}{\rho_{\rm ej}}\right)_{(a,t)} \sin\varphi = -\left(\frac{2}{r} + \frac{v'_{\rm ej}}{v_{\rm ej}} + \frac{1}{v_{\rm ej}}\frac{\dot{\rho}_{\rm ej}}{\rho_{\rm ej}}\right)_{(a,t)} \sin\varphi. \tag{1.18}$$

On the other hand, defining $\hat{x}$ as a unit vector in the direction of $\vec{v}_{\rm rel}(a)$, the projection of $\vec{v}_{\rm rel}(r)$ on $\hat{x}$ is

$$\hat{x} \cdot \vec{v}_{\rm rel}(r) = v_{\rm ej} \cos(\phi + \varphi) - v_{\rm orb} \cos(\pi/2 - \varphi) \tag{1.19}$$

In the limit when $\delta r \ll 1$, also $\delta r \simeq -y \sin\varphi$ and $\sin\phi \simeq y/r \cos\phi$ (see Figure 1.2). Then, the last expression together with equation (1.17) becomes

$$\hat{x} \cdot \vec{v}_{\rm rel}(r) \simeq v_{\rm ej}(a)\, \cos\varphi + v_{\rm orb} \sin\varphi \left(\frac{v_{\rm ej}}{r} + \frac{\partial v_{\rm ej}}{\partial r}\right)_{(a,t)} y\, \cos\varphi\, \sin\varphi. \tag{1.20}$$

We can write the relative velocity to the NS of the ejected material as

$$v_{\rm rel} \simeq v_{\rm rel}(a,t) + \delta v_{\rm rel}, \tag{1.21}$$

where

$$\delta v_{\rm rel} \simeq \hat{x} \cdot [\vec{v}_{\rm rel}(r) - \vec{v}_{\rm rel}(a)] = -\left(\frac{v_{\rm ej}}{r} + \frac{\partial v_{\rm ej}}{\partial r}\right)_{(a,t)} y\, \cos\varphi\, \sin\varphi.$$

Then, from a simple comparison of equations (1.12) and (1.21), we obtain

$$\epsilon_\nu = -\left(\frac{v_{\rm ej}}{r} + \frac{\partial v_{\rm ej}}{\partial r}\right)_{(a,t)} \frac{\cos\varphi \sin\varphi}{v_{\rm rel}(a)}. \tag{1.22}$$

For the homologous explosion model adopted to describe the expansion dynamics of the ejecta, the parameters ϵ_ρ and ϵ_ν, using equation (1.5) with (1.7) and equation (1.3), respectively, are given by

$$\epsilon_\rho(t) = -\frac{1}{a}\left[\frac{-1}{\ln\left(1/\hat{r}_c\tau^n\right)} + \frac{m}{1 - 1/\hat{r}_s\tau^n}\right] \frac{v_{\rm orb}}{v_{\rm rel}(a,t)}\,, \quad \epsilon_\nu(t) = \frac{2}{a}\left(\frac{v_{\rm ej}}{v_{\rm rel}}\right)^2_{(a,t)} \frac{v_{\rm orb}}{v_{\rm rel}(a,t)}.$$

Replacing the above equations in equation (1.15), the angular momentum per unit time transported by the ejecta crossing the capture region is:

$$\dot{L}_{\rm acc} = 8\pi\, \hat{\rho}_{\rm core} \frac{G M^0_{\rm NS} a^2}{(1+q)^3} H(\tau), \tag{1.23}$$

where

$$H(\tau) = \ln\left(\frac{1}{\hat{r}_c\tau^n}\right) \frac{\left(\hat{r}_s\tau^n - 1\right)^m (1 - \chi\mu_B)}{\tau^{3n}\left(1 + \eta/\tau^2\right)^{-7/2}} \left(\frac{M_{\rm NS}(\tau)}{M^0_{\rm NS}}\right)^4 \left(\frac{-1}{\ln\left(\hat{r}_c\tau^n\right)} - \frac{m\, \hat{r}_s\tau^n}{\hat{r}_s\tau^n - 1} + \frac{6\eta}{\tau^2 + \eta}\right).$$

Thus, the specific angular momentum will be given by: $l_{\rm acc} = \dfrac{\dot{L}_{\rm acc}}{\dot{M}_B}$. Figure 1.3 shows the time evolution of the Bondi-Hoyle accretion rate, obtained from the numerical integration of equation (1.8), of the angular momentum transported by the ejecta, obtained from

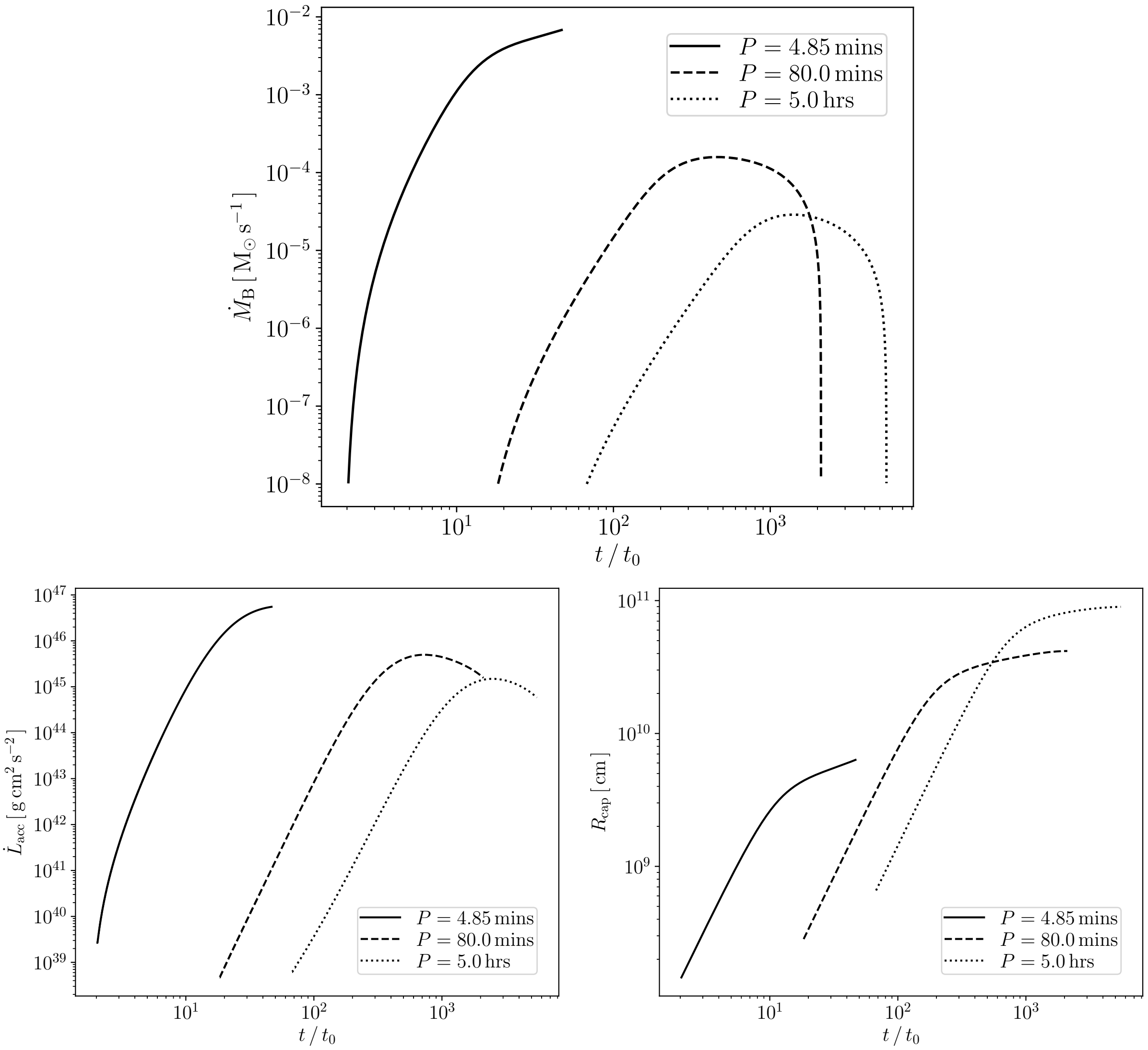

Figure 1.3.: Time evolution of the mass accretion rate (upper panel, in units $M_\odot$ s^{-1}), the angular momentum per unit time transported by the SN ejecta (left bottom panel, in units g cm^2 s^{-2}), and the Bondi-Hoyle capture radius of the NS (rigth bottom panel, in units of cm).The binary parameters adopted were: expansion parameter $n = 1$, an ejecta outermost layer velocity $v_{\rm star,0} = 2 \times 10^9$ cm s^{-1} and the SN ejecta profile is the one obtained for the CO$_{\rm core}$ of the $M_{\rm ZAMS} = 30\ M_\odot$ progenitor of Table 1.1. For the above progenitor and velocity $t_0 = 3.825$ s. Three selected orbital periods are shown: $P = 4.85$ min, 80.0 min and 5.0 h which correspond to binary separation distances $a = 1.48 \times 10^{10}$ cm, 9.61×10^{10} cm, and 2.32×10^{11} cm, respectively. The solid line corresponds to a case in which the NS reaches the critical mass and collapses to a BH (end point of the curve). In the two other cases, owing to the longer orbital period, there is no induced gravitational collapse of the NS to a BH (see Sec. 1.3 for further details).

equation (1.23), and of the capture radius given by equation (1.2) for selected orbital periods. In these simulations we have adopted, for the sake of example, the $M_{\rm ZAMS} = 30\ M_\odot$ CO$_{\rm core}$ progenitor, an expansion parameter $n = 1$, a supernova ejecta velocity $v_{0_{\rm star}} = 2 \times 10^9$ cm s^{-1}, and an initial NS mass, $M_{\rm NS}(t_0) = 2.0\ M_\odot$. Following Fryer et al. [90], we adopt binary parameters such that there is no Roche lobe overflow prior to the SN explosion. For the above CO$_{\rm core}$ and NS parameters, such a condition implies a minimum orbital binary period $P_0 = 4.85$ min.

We can see from Figure 1.3 that the shorter(smaller) the orbital period(separation) the higher the accretion rate and the shorter the time it peak. In Appendix A.1 we derive, following simple arguments, analytic formulas for the peak accretion rate and time which can be useful to get straightforward estimates of these kind of systems.

In Figure 1.3 we can see that the evolution of the accretion rate has a shape composed of a rising part, followed by an almost flat maximum and finally it decreases with time. The rising part corresponds to the passage and accretion of the first layers of the ejecta. The sharpness of the density cut-off of the outermost ejecta layer defines the sharpness of this rising accretion rate. The maximum rate is given by the accretion of the ejecta layers with velocities of the same order as the orbital velocity of the NS. These layers are located very close to the innermost part of the supernova ejecta. Then, the rate start to decrease with the accretion of the innermost layers whose density cut-off determines the sharpness of this decreasing part of the mass accretion rate. See also Appendix A.1 for further details.

1.2.2. Circularization of the Supernova ejecta around the NS

We turn now to the determination of weather or not the SN ejecta possess enough angular momentum to circularize around the NS before being accreted by it. Since, initially, the NS is slowly rotating or non-rotating, we can describe the exterior spacetime of the NS before the accretion process by the Schwarzschild metric. A test-mass particle circular orbit of radius $r_{\rm st}$ possesses in this metric a specific angular momentum given by

$$l_{\rm st} = c\sqrt{\frac{GM_{\rm NS}r_{\rm st}}{c^2}}\left(1-\frac{3GM_{\rm NS}}{c^2 r_{\rm st}}\right)^{-1/2}. \qquad (1.24)$$

Assuming that there are no angular momentum losses once the ejected material enters the NS capture region, hence $l_{\rm st} = l_{\rm acc} = \dot{L}_{\rm acc}/\dot{M}_B$, the material circularizes around the NS at the radii:

$$r_{\rm st} = \frac{1}{2}\left[\frac{l_{\rm acc}^2}{GM_{\rm NS}} + \sqrt{\left(\frac{l_{\rm acc}^2}{GM_{\rm NS}}\right)^2 - 12\left(\frac{l_{\rm acc}}{c}\right)^2}\,\right]. \qquad (1.25)$$

The most bound circular orbit, $r_{\rm mb}$, around a non-rotating NS is located at a distance $r_{\rm mb} = 6GM_{\rm NS}/c^2$ with an angular momentum per unit mass $l_{\rm mb} = 2\sqrt{3}GM_{\rm NS}/c$. The most bound circular orbit is located outside the NS surface for masses larger than 1.78 $M_\odot$, 1.71 $M_\odot$, and 1.67 $M_\odot$ for the GM1, TM1, and NL3 EOS, respectively [49]. It is easy to check (see Figure 1.3) that the SN ejected material has an angular momentum larger than this value, and therefore the ejecta entering into the NS capture region will necessarily circularize at radii $r_{\rm st} > r_{\rm mb}$. We have obtained from our simulations, $r_{\rm st}/r_{\rm mb} \sim 10$–$10^3$.

Even if the SN ejecta possess enough angular momentum to form a disk around the NS, which would prevent it from falling rapidly onto the NS, the viscous forces (and other angular momentum losses) might allow the material to be accreted by the NS when it arrives at the inner boundary of the disk. In the α-disk formalism, the kinetic viscosity is $\nu = \eta/\rho = \alpha c_{s,\rm disk} H$, where η is the dynamical viscosity, H the disk scale height, and

$c_{s,\rm disk}$ the sound velocity of the disk. Following Chevalier [46], the infall time in a disk at radius r is

$$t_{\rm fall} \sim \frac{r_{\rm st}^2}{\alpha c_{\rm s,disk} H} \sim \frac{r_{\rm st}^{3/2}}{\alpha\sqrt{GM_{\rm NS}}}\sqrt{1-\frac{2GM_{\rm NS}}{c^2 r_{\rm st}}}, \tag{1.26}$$

where it is assumed that $H \sim r_{\rm st}$ (thick disk) and $c_{s,\rm disk}$ is of the order of orbital velocity seen by an observer corotating with the particle. Finally, $\alpha \sim 0.01$–0.1 is dimensionless and measures the viscous stress. In our simulations, we have obtained falling times $t_{\rm fall}/\Delta_{\rm acc} \sim 10^{-3}$, where $\Delta_{\rm acc}$ is the characteristic accretion time. Therefore, the SN material can be accreted by the NS in a short time interval without introducing any significant delay.

1.2.3. Asymmetric Supernova and elliptic orbits

In this section, we extend the formalism of the Bondi-Hoyle accretion, presented in the beginning of Section 1.2, in order to introduce first an asymmetric expansion of the SN ejecta and then, an initial binary orbit with an eccentricity greater than zero. This with the scope of evaluate the effects resulting on the hypercritical accretion process onto the NS binary companion.

The observational evidence accumulated in the last years points strongly to SN asymmetric explosions. The high average velocities ($\sim 500\,{\rm km\,s^{-1}}$) present in the observed distribution of pulsar velocities [118] is reconciled with asymmetric stellar collapses and explosions explained by initial asymmetric pre-supernova density profiles [36, 255, 256]. The polarization in the spectra of Type II and Type Ib/c indicates asymmetric envelopes [159, 177, 296]. The double-peak profile of the oxygen emission line of Type Ib/c SN is a distinct signature of an aspherical explosion [171, 282]. Additionally, jets have been mapped for Cas A in the optical [73] and its spatial distribution of ^{44}Ti observed by NuSTAR space telescope shows a global asymmetry [104].

To introduce an asymmetric expansion of the SN ejecta, we assume an homologous evolution for each component of the SN ejecta velocity but with different expansion parameter, i.e:

$$v_{\rm ej,x} = \frac{n_x x}{t} \quad , \quad v_{\rm ej,y} = \frac{n_y y}{t} \quad , \quad v_{\rm ej,z} = \frac{n_z z}{t}. \tag{1.27}$$

Then, the outermost SN layer expands as:

$$\frac{R_{\rm star}(t)}{R_{0,\rm star}} = \left(\frac{t}{t_0}\right)^{n_x}\sqrt{\left(\cos^2\theta + \left(\frac{t}{t_0}\right)^{-2n_x\beta}\sin^2\theta\right)\sin^2\phi + \cos^2\phi}\,, \tag{1.28}$$

where ϕ is the polar angle and θ is the azimutal angle. We have assumed $n_x = n_z$ and $\beta = 1 - n_x/n_y$, that will be called the *asymmetric parameter*. Following equation (1.5), the SN density profile, on the equatorial plane, evolves as:

$$\rho_{\rm ej}(r,\theta,t) = \hat{\rho}_{\rm ej}\ln\left(\frac{r}{\hat{R}_{\rm core}(t)}\right)\left(\frac{R_{\rm star}(t)}{r}-1\right)^m\left[\frac{(t/t_0)^{-3n_x}}{\sqrt{\cos^2\theta + (t/t_0)^{-2n_x\beta}\sin^2\theta}}\right]^3 \tag{1.29}$$

In order to use the Bondi-Hoyle accretion formula, equation (1.1), to estimate the mass accretion rate on the NS, we also need to calculate the relative velocity of the SN ejecta with the NS. Assuming that the NS follows a circular orbit around the SN center when the C))$_{\rm core}$ collapses, the NS position, $\vec{r}_{\rm NS}$, and the NS orbital velocity, $\vec{v}_{\rm NS}$, are:

$$\vec{r}_{\rm NS} = a\left[\cos\theta_{\rm NS}\,\hat{x} + \sin\theta_{\rm NS}\,\hat{y}\right]\,, \quad \vec{v}_{\rm NS} = v_{\rm orb}\left[\sin\theta_{\rm NS}\,(-\hat{x}) + \cos\theta_{\rm NS}\,\hat{y}\right]\,, \tag{1.30}$$

where $\theta_{\rm NS} = \theta_{\rm NS}(\tau) = (v_{\rm orb}/v_{0_{\rm star}})\,(R_{0_{\rm star}}/a)\,\tau$. Thus, along the line that joins the SN center with the NS position, the magnitude of the relative velocity equals to:

$$|\vec{v}_{\rm rel}|^2 = v_{\rm orb}^2\left[\left(\frac{\eta\hat{r}}{\tau}\right)^2\left(1+\beta(\beta-2)\sin^2\theta_{\rm NS}\right) - \frac{2\beta\eta\hat{r}}{\tau}\sin\theta_{\rm NS}\cos\theta_{\rm NS} + 1\right] \tag{1.31}$$

Using equation (1.31) and (1.29) is possible to integrate equation (1.1) and obtains the time evolution of the Bondi-Hoyle mass accretion rate. The results of this integration are shown in Figure 1.4. In these cases, we adopt the same initial binary parameters as in Figure 1.3 and we consider three values for the asymmetric parameter: $\beta = 0.0$ (that recovers the spherical expansion), $\beta = 0.3$ (with $n_x > n_y$) and $\beta = -0.3$ (with $n_y > n_x$). For the longest binary periods, the NS suffers episodes of non-accretion while the SN ejecta expands.

On the other hand, it is straightforward to introduce an initial elliptic orbit for the binary system. In this case, the NS position, $\vec{r}_{\rm NS}$, and velocity, $\vec{v}_{\rm NS}$, are:

$$\vec{r}_{\rm NS} = \frac{a(1-\epsilon^2)}{1+\epsilon\cos\theta}\left[\cos\theta\,\hat{x} + \sin\theta\,\hat{y}\right]\,, \quad \vec{v}_{\rm NS} = \frac{v_{\rm orb}}{\sqrt{1-\epsilon^2}}\left[-\sin\theta\,\hat{x} + (\epsilon + \cos\theta)\,\hat{y}\right] \tag{1.32}$$

where ϵ is the eccentricity of the orbit and the evolution of the angular velocity is given by:

$$\frac{d\theta}{dt} = \sqrt{\frac{G(M_{\rm CO}+M_{\rm NS})}{a^3(1-\epsilon^2)^3}}\,(1+\epsilon\cos\theta)^2 \tag{1.33}$$

Coming back to the spherical SN expansion (i.e. $\vec{v}_{\rm ej} = n\vec{r}/t$), the relative velocity of the SN ejecta with respect to the NS is:

$$|\vec{v}_{\rm rel}|^2 = v_{\rm orb}^2\left(\left(\frac{\eta\hat{r}}{\tau}\right)^2 - \frac{\eta\hat{r}}{\tau}\frac{2\epsilon\sin\theta}{\sqrt{1-\epsilon^2}} + \frac{1+\epsilon+2\epsilon\cos\theta}{1-\epsilon^2}\right) \tag{1.34}$$

The Bondi-Hoyle mass accretion rate can be computed integrating equation (1.1), having replaced $v_{\rm rel}$ by (1.34), simultaneously with equation (1.33). Figure 1.5 shows the evolution of the mass accretion rate and the Bondi-Hoyle capture radius for different values of the eccentricity: $\epsilon = 0.01$, 0.2 and 0.4. An initial eccentricity for the binary orbit can increase the accretion rate by at least one order of magnitude. The mass accretion could be substantially changed, in magnitude and shape, depending of the initial angular position of the NS. In Figure 1.5, we represent the cases with two different NS initial angular position: $\theta(t_0) = 0.0$ (upper panel) and $3\pi/2$ (lower panel).

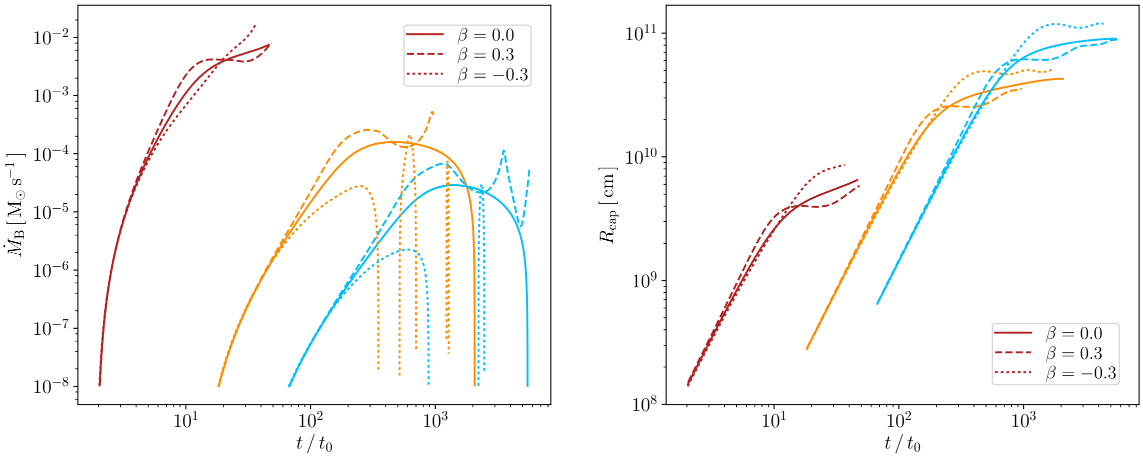

Figure 1.4.: Time evolution of the mass accretion rate (left panel, in units $M_\odot$ s^{-1}) and the Bondi-Hoyle capture radius of the NS (right panel, in units of cm). Here has been introduced an asymmetric expansion for the SN ejecta following equations (1.27) and (1.28). It considers three values for the asymmetric parameter: $\beta = 0.0$ (that recovers the spherical expansion), $\beta = 0.3$ ($n_x > n_y$) and $\beta = -0.3$ ($n_y > n_x$). The binary parameters adopted are the same as in Figure 1.3. Three selected orbital periods are shown: $P = 4.85$ min (red line), 80.0 min (orange line) and 5.0 h (blue line).

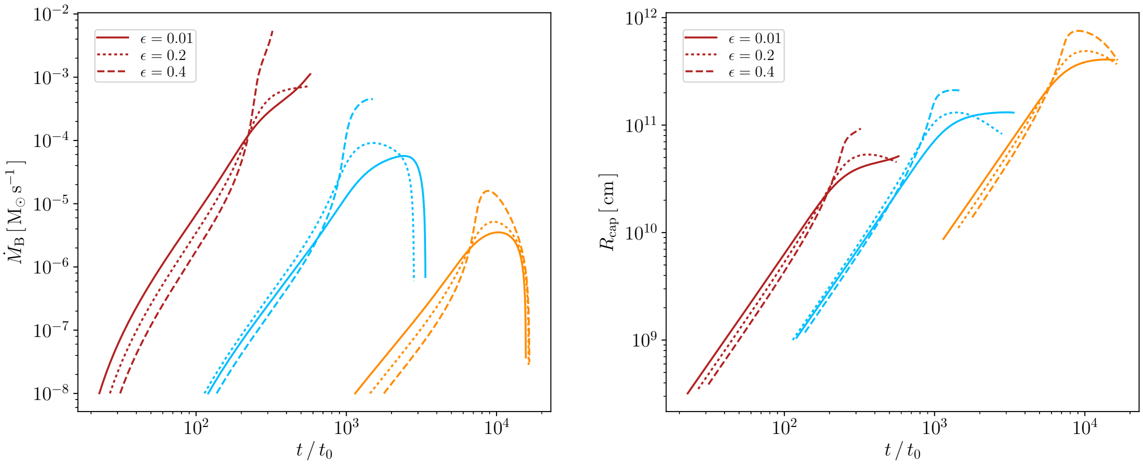

(a) $\theta(t_0) = 0.0$

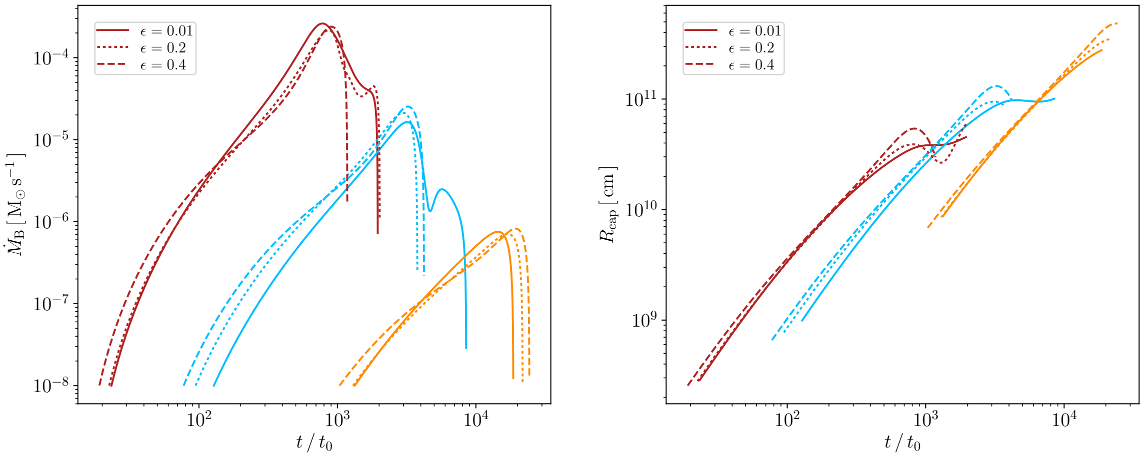

(b) $\theta(t_0) = 3\pi/2$

Figure 1.5.: Time evolution of the mass accretion rate (left panel, in units $M_\odot$ s^{-1}) and the Bondi-Hoyle capture radius of the NS (right panel, in units of cm). Here has been introduced an initial elliptic orbit for the binary system, this make that the accretion rate will depend also on the NS initial angular position at the explosion moment. The binary parameters adopted are the same as in Figure 1.3. Three selected orbital periods are shown: $P = 100.0$ mins (red line), 8.3 hrs (orange line) and 2.1 dys (blue line).

1.3. Time Evolution of the Accreting NS

Our first estimate of the angular momentum transported by the SN ejecta has shown that the material has enough angular momentum to circularize around the NS for a short time and form a kind of thick disk. The viscous force torques in the disk (and other possible torques) allow a sufficient angular momentum loss until the material arrives at the inner boundary of the disk, $R_{\rm in}$, then falling into the NS surface. Thus, the accreted material will transfer both baryonic mass and angular momentum to the NS.

The equilibrium NS configurations form a two-parameter family given, for example, by the mass (baryonic or gravitational) and angular momentum (or angular velocity). Namely the NS gravitational mass, $M_{\rm NS}$, is in general a function of the NS baryonic mass, M_b, and angular momentum, $J_{\rm NS}$. In a similar way the angular momentum contributes to the mass of a BH [48]. It is then clear that the evolution of the NS gravitational mass is given by:

$$\dot{M}_{\rm NS}(t) = \left(\frac{\partial M_{\rm NS}}{\partial M_b}\right)_J \dot{M}_b + \left(\frac{\partial M_{\rm NS}}{\partial J_{\rm NS}}\right)_{M_b} \dot{J}_{\rm NS}, \tag{1.35}$$

We assume that all the (baryonic) mass entering the NS capture region will be accreted by the NS, i.e:

$$M_b(t) = M_b(t_0) + M_B(t), \tag{1.36}$$

then $\dot{M}_b \equiv \dot{M}_B$. The relation between the NS gravitational mass, the baryonic mass, and the angular momentum for a rotating NS equilibrium configuration fully including the effects of rotation in general relativity, as well as other NS properties, are summarized in Appendix A.2.

The torque on the NS by the accreted matter is given by

$$\dot{J}_{\rm NS} = \xi l(R_{\rm in})\dot{M}_B, \tag{1.37}$$

where $R_{\rm in}$ is the disk inner boundary radius, $l(R_{\rm in})$ is the angular momentum per unit mass of the material located at $r = R_{\rm in}$, and $\xi \leq 1$ is a parameter that accounts for the efficiency of the angular momentum transfer. The precise value of ξ depends mainly: 1) on possible angular momentum losses (e.g. by jetted emission during accretion) and 2) on the deceleration of the matter in the disk inner radius zone.

The inner disk radius is given by the maximum between the radius of the last stable circular orbit, $r_{\rm lso}$, and the NS radius, $R_{\rm NS}$. Namely, $R_{\rm in} = \max(r_{\rm lso}, R_{\rm NS})$. When the disk extends until the NS surface, $l(R_{\rm in})$ is given by the Keplerian orbit with radius equal to the NS equatorial radius. On the other hand, if $R_{\rm NS} < r_{\rm lso}$, $l(R_{\rm in})$ is given by the last stable circular orbit. Summarizing:

$$l(R_{\rm in}) = \begin{cases} l_{\rm K}(R_{\rm NS}), & \text{for } R_{\rm NS} > r_{\rm lso} \Rightarrow R_{\rm in} = R_{\rm NS}, \\ l_{\rm lso}, & \text{for } R_{\rm NS} \leq r_{\rm lso} \Rightarrow R_{\rm in} = r_{\rm lso}. \end{cases} \tag{1.38}$$

Here, we have worked with three selected NS nuclear equation of state (EOS): NL3, TM1 and GM1 [49]. For these EOS and assuming that the NS is initially non-rotating, we have that $r_{\rm lso} = 6GM_{\rm NS}/c^2 > R_{\rm NS}$ for $M_{\rm NS} \gtrsim [1.78, 1.71, 1.67]\ M_\odot$, for the NL3, TM1 and GM1 EOS, respectively. For rotating NSs, the minimum mass over which the last stable orbit lies outside the NS surface becomes a function of the NS angular momentum (see [50] and Appendix A.2).

For the axially symmetric exterior spacetime around a rotating NS, the last stable circular orbit, $l_{\rm lso}$, for co-rotating particles, is well approximated by [14, 50]:

$$l_{\rm lso} \approx 2\sqrt{3}\frac{GM_{\rm NS}}{c}\left[1 - \frac{1}{10}\left(\frac{j_{\rm NS}}{M_{\rm NS}/M_\odot}\right)^{0.85}\right], \tag{1.39}$$

where $j_{\rm NS} \equiv cJ_{\rm NS}/(GM_\odot^2)$, and which is independent on the nuclear EOS.

On the contrary, when, $r_{\rm lso} < R_{\rm NS}$ and thus $R_{\rm in} = R_{\rm NS}$, we shall adopt for this case the Hartle's slow-rotation approximation. The angular momentum per unit mass of a Keplerian orbit with a radius equal to the NS radius is, within this approximation, given by [31]

$$l_{\rm K}\,(u) = \frac{GM_{\rm NS}}{c\sqrt{u\,(1-3u)}}\left[1 - j_{\rm NS}\frac{3\,u^{3/2}(1-2u)}{1-3u} + j_{\rm NS}^2\frac{u^4(3-4u)}{(1-2u)^2(1-3u)}\right], \tag{1.40}$$

where $u \equiv GM_{\rm NS}/(c^2 R_{\rm NS})$. This formula can be also obtained by taking the second order slow rotation limit of the angular momentum of the last stable circular orbit around a Kerr BH [29, 31, 222].

Therefore, by solving (numerically) simultaneously equations (1.8) and (1.37), with the aid of equations (1.35)–(1.40), it is possible to follow the evolution of the NS mass and angular momentum during the accretion process. The integration is continued until the NS gets outside the stability zone or all the SN ejecta passes the NS capture radius. The stability of the accreting NS is limited by two main instability conditions: the mass-shedding or Keplerian limit, and the secular axisymmetric instability. Mass-shedding occurs when the centrifugal force balances the gravitational one. Thus, for a given gravitational mass (or central density), it is given by the rotating configuration with angular velocity equal to the Keplerian velocity of test-particles orbiting at the star's equator. In this limit the matter at the surface is marginally bound to the star and small perturbations will cause mass loss to bring the star stable again or otherwise to bring it to a point of dynamical instability point [275].

At the secular axisymmetric instability point the star is unstable against axisymmetric perturbations. It is expected to evolve first quasi-stationary to then find a dynamical instability point where gravitational collapse takes place [275]. Using the turning-point method [76], Cipolletta et al. [49] computed the critical mass due to this instability point for the NL3, GM1 and TM1 EOS (see equation (A.14) in Appendix A.2).

In Figure 1.6, we show the evolution of the NS mass as a function of its angular momentum during the accretion process for two selected efficiency parameter for the NS angular momentum rate: $\xi = 0.5$ and $\xi = 1.0$, and for selected values of the initial NS mass:

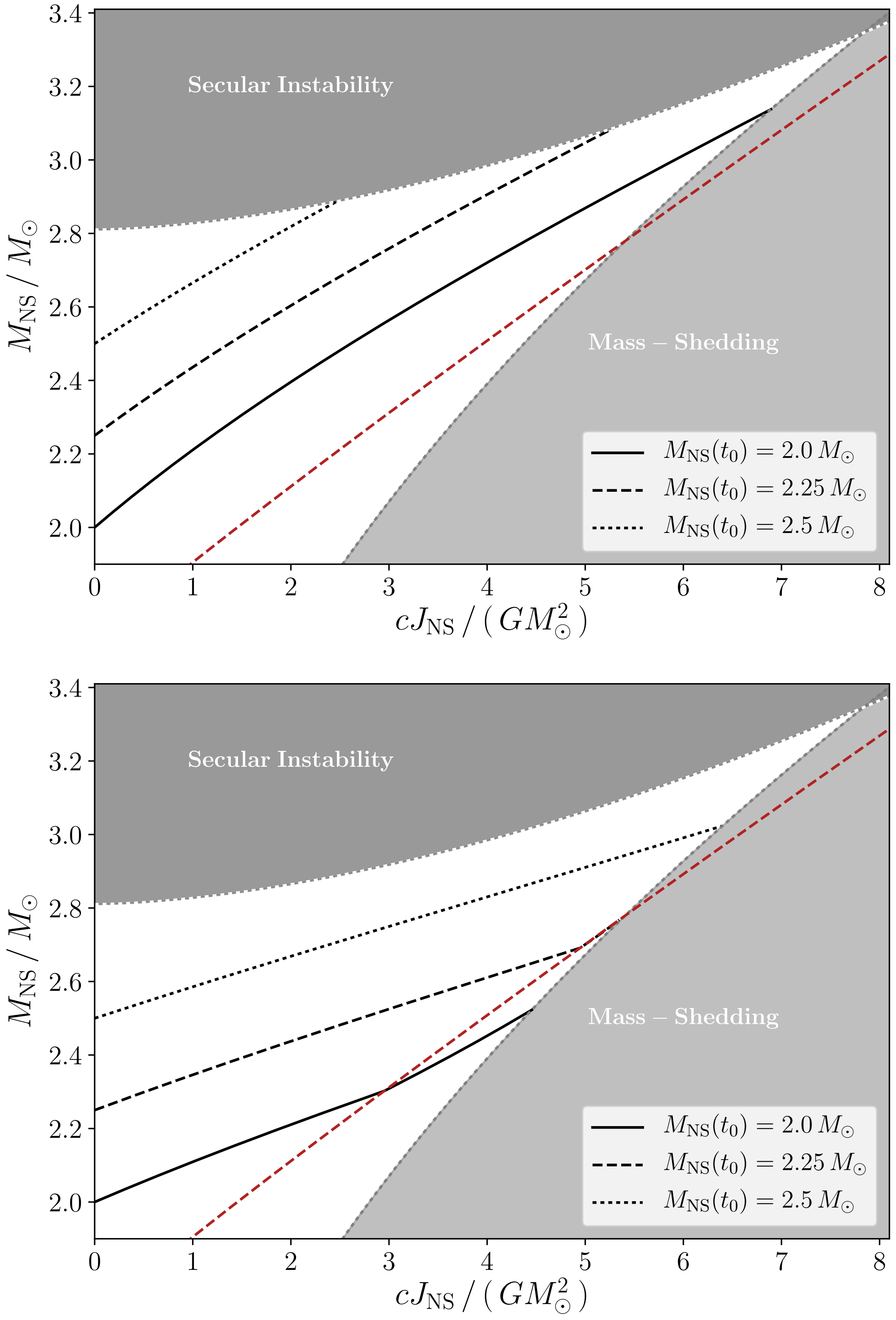

Figure 1.6.: NS mass as a function of its angular momentum gain for two selected efficient parameter: $\xi = 0.5$ (upper panel) and $\xi = 1.0$ (bottom panel). Three evolutionary paths of the NS are shown, each starting from a different initial NS mass $M_{\rm NS}^0 = 2.0$, 2.25, and 2.5 $M_\odot$, and without loss of generality we have adopted the NL3 nuclear EOS. We use here the ejecta from the explosion of a CO$_{\rm core}$ by the 30 $M_\odot$ ZAMS progenitor, $v_{\rm star,0} = 2 \times 10^9$ cm s^{-1} and expansion parameter $n = 1$. The red color line represents the configurations at which $r_{\rm lso} = R_{\rm NS}$: the configurations below this line have stable orbits down the NS surface, while configurations above it have an external ISCO.

$M^0_{\rm NS} = 2.0$, 2.25, and 2.5 $M_\odot$. The NS fate will depend on the initial mass and the efficient parameter. When the transfer of angular momentum to the NS is highly efficient ($\xi = 1.0$), all the configurations reach the mass-shedding limit. Meanwhile, when $\xi = 0.5$, we see how the NS starting with $M^0_{\rm NS} = 2.0\ M_\odot$ reaches the mass-shedding limit while, for higher initial masses, the NS ends at the secular axisymmetric instability region. It's important to recall, that only the NSs that end at the mass-shedding limit, reach the maximum possible value of the dimensionless angular momentum: $cJ_{\rm NS}/(GM^2_{\rm NS}) \approx 0.7$. The ones that become secularly unstable, do it with lower angular momentum.

1.4. Mass flux through the capture radius

Up to here, we have estimated the mass accretion rate on the NS in the IGC scenario following the Bondi-Hoyle accretion formalism. However, as was pointed by Fryer et al. [90], this formalism is valid in steady-state systems. Additionally, it is constructed assuming spherical symmetry, with the accretor moving at constant speed through an uniform medium [see 68]. Neither of these conditions are filled by the IGC scenario, then we need to determinate the validity of the formalism presented in the last sections.

As a first step, in order to evaluate the accuracy of the Bondi-Hoyle accretion formalism applied to describe the IGC scenario, we calculate the mass flux that crosses the NS capture radius during the expansion of the SN ejecta. The material that could be potentially accreted by the NS would be the one that is bounded to its gravitational potential, i.e. its kinetic energy is less that its gravitational potential energy:

$$\frac{1}{2}|\vec{v}_{\rm rel}|^2 \leq \frac{GM_{\rm NS}}{r}\ , \tag{1.41}$$

being r the distant of the material to the SN ejecta center. If we assume that the NS follows a circular orbit around the SN center and since the SN expansion is spherically symmetric, without lost of generality, we can assume that the NS is static at $(\,a, 0, 0\,)$ with velocity $(\,0, v_{\rm orb}, 0\,)$. Thus, the relative velocity of the ejecta material with respect to the NS can be written as:

$$\vec{v}_{\rm rel} = v_{\rm orb}\left[\,\alpha(\tau)(x-1)\,\hat{x} + (\alpha(\tau)y - 1)\,\hat{y} + \alpha(\tau)z\,\hat{z}\,\right]\ , \tag{1.42}$$

with $\alpha(\tau) = (a/v_{\rm orb})\,/(t_0\tau)$. The last expression is written in cartesian coordinates. The NS capture surface is given by:

$$f_{\rm cap}(x,y,z) = -\frac{2M_{\rm NS}(\tau)/M}{\sqrt{x^2+y^2+z^2}} + \alpha(\tau)^2\left((x-1)^2 + y^2 + z^2\right) - 2\alpha(\tau)\,y + 1 = 0\,. \tag{1.43}$$

In the last two equations, the center of the reference system is on the NS position and the spatial coordinates (x, y, z) are in units of the binary separation, a. The mass flux through the capture surface is defined as:

$$\Phi_M(f_{\rm cap}) = \int_S \rho_{\rm ej}(x,y,z,\tau)\ (\vec{v}_{\rm rel} - \vec{v})\cdot d\vec{S}\,. \tag{1.44}$$

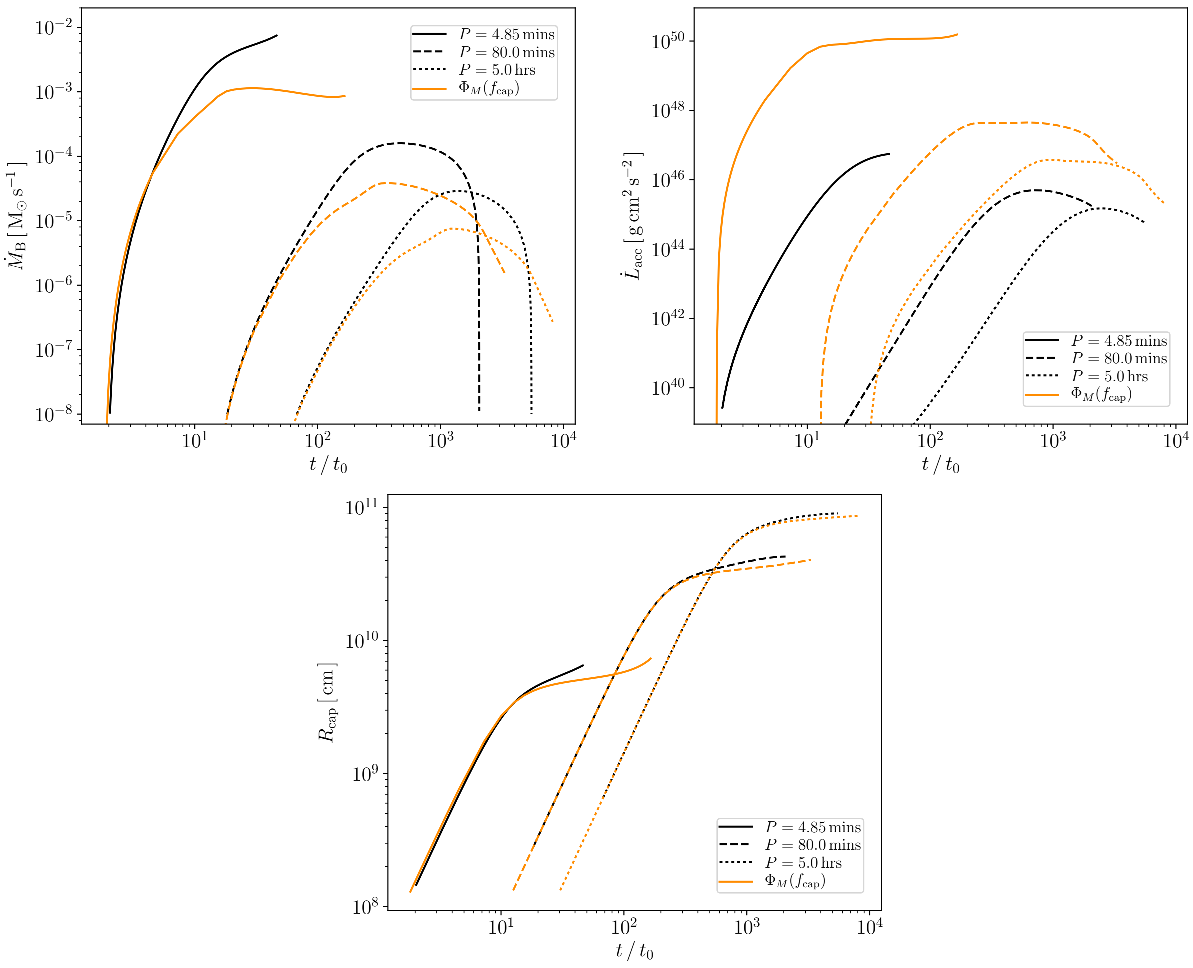

Figure 1.7.: Comparison of the evolution of the mass flux (left upper panel), angular momentum flux (right upper panel) and capture radius (bottom panel) obtaining integrating equations (1.44) and (1.48) (in orange lines) with results obtained with the Bondi-Hoyle formalism (in black lines). The $\rm CO_{core}$ progenitor and the initial binary parameters are the same as in Figure 1.3

Using equation (1.43), the surface element, $d\vec{S}$, is:

$$d\vec{S} = \frac{\vec{\nabla} f_{\rm cap}}{|\vec{\nabla} f_{\rm cap}|}\,ds = \frac{(Bx-\alpha^2)\;\hat{x} + (By-\alpha)\;\hat{y} + Bz\;\hat{z}}{\sqrt{(B-\alpha^2)(3B(x^2+y^2+z^2)-\alpha^2+1)}}\,ds \tag{1.45}$$

with

$$B = \frac{M_{\rm NS}/M}{(x^2+y^2+z^2)^{3/2}} + \alpha^2\,.$$

The second term in equation (1.43) is related with the change in time of the capture surface, and is defined as:

$$\vec{v}\cdot\frac{\vec{\nabla} f_{\rm cap}}{|\vec{\nabla} f_{\rm cap}|} = -\frac{\dot{f}_{\rm cap}}{|\vec{\nabla} f_{\rm cap}|}\,, \tag{1.46}$$

where

$$\dot{f}_{\rm cap} = \frac{2\dot{M}_{\rm NS}/M}{\sqrt{x^2+y^2+z^2}} + \frac{\alpha^2}{\tau}\left(x^2+y^2+z^2+1\right) - \frac{\alpha}{\tau}\left(2\alpha x + y\right)\,. \tag{1.47}$$

In the same way, the flux of angular momentum crossing the capture surface is:

$$\begin{aligned}\Phi_L(f_{\rm cap}) &= \int_S \rho_{\rm ej}(x,y,z,\tau)|\vec{r}\times v_{\rm rel}|\ (\vec{v}_{\rm rel}-\vec{v})\cdot d\vec{S} \\ &= \int_S \rho_{\rm ej}(x,y,z,\tau)\sqrt{(\alpha y - x)^2 + (1+\alpha^2)\,z^2}\ (\vec{v}_{\rm rel}-\vec{v})\cdot d\vec{S} \qquad (1.48)\end{aligned}$$

In Figure 1.7 is shown the evolution of the mass and angular momentum flux through the NS capture surface obtained by the integration of equations (1.44) and (1.48). Also is shown the evolution of the capture radius defined as the distance to the capture surface at the equatorial plane. To compare, we have also plotted the results obtained using the Bondi-Hoyle formalism presented in Section 1.2. The $\mathrm{CO_{core}}$ progenitor and the initial binary parameters are the same as in Figure 1.3. In general, the mass fluxes obtained are around one order of magnitude smaller that the accretion rate given by the Bondi-Hoyle formalism, but are still high enough to make the NS collapses in a short time interval. On the contrary, the angular momentum flux is greater by more than three order of magnitude. This can be explained in the fact that when we estimate the angular momentum transported by the SN ejecta, as a first order approximation, we have assumed that the capture radius is much smaller that the binary separation. In Figure 1.7, it can be seen that the ration $R_{\rm cap}/a$ grows up to ~ 0.1. It's important to notice, that no matter our estimations underestimate the angular momentum transported by the SN ejecta material, the picture of the disk accretion is still valid in the IGC scenario and the NS will evolve accreating from a disk.

1.5. Concluding remarks and perspectives

We have analysed the IGC paradigm of long GRBs associated with supernovae. The progenitor is a binary system composed of a $\mathrm{CO_{core}}$ and a NS in which the explosion of the $\mathrm{CO_{core}}$ as a SN triggers a hypercritical accretion process onto the NS. We have estimated the accretion on the NS with the Bondi-Hoyle formalism and then and computed the angular momentum transported by the SN ejecta expanding in the tight $\mathrm{CO_{core}}$-NS binary system. We have shown that the angular momentum of the ejecta is high enough to circularize, although for a short time, around the NS forming a kind of thick disk. We have extended our model introducing an asymmetric expansion for the SN motion and an initial eccentricity for the binary orbit.

We have computed both the evolution of the NS mass and angular momentum assuming that the material falls onto the NS surface from an inner disk radius position given by the mostly bound circular orbit around the NS or by the NS equatorial radius. The properties of the mostly bound orbit, namely binding energy and angular momentum, have been computed in the axially symmetric case with full rotational effects in general relativity. We have computed the changes of these properties in a dynamical fashion accounting for the change of the exterior gravitational field due to the increasing NS mass and angular momentum. We have shown that the fate of the NS depends on its initial mass. Only those NSs reaching the mass-shedding limit are spun-up up to the maximum

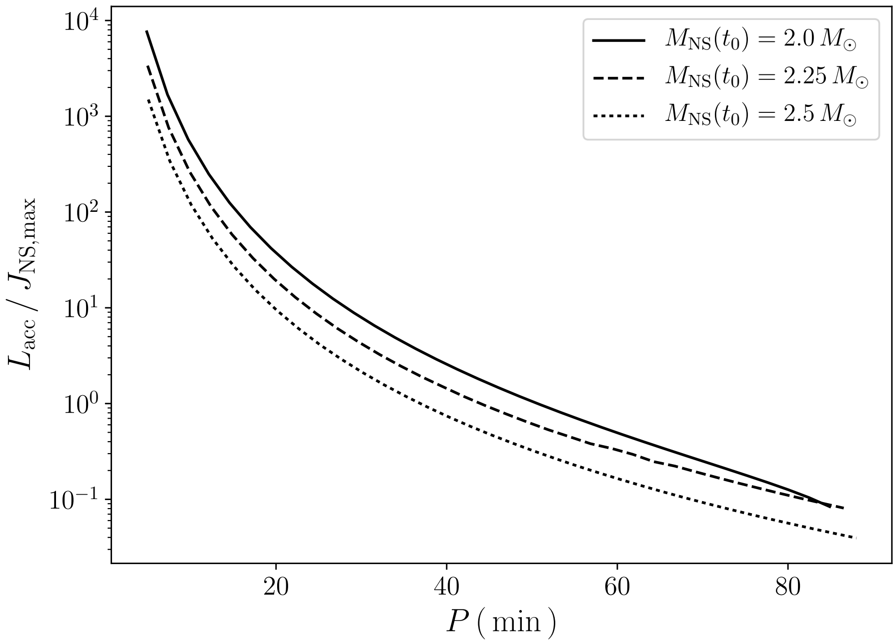

Figure 1.8: Ratio between the total angular momentum transported by the ejecta circularized around the NS and the maximum angular momentum of the NS when it reaches the instability point, for the NL3 EOS.

value of the angular momentum, $J_{\rm NS,max} \approx 0.7G(M_{\rm crit}^{J\neq 0})^2/c$. In the cases in which the NS collapses, since the NS dimensionless angular momentum reaches a maximum value < 1, the new BH formed out of the gravitational collapse of the NS is initially not maximally rotating. Further accretion of mass and angular momentum from material kept bound into the system might lead the BH to approach maximal rotation, however it is out of the scope of this work to explore such a possibility and will be the subject of a forthcoming works.

We can compute the total angular momentum transported by the SN ejecta material, $L_{\rm acc}$, by integrating the angular momentum per unit time $\dot{L}_{\rm acc}$ during the entire time interval of the accretion process up to the point when the NS reaches the instability region. If we compare the value of $L_{\rm acc}$ with the maximum possible angular momentum that an NS can support, $J_{\rm NS,max}$, we have $L_{\rm acc} > J_{\rm NS,max}$, see Figure 1.8, there is an excess of angular momentum in the system With even a mild amount of angular momentum, this accretion drives a strong outflow along the axis of angular momentum [79, 86], ejecting up to 25% of the infalling material, removing much of the angular momentum. The ejecta may undergo rapid neutron capture producing r-process elements [86]. Much more work is needed to determine if there are any observation implications of these expelled materials.

To conclude, we have advanced the first estimates of the role of the angular momentum transported by the SN ejecta into the final fate of the NS companion in the IGC scenario. In order to keep the problem tractable and to extract the main features of these complex systems, we have adopted a series of approximations. (1) We have applied the Bondi-Hoyle-Lyttleton formalism to compute the accretion rate onto the NS; the IGC scenario are time-varying systems that might challenge the validity of this framework which is valid for steady-state systems [see 68, and references therein]. (2) We have adopted Taylor series expansions of the SN ejecta density and velocity around the NS under the assumption that the Bondi-Hoyle radius is small as compared with the binary separation; this has to be considered a first order solution to the problem since for the conditions of the IGC scenario we have $R_{\rm cap} \sim (0.01\text{–}0.1)\,a$. (3) We have adopted an homologous expansion model for the

SN ejecta which could lead to the suspicion of producing artificially higher accretion rates onto the NS due to the low-velocity inner layers of the ejecta. However, it was already shown [see figure 3 in 90] that the homologous model leads to an accretion process lasting for a longer time with respect to more realistic explosion models but with lower accretion rates such that the time-integrated accretion rate leads to a lower amount of accreted material by the NS. (4) We have adopted some characteristic values for the homologous expansion parameter of the SN ejecta ($n = 1$), for the initial velocity of the outermost SN ejecta layer ($v_{0_{\rm star}} = 2 \times 10^9$ cm s^{-1}), for the efficiency of the angular momentum transfer from the circularized matter to the NS ($\xi = 0.5 - 1.0$). Thus, a systematic analysis of simulations exploring the entire possible range of the above parameters as well as full 2D and/or 3D of the SN explosion and accretion are required in order to validate and/or improve our results.

2. Family-1 (i.e. XRFs) and Family-2 (i.e. BdHNe) for Long GRBs

2.1. Introduction

In Chapter 1 was presented the IGC paradigm as progenitor of long-GRBs associated with SNe Ib/c. The initial in-state configuration is a close binary system composed of a $\mathrm{CO_{core}}$ star and a NS. The SN explosion of the $\mathrm{CO_{core}}$ triggers an hypercritical accretion process on the NS companion. The out-state configuration from this process depends of the initial binary parameter and the SN characteristics. Up to now, we have estimated the accretion rate on the NS based on the Bondi-Hoyle accretion formalism and followed its mass and angular momentum evolution during the accretion process. Below, we show that exist limiting binary parameters leading to lower accretion rates onto the NS and to a total accreted matter not sufficient to bring the NS to the gravitational collapse, namely, not sufficient to reach the NS critical mass. The identification of such limiting parameters introduces a dichotomy in the final product of $\mathrm{CO_{core}}$-NS binary, with consequent different observational signatures [i.e. see 243, 246, and also see Chapter 4]: Family-1 long GRBs (i.e. XRFs) in which the NS does not collapse to a BH, and the final system being a new NSs binary or two runaway NSs, if the system remains bound or gets disrupted, respectively; and Family-2 long GRBs (i.e BdHNe) in which the NS collapses to a BH, leading to a new NS-BH binary [88].

We organize this chapter as follows. In Section 2.2, we continue the calculations of Chapter 1 and compute the maximum orbital period, $P_{\max}$ (having fixed the other system parameters, i,e. NS initial mass, $\mathrm{CO_{core}}$ progenitor and SN velocity) up to which the induced gravitational collapse of the NS to a BH by accretion can occur, defining the information family's dichotomy. In Section 2.3, we discuss a possible evolutionary scenario leading to the IGC in-state binary systems and compare and contrast our picture with existing binary evolution simulations in the literature. We also discuss the disruptions of the final configurations in the IGC scenario following Fryer et al. [88]. Finally, in Section 2.4, we summarize our results.

2.2. The Induced Gravitational Collapse of the NS

Base on the results of Section 1.3, we proceed now to calculate the binary parameters which discriminate systems in which the NS can reach by accretion its critical mass ($M_{\rm crit}$) and consequently collapse to a BH, from the systems in which the accretion is not sufficient to induce such a collapse. Thus, a NS with initial mass $M_{\rm NS}(t_0) = M_{\rm NS}^0$ can reach $M_{\rm crit}$ if it accretes an amount of mass $\Delta M_{\rm acc} = M_{\rm crit} - M_{\rm NS}^0$ from the SN ejecta. Given the initial NS mass, the $\rm CO_{core}$ mass, and the SN ejecta profile and its velocity, the accretion rate increases for shorter binary separation, namely for shorter orbital periods (see Figure 1.3 and [90]). Therefore, there exists a maximum orbital period, denoted here as $P_{\rm max}$, up to which, given $M_{\rm NS}^0$ (and all the other binary parameters), the NS can accrete this precise amount of mass, $\Delta M_{\rm acc}$.

For example, for a NS with an initial gravitational mass $M_{\rm NS}^0 = 2\ M_\odot$ accreting the ejected material from the SN explosion of the 30 $M_\odot$ ZAMS progenitor (see Table 1.1), $v_{0_{\rm star}} = 2 \times 10^9$ cm s^{-1}, expansion parameter $n = 1$ and angular momentum transfer efficiency $\xi = 0.5$, we find $P_{\rm max} \approx 26$ min. Figure. 2.1 shows the evolution of such a NS for two different binary periods, $P = 5$ min $< P_{\rm max}$ and $P = 50$ min $> P_{\rm max}$. We can see that only for the system with $P < P_{\rm max}$ the NS accretes enough matter to reach the critical mass for gravitational collapse, given by equation (A.14).

Figure 2.2 shows $P_{\rm max}$, obtained from our numerical simulations, for different values of the NS initial gravitational mass, keeping all the other binary parameters fixed. In this figure we show the results for two pre-supernova progenitors listed in Table 1.1: the $\rm CO_{core}$ progenitors with $M_{\rm ZAMS} = 20\ M_\odot$ (left panel) and 30 $M_\odot$ (right panel), and for two values of the angular momentum transfer efficient parameter: $\xi = 1.0$ (upper panel) and $\xi = 0.5$ (lower panel); additionally we adopt a free expansion for the SN explosion ($n = 1$), and a velocity of the outermost SN ejecta layer, $v_{0_{\rm star}} = 2 \times 10^9$ cm s^{-1}.

A few comments on Figure 2.2 are in order:

1. The increase of $P_{\rm max}$ with the initial NS mass value $M_{\rm NS}^0$ can be easily understood from the fact that the larger $M_{\rm NS}^0$ the lower the amount of mass needed to reach the critical NS mass.

2. There is a transition in the behavior at $M_{\rm NS}^0 \approx 1.7\ M_\odot$. This occurs because configurations with $M_{\rm NS}^0 \lesssim 1.7\ M_\odot$ have the disk extending up to the NS surface, correspondingly we used the angular momentum per unit mass given by equation (1.40). For larger initial masses, accretion occurs from the last stable orbit and we used equation (1.39). Thus, the difference around this transition point are attributable to the use of the slow rotation approximation for masses $M_{\rm NS}^0 < 1.7\ M_\odot$.

3. In order to see the effect of the angular momentum transfer efficiency parameter we adopted in the simulations the maximum possible value, $\xi = 1$, and a lower value case, $\xi = 0.5$. Values of ξ lower than unity account for possible angular momentum losses between the inner disk radius and the NS surface. This implies that the values

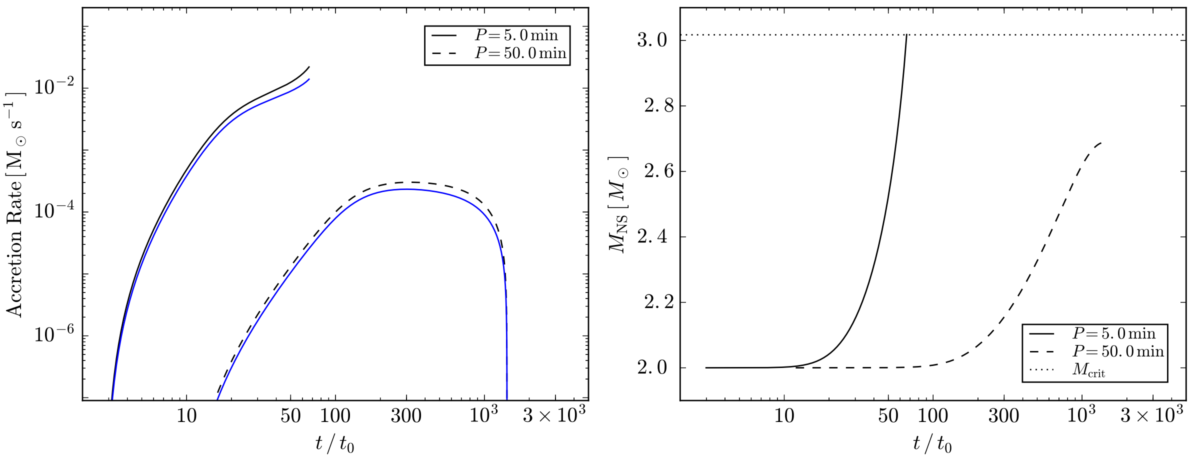

Figure 2.1.: *Left panel:* time evolution of the baryonic mass accretion rate (black curve) obtained from equation (1.8) and rate of increase of the NS gravitational mass (blue curve) obtained from equation (1.35). *Right panel:* Evolution of the NS gravitational mass. We use Here the ejecta from the explosion of a CO$_{\rm core}$ left by the 30 $M_\odot$ ZAMS progenitor, $v_{0_{\rm star}} = 2 \times 10^9$ cm s^{-1}, expansion parameter $n = 1$ and angular momentum transfer efficiency, $\xi = 0.5$. Two binary periods are here used: $P = 5$ min $< P_{\rm max}$ (solid curves) and $P = 50$ min$> P_{\rm max}$(dashed curves). For these binary parameters $P_{\rm max} \approx 26$ min. It can be seen only the NS in the system with $P < P_{\rm max}$ accretes enough matter to reach the critical mass (dotted line) for gravitational collapse.

of $P_{\rm max}$ with $\xi = 1.0$, in Figure 2.2, are upper limits to the maximum orbital period for BH formation. Namely, a value $\xi < 1$ leads to lower values of $P_{\rm max}$. For instance, in the right panel of Figure 2.2 we see that for $M_{\rm NS}^0 = 1.8\ M_\odot$ and the NL3 EOS, $P_{\rm max} \approx 70$ min when $\xi = 1.0$ and for the same initial mass and EOS, $\xi = 0.5$ would instead lead to $P_{\rm max} \approx 20$ min.

4. When it is adopted the highly efficient angular momentum transfer ($\xi = 1$), the NS in the systems of Figure 2.2 ends at the mass-shedding limit. This is the reason why the values for $P_{\rm max}$ are the same, independently of the EOS adopted. In the case of lower values of ξ, the NS might end directly at the secular axisymmetric instability with a lower values of the critical mass with respect to the maximum mass along the Keplerian mass-shedding sequence. We have checked, for instance in the case of $\xi = 0.5$ and the NL3 EOS, that this occurs when the initial NS mass is close to the non-rotating critical mass value, e.g. for $M_{\rm NS}^0 \gtrsim 2.2\ M_\odot$ [see Figure 1.6]. In this case, the EOS leads to different values of the $P_{\rm max}$. Since the others EOS adopted in this work (TM1 and GM1) give lower values of the critical NS mass with respect to the NL3 EOS (see Table A.1 and [49]), the maximum orbital period to have BH formation is longer for the same NS mass.

5. We studied here different progenitors. At first sight, it might appear contradictory that the left panel of Figure 2.2, which is for a less massive CO$_{\rm core}$ with respect to the one the right panel, shows longer values of the maximum orbital period for BH formation. The reason for this is as follows. First, the binary separation satisfies $a \propto (M_t P^2)^{1/3}$ where M_t is the total binary mass. Thus, for given NS mass and binary period, a less massive CO$_{\rm core}$ implies a less massive binary and a smaller orbit by a factor $a_1/a_2 = (M_{t1}/M_{t2})^{1/3}$. A tighter orbit implies a supernova ejecta density at the NS position higher by a factor $\rho_{\rm ej,1}/\rho_{\rm ej,2} = (a_2/a_1)^3 = M_{t2}/M_{t1}$, hence the accretion rate which is proportional to the density [see equation (1.1)].

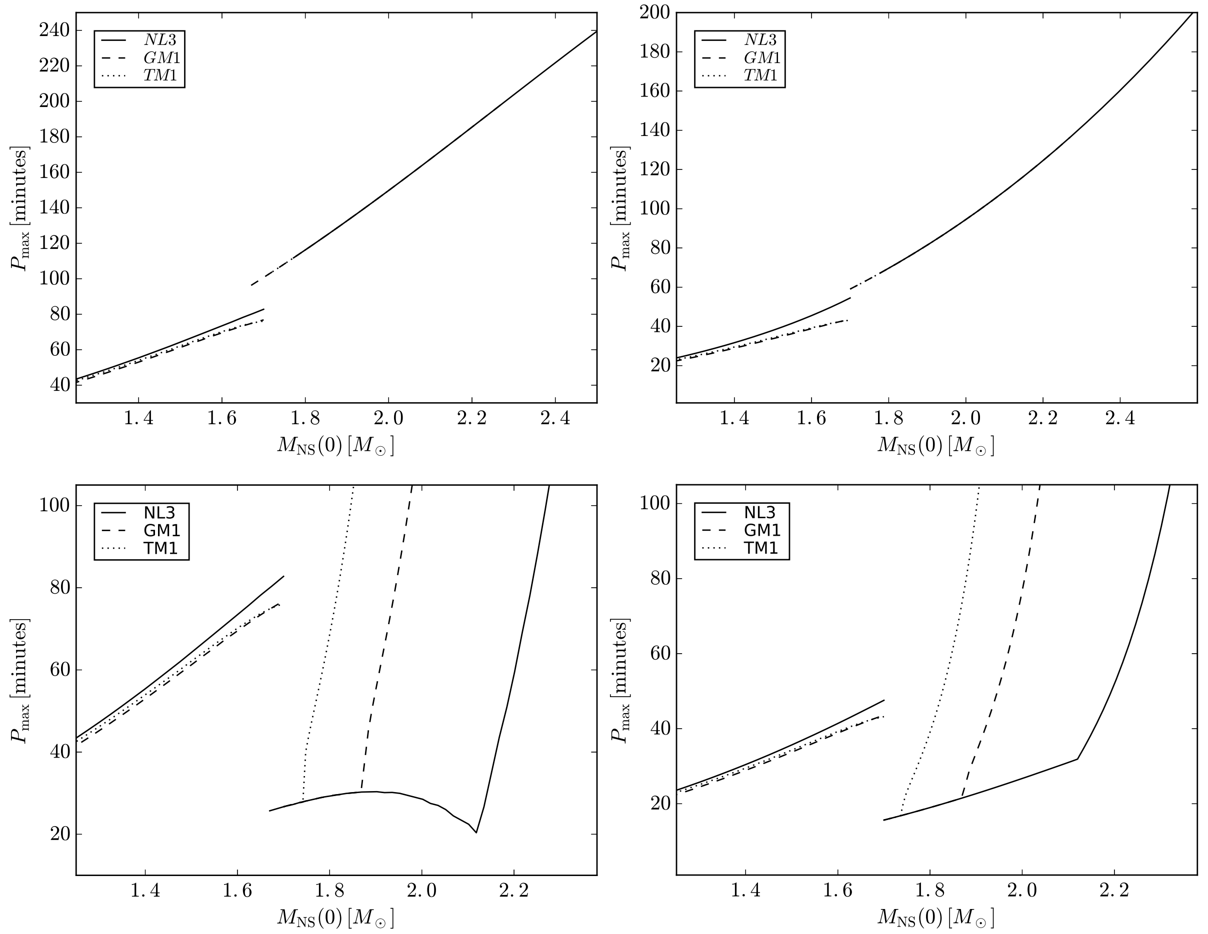

Figure 2.2.: Maximum orbital period for which the NS with initial mass $M_{\rm NS}^0$ collapses to a BH by accretion of SN ejecta material. We have adopted a free expansion for the supernova ejecta ($n = 1$), an outermost SN layer velocity $v_{0_{\rm star}} = 2 \times 10^9$ cm s^{-1}. The plots of the left and right columns show the results for CO$_{\rm cores}$ left by $M_{\rm ZAMS} = 20\ M_\odot$ and $30\ M_\odot$ progenitors, respectively (see Table 1.1). For the plots at the upper panel were used the maximum possible value of the angular momentum transfer efficiency parameter ($\xi = 1.0$) while for the bottom plots were assumed $\xi = 0.5$. The apparent transition at $M_{\rm NS}^0 \approx 1.7\ M_\odot$ is explained as follows: configurations with $M_{\rm NS}^0 \lesssim 1.7\ M_\odot$ have the disk extending up to the NS surface, correspondingly we used the angular momentum per unit mass given by equation (1.40), instead for larger initial masses the accretion occurs from the last stable orbit and we used equation (1.39). Thus, the difference around this transition point are attributable to the use of the slow rotation approximation for masses $M_{\rm NS}^0 < 1.7\ M_\odot$.

Thus we have shown that in systems with $P \leq P_{\max}$ the induced gravitational collapse of the accreting NS to a BH occurs. These systems explain the BdHNe [14, 88, 90]. In systems with $P > P_{\max}$, the NS does not accrete enough matter from the SN ejecta and the collapse to a BH does not occur. These systems explain XRFs. In both cases, after the SN explosion the binary can either get disrupted or remain bound depending upon the mass loss and/or natal kick imparted to the system [215]. In the case when the system remains bound, the out-states of BdHNe are νNS-BH binaries, while for the XRFs are binaries composed of a $\sim$ 1.4–1.5 νNS, and a massive NS which accreted matter from the SN ejecta.

It is worth to mention that we do not simulate in this work the complex process of gravitational collapse rather we assume BH formation at the moment when the NS reaches the critical mass value. We also adopt the mass of the newly formed BH as given by the critical NS mass value.

2.3. The Evolutionary Scenario for the IGC Paradigm

With the knowledge of the proper set of parameters for which the gravitational collapse of the NS to a BH is induced by accretion, and consequently, also the parameters for which such a process does not occur, it becomes appropriate to discuss the possible progenitors of such binaries. A possible evolutionary scenario was discussed by Rueda & Ruffini [227], taking advantage of the following facts: (1) a viable progenitor for the IGC paradigm systems is represented by X-ray binaries such as Cen X-3 and Her X-1 [108, 156, 221, 257, 280, 307]; (2) evolution sequences for X-ray binaries, and evolution scenarios leading to systems in which two SN events occur during their life, had been already envisaged [see, e.g., 135, 195].

In base of the evolutionary binary paths considered in [93, 197, 198, 215], the in-states configurations of the IGC scenario could be get by following the evolution of an initial binary system composed of two main-sequence stars, M_1 and M_2, with a mass ratio $M_2/M_1 \gtrsim 0.4$. Initially, the binary system formed by the two main sequence stars is detached and each star is inside its own Roche Lobes. When the star 1, likely with $M_1 \gtrsim 11\ M_\odot$, exhausts the hydrogen in its core, it leaves the main sequence, expands and overfills its Roche lobe starting to transfer mass in a quasi-conservative and stable way to its companion. When star 1 losses its hydrogen envelope the transfer of mass is stopped and a naked helium core remains. Star 1 evolves and leaves a NS through a first core-collapse event. The star 2, now with $M_2 \gtrsim 11\ M_\odot$ after some almost conservative mass transfer, evolves filling its Roche lobe. Due to the large mass ratio of the binary components, it then starts a spiral-in of the NS into the envelope of the star 2, i.e. a common-envelope phase occurs. If the binary system survives to this common-envelope phase, namely it does not merge, it will be composed of a helium star and a NS in a tight orbit. The helium star then expands filling its Roche lobe and a non-conservative mass transfer to the NS, takes place. After losing its helium envelope, the above scenario naturally leads to a binary system composed of a $\mathrm{CO}_{\mathrm{core}}$ star and a massive NS whose fate has been discussed in the present work.

It have been argued, that during the common-envelope phase the NS might accrete at super-Eddington accretion rates ($\sim 0.1 M_\odot\,\mathrm{yr}^{-1}$) [19, 46, 93, 120] and collapse to form a BH [34]. However, as has been point by Brown et al. [34], the accretion on the NS could be not so high in this phase, due to the angular momentum of the matter [see also 168, 169]. Also, the NS magnetic field could introduce some caveat in this picture. Moreover, the observation of double NS binaries systems with nearly equal mass and the tight-orbit binary pulsar with CO white dwarf companions, that just could be formed by a common envelope phase, seems to go contrary with this argument [285].

The above evolutionary path advanced by Rueda & Ruffini [227], see Figure 2.3, is in agreement with the recent results of Tauris et al. [284], who performed simulations of the evolution of a helium core in a tight binary with an NS companion. The helium envelope is

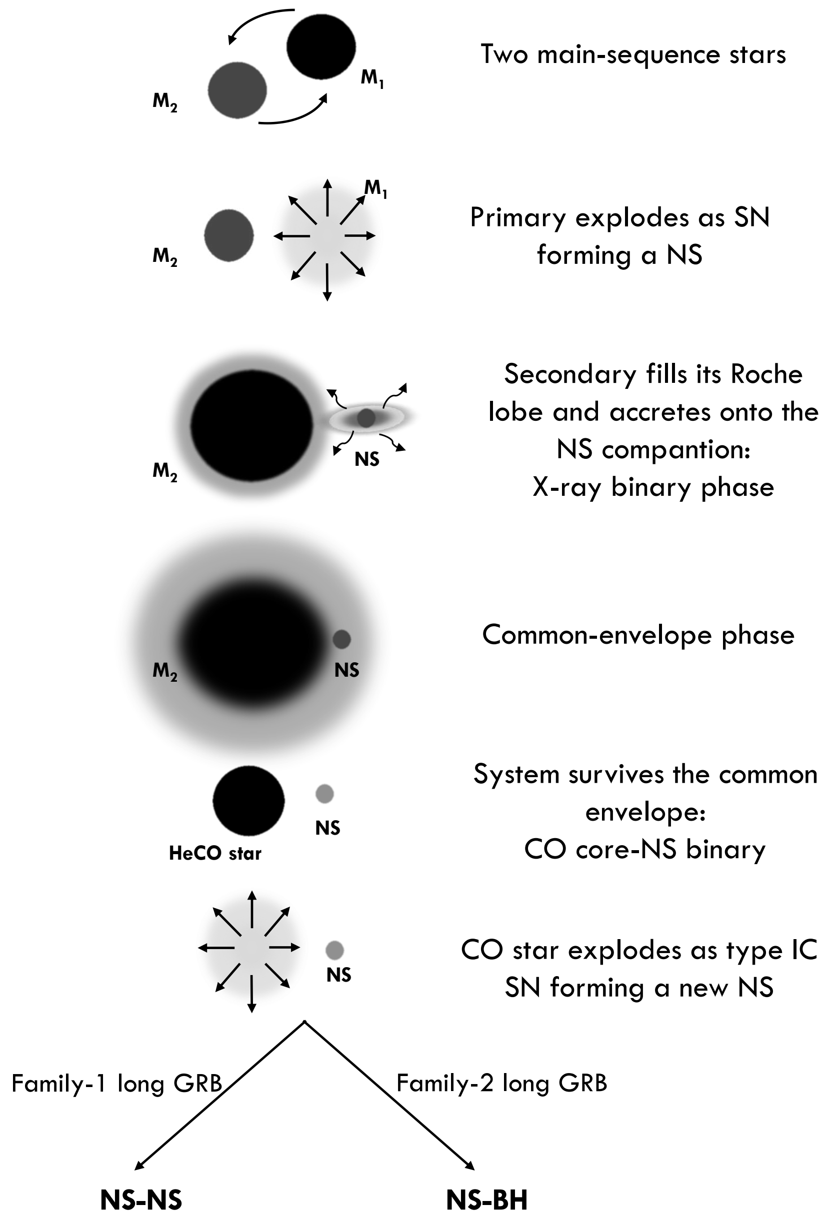

Figure 2.3: Scheme of a possible evolutionary scenario leading to the IGC binary system progenitors as outlined in [227].

stripped-off during the evolution as a result of both mass-loss and binary interactions and at the end it might lead to an SN of type Ib or Ic in the presence of the NS companion. In the X-ray binary/SN community, these systems are called “ultra-stripped” binaries and have been invoked to both explain the population of NS-NS binaries as well as a growing set of low-luminosity and/or rapid decay-rate SNe. The “ultra-stripped” binaries are expected to comprise 0.1–1% of the total SNe [283].

The simulations in Tauris et al. [284] show the possibility of having binaries with orbital periods as short as $\sim$ 50 minute at the moment of the SN explosion. However, they were interested in the so-called ultra-stripped SNe (whoose observational features cab be matched by low-mass ejecta), and therefore they explored systems with helium stars of low initial masses $M_{\rm He} = 2.5$–$3.0\ M_\odot$, less massive than the ones we expect for the CO$_{\rm cores}$ in the IGC scenario.

Besides comparing the value of the pre-SN CO$_{\rm core}$ mass, it is also instructive to compare the radii we have assumed for the pre-SN $\mathrm{CO_{core}}$ with the ones obtained by Tauris et al. [284]. For example, they obtained a radius of the metal core of the $\approx 3\ M_\odot$ helium star forming initially a binary of orbital period 0.1 day with an NS companion of $1.35\ M_\odot$, is $R \approx 0.024\ R_\odot$. The most similar case we can compare with, corresponds to the $\mathrm{CO_{core}}$ formed by the $M_{\rm ZAMS} = 15\ M_\odot$ progenitor (see Table 1.1), $M_{\rm CO} \approx 3.5\ M_\odot$, for which we have adopted a radius of $\approx 4.5 \times 10^9$ cm$\approx 0.06\ R_\odot$. This radius is ≈ 2.5 times larger than the above $3\ M_\odot$ helium star of Tauris et al. [284]. This implies that the assumption in Fryer et al. [90] that, due to the 3-4 orders of magnitude of pressure jump between the $\mathrm{CO_{core}}$ and helium layer, the star will not expand significantly when the helium layer is removed, seems to be appropriate. As was discussed there, differences of ~ 2 in the value of the radius could be due to the different binary interaction ingredients as well as to subtleties of the numerical codes, e.g. between the MESA and the KEPLER codes.

On the other hand, the relatively long possible orbital periods we have obtained (with respect to our minimum value P_0) to have BH formation weakens the role of the precise value of the $\mathrm{CO_{core}}$ radius on the accretion process and the final fate of the system. If the radius of the $\mathrm{CO_{core}}$ is N times the radius of the core of the system with $P = P_0$, then the evolution of the system will be approximately the one of a system with orbital period $P = N^{3/2} P_0$. For example, we have adopted a radius $R_{\rm CO} \approx 7.7 \times 10^9$ cm$\approx 0.1\ R_\odot$ for the $\mathrm{CO_{core}}$ with mass $M_{\rm CO} \approx 9.4\ M_\odot$ (see Table 1.1), and thus a minimum orbital period (to have no Roche lobe overflow) of $P_0 \approx 5$ min, if it forms a binary with a $2\ M_\odot$ NS companion. The maximum value of the orbital period for which we obtained BH formation for those mass parameters was $P_{\rm max} \approx 26$ min (for the NL3 EOS and adopting an efficient for the transfer of angular momentum: $\xi = 0.5$), which would imply that even with a $\mathrm{CO_{core}} \approx 5^{2/3} \approx 4$ times larger, BH formation would occur. Despite this fact, the precise value of the $\mathrm{CO_{core}}$ mass and radius depends on the binary interactions, hence on the evolutionary path followed by the system; therefore, it is appropriate to compute the binary evolution proposed in this work to confirm or improve our estimates for the $\mathrm{CO_{core}}$ masses and radii.

2.3.1. Post-explosion orbits and formation of NS-BH binaries

We have determined that the most tightest $\mathrm{CO_{core}}$-NS binaries ($a < 10^{11}$ cm) form the progenitors of the BdHNe. In these systems, the SN explosion of the $\mathrm{CO_{core}}$ leads a νNS as remnant, and the hypercritical accretion of the SN ejecta on the NS companion induced its gravitational collapse leading the formation of a BH. In Fryer et al. [88] was examined the question if BdHNe can indeed form NS-BH binaries or, on the contrary, these systems are disrupted by the SN explosion. Here we resume the main results of their study.

The mass ejected during the SN alters the binary orbit, causing it to become wider and more eccentric. Assuming instantaneous mass loss, the post-explosion semi-major axis will be given by [116]: $a/a_0 = (M_0 - \Delta M)/(M_0 - 2a_0\Delta M/r)$, where a_0 and a are the initial and final semi-major axes respectively, M_0 is the total initial mass of the binary system, ΔM is the change of mass (equal to the amount of mass ejected in the SN), and r is the orbital separation at the time of explosion . For circular orbits, like the ones expected for systems after going through a common envelope evolution, we find that the

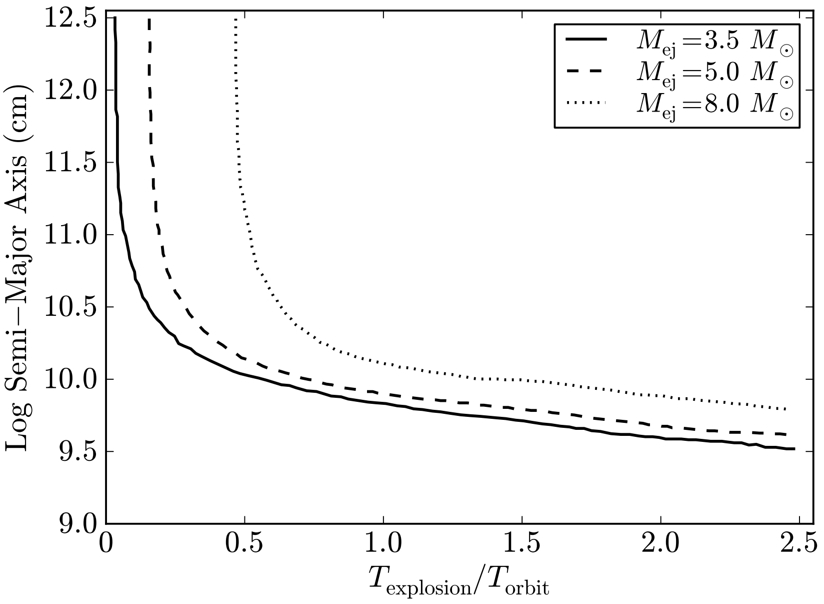

Figure 2.4.: Semi-major axis versus explosion time for 3 different mass ejecta scenarios: $3.5\,M_{\odot}$ (solid), $5.0\,M_{\odot}$ (dotted), $8.0\,M_{\odot}$ (dashed) including mass accretion and momentum effects. The $\mathrm{CO_{core}}$ collapse to form a $1.5\,M_{\odot}$ νNS and the companion NS has an initial mass of $2.0\,M_{\odot}$. If the SN explosion will be instantaneous, all the system with ejecta mass above $3.5\,M_{\odot}$ would be disrupted. Instead, it seen that all systems with explosion times above 0.7 times the orbital time are bound and the final separations are on par with the initial separations.
NOTE — Figure taken from Fryer et al. [88]

system is disrupted if it loses half of its initial mass after a SN event, leaving two single compact objects. In typical systems, most of the binaries become unbound during the SN explosion owing to the ejected mass and momentum imparted (kick) to the νNS in the explosion. In general, it is believed that the fraction of massive binaries that can produce double compact object binaries is low: ∼0.001–1% [66, 93, 215].

However, for the close binaries progenitors of the BdHNe, a number of additional effects can alter the above picture. First, for these close binaries, the SN explosion can no longer be assumed to be instantaneous. The explosions follow a so-called homologous velocity profile, and although the shock front is moving above $10{,}000\,\mathrm{km\,s^{-1}}$, the denser, lower-velocity ejecta can be moving at below $1000\,\mathrm{km\,s^{-1}}$. Thus, the SN ejecta overcomes a companion in a roughly time 10–1000 s and the orbital period, for these system, ranges from only 100–1000 s. Also, the NS companion accretes both matter and momentum from the SN ejecta, reducing the mass-loss from the system with respect to typical binaries with larger orbital separations and much less accretion. In addition, as with common envelope scenarios, the bow shock produced by the accreting NS transfers orbital energy into the SN ejecta.

Figure 2.4 shows the orbital evolution during the SN expansion for three binaries with different ejecta mass. The initial configuration consists of a $\mathrm{CO_{core}}$ and a 2.0 $M_{\odot}$ NS companion with a initial orbital separation of 7×10^{9} cm. For these calculations, it was assumed that $0.5\,M_{\odot}$ is accreted with the momentum of the SN material by the NS and 30% of the orbital velocity is lost per orbit. Not only do the systems remain bound even for explosion times greater than the half of the orbital period but, if the explosion time is long, the final semi-major axis can be on par with the initial orbital separation.

For many of the kick mechanisms in the literature, the kick is often aligned with the rotation axis (e.g., see [85, 87] for the neutrino-driven mechanisms and [85, 92, 264] for asymmetric explosions driven by convection). However, it is still possible to have some misalignment leading to some eccentricity and "tumbling" of the system with specific signatures in the light curve following the prompt emission of the GRB. If the kick is aligned with the orbital plane, the system can remain bound even with kick velocities as high as 1000 km s^{-1}. However, if the kick is in the same direction as the star is moving, the systems can be disrupted if the kick is above 500–700 km s^{-1} if the accretion phase is longer than an orbital period [see 88, for more details].

2.4. Concluding remarks and perspectives

Since the accretion rate decreases for increasing values of the orbital period, we have shown that there exists a specific value of it over which BH formation is not possible because the NS does not accrete sufficient matter to reach the critical mass. We denoted this maximum period for gravitational collapse as $P_{\rm max}$ and computed it as a function of the initial NS mass for selected pre-supernova $\rm CO_{cores}$ and angular momentum efficient parameter (see Figure 2.2). Therefore, in systems with $P \leq P_{\rm max}$, BH formation occurs and these systems, within the IGC paradigm, can explain BdHNe [14, 88, 90]. In systems with $P > P_{\rm max}$, the NS does not accrete enough matter from the supernova ejecta and the collapse to a BH does not occur: these systems, within the IGC paradigm, are used to explain the nature of XRFs.

The complexity of the above processes leading to two possible outcomes can be summarized schematically within the concept of *Cosmic-Matrix (C-matrix)* [228, 229, 243]. The C-matrix describes these systems as a four-body problem in analogy to the case of particle physics (see Figure 2.5). The *in-state* is represented by the $\rm CO_{core}$ and the NS companion. The interaction between these two objects given by the hypercritical accretion process triggered by the SN explosion onto the NS companion, and which is examined in this work, lead to two possible *out-states*: in the case of a BdHNe it is formed by the νNS, i.e. the neutron star left by the SN explosion of the $\rm CO_{core}$, and a BH formed from the gravitational collapse of the NS companion of the $\rm CO_{core}$ in the in-state. As we have mentioned in XRFs the accretion is not enough to lead to the gravitational collapse of the NS then the out-state is a νNS and another NS (of course more massive than the initial one present in the in-state).

The relative rate of BdHNe with respect of XRFs can give us crucial information on the value of the NS critical mass, hence on the stiffness of the nuclear EOS; and thus population synthesis analyses leading to the theoretically inferred rated of event are needed to unveil this important information [see, e.g 81, 244, for the complementary case of short GRBs] . As a first starting point toward such analysis, we have discussed a possible evolutionary scenario leading to tight $\rm CO_{core}$-NS binaries (see Figure 2.3).

Another important point for the IGC paradigm is to determine if their final out-states remains bounded or the system is disrupted forming two single compact object after the

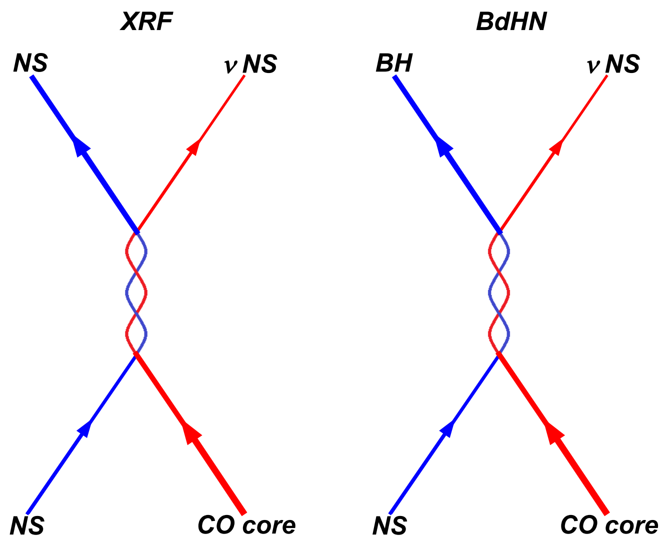

Figure 2.5: Cosmic-matrix of XRFs and BdHNe as introduced in Ruffini [228, 229], Ruffini et al. [243]. See text for details.

SN explosion of the $\mathrm{CO}_{\mathrm{core}}$. In the case of BdHNe, this question has been addressed by Fryer et al. [88]. They have shown that, on the contrary to the canonical SN explosion occurring in binary progenitors studied in population synthesis calculations, BdHNe remain bound even if a large fraction of the binary system's mass is lost in the explosion. Indeed, they might exceed the canonical 50% limit of mass loss without being disrupted. This impressive result is the combined result of: (1) the hypercritical accretion onto the NS companion which alters both the mass and momentum of the binary; (2) the explosion timescale which is on par with the orbital period, hence the mass ejection cannot be assumed to be instantaneous; (3) the bow shock created, as the accreting NS plows through the supernova ejecta, transfers angular momentum acting as a viscosity on the orbit.

It is interesting that in parallel to the above conclusions we can also draw some inferences on the astrophysics of NS-NS binaries. Our results suggest that the systems in which the accreting NS does not reach the critical mass (i.e the XRFs) are natural candidates to produce such binaries [246]. We have shown that this will occur for $\mathrm{CO}_{\mathrm{core}}$-NS binaries with long orbital periods; thus it is possible that many of these systems become unbound by the SN explosion produced by the $\mathrm{CO}_{\mathrm{core}}$. The XRF to BdHNe occurrence rate ratio can shed light on the ratio of bound/unbound IGC binaries [88]. The short orbital periods $P < P_{\max}$ needed for BdHNe obtained from our theoretical model imply that XRF must be much more common than BdHNe, as it is indeed observed [see, e.g., 107, 246, and references therein]. The few systems which will keep bound become NS-NS binaries where at least one of the components can be massive and with a rotation period in the millisecond region. If the NS accretes from the LSO, then at the end of the process it will have an angular momentum $J_{\mathrm{NS}} \sim 2\sqrt{3} G M_{\mathrm{acc}} M_{\mathrm{NS}}/c \approx 4.3 \times 10^{48} [M_{\mathrm{acc}}/(0.1 M_\odot)][M_{\mathrm{NS}}/(1.4 M_\odot)]$ g cm^2 s^{-2}, where M_{acc} is the total accreted mass. Thus, the NS will have a rotation period $P = 2\pi I_{\mathrm{NS}}/J_{\mathrm{NS}} \approx 1.6\,(0.1 M_\odot/M_{\mathrm{acc}})(R_{\mathrm{NS}}/10^6\,\mathrm{cm})^2$ ms, where $I_{\mathrm{NS}} \sim 2/5 M_{\mathrm{NS}} R_{\mathrm{NS}}^2$ is the NS moment of inertia. That known binary millisecond pulsars could be formed in XRFs is a very exciting result that deserves further scrutiny.

3. Physics inside the NS atmosphere during the hypercritical accretion process and neutrino emission

3.1. Introduction

In Chapters 1 and 2, we have studied the hypercritical accretion process in the framework of the IGC paradigm. We estimated the accretion rate on the NS using the Bondi-Hoyle formalism and showed that the longer the orbital period/larger binary separation, the lower the accretion rate (see Figure A.1); hence the lower the accretion luminosity and the longer the time at which peak luminosity occurs. These features confirm what advanced in Becerra et al. [14], Ruffini et al. [243, 246], namely that less energetic long GRBs correspond to the binaries with wider orbits. Specifically, XRFs correspond to the binaries in which the NS does not reach the point of gravitational collapse to a BH. Since there is a limiting orbital period, $P_{\rm max}$, up to which the NS can reach the critical mass and collapse to a BH (these systems are the BdHNe 88, 90), the XRFs are the binaries with $P > P_{\rm max}$ (see Section 2.2 for details).

We turn, now, to analyse in detail the properties of the system inside the Bondi-Hoyle accretion region. Figure 1.3 shows the mass accretion rate onto the NS of initial mass 2.0 $M_\odot$. We can see that the accretion rate can be as high as $\sim 10^{-2}$ $M_\odot$ s^{-1}. To begin, for these high accretion rates we can draw some general properties:

1. The NS magnetic field can be neglected [83, 227]. In spherically, symmetric accretion process, the magnetospheric radius is given by [287, see e.g.]: $R_{\rm mag} = \left(B^2 R_{\rm NS}^6/(\dot{M}_B\sqrt{2GM_{\rm NS}})\right)^{2/7}$, with B the NS magnetic field. This relation comes to equal the magnetic pressure with the random pressure of the infalling matter. If we assume $B = 10^{12}$ Gauss, that would be a high magnetic field and typical values for the NS parameters, $[\,R_{\rm NS} = 10\,{\rm km}$ and $M_{\rm NS} = 1.4\,]$, the magnetosphere radius lies inside the NS radius for $\dot{M}_B > 2.6 \times 10^{-8}$ $M_\odot$ s^{-1}. In the case of disk accretion, the disk interior radius is given by $R_{\rm in} = kR_{\rm mag}$, where k is an dimensionless parameter determined by the flow structure. Analytical models predict values from $0.5 - 1.0$ [100, 300] while MHD simulations give $0.4 - 0.72$ [154, 163].

2. The photons are trapped in the accretion flow. The trapping radius, defined at which the photons emitted diffuse outward at a slower velocity than the one of the

infalling material, is [45]:

$$r_{\text{trapping}} = \min\{\dot{M}_B \kappa/(4\pi c), R_{\text{cap}}\}, \tag{3.1}$$

where κ is the opacity. For the CO_{core}, Fryer et al. [90] estimated a Rosseland mean opacity roughly 5×10^3 cm^2 g^{-1}. For the range of accretion rates, we obtain that $\dot{M}_B \kappa/(4\pi c) \sim 10^{13}$–$10^{19}$ cm, a radius much bigger than the NS capture radius which is in our simulations at most 1/3 of the binary separation. Thus, in our systems the trapping radius extends all the way to the Bondi-Hoyle region, hence the Eddington limit does not apply and hypercritical accretion onto the NS occurs.

3. Under these conditions of photons being trapped within the accretion flow, the gain of gravitational energy of the accreted material is mainly radiated via neutrino emission [83, 90, 227, 239, 319].

During the hypercritical accretion on the NS in an IGC scenario, the neutrino emission at the based of the NS surface dominates the cooling and allows the NS to increase its mass. For accretion rate between $10^{-2} - 10^{-4}$ $M_\odot$ s^{-1}, the range of temperature and density developed on the NS surface leads the e^+e^--pair annihilation to be the dominant channel for the neutrino emission, reaching luminosities up to 10^{52} erg s^{-1} and mean neutrino energies of the order of 20 MeV. These make the XRFs and the BdHNe astrophysical laboratories for MeV-neutrino physics additional to core-collapse SNe. The neutrinos created in the accretion zone experience an interesting phenomenology before escaping to the outer space, i.e. outside the Bondi-Hoyle region. The neutrinos density produced in the hypercritical accretion process is such that the neutrino self-interactions, as in the case of SNe, dominate the neutrino flavor evolution, giving rise to appearance of collective effects. As a result, an entirely different neutrino flavor content emerges from the Bondi-Hoyle surface.

In order to deepen the study of the neutrinos emission at the base of the NS into the IGC framework, we organize this chapter as follow: in Section 3.2 we study the hydrodynamics inside the NS accretion region. We build NS accreting atmospheres in order to determinate the conditions of the neutrino emission on the NS surface. In Section 3.3 we introduce the main features of the neutrino oscillation phenomenology for the IGC scenario and we compare the final neutrino emission spectra with the one created near the NS surface, based on the results obtained in Uribe et al. [291]. Finally, we present in Section 3.4 the conclusions and some perspectives for future research.

3.2. Accretion zone structure and equation of state

We analyse the NS accretion zone following the theoretical framework established for SN fallback accretion [45, 83, 120]. Figure 3.1 shows schematically the structure of the NS atmosphere: the SN material entering the NS capture region shocks as it piles up onto the NS surface. As the atmosphere compresses, it becomes sufficiently hot to emit neutrinos allowing the matter to reduce its entropy and be incorporated into the NS.

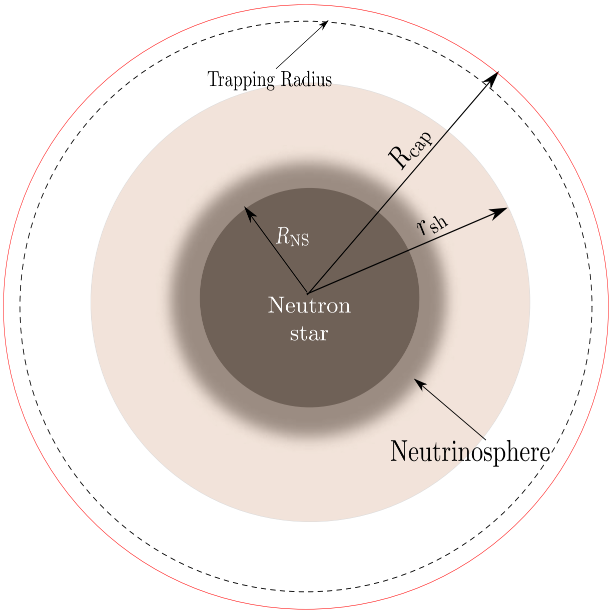

Figure 3.1: Structure of the NS acrretion atmosphere. The ejecta from the SN enter the NS capture region (red circle) at a distance $r = R_{\rm cap}$ [see equation (1.2)] from the NS center and start to fall to the NS surface. The material shocks as it piles on top the NS surface. The shock decelerates the material while it moves towards the NS and near the surface, at the *neutrinosphere*, it looses energy by the emission of neutrinos. The neutrino emission allows the material to reduce its entropy to be finally accreted by the NS.

In order to model the evolution of the NS accretion zone, we assume that it passes through a sequence of quasi-steady state envelopes, each characterized by the mass accretion rate $\dot{M}$, the NS mass, $M_{\rm NS}$ and its radius $R_{\rm NS}$. The spacetime outside the NS is described by the Schwarzschild metric:

$$ds^2 = -\left(1 - \frac{r_{\rm sch}}{r}\right) dt^2 + \left(1 - \frac{r_{\rm sch}}{r}\right)^{-1} dr^2 + r^2 \left(d\theta^2 + \sin^2\theta d\phi^2\right), \tag{3.2}$$

where $r_{\rm sch} = 2GM_{\rm NS}/c^2$ is the Schwarzschild radius. The steady-state relativistic fluid equations for mass, momentum and energy conservation in this geometry are:

$$\begin{aligned} \frac{1}{r^2}\frac{d}{dr}\left(r^2\rho u\right) &= 0, \\ \frac{1}{2}\frac{d}{dr}\left(\frac{u}{c}\right)^2 + \frac{r_{\rm sch}}{2r} + \frac{1}{w}\frac{dP}{dr}\left[\left(\frac{u}{c}\right)^2 + 1 - \frac{r_{\rm sch}}{r}\right] &= 0, \\ \frac{d}{dr}\left(\rho c^2 + U\right) - \frac{w}{\rho}\frac{d\rho}{dr} + \frac{Q_\nu}{u} &= 0, \end{aligned} \tag{3.3}$$

where u is the radial component of the four-velocity, Q_ν is the total energy loss rate per unit volume by neutrino cooling, $w = \rho c^2 + U + P$ is the relativistic enthalpy, ρ is the mass density, P is the pressure and U is the internal energy density.

The boundary conditions are determined by the conservation of mass, momentum and energy flows through the shock front at $r = r_{\rm sh}$. These one are expressed by the Rankine-Hugoniot conditions [155]:

$$\rho_p u_p - \rho_{\rm sh} u_{\rm sh} = 0, \tag{3.4}$$

$$w_p u_p^t u_p - w_{\rm sh} u_{\rm sh}^t u_{\rm sh} = 0, \tag{3.5}$$

$$w_p u_p^2 + P_p - w_{\rm sh} u_{\rm sh}^2 - P_{\rm sh} = 0, \tag{3.6}$$

where u^t is the time component of the four-velocity, determined by the condition $g_{\mu\nu}u^\mu u^\nu = -c^2$. The indexes '$p$' and 'sh' denote the quantities in the pre-shock and post-shock zone, respectively. Outside the shock front, the material is in approximate free fall, thus:

$$u_p = \sqrt{\frac{2GM_{\rm ns}}{r}}, \qquad \rho_p = \frac{\dot{M}}{4\pi r^2 v_p}, \qquad P_p = \frac{1}{2}\rho_p v_p^2. \tag{3.7}$$

We consider a gas of electrons, positrons, ions and photons. Then, the total pressure and density energy are:

$$P_{\rm tot}(\rho, T) = P_\gamma + P_{\rm ion} + P_{\rm e^-} + P_{\rm e^+}, \tag{3.8}$$

$$U_{\rm tot}(\rho, T) = U_\gamma + U_{\rm ion} + U_{\rm e^-} + U_{\rm e^+}. \tag{3.9}$$

For the pressure and the internal energy of the radiation field, we adopt a blackbody in thermodynamic equilibrium:

$$P_\gamma = \frac{1}{3}aT^4, \qquad U_\gamma = 3P_\gamma, \tag{3.10}$$

with $a = 4\sigma/c = 7.56 \times 10^{-15}$ erg cm^{-3} K^{-4}, where σ is the Stefan-Boltzmann constant.

For the ion gas, we assume a perfect gas:

$$n_{\rm ion} = \frac{\rho}{Am_u}, \qquad P_{\rm ion} = n_{\rm ion}\kappa_B T, \qquad U_{\rm ion} = \frac{3}{2}P_{\rm ion}, \tag{3.11}$$

where $n_{\rm ion}$ is the ion number density, $m_u = 1.6604 \times 10^{-24}$ g is the atomic mass unit and κ_B is the Boltzmann constant.

Finally, the electrons and positrons are described by the Fermi-Dirac distributions:

$$n_{\rm e^\pm} = \frac{m_e^3 c^3}{\pi^2\hbar^3}\sqrt{2}\,\beta^{3/2}\left[\mathcal{F}_{1/2}(\eta_{\rm e^\pm}, \beta) + \beta\mathcal{F}_{3/2}(\eta_{\rm e^\pm}, \beta)\right], \tag{3.12}$$

$$P_{\rm e^\pm} = \frac{8\,m_e^4 c^5}{3\sqrt{2}\,\pi^2\hbar^3}\beta^{5/2}\left[\mathcal{F}_{3/2}(\eta_{\rm e^\pm}, \beta) + \frac{1}{2}\beta\mathcal{F}_{5/2}(\eta_{\rm e^\pm}, \beta)\right], \tag{3.13}$$

$$U_{\rm e^\pm} = \frac{m_e c^2}{\pi^2}\frac{2\sqrt{2}\,m_e^3 c^3}{\hbar^3}\beta^{5/2}\left[\mathcal{F}_{3/2}(\eta_{\rm e^\pm}, \beta) + \beta\mathcal{F}_{5/2}(\eta_{\rm e^\pm}, \beta)\right], \tag{3.14}$$

where $\mathcal{F}_k(\eta, \beta) \equiv \int_0^\infty \frac{x^k(1+0.5x\beta)^{1/2}dx}{{\rm e}^{x-\eta}+1}$ is the relativistic Fermi-Dirac integral, $\beta \equiv \kappa_B T/(m_e c^2)$ is the relativity parameter and $\eta \equiv (\mu - m_e c^2)/\kappa_B T$ is the degeneracy parameter, with μ the chemical potential. Since the electrons and positrons are in equilibrium with radiation ($e^+ + e^- \to \gamma + \gamma$), their chemical potential are related by $\mu_{\rm e^-} + \mu_{\rm e^+} = 0$ and then $\eta_{\rm e^+} = -\eta_{\rm e^-} - 2/\beta$. For each value of density and temperature, $\eta_{\rm e^-}$ is determined from the charge neutrality condition:

$$n_{\rm e^-} - n_{\rm e^+} = \frac{Z}{A}\frac{\rho}{m_u} = Zn_{\rm ion}. \tag{3.15}$$

3.2.1. Neutrino emission and shock position

We turn now to discuss the neutrino emission processes taken into account in our calculations. We follow the results reported in Itoh et al. [128] for the neutrino energy loss rates computed within the Weinberg-Salam theory [252, 306]. We use here the formulas which fit the numerical results in the following regime of density and temperature: 10^0 g cm^{-3} $< \rho < 10^{14}$ g cm^{-3} and 10^7 K$< T < 10^{11}$ K [128].

We consider the following channels of neutrino emission. i) Pair annihilation: $e^+ + e^- \rightarrow \nu + \bar{\nu}$ [127, 190]; this neutrino energy loss rate is here denoted by $\epsilon_{e^-e^+}$. ii) Photo-neutrino process: $\gamma + e^\pm \rightarrow e^\pm + \nu + \bar{\nu}$ [127, 190], denoted by ϵ_γ. iii) Plasmon decay: $\bar{\gamma} \rightarrow \nu + \bar{\nu}$ [148, 149], denoted by $\epsilon_{\rm pl}$. iv) Bremsstrahlung processes [129, 131–133], denoted by $\epsilon_{\rm BR}$, which can be due to electron-nucleon interaction $e^\pm + N \rightarrow N + \nu + \bar{\nu}$ or to nucleon-nucleon interaction $N + N \rightarrow N + N + \nu + \bar{\nu}$. It is important to mention that two different expressions for the total Bremsstrahlung emission are shown in Itoh et al. [128] depending if the Coulomb parameter, $\Gamma \equiv (Ze)^2/(r_i k_B T)$ where $r_i = [3/(4\pi n_{\rm ion})]^{1/3}$, is higher or lower than the critical value $\Gamma \approx 180$, over which the system crystallizes. So the total energy loss rate per unit volume due to neutrino emission is $Q_\nu = \epsilon_{e^-e^+} + \epsilon_\gamma + \epsilon_{\rm pl} + \epsilon_{\rm BR}$.

Since the infalling material is strongly decelerated by the accretion shock, the post-shock kinetic energy is much less that the internal and gravitational energy. Then, assuming a polytropic gas [$P = (\gamma - 1)U \propto \rho^\gamma$] and subsonic velocities inside the shock radius, $(v/c)^2 \ll 1$, Eqs. (3.4) can be solved for the radial dependence of the fluid variables ρ, P and u [120]:

$$\rho = \rho_{\rm sh} f(r)^{\frac{1}{\gamma-1}}, \quad P = P_{\rm sh} f(r)^{\frac{\gamma}{\gamma-1}}, \quad u = \frac{u_{\rm sh}}{r^2} f(r)^{\frac{1}{1-\gamma}} \quad , \tag{3.16}$$

with

$$f(r) \equiv \frac{(1 - r_{\rm sch}/r)^{-1/2} - 1}{(1 - r_{\rm sch}/R_{\rm sh})^{-1/2} - 1} \, .$$

Since neutrinos are the main energy sink of the system, the position of the shock can be estimated from the balance between the neutrino emission and the release of the potential gravitational energy due to the accretion process, i.e.:

$$\int_{R_{\rm ns}}^{R_{\rm sh}} Q_\nu \left(1 - \frac{2GM_{\rm NS}}{c^2 r}\right)^{-1/2} 2\pi r^2 {\rm d}r = c^2 \dot{M} \left[\left(1 - \frac{2GM_{\rm NS}}{c^2 R_{\rm NS}}\right)^{-1/2} - 1\right] , \tag{3.17}$$

where we have assumed the rate at which gravitational energy is released as the kinetic energy gained in the free fall from infinity, and we have considered the proper volume of the cooling region and the proper cooling rate. Figure 3.2 shows the NS surface temperature and the shock position as a function of the mass accretion rate for three different adiabatic index: $\gamma = 1.33$, 1.4, 1.46. The position of the shock radius is determined by the value og γ, but the temperature and density of the matter at the NS surface it's independent of it. The approximation of a polytropic equation of state was validated by numerical simulations in Fryer et al. [83], who showed the infall NS atmosphere is well approximated by a polytropic gas of index $\gamma = 1.4$. For acretion rate lying between $\sim 10^{-4}$–$10^{-2}\, M_\odot\,{\rm s}^{-1}$, we estimate neutrino temperatures lying between $5.4 - 9.2\,$MeV (i.e. neutrino energies $E_\nu \approx 3k_B T \approx 15 - 30\,$MeV), predicting energies only slightly below those produced by detailed calculations [79].

Under the conditions (non-degenerate, relativistic, hot plasma) of our hypercritically accreting NS, the most efficient neutrino emission is given by the e^+e^- pair annihilation leading to neutrino-antineutrino (see Figure 3.5 below). In these T-ρ conditions, $\epsilon_{\mathrm{e^-e^+}}$ reduces to the simple expression [316]:

$$\epsilon_{\mathrm{e^-e^+}} = 1.39 \times 10^{25} \left(\frac{k_B T}{1\,\mathrm{MeV}}\right)^9 \quad \mathrm{erg\,cm^{-3}\,s^{-1}}. \tag{3.18}$$

Owing to the strong dependence of the neutrino emission on temperature, most of the neutrinos are emitted from a spherical shell around the NS of thickness Δr_{ER}. Thus, we can approximate equation (3.17) to:

$$\left(\frac{4\pi R_{\mathrm{NS}}^2 \Delta r_{\mathrm{ER}}}{\sqrt{1-\frac{2GM_{\mathrm{NS}}}{c^2 R_{\mathrm{NS}}}}}\right) Q_\nu \approx c^2 \dot{M} \left[\left(1-\frac{2GM_{\mathrm{NS}}}{c^2 R_{\mathrm{NS}}}\right)^{-1/2} - 1\right], \tag{3.19}$$

where Δr_{ER} can be estimated as one temperature scale height, i.e.:

$$\Delta r_{\mathrm{ER}} \approx H_T = \frac{T}{|(dT/dr)|}, \quad \text{with} \quad \frac{dT}{dr} = \left(\frac{\partial \ln T}{\partial \ln \rho}\right)_P \frac{d\ln \rho}{dr} + \left(\frac{\partial \ln T}{\partial \ln P}\right)_\rho \frac{d\ln P}{dr}. \tag{3.20}$$

The thickness of the neutrino emission region is very poorly dependent on the accretion rate; indeed equation (3.20) gives $\Delta r_{\mathrm{ER}} \approx 0.76$–$0.77\,R_{\mathrm{NS}}$ for $\dot{M} = 10^{-8}$–10^{-1} $M_\odot$ s^{-1}. Using equation (3.19) instead of equation (3.17) leads to NS accreting atmosphere within a 3% error.

For the sake of example, we show in Figure 3.3 the entropy, temperature, density and pressure profile from the NS surface (we have assumed a NS of $M_{\mathrm{NS}} = 2.0\,M_\odot$ with $R_{\mathrm{NS}} = 10^6$ cm) to the shock radius for a specific value of the mass accretion rate $10^{-2}\,M_\odot$ s^{-1}. For the ions we adopt here $Z = 6$ and $A = 12$. It can be seen here that the entropy gradient of the NS atmosphere is negative, and it is thus subjected to convective instabilities (see Chapter 4).

3.2.2. Neutrino and photon optical depth

We have assumed that the neutrinos produced at the base of the NS surface are the main sink of the gravitational potential energy gained by the infalling material. We proceed now to assess the validity of this statement through the calculation of the neutrino opacity.

The total neutrino opacity is:

$$\kappa_\nu = \kappa_{\nu,\mathrm{abs}} + \kappa_{\nu,\mathrm{scat}}, \tag{3.21}$$

where $\kappa_{\nu,\mathrm{abs}}$ and $\kappa_{\nu,\mathrm{scat}}$ correspond to the opacity produced by absorption and scattering

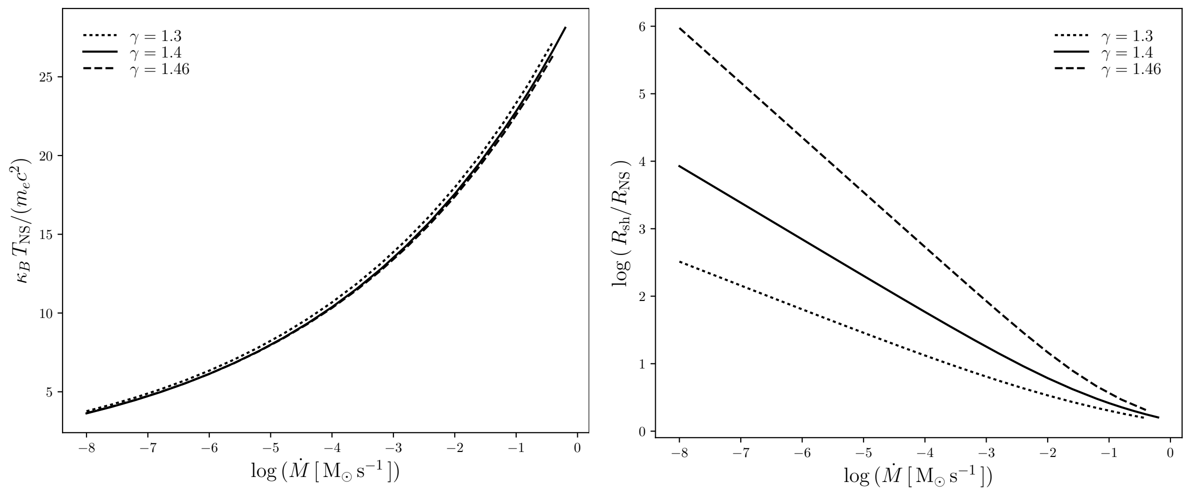

Figure 3.2.: Temperature of the NS surface (left panel) and ratio between the shock radius and the NS radius (right plot) as a function of the mass accretion rate in the range $\dot{M} = 10^{-8}$–10^{-1} $M_\odot$ s^{-1}. It has shown the results for three values of the polytropic index: $\gamma = 1.33$, 1.4 and 1.46. The shock radius position increase with γ in order to the NS surface develops conditions to the neutrino emission becomes efficient and takes away the gravitational energy gained during the accretion process

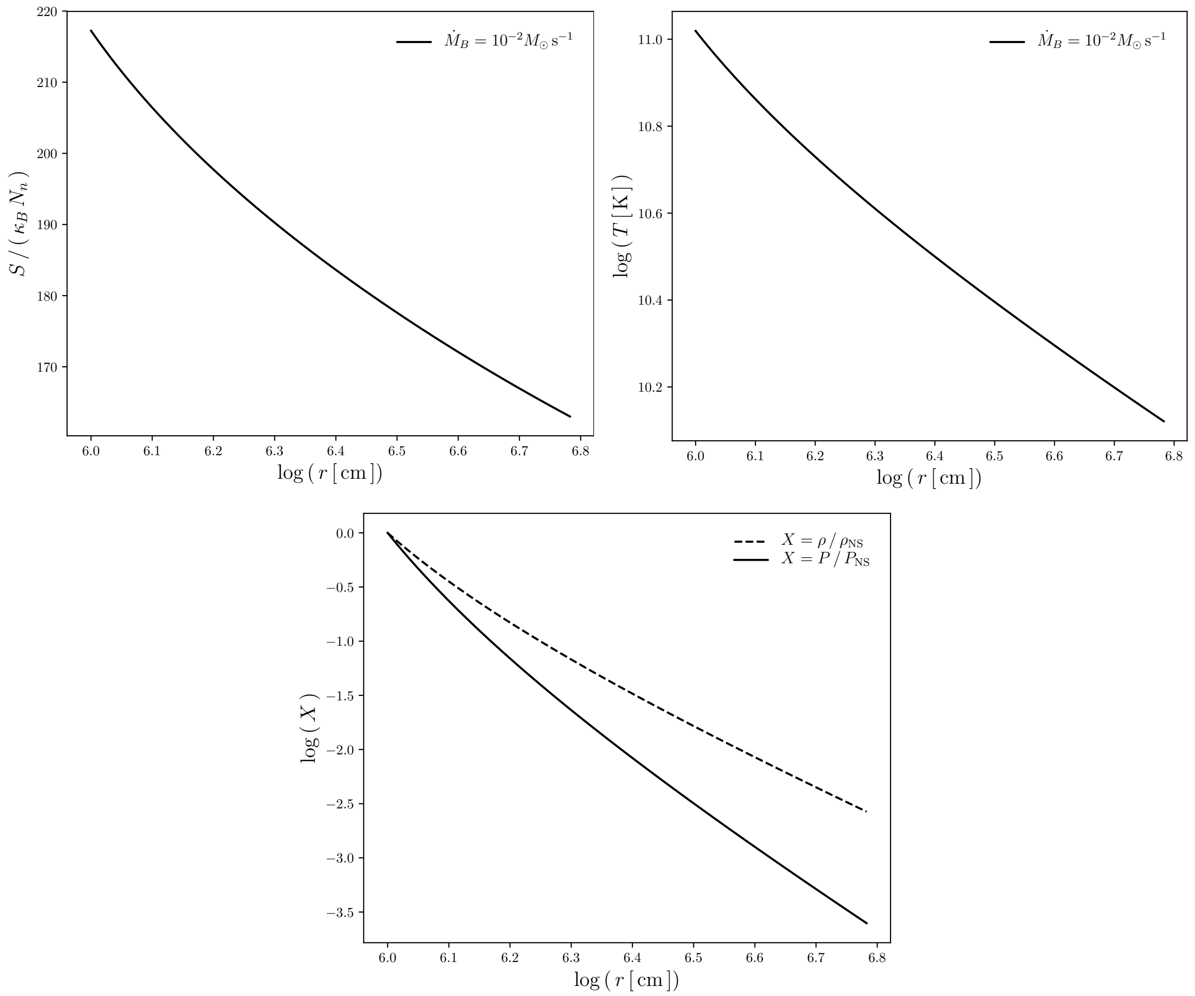

Figure 3.3.: Entropy (upper left plot), temperature (upper right plot), density and pressure profile (bottom plot) of a NS accreting atmosphere for $\dot{M} = 10^{-2}\, M_\odot$ s^{-1}. It has been assumed $\gamma = 1.4$. The pressure and density are normalized to $P_{\rm NS} \approx 8.27 \times 10^{29}$ dyn cm^{-2} and $\rho_{\rm NS} \approx 1.76 \times 10^{9}$ g cm^{-3}, respectively.

processes. In general, the opacity can be written as

$$\kappa = \frac{\sigma_i n_i}{\rho}, \tag{3.22}$$

where n_i is the particle density and σ_i is the process cross section. We adopt the following scattering and absorption process:

Scattering processes: neutrinos transfer momentum to the matter by the scattering off nuclei and electrons and positrons:

- Coherent neutrino nucleus scattering: $\nu + (A, Z) \rightarrow \nu + (A, Z)$ [290]

  $$\sigma_A = \frac{1}{16}\sigma_0 \left(\frac{E_\nu}{m_e c^2}\right)^2 A^2 \left[1 - \frac{Z}{A} + (4\sin^2\theta_w - 1)\frac{Z}{A}\right]^2 \quad \text{with} \quad , \tag{3.23}$$

  with $\sigma_0 = \frac{4G_F^2(m_e c^2)^2}{\pi(\hbar c)^4} \approx 1.71 \times 10^{-44}\,\text{cm}^2$, where G_F is the Fermi weak neutrino coupling constant and θ_w is the Weinberg angle, $\sin^2\theta_w \approx 0.231$ [202]. The scattering is coherent in the sense that nucleus acts as a single particle and the initial and final neutrino energy are nearly equal.

- Neutrino-electron scattering [32, 37]:

  $$\sigma_e(E) = \frac{3}{8}\sigma_0 \beta \frac{E}{m_e c^2}\left(1 + \frac{\eta_e}{4}\right)\left[(C_v + C_a)^2 + \frac{1}{3}(C_v + Ca)^2\right] \tag{3.24}$$

  where $C_v = 1/2 + 2\sin^2\theta_w$ for electron neutrino and antineutrino types, $C_a = 1/2$ for neutrino and $C_a = -1/2$ for antineutrinos.

Absorption processes: Since we have shown that the most efficient neutrino cooling process near the NS surface is the electron-positron annihilation, the inverse process namely the annihilation of neutrinos, $\nu + \bar{\nu} \rightarrow e^- + e^+$, represents the main source of opacity. The total average cross sections are given by [103]:

$$\sigma_\nu(E_\nu) = \frac{4}{3}K_{\nu\bar{\nu}}\sigma_0\langle E_\nu\rangle\langle E_{\bar{\nu}}\rangle, \qquad \sigma_{\bar{\nu}}(E_{\bar{\nu}}) = \frac{4}{3}K_{\nu\bar{\nu}}\sigma_0\langle E_{\bar{\nu}}\rangle\langle E_\nu\rangle, \tag{3.25}$$

where $K_{\nu\bar{\nu}} = (1 + 4\sin^2\theta_w + 8\sin^4\theta_w)/12 = 0.195$. The energy of the neutrino and antineutrinos are calculated through the second energy momentum (see equation (B.10) in Appendix B.1):

$$\langle E_\nu\rangle = \langle E_{\bar{\nu}}\rangle = \frac{\varepsilon^1}{\varepsilon^0} = 4.1\,k_B T, \quad \text{and} \quad \langle E_\nu^2\rangle = \frac{\varepsilon^2}{\varepsilon^0} = 20.8\,(k_B T)^2\,. \tag{3.26}$$

Then, the total neutrino opacity is:

$$\kappa_\nu = \left[\sigma_A\left(\frac{\rho}{A m_u}\right) + \sigma_e(E_\nu)\,n_{e^-} + \sigma_\nu(E_\nu)n_\nu\right]/\rho, \tag{3.27}$$

The neutrino optical depth can then be obtained as:

$$d\,\tau_\nu = \kappa_\nu\,\rho\,dr = \frac{dr}{\lambda_\nu}, \tag{3.28}$$

where $\lambda_\nu = (\kappa_\nu\,\rho)^{-1}$ is the neutrino mean free path.

Thus, the optical depth at the base of the neutrino emission region can be estimated as: $\tau_{\nu,\mathrm{ER}} \approx \kappa_\nu\,\rho_{\mathrm{NS}}\Delta r_{\mathrm{ER}} = \Delta r_{\mathrm{ER}}/\lambda_{\nu,\mathrm{ER}}$. Large values for the optical depth means ($\tau_\nu \gg 1$) implies that the neutrinos are reabsorbed by the matter and cannot freely scape from the system.

In order to verify that photons are trapped in the infalling material, we evaluate the photon mean free path and photon emissivity:

$$\tau_\gamma = \kappa_R\,\rho\Delta\,r_{\mathrm{ER}}, \qquad \dot{q}_\gamma \approx \frac{1}{\Delta\,r_{\mathrm{ER}}}\frac{\sigma T^4}{\tau_\gamma}, \tag{3.29}$$

where σ is the Stefan-Boltzmann constant, τ_γ is the photon optical depth, and κ_R is the Rosseland mean opacity:

$$\kappa_R = 0.4 + 0.64 \times 10^{23}\left(\frac{\rho}{\mathrm{g\,cm^{-3}}}\right)\left(\frac{T}{K}\right)^{-3}\ \mathrm{g^{-1}\,cm^2}, \tag{3.30}$$

being the first term due to the electron scattering and the second one to the free-free absorption.

We show in Figure 3.4 the neutrino and photon optical depth profile in the NS accretion region for three different values of the mass accretion rate. We can see the photon optical depth is much higher than unity for photons, implying they are indeed trapped at any radius. On the contrary, the neutrino optical depth is much lower than unity, implying they efficiently cool the atmosphere which allows the system to proceed the accretion at hypercritical rates.

We show in Figure 3.5 the T-ρ diagram of the NS surface for accretion rates $\dot{M} = 10^{-8}$–$10^{-1}\ M_\odot\ \mathrm{s}^{-1}$ which covers both XRFs and BdHNe (see, e.g., Figure A.1). Higher temperatures and densities correspond to higher accretion rates. We show contours indicating where the neutrino emissivities of the different neutrino emission processes are equal. It can be seen from Figures 3.4 and 3.5 that: (1) pair annihilation neutrino process are highly dominant over the other neutrino emission mechanisms; (2) neutrinos can efficiently escape taking away most of the energy (high emissivity); (3) photons are trapped hence they have negligible emissivity; (4) even for the largest accretion rates the neutrino optical depth in the accretion zone is below unity and so the system is not opaque to neutrinos.

As discussed in Fryer et al. [83], the neutrinos can balance efficiently the gravitational

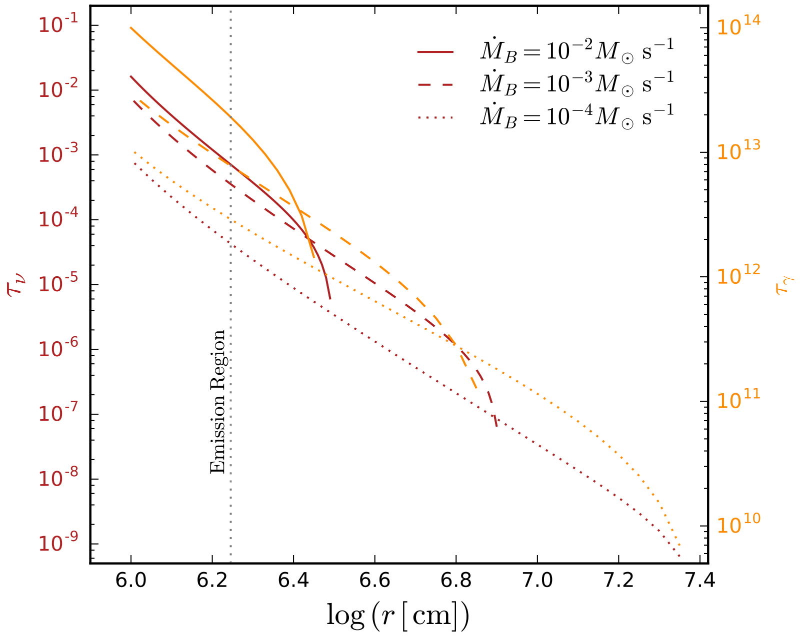

Figure 3.4.: Neutrino (left y-scale, τ_ν) and photon (right y-scale, τ_γ) optical depths in the NS star accretion region (from the shock radius to the NS surface) for selected accretion rates.

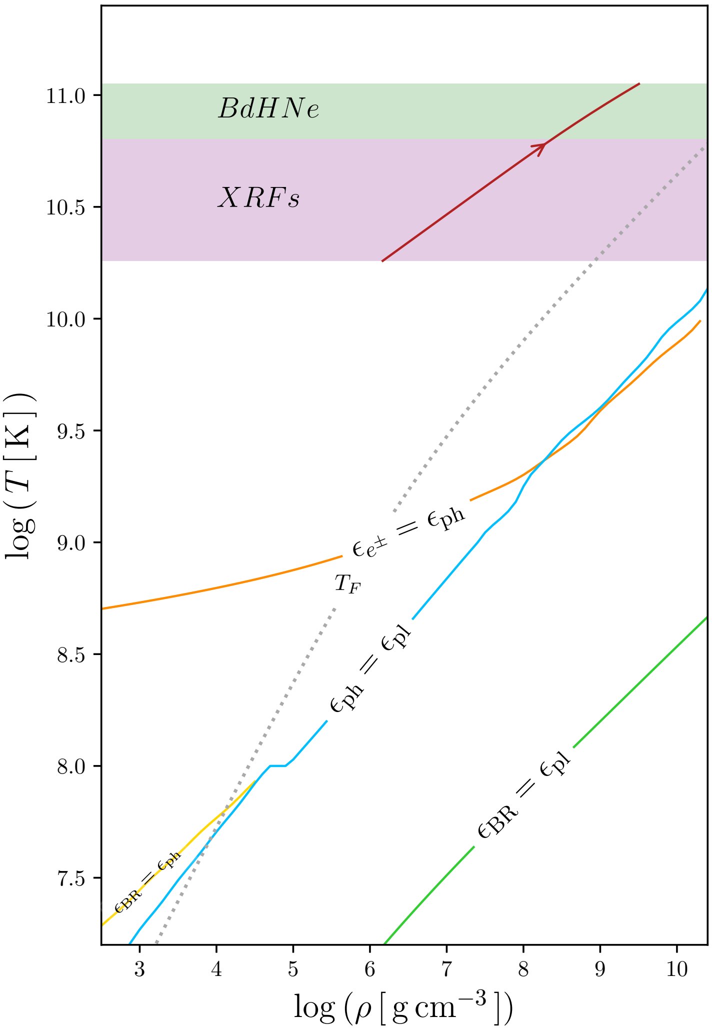

Figure 3.5.: Temperature-density diagram of the accreting atmosphere equation of state. In order to see the dominant neutrino processes, we show contours at which the emissivities of the different neutrinos process become equal: $\epsilon_{e^\pm}$ correspond to the pair annihilation process, ϵ_γ to the photo-neutrino emission, $\epsilon_{\rm pl}$ to the plasmon decay and $\epsilon_{\rm BR}$ to the Bremsstralung emission. The solid red curve shows the corresponding T-ρ values of the NS surface in the range of accretion $\dot{M} = 10^{-8}$–10^{-1} $M_\odot$ s^{-1} which covers typical rates achieved in XRFs and BdHNe (see Figure A.1). The arrow indicates the direction of increasing accretion rate. Thus, while accreting, the NS moves from the left lower part of the red curve to the right upper part of it. It is clear that in this regime of XRFs and BdHNe, the e^-e^+ pair annihilation dominates the neutrino emission. For the sake of reference we show the electron Fermi temperature, T_F, in dotted line.

energy gain. The effective accretion onto the NS can be estimated as:

$$\dot{M}_{\rm eff} \approx \Delta M_{\rm ER} \frac{L_{\rm ER}}{E_{\rm ER}}, \tag{3.31}$$

where $\Delta M_{\rm ER}$, $L_{\rm ER}$ are the mass and neutrino luminosity in the emission region (i.e. $\Delta r_{\rm ER}$), and $E_{\rm ER} = (1/2)GM_{\rm NS}\Delta M_{\rm ER}/(R_{\rm NS} + \Delta r_{\rm ER})$ is half the gravitational potential energy gained by the material falling from infinity to the $R_{\rm NS}+\Delta r_{\rm ER}$. Since $L_{\rm ER} \approx 2\pi R_{\rm NS}\Delta r_{\rm ER}\epsilon_{\rm e^-e^+}$ with $\epsilon_{\rm e^-e^+}$ the electron-positron pair annihilation process emissivity given by equation (3.18), it can be checked that for $M_{\rm NS} = 1.4\ M_\odot$ this accretion rate leads to values $\dot{M}_{\rm eff} \approx 10^{-9}$–$10^{-1}\ M_\odot\ {\rm s}^{-1}$ and $L_{\rm ER} \approx 10^{48}$–$10^{57}$ MeV s^{-1} for temperatures $k_BT = 1$–10 MeV.

3.3. Neutrino oscillations in the IGC paradigm

We have shown that the neutrinos have an important role during the hypercritical accretion of the IGC scenario. The high temperature developed on the NS surface leads to e^+e^- pairs that, via weak interactions, annihilate into $\nu\bar{\nu}$ pairs with neutrino luminosities of up to 10^{52} erg s^{-1} for the highest accretion rates. Under these conditions, XRFs and BdHNe become astrophysical laboratories for MeV-neutrino physics additional to core-collapse SNe. In this section, following Uribe et al. [291], we extend the analysis of the above neutrino emission to assess the occurrence of neutrino flavor oscillation in long GRBs, i.e. in the hypercritical accretion process of XRFs and BdHNe.

3.3.1. Neutrino spectrum at the NS surface

During the hypercritical accretion process on the NS, the main source of neutrinos is the e^-e^+ pair annihilation process (see Figure 3.5). From this fact, we can conclude that neutrinos and antineutrinos are created in equal number. For the non-degenerate, relativistic, hot plasma of the NS surface, the ratio of emission rates between electronic and nonelectronic neutrino flavors can be express in terms of the weak interaction constants (see equation (B.10) in Appendix B.1):

$$\frac{\varepsilon_e^0}{\varepsilon_x^0} = \frac{\varepsilon_e^0}{\varepsilon_\mu^0 + \varepsilon_\tau^0} = \frac{C_{+,e}^2}{C_{+,\mu}^2 + C_{+,\tau}^2} \approx \frac{7}{3}. \tag{3.32}$$

Hereafter, we use only two flavors: the electronic neutrinos and antineutrinos $\nu_e, \bar{\nu}_e$, and a superposition of the other flavors $\nu_x, \bar{\nu}_x$ $(x = \mu + \tau)$. Being $n^c_{\nu_i(\bar{\nu}_i)}$ and $F^c_{\nu_i(\bar{\nu}_i)}$ the neutrino (antineutrino) density and flux in the moment of their creation, respectively, from the last result we have:

$$n^C_{\nu_i} = n^C_{\bar{\nu}_i},\ F^C_{\nu_i} = F^C_{\bar{\nu}_i}\ \ \forall i \in \{e, \mu, \tau\} \quad \text{and} \quad \frac{n^C_{\nu_e}}{n^C_{\nu_x}} = \frac{n^C_{\bar{\nu}_e}}{n^C_{\bar{\nu}_x}} = \frac{F^C_{\nu_e}}{F^C_{\nu_x}} = \frac{F^C_{\bar{\nu}_e}}{F^C_{\bar{\nu}_x}} \approx \frac{7}{3}. \tag{3.33}$$

Table 3.1.: Characteristics inside the neutrino emission zone and the neutrino spectrum for selected values of the accretion rate $\dot{M}_B$. The electron fraction is $Y_e = 0.5$ and the pinching parameter for the neutrino spectrum is $\eta_{\nu\bar{\nu}} = 2.0376$

$\dot{M}_B$ $(M_\odot\, s^{-1})$	ρ $(\mathrm{g\,cm^{-3}})$	k_BT (MeV)	$\eta_{e\mp}$	$n_{e^-} - n_{e^+}$ $(\mathrm{cm^{-3}})$	$k_BT_{\nu\bar{\nu}}$ (MeV)	$\langle E_\nu \rangle$ (MeV)	$F^C_{\nu_e,\bar{\nu}_e}$ $(\mathrm{cm^{-2}\,s^{-1}})$	$F^C_{\nu_x,\bar{\nu}_x}$ $(\mathrm{cm^{-2}\,s^{-1}})$	$n^C_{\nu_e\bar{\nu}_e}$ $(\mathrm{cm^{-3}})$	$n^C_{\nu_x\bar{\nu}_x}$ $(\mathrm{cm^{-3}})$
10^{-8}	1.46×10^6	1.56	∓ 0.325	4.41×10^{29}	1.78	6.39	4.17×10^{36}	1.79×10^{36}	2.78×10^{26}	1.19×10^{26}
10^{-7}	3.90×10^6	2.01	∓ 0.251	1.25×10^{30}	2.28	8.24	3.16×10^{37}	1.36×10^{37}	2.11×10^{27}	9.00×10^{26}
10^{-6}	1.12×10^7	2.59	∓ 0.193	3.38×10^{30}	2.93	10.61	2.40×10^{38}	1.03×10^{38}	1.60×10^{28}	6.90×10^{27}
10^{-5}	3.10×10^7	3.34	∓ 0.147	9.56×10^{30}	3.78	13.69	1.84×10^{39}	7.87×10^{38}	1.23×10^{29}	5.20×10^{28}
10^{-4}	8.66×10^7	4.30	∓ 0.111	2.61×10^{31}	4.87	17.62	1.39×10^{40}	5.94×10^{39}	9.24×10^{29}	3.96×10^{29}
10^{-3}	2.48×10^8	5.54	∓ 0.082	7.65×10^{31}	6.28	22.70	1.04×10^{41}	4.51×10^{40}	7.00×10^{30}	3.00×10^{30}
10^{-2}	7.54×10^8	7.13	∓ 0.057	2.27×10^{32}	8.08	29.22	7.92×10^{41}	3.39×10^{41}	5.28×10^{31}	2.26×10^{31}

Resuming, equation (3.33) implies that, in the specific environment of our system, of the total number of neutrinos+antineutrinos emitted, $N_\nu + N_{\bar{\nu}}$, 70% are electronic neutrinos $(N_{\nu_e} + N_{\bar{\nu}_e})$, 30% are non-electronic $(N_{\nu_x} + N_{\bar{\nu}_x})$, while the total number of neutrinos is equal to the total number of antineutrinos, i.e. $N_\nu = N_{\bar{\nu}}$, where $N_\nu = N_{\nu_e} + N_{\nu_x}$ and $N_{\bar{\nu}} = N_{\bar{\nu}_e} + N_{\bar{\nu}_x}$. The distribution function of the neutrinos emitted at the NS surface can be fitted by [291]:

$$f_{\nu_i} = f_{\bar{\nu}_e} = \frac{2\pi^2 \left(\hbar c\right)^3 n^C_{\nu_i}}{\left(k_B T_{\nu\bar{\nu}}\right)^3 \mathcal{F}_2\left(\eta_{\nu\bar{\nu}}\right)} \frac{1}{1 + \exp\left(E/k_B T_{\nu\bar{\nu}} - \eta_{\nu\bar{\nu}}\right)}, \tag{3.34}$$

with the neutrino density given by:

$$n^C_{\nu_i(\bar{\nu}_i)} = w_{\nu_i(\bar{\nu}_i)} \frac{L_\nu}{4\pi R^2_{\mathrm{NS}} \langle E_\nu \rangle \langle v \rangle} = w_{\nu_i(\bar{\nu}_i)} \frac{\varepsilon^0_i \Delta r_{\mathrm{ER}}}{c/2} \tag{3.35}$$

where the neutrino's average radial velocity at $r = R_{\mathrm{NS}}$ is $\langle v \rangle = c/2$ [56], $w_{\nu_e} = w_{\bar{\nu}_e} = 0.35$ and $w_{\nu_x} = w_{\bar{\nu}_x} = 0.35$. The neutrino fluxes will be $F^C_{\nu(\bar{\nu}_i)} = \langle v \rangle n^c_{\nu_i(\bar{\nu}_i)}$. The effective neutrino temperature, $T_{\nu\bar{\nu}}$, and the effective neutrino parameter (known also as $p$inching parameter), $\eta_{\nu\bar{\nu}}$, can be found solving:

$$4.1 k_B T = k_B T_{\nu\bar{\nu}} \frac{\mathcal{F}_3\left(\eta_{\nu\bar{\nu}}, 0\right)}{\mathcal{F}_2\left(\eta_{\nu\bar{\nu}}, 0\right)} \quad \text{and} \quad 20.8 \left(k_B T\right)^2 = \left(k_B T_{\nu\bar{\nu}}\right)^2 \frac{\mathcal{F}_4\left(\eta_{\nu\bar{\nu}}, 0\right)}{\mathcal{F}_2\left(\eta_{\nu\bar{\nu}}, 0\right)} \tag{3.36}$$

For the range of temperature we are interested (see Figure 3.5) we find $T_{\nu\bar{\nu}} = 1.1331 T$ and $\eta_{\nu\bar{\nu}} = 2.0376$. It can be checked that the distribution of equation (3.34) obeys:

$$\int f_{\nu_i} \frac{d^3\mathbf{p}}{\left(2\pi\hbar\right)^3} = n^C_{\nu_i} \qquad \text{and} \qquad \int E f_{\nu_i} \frac{d^3\mathbf{p}}{\left(2\pi\hbar\right)^3} = \langle E_\nu \rangle n^C_{\nu_i} = \varepsilon^1_i \tag{3.37}$$

For the range of accretion rates developed during the accretion process, in Table 3.1 we have collected the principal values that described NS accreting atmosphere and the neutrino emission based of the NS atmosphere constructed in Section 3.2.

It is important to say, that the distribution functions give by equation (3.34) is not unique. A different solution based on a Maxwell-Boltzmann distribution can be found in [74, 144, 184].

3.3.2. Neutrino oscillations phenomenology

The equations of motion (EoM) that govern the evolution of an ensemble of mixed neutrinos are the quantum Liouville equations:

$$i\dot{\rho}_{\mathbf{p}} = [H_{\mathbf{p}}, \rho_{\mathbf{p}}] \qquad ; \qquad i\dot{\bar{\rho}}_{\mathbf{p}} = [\bar{H}_{\mathbf{p}}, \bar{\rho}_{\mathbf{p}}] \tag{3.38}$$

where we have adopted the natural units $c = \hbar = 1$. In these equations $\rho_{\mathbf{p}}$ $(\bar{\rho}_{\mathbf{p}})$ is the matrix of occupation numbers. On the other hand, the Hamiltonian can be written as a sum of three interaction terms:

$$\mathsf{H} = \mathsf{H}_{\text{vacuum}} + \mathsf{H}_{\text{matter}} + \mathsf{H}_{\nu\nu}. \tag{3.39}$$

The first term is the Hamiltonian in vacuum, the second term is the matter Hamiltonian and the last term the neutrino-neutrino interaction Hamiltonian. Each Hamiltonian is characterized by its own potential: $\omega_{p,r}$, λ_r and μ_r, the vacuum, matter and self-interaction neutrino potentials, respectively. All the interaction potentials depend on r, the distance travel for the neutrino from the NS surface, and each effective potential strength is parametrized as follows [56]:

$$\omega_{p,r} = \frac{\Delta m^2}{2p\langle v_r\rangle}, \tag{3.40}$$

$$\lambda_r = \sqrt{2}G_F \left(n_{e^-}(r) - n_{e^+}(r)\right) \frac{1}{\langle v_r\rangle}, \tag{3.41}$$

$$\mu_r = \frac{\sqrt{2}G_F}{2} \left(\sum_{i\in\{e,x\}} n^C_{\nu_i\bar{\nu}_i}\right) \left(\frac{R_{\text{NS}}}{r}\right)^2 \left(\frac{1-\langle v_r\rangle^2}{\langle v_r\rangle}\right), \tag{3.42}$$

with $\langle v_r\rangle$ the average value of the neutrino projected velocity:

$$\langle v_r\rangle = \frac{1}{2}\left[1 + \sqrt{1 - \left(\frac{R_{\text{NS}}}{r}\right)^2}\,\right]. \tag{3.43}$$

The self-interaction neutrino potential has been written using the *single-angle limit* approximation. This consists in *imposing* a self-maintained coherence in the neutrino system, i.e. it is assumed that the flavor evolution of all neutrinos emitted from an extended source is the same as the flavor evolution of the neutrinos emitted from the source along a particular path. Under this premise, the propagation angle between the test neutrino and the background neutrinos is fixed.

For the NS accreting atmosphere constructed in Section (3.2), Figure 3.6 shows the behavior of the effective potentials for two selected mass accretion rate: $\dot{M} = 10^{-2} M_\odot\,\text{s}^{-1}$ and

$10^{-8} M_\odot\,\mathrm{s}^{-1}$. The neutrino self-interaction potential decays with the radial distance from the NS faster than the matter potential, as can be predictive from equations (3.40)-(3.42).

For the high accretion rates ($\dot{M} > 5 \times 10^{-5}\, M_\odot\,\mathrm{s}^{-1}$), we identify three different regions along the neutrino trajectory inside the Bondi-Hoyle radius, in which the oscillations are dominated by intrinsically different neutrino phenomenology. Just after the neutrino creation in the regions of the accretion zone, very close to the surface of the NS the potentials obey the following hierarchy: $\lambda_r \gtrsim \mu_r \gg \omega_r$. Then, the neutrinos undergo kinematic decoherence along the same length scale of a single cycle of the so-called bipolar oscillations. Bipolar oscillations imply very fast flavor conversion between neutrino pairs $\nu_e\bar{\nu}_e \leftrightarrow \nu_\mu\bar{\nu}_\mu \leftrightarrow \nu_\tau\bar{\nu}_\tau$ and, the oscillation length in this region can be so small as of the order tens of meters ($\tau \approx (0.05-1)\,\mathrm{km}$). Kinematic decoherence induces a fast flux equipartition among the different flavors, i.e a few kilometres from the emission region, we can assume $\nu_e : \nu_\mu : \nu_\tau = 1 : 1 : 1$ [291].

After leaving the emission region, beyond $r \approx R_{\mathrm{NS}} + \Delta r_{\mathrm{ER}}$, where Δr_{ER} is the width defined in equation (3.20), the effective neutrino density quickly falls in a asymptotic behavior $\mu_r \approx 1/r^4$ while the decay of λ_r is slower. Hence, very soon the neutrino flavor evolution is determined by the matter potential. Matter suppresses neutrino oscillations and we do not expect significant changes in the neutrino flavor content along a large region. Nevertheless, the matter potential can be so small that there will be a region along the neutrino trajectory in which it can be compared with the neutrino vacuum frequencies and the higher and lower resonant density conditions will be satisfied, i.e.:

$$\lambda(r_H) = \omega_H = \frac{\Delta m^2}{2\langle E_\nu \rangle} \quad \text{and} \quad \lambda(r_L) = \omega_L = \frac{\Delta m^2_{21}}{2\langle E_\nu \rangle}, \tag{3.44}$$

where Δm^2 and Δm^2_{21} are, respectively, the squared-mass differences found in atmospheric and solar neutrino observations. When the above resonance conditions are satisfied the (Mikheyev-Smirnov-Wolfenstein) MSW effects [182, 308] happen and the flavor content of the flux of electronic neutrinos and antineutrinos will be again modified. In Uribe et al. [291] was followed the neutrino flavor evolution all the way from their emission on the NS surface until they reach the Bondi-Hoyle radius. We present in Figure 3.7 the relative fluxes F_ν/F_ν^C between the creation and emission fluxes for the specific case of $\dot{M} = 10^{-2} M_\odot\ \mathrm{s}^{-1}$. Although no energy spectrum distortion is expected, the neutrino flavor content emerging from the Bondi-Hoyle surface to the outer space is different from the original one at the bottom of the accretion zone. The initial 70% and 30% distribution of electronic and non-electronic neutrinos becomes 55% and 45% or 62% and 38% for normal or inverted hierarchy, respectively. Since the $\nu \leftrightarrow \bar{\nu}$ oscillations are negligible [212, 213, 314] the total neutrino to antineutrino ratio is kept constant.

For accretion rates $\dot{M} < 5 \times 10^{-5} M_\odot\ \mathrm{s}^{-1}$, either the matter potential is close enough to the vacuum potential and the MSW condition is satisfied, or both the self-interaction and matter potentials are so low that the flavor oscillations are only due to the vacuum potential (see Figure 3.6). In both cases, bipolar oscillations are not presented and it is not possible to guarantee that decoherence will be complete. The resonance region could be located around closer to the NS surface, anticipating the MSW condition $\lambda_r \sim \omega_r$. This changes the neutrino flavor evolution and, of course, the emission spectrum. Hence,

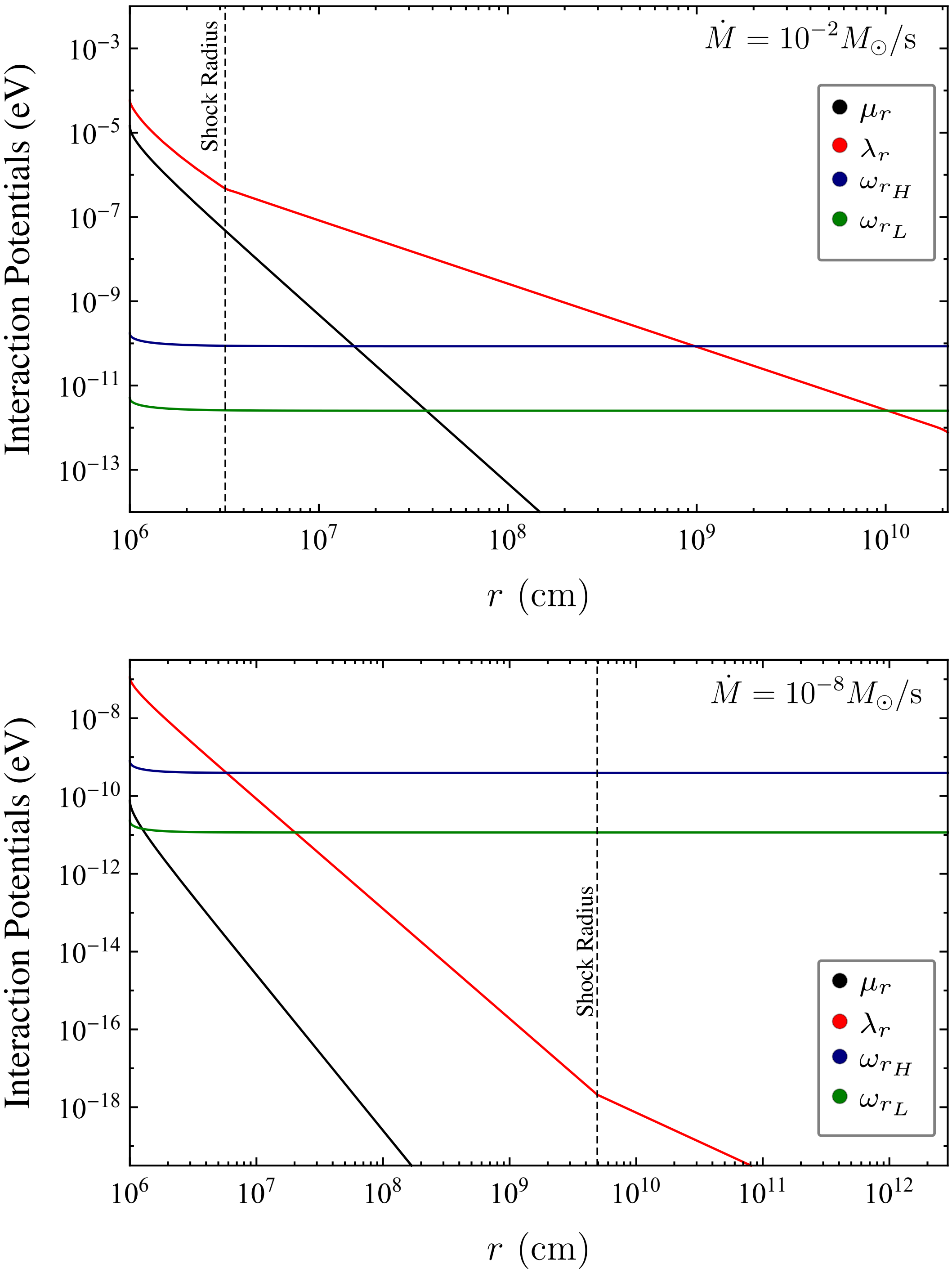

Figure 3.6.: Interaction potentials as functions of the radial distance from the NS center for two selected accretion rates $\dot{M} = 10^{-2}\, M_\odot\, \mathrm{s}^{-1}$ (upper panel) and $10^{-8}\, M_\odot\, \mathrm{s}^{-1}$ (bottom panel), see Table 3.1. Each plot runs from the NS surface to the Bondi-Hoyle surface. μ_r stands for the self-interaction neutrino potential, λ_r is the matter potential and ω_H and ω_L are the higher and lower resonances corresponding to the atmospheric and solar neutrino scales, respectively. Outside the Bondi-Hoyle region the neutrino and electron densities depend on the direction of their path relative to the SN and the particular ejecta density profile.

NOTE— Image taken from Uribe et al. [291]

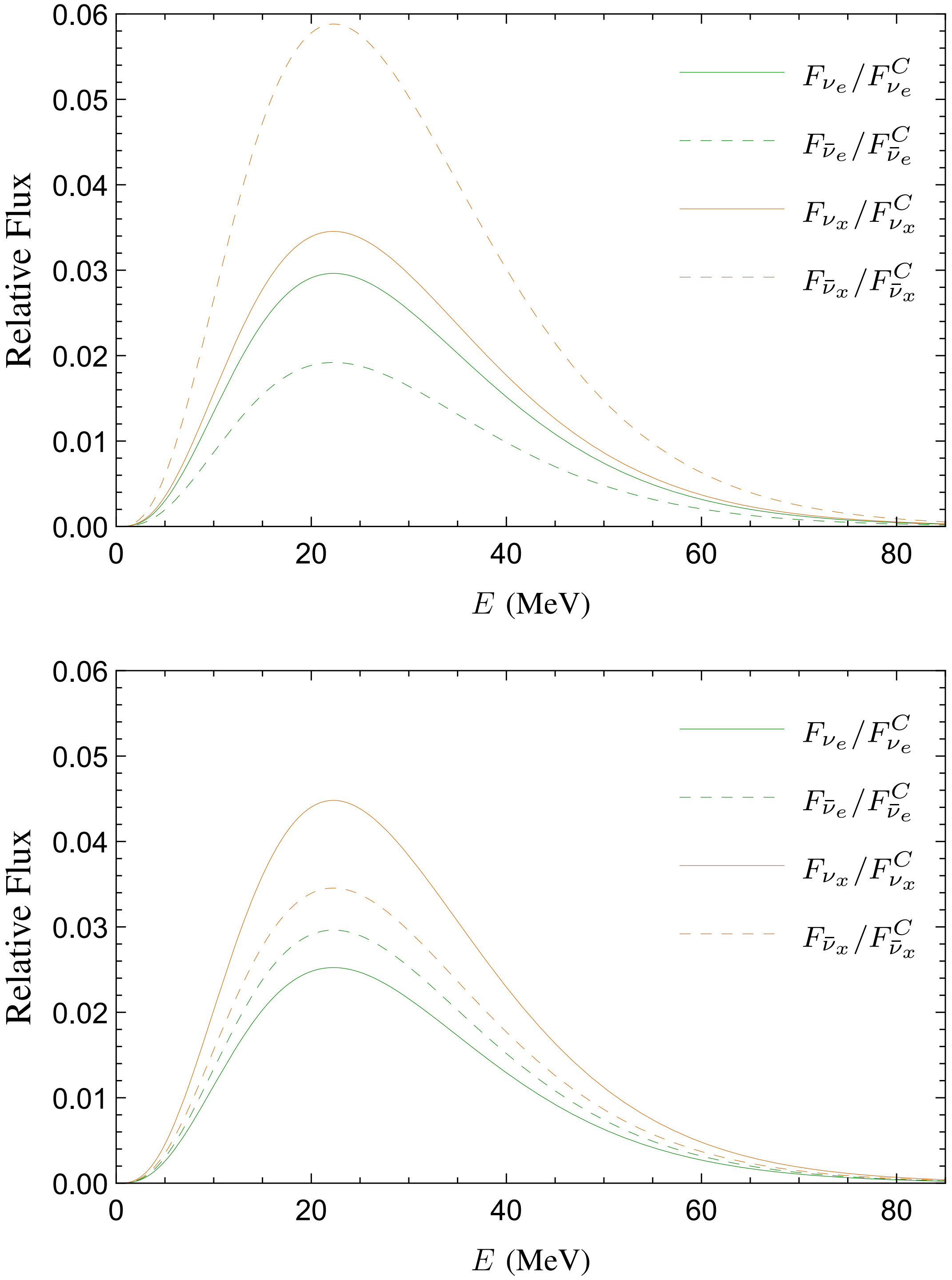

Figure 3.7.: Relative fluxes for different neutrino flavors between the creation neutrino flux, F^C_ν, at the bottom accretion zone due to e^+e^- pair annihilation and the emission flux, F_ν, after past the region with dominant neutrino-neutrino potential and the region with dominant neutrino-matter potential. It's presented the case for $\dot{M} = 10^{-2}M_\odot$/s. Each column corresponds to a neutrino mass hierarchy: normal hierarchy on the left and inverted hierarchy on the right.

NOTE— Image taken from Uribe et al. [291]

the signature neutrino-emission spectrum associated with the least luminous XRFs might be different from the ones described here.

3.4. Conclusions and perspectives

Although, in Chapter 1 we show that the SN ejecta carry enough angular momentum to form a disk-like structure around the NS before being accreted, here, in order to study the hydrodynamics inside the accretion zone, we have assumed isotropic accretion on the NS. We consider this study a first approximation to a more detailed picture, that has allowed us to set the main framework and accounts for the general physical properties of the system.

Explicitly, in order to solve the hydrodynamics equations, we have assumed: spherically symmetric accretion onto a non–rotating NS, a quasi-steady-state evolution parametrized by the mass accretion rate, a polytropic equation of state, and subsonic velocities inside the shock radius. The matter is described by a perfect gas made of ions, electrons, positrons and radiation with electron and positron obeying a Fermi-Dirac distribution. The electron fraction was fixed and equal to 0.5. We considered pair annihilation, photo-neutrino process, plasmon decay and bremsstrahlung to calculate neutrino emissivities. Under the above conditions we have found that the pair annihilation dominates the neutrino emission for the accretion rates involved in XRFs and BdHNe. The photons are trapped within the infalling material and the neutrinos are transparent, taking away most of the energy from the accretion (see Figures 3.4 and 3.5).

Future work could be made in order to relax some of the above assumptions, e.g. the assumption of spherical symmetry to introduce a disk-like accretion picture. In this line it is worth mentioning that some works have been done in this direction [see, e.g., 322, 323], although in a Newtonian framework, for complete dissociated matter, and within the thin-disk approximation. In these models disk heights of the order of $H/r \sim 0.1$ are obtained near the neutron star surface which suggests that the results might be similar to the ones of a spherical accretion as the ones we have adopted. A generalization including general relativistic effects in axial symmetry to account for the fast rotation that the NS acquires during the accretion process is also needed. This was already implemented for the computation of the accretion rates at the Bondi-Hoyle radius position in Chapter 1, but it needs still to be implemented in the computation of the matter and neutrino density-temperature structure near the NS surface. In addition, the description of the equation of state of the infalling matter can be further improved by taking into account beta and nuclear statistical equilibrium.

This first study of the accretion NS atmosphere, has allowed us, also, to identify key theoretical and numerical features involved in the study of neutrino oscillations in the IGC scenario of GRBs. From this understanding, we can infer that neutrino oscillations might be markedly different in a disk-like accretion process. First, depending on the value of the NS mass, the inner disk radius may be located at an $r_{\mathrm{inner}} > R_{\mathrm{NS}}$. On the other hand, depending on the accretion rate, the density near the inner radius can be higher than in the present case and move the condition for neutrino cooling farther from the inner disk radius, at $r > r_{\rm inner}$. Both of these conditions would change the geometric set up of the neutrino emission. Furthermore, possible larger values of T and ρ may change the mechanisms involved in neutrino production. For example, electron-positron pair capture, namely $p+e^- \to n+\nu_e$, $n+e^+ \to p+\bar{\nu}_e$ and $n \to p+e^- +\bar{\nu}_e$, may become as efficient as the e^-e^+ pair annihilation. This, besides changing the intensity of the neutrino emission, would change the initial neutrino-flavor configuration.

It raises naturally the question of the possibility for the neutrinos emitted during the hypercritical accretion process in XRFs and BdHNe to be detected in current neutrino observatories. For instance, detectors such as Hyper-Kamiokande are more sensitive to the inverse beta decay events produced in the detector, i.e. $\bar{\nu}_e + p \to e^+ + n$ [see 1, for more details], consequently, the $\bar{\nu}_e$ are the most plausible neutrinos to be detected. Liu et al. [161] have pointed out that for a total energy in $\bar{\nu}_e$ of 10^{52} erg and $\langle E_{\bar{\nu}_e}\rangle \sim 20$ MeV, Hyper-Kamiokande would detect neutrinos up to a horizon distance of about 0.6 Mpc. In the more energetic case of BdHNe we have typically $\langle E_{\nu,\bar{\nu}}\rangle \sim 20$ MeV (see Table 3.1) and a total energy carried out $\bar{\nu}_e$ of the order of the gravitational energy gain by accretion, i.e. $E_g \sim 10^{52}$–10^{53} erg. Therefore we expect BdHNe neutrinos to be detectable up to distances $\sim$ 0.1–1 Mpc. These order-of-magnitude estimates need to be confirmed by detailed calculations, including the vacuum oscillations experienced by the neutrinos during their travel to the detector.

An IGC binary leading either to an XRF or to a BdHNe is a unique neutrino-physics laboratory in which there are at least three neutrino emission channels at the early stages of the GRB-emission process: (i) the neutrinos emitted in the explosion of the $\rm CO_{core}$ as SN; (ii) the neutrinos studied in this work created in the hypercritical accretion process triggered by the above SN onto the NS companion, and (iii) the neutrinos from fallback accretion onto the νNS created at the center of the SN explosion. It remains to establish the precise neutrino time sequence as well as the precise relative neutrino emissivities from all these events. This is relevant to establish both the time delays in the neutrino signals as well as their fluxes which will become a unique signature of GRB neutrinos following the IGC paradigm.

4. Observational applications for the IGC scenario for long-GRBs

4.1. Introduction

Gamma-ray bursts (GRBs) are the brightest explosions in the universe with isotropic luminosities between $10^{47} - 10^{54}$ erg s^{-1}. The first GRB was detected by the Vela satellites on July of 1967, but its discovery was made public until 1973 [146]. Following, with the launch of the *Compton Gamma Ray burst Observatory*(CGRO) in 1990 and the observations by the BATSE detector [173], a phenomenological classification based on the prompt T_{90} duration was advanced: GRBs were classified into long GRBs with $T_{90} > 2$ s, and short GRBs with $T_{90} < 2$ s [61, 145, 150, 286]. In 1997, for the first time, Beppo-SAX satellites detected the x-ray afterglow of long GRBs [52] and an accurate localization of these events allowed also the measurement of their optical/radio counterparts [75, 294]. This discovery made the determination of the GRBs redshift possible and the confirmation of their cosmological nature, their high energies releases $\approx 10^{50} - 10^{54}$ erg and their origin in star forming regions in host galaxies [180]. Beppo-SAX also detected the temporal and spatial coincidence of GRB 980425 with SN 1998bw [95]. This observation suggested the connection between GRBs and SNe, and was soon supported by many additional events [see e.g. 59, 117, 311].

Nowadays, the study of GRBs continues with the detections of Swift [98] and Fermi [6] missions. The Swift burst alert telescope (BAT), operating in the 15–150 keV energy band, can detect GRB prompt emissions and accurately determine their position in the sky within 3 arcmin. Within 90 s Swift can re-point the narrow-field X-ray telescope (XRT), operating in the 0.3–10 keV energy range, and relay the burst position to the ground. The Fermi satellite detects ultra-high energy photons from 20 MeV to 300 GeV with the large area telescope (LAT), and detects photons from 8 keV to 30 MeV with the gamma-ray burst monitor (GBM).

Long GRBs have been associated with the death of massive stars. It has been assumed that these event originate from a “collapsar” [33, 166, 200, 310] which, in turn, originates from the collapse of the core of a single massive star to a BH surrounded by a thick massive accretion disk [209]; or a “magnetar” [292], powered by the spin-down of a newly-formed, rapidly-spinning magnetar [321] .

Alternatively, it has been proposed the IGC paradigm as progenitor of long GRBs: a CO$_{\text{core}}$ undergoes a SN explosion in presence of a NS companion in a tight binary system.

This scenario was shown to be consistent with population synthesis analysis [88, 93]. The SN explosion induces a hypercritical accretion of its ejecta onto the companion NS, leading to the formation of a more massive NS, when the NS critical mass $M_{\rm crit}$ is not reached, or to the formation of a BH with the associated GRB emission in the opposite case [see, e.g., 90, 227]. Two different sub-classes of long bursts originates from this picture, depending on the distance between the $\rm CO_{core}$ and the NS binary companion (see Chapter 2): the XRFs, which clearly include low-luminous GRBs, such as GRB 060218 [38], when no BH is formed, and the BdHNe, such as GRB 130427A [243], when a BH is formed. These division is in agreement with the considerations by Guetta & Della Valle [107], Liang et al. [160], Soderberg et al. [271] for a sub-classification of long bursts into low-luminous and high-luminous GRBs.

The IGC paradigm have been supported by new astrophysical observations: the great majority of GRBs are related to type Ic SNe, which have no trace of hydrogen and helium in their optical spectra, and are spatially correlated with bright star-forming regions in their host galaxies [77, 277]. Most massive stars are found in binary systems [268] where most type Ic SNe occur and which favor the deployment of hydrogen and helium from the SN progenitors [269], and the SNe associated with long GRBs are indeed of type Ic [59]. In addition, these SNe associated with long bursts are broad-lined Ic SNe (hypernovae) showing the occurrence of some energy injection leading to a kinetic energy larger than that of the traditional SNe Ic [165].

We organized this chapter as follows. We present in Section 4.2 estimates of the expected luminosities during the hypercritical accretion process. In Section 4.3 we describe the convective instabilities developed at the accreting NS atmosphere. We show in Section 4.4 the asymmetries that the accreting NS produces on the SN ejecta. In Section 4.5 and 4.6 we resume the principal observational properties and the theoretical interpretation into the IGC paradigm for the subclasses of long GRBs: XRFs and BdHNe, respectively. For the case of XRFs in subsection 4.5.3 we show how the radiation from the accretion process as well as the asymmetries in the ejecta influence the SN emission both in X-rays and in the optical. For the case of BdHNe, in subsection 4.6.3 we present the results of the simulation of the interaction of the e^+e^--baryon plasma with the high-density regions of the SN ejecta and associate it as the origin of early X-ray flares in GRBs. Finally in Section 4.7 we summarize the results of this chapter.

4.2. Accretion Luminosity

If we want to make a comparison with observed light-curves of XRFs and BdHNes systems, we need to estimate the luminosity produced during the accretion process. The gain of gravitational potential energy in the accretion process is the total one available to be released e.g. by neutrinos and photons. The total energy released in the star in a time-interval dt during the accretion of an amount of mass dM_b with angular momentum $l\dot{M}_b$, is given by [see, e.g., 14, 265]:

$$L_{\rm acc} = (\dot{M}_b - \dot{M}_{\rm NS})c^2 = \dot{M}_b c^2 \left[1 - \left(\frac{\partial M_{\rm NS}}{\partial J_{\rm NS}} \right)_{M_b} l - \left(\frac{\partial M_{\rm NS}}{\partial M_b} \right)_{J_{\rm NS}} \right], \tag{4.1}$$

where we have used equation (1.35). This upper limit to the energy released is just the amount of gravitational energy gained by the accreted matter by falling to the NS surface and which is not spent in changing the gravitational binding energy of the NS. Since $L_{\rm acc} \propto \dot{M}_b$, it evolves with time similarly to $\dot{M}_B$.

The total energy release in the time interval from t to $t + dt$, $\Delta E_{\rm acc} \equiv \int L_{\rm acc} dt$, is given by the difference in binding energies of the initial and final NS configurations. The typical luminosity will be $L_{\rm acc} \approx \Delta E_{\rm acc}/\Delta t_{\rm acc}$ where $\Delta t_{\rm acc}$ is the duration of the accretion process. $L_{\rm acc}$ is clearly a function of the NS initial mass and the NS critical mass, $M_{\rm crit} \in [\,2.2, 3.4\,]\, M_\odot$ depending of the EOS and the NS angular momentum (see Appendix A.2).

The duration of the accretion process is given approximately by the flow time of the slowest layers of the SN ejecta to the NS. If the velocity of these layers is $v_{\rm inner}$, then $\Delta t_{\rm acc} \sim a/v_{\rm inner}$, where a is the binary separation. For $a \sim 10^{11}$ cm and $v_{\rm inner} \sim 10^8$ cm s^{-1} we obtain $\Delta t_{\rm acc} \sim 10^3$ s, while for shorter binary separation, e.g. $a \sim 10^{10}$ cm ($P \sim 5$ min), $\Delta t_{\rm acc} \sim 10^2$ s, as validated by the results of our numerical integrations shown e.g. in Figures. 1.3 and 2.1 and see also Appendix A.1.

We have shown in Figure 2.1 the evolution of both the baryonic mass $\dot{M}_b$ and the gravitational mass $\dot{M}_{\rm NS}$ for a specific example. We see that these two quantities show a similar behavior, therefore we should expect the difference between them, which gives the available energy to be released (4.1), evolves with time analogously. Besides, we can see that the NS in the system with $P = 5$ min accretes $\approx 1\ M_\odot$ in $\Delta t_{\rm acc} \approx 100$ s. With the aid of equation (A.13) we can estimate the difference in binding energies between a 2 $M_\odot$ and a 3 $M_\odot$ NS, i.e. $\Delta E_{\rm acc} \approx 13/200(3^2 - 2^2)\ M_\odot c^2 \approx 0.32\ M_\odot c^2$ leading to a maximum luminosity $L_{\rm acc} \approx 3 \times 10{-}3\ M_\odot c^2 \approx 0.1 \dot{M}_b c^2$.

Such an accretion power could lead to signatures observable in long GRBs [see, e.g., 90, 137] since it could be as high as $L_{\rm acc} \sim 0.1 \dot{M}_b c^2 \sim 10^{47}$–$10^{51}$ erg s^{-1} for accretion rates in the range $\dot{M}_b \sim 10^{-6}$–$10^{-2}\ M_\odot$ s^{-1}.

4.3. Convective instabilities

As the material piles onto the NS and the atmosphere radius, the accretion shock moves outward. The post-shock entropy is a decreasing function of the shock radius position which creates an atmosphere unstable to Rayleigh-Taylor convection during the initial phase of the accretion process (see Figure 3.3). These instabilities can accelerate above the escape velocity driving outflows from the accreting NS with final velocities approaching the speed of light [79, 86]. Assuming that radiation dominates (i.e. $P_{\rm tot} = aT^4/3$), the entropy of the material at the base of the atmosphere is [83]:

$$S_{\rm bubble} \approx 16 \left(\frac{M_{\rm NS}}{1.4\, M_\odot}\right)^{7/8} \left(\frac{\dot{M}_{\rm B}}{M_\odot\, {\rm s}^{-1}}\right)^{-1/4} \left(\frac{r}{10^6\, {\rm cm}}\right)^{-3/8}, \tag{4.2}$$

in units of k_B per nucleon.

This material will rise and expand, cooling adiabatically, i.e. $T^3/\rho =$ constant, for radiation dominated gas. If we assume a spherically symmetric expansion, then $\rho \propto 1/r^3$ and we obtain

$$k_B T_{\rm bubble} = 195\, S_{\rm bubble}^{-1} \left(\frac{r}{10^6\, {\rm cm}}\right)^{-1} {\rm MeV}. \tag{4.3}$$

However, it is more likely that the bubbles expand in the lateral but not in the radial direction [79], thus we have $\rho \propto 1/r^2$, i.e.

$$T_{\rm bubble} = T_0(S_{\rm bubble}) \left(\frac{r_0}{r}\right)^{2/3}, \tag{4.4}$$

where $T_0(S_{\rm bubble})$ is given by equation (4.3) evaluated at $r = r_0 \approx R_{\rm NS}$.

This temperature implies a bolometric blackbody flux at the source from the bubbles

$$\begin{aligned} F_{\rm bubble} &= \sigma T_{\rm bubble}^4 \approx 2 \times 10^{40} \left(\frac{M_{\rm NS}}{1.4\, M_\odot}\right)^{-7/2} \left(\frac{\dot{M}_{\rm B}}{M_\odot\, {\rm s}^{-1}}\right) \\ &\times \left(\frac{R_{\rm NS}}{10^6\, {\rm cm}}\right)^{3/2} \left(\frac{r_0}{r}\right)^{8/3} {\rm erg\, s^{-1} cm^{-2}}\,. \end{aligned} \tag{4.5}$$

In Fryer et al. [90] it was shown that the above thermal emission from the rising bubbles produced during the hypercritical accretion process can explain the early ($t \lesssim 50$ s) thermal X-ray emission observed in GRB 090618 [137, 138]. In that case $T_{\rm bubble}$ drops from 50 keV to 15 keV expanding from $r \approx 10^9$ cm to 6×10^9 cm, for an accretion rate $10^{-2}\ M_\odot\ {\rm s}^{-1}$.

Also, from the above formulas we can explain the blackbody emission observed in XRF 060218 [38]. The observed temperature ($k_B T \approx 0.2$ keV) and radius of the emitter (a few 10^{11} cm) are consistent with the temperature and surface radius of the above bubbles formed in a system with a NS of initial mass 1.4 $M_\odot$, supernova-progenitor of $M_{\rm ZAMS} = 20\, M_\odot$, and orbital period 2.5 h: it can be easily checked via equation (4.4) that for $r \sim 10^{11}$ cm and an accretion rate of the order of $10^{-6}\ M_\odot\ {\rm s}^{-1}$, the bubbles would have a temperature consistent with the one observed in XRF 060218. Further details on this specific case and additional examples will be presented below.

It is worth mentioning the possibility that, as discussed in Fryer et al. [86], r-process nucleosynthesis occurs in these outflows. This implies that long GRBs can be also r-process sites with specific signatures from the decay of the produced heavy elements, possibly similar as in the case of the *kilonova* emission in short GRBs [see, e.g., 281, and references therein]. The signatures of this phenomenon in XRFs and BdHNe, and its comparison with kilonovae, deserves to be explored.

4.4. Supernova Asymmetries induced by the NS Hypercritical accretion: first particle simulation

For isolated SN explosions, or for very wide binaries with negligible accretion rates, the density of the SN ejecta would approximately follow the homologous evolution given by equation (1.5) with constant ejecta mass, i.e. $M_{\rm env}(t) = M^0_{\rm env}$, i.e. the density will decrease with time following a simple power-law $\rho_{\rm ej}(t) \propto t^{-3n}$, with n the expansion parameter, keeping its spherical symmetry about the explosion site (see, e.g., Figure 4.1). However, for explosions occurring in close binaries with compact companions such as NSs or BHs, the SN ejecta is subjected to a strong gravitational field which produces at least two non-negligible effects: 1) an accretion process on the NS that subtracts part of the ejecta mass, and 2) a deformation of the SN fronts closer to the accreting NS companion. As we show below, the conjunction of these effects can generate large changes in the density profile of the ejecta in a region around the orbital plane.

In order to visualize the above effects we have simulated the evolution of the SN layers in presence of the NS during the accretion process (see Figures 4.1 and 4.2). Thus, we followed the three-dimensional motion of N particles in the gravitational field of the orbiting NS. We consider the gravitational field of the NS on the SN ejecta including the effects of the orbital motion as well as the changes in the NS gravitational mass as described above in Chapters 1 and 2 via the Bondi-Hoyle formalism. The SN matter is described as formed by point-like particles whose trajectory was computed by solving the Newtonian equation of motion:

$$\frac{d^2\vec{r}_{\rm sn}(t)}{dt^2} = -GM_{\rm NS}(t)\frac{\vec{r}_{\rm sn}(t) - \vec{r}_{\rm NS}(t)}{|\vec{r}_{\rm sn}(t) - \vec{r}_{\rm NS}(t)|^3} \, . \tag{4.6}$$

We have also performed SPH simulation of this process (see next Chapter). The initial conditions of the SN ejecta are computed assuming the SN layers move via homologous velocity distribution in free expansion (i.e. evolving with $n = 1$). The initial power-law density profile of the CO envelope is simulated by populating the inner layers with more particles, as follows. The total number of particles is $N = N_r \times N_\theta \times N_\phi$ and for symmetry reasons, we simulate only the north hemisphere of the SN; thus the polar and azimuthal angles are divided as $\Delta\theta = (\pi/2)/N_\theta$ and $\Delta\phi = 2\pi/N_\phi$, respectively. For the radial coordinate we first introduce the logarithmic coordinate $x = \log(r)$ and $\Delta x = (x_s - x_c)/N_r$, where $x_s = \log(R_{\rm star})$ and $x_c = \log(R_{\rm core})$. Thus,the thickness of each layer is $\Delta r = r_i(10^{\Delta x} - 1)$, where r_i is the location of the layer. The mass of each particle of the i-layer is: $m_i = 4\pi r_i^3 \ln(10)\Delta x \rho(r_i)/(2N_\theta N_\phi)$.

Let us assume, for the sake of example, the $M_{\rm ZAMS} = 30\ M_\odot$ progenitor of table 1.1 which gives a $\mathrm{CO}_{\rm core}$ with envelope profile $\rho^0_{\rm ej} \approx 3.1 \times 10^8 (8.3 \times 10^7/r)^{2.8}$ g cm^{-3} and $R^0_{\rm star} = 7.65 \times 10^9$ cm. This implies that, for a total number of $N = 10^6$ particles in the simulation, the particles of the innermost radius $r_i = R_{\rm core} = 8.3 \times 10^7$ cm with density $\rho^0_{\rm ej}(r_i) = 3.1 \times 10^8$ g cm^{-3} have mass $m_i \approx 2 \times 10^{-5}$ $M_\odot$ while, the particles of the outermost radius $r_i = R^0_{\rm star}$, would have $m_i \approx 6 \times 10^{-6}$ $M_\odot$. In addition, we assume that particles crossing the Bondi-Hoyle radius are captured and accreted by the NS so we removed them from the system as they reach that region. We removed these particles according to the results obtained from the numerical integration of equation (1.8).

Figure 4.1 shows in detail the orbital plane of an IGC binary at selected times of its evolution. The NS has an initial mass of 2.0 $M_\odot$; the CO$_{\rm core}$ is the one obtained by the $M_{\rm ZAMS} = 30$ $M_\odot$ progenitor (see Table 1.1), which leads to a total ejecta with mass 7.94 $M_\odot$ and an iron core that left a νNS of 1.5 $M_\odot$. The orbital period of the binary is $P \approx 5$ min, i.e. a binary separation $a \approx 1.5 \times 10^{10}$ cm, and we have adopted an angular momentum transfer efficiency parameter $\xi = 0.5$. The evolution of the accretion rate and the gravitational mass of the NS in this system are the ones shown in Figure 2.1. As it can be seen, for the above parameters the NS reaches the critical mass and collapses to form a BH (see also Figure 2.2).

In the simulation shown in Figure 4.1 we adopted two millions of particles per solar mass of ejecta so in this simulation we have followed the three-dimensional motion of $N = 2 \times 10^6 (M^0_{\rm env}/M_\odot) \approx 1.6 \times 10^7$ particles in the gravitational field of the orbiting NS. To estimate the ejecta density we have chosen a thickness Δz around the orbital plane. For the plots in Figure 4.1 we have adopted $\Delta z \approx 0.05a \approx 7.1 \times 10^8$ cm.

The left upper panel shows the binary at the initial time of the process, i.e. $t = t_0 = R^0_{\rm star}/v_{\rm star,0} = 3.82$ s, the first instant of the ejecta radial expansion.

The right upper panel shows the instant at which the accretion process begins, namely at $t = t_{\rm acc,0} \approx a/v_{0,\rm star} = 7.7$ s. Owing to their fast velocity, the accretion rate of the first layers is low and they escape almost undisturbed, so the SN ejecta at these times keeps its original spherical symmetry.

The left lower panel shows the binary at the instant in which the accreting NS reaches the critical mass, hence the instant of formation of the BH, at $t = t_{\rm coll} = 254$ s $\approx 0.85P$. The BH mass is thus set by the critical NS mass, i.e. $M_{\rm BH} = M_{\rm crit} \approx 3$ $M_\odot$ (see Figure 2.1). This figure also evidences the asymmetry on the SN density as induced by the presence of the companion and its increasing gravitational field due to the ongoing accretion process onto it. Indeed, it can be seen how the SN 'center' has been shifted from the explosion site originally at the $(0, 0)$ position (see left upper panel), to the approximate position $(0, 2)$. Thus, the layers of the ejecta are displaced as a result of the gravitational attraction of the orbiting NS. This can be understood as follows. When the NS passes over the northern hemisphere, it attracts the northern region of the ejecta towards it. Consequently, that part of the ejecta gain velocity in the northern direction. The same effect occurs in the other regions of the orbit, however the effect is asymmetric because, by the time the NS passes, say over the southern hemisphere, it attracts layers moving at slower velocity with respect to the ones it had attracted in the northern hemisphere before. The reason for this is that the southern fastest layers have moved further already while the NS were passing the northern side. This effect is indeed incorporated in our simulation which follows the trajectory of each of the 14 million particles.

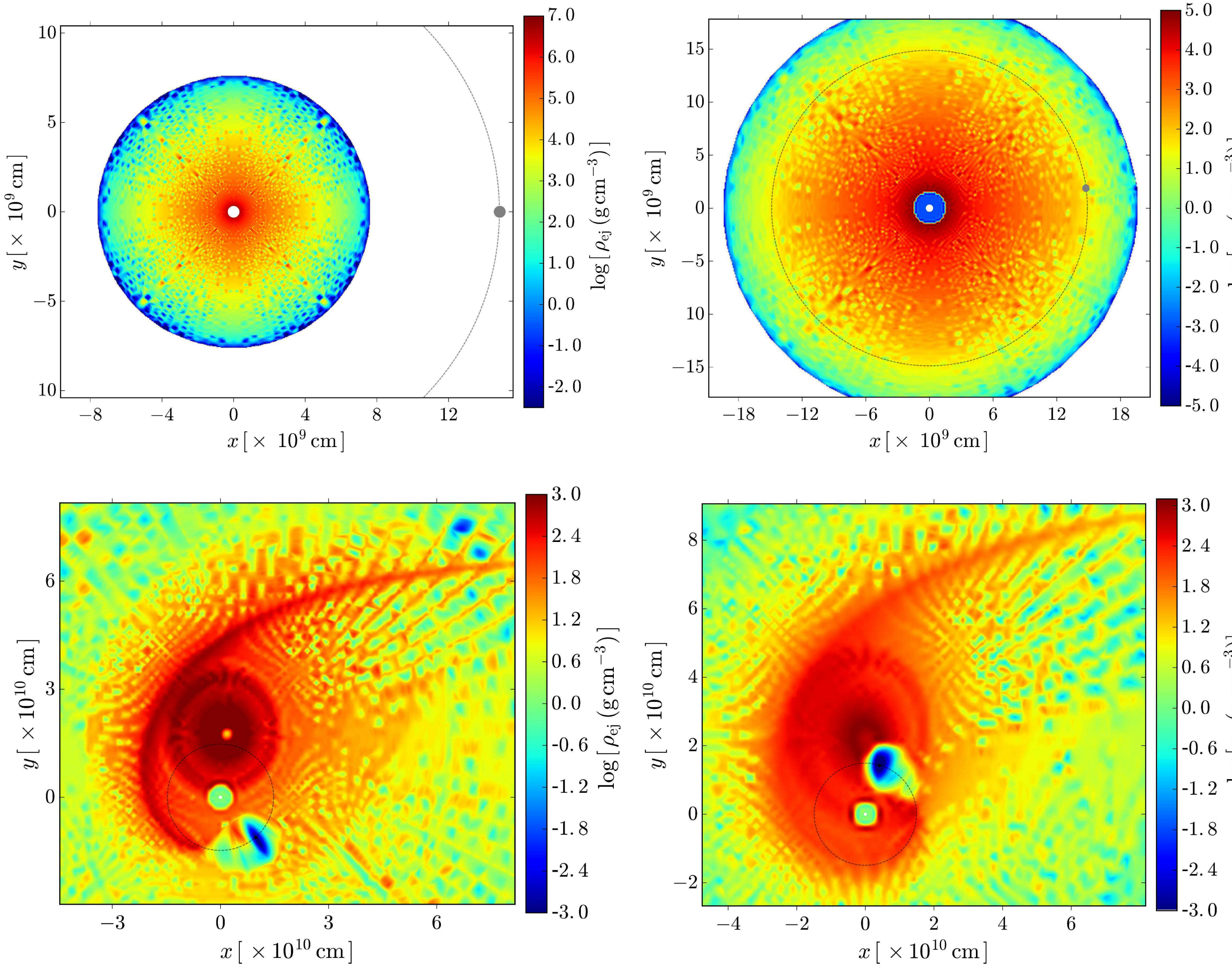

Figure 4.1.: Snapshots of the IGC binary system and the SN ejecta density at selected times of the evolution. In this example we have adopted the $M_{\rm ZAMS} = 30\ M_\odot$ progenitor with an ejecta mass of $7.94\ M_\odot$ and a core that left a νNS of $1.5\ M_\odot$. We assume homologous evolution of the SN ejecta with expansion parameter $n = 1$ and ejecta outermost layer velocity $v_{0_{\rm star}} = 2\times10^9$ cm s^{-1}. For the NS we adopt an initial mass $2.0\ M_\odot$. The binary has an orbital period $P \approx 5$ min, i.e. a binary separation distance $a \approx 1.5\times10^{10}$ cm. The coordinate system is centered on the νNS born in the SN: it is here represented with a white-filled circle located at $(0, 0)$. The NS, represented by the gray-filled circle, is orbiting counterclockwise and its trajectory is indicated with a thin-dashed circle. The colorbar indicates values of ejecta density. We have chosen a thickness Δz around the orbital plane to estimate the ejecta density: $\Delta z \approx 0.05a \approx 7.1\times10^8$ cm for all these figures. *Left upper panel:* initial time of the process, $t = t_0 = R^0_{\rm star}/v_{\rm star,0} = 3.82$ s. The SN ejecta starts to expand radially outward and the NS is located at the position $(a, 0)$. *Right upper panel:* beginning of the accretion process, i.e. passage of the first SN ejecta layers through the NS gravitational capture region. Thus, this time is $t = t_{\rm acc,0} \approx a/v_{0,\rm star} = 7.7$ s. *Left lower panel:* instant when the NS reaches, by accretion, the critical mass and collapses to a BH. This occurs at $t = t_{\rm coll} \approx 254\ {\rm s} \approx 0.85P$. The BH, here represented by the black-filled circle, has a mass set by the critical NS mass, i.e. $M_{\rm BH} = M_{\rm crit} \approx 3\ M_\odot$. It can be seen here the asymmetry of the SN ejecta density induced that have been generated by the nearby presence of the NS and the accretion process onto it. *Right lower panel:* system 100 s after the BH formation, namely $t = t_{\rm coll} + 100\ {\rm s} = 354\ {\rm s} \approx 1.2P$. This figure shows the new binary system composed by the νNS [white-filled circle at the $(0, 0)$ position] out of the SN, and a BH [at the $(0.5, 1.7)$ position] out of the gravitational collapse of the NS due to the hypercritical accretion process. The asymmetry of the SN ejecta is now even larger than the one showed by the left lower panel figure. The asymmetry of the SN ejecta is such that its 'center' has been displaced, from the explosion site originally at the position $(0, 0)$, to the approximate position $(0, 2)$, due to the action of the orbiting NS.

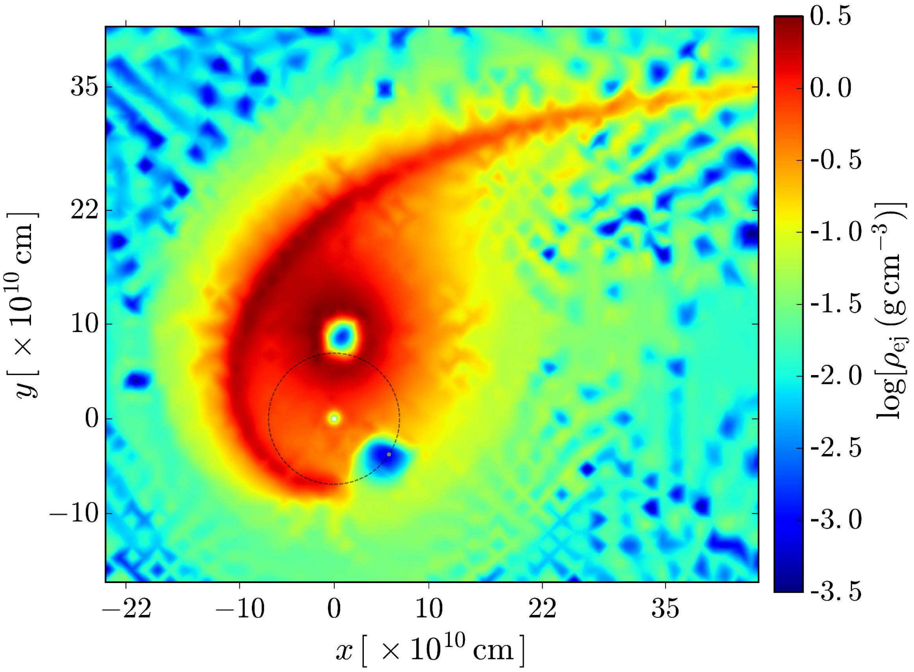

Figure 4.2.: Snapshot of an IGC binary system analogous to the one of Figure 4.1 but with an orbital period of $P \approx 50$ min (i.e. binary separation $a \approx 7 \times 10^{10}$ cm). In this case the accreting NS (gray-filled circle), which is orbiting counterclockwise (thin-dashed circle), does not collapse to the BH. The νNS left by the supernova is represented by the white filled circle at the position $(0, 0)$. It is clear from this figure the asymmetry of the supernova ejecta: indeed the supernova 'center' has been displaced, from the explosion site originally at the position $(0, 0)$, to the approximate position $(0, 9)$, due to the action of the orbiting NS. The snapshot corresponds to a time $t = 2667$ s ≈ 44 min, which corresponds to roughly 1/4 the total accretion process. To estimate the ejecta density we have adopted $\Delta z = 0.08a \approx 5.3 \times 10^9$ cm.

It can be also seen in this figure a stream of matter **(one-armed flow)** of negligible mass with respect to the total mass escaping from the system. As we have mentioned above, the NS attracts some layers increasing their velocity. As a result some material can reach escape velocity to leave the binary system forming this unbound debris. The appearance of a one-armed flow (instead of two-armed flows) is because the center-of- mass is located roughly at the $\mathrm{CO_{core}}$ position, thus the NS is in practice orbiting the $\mathrm{CO_{core}}$. If the two masses were of comparable masses, (e.g. as in the case of binary NS mergers), they would move around a common center-of-mass lying in between them. In such systems the momentum transfer is more symmetric leading to a symmetric two-armed flow structure. The one-armed flow in our system is, in this sense, more similar to the one that appears in the tidal disruption of a small body by a supermassive BH.

The right lower panel shows the system 100 s after the BH formation, namely at $t = t_{\rm coll} + 100$ s $=354$ s $\approx 1.2P$. Thus, this figure shows the new binary system formed by the νNS, out of the SN, and the BH from the gravitational collapse of the NS. The νNS is at the $(0, 0)$ position and it is represented by the white filled circle. The BH is in this instant of time located at the $(0.5, 1.7)$ position and it is represented by the black filled circle. It can be seen the increasing asymmetry of the SN ejecta around the orbital plane. We note the presence of ejecta in the vicinity of the newly formed BH, the latter sited at the approximate position $(0.5, 1.5)$. It is interesting that part of these ejecta can indeed cause a subsequent accretion process onto the newly formed BH. The possible outcomes of this process deserve further attention.

We have shown above the evolution of an IGC binary with very short orbital period of $P \approx 5$ min, for which it occurs the gravitational collapse of the NS of the CO$_{\rm core}$. Besides the formation of a BH, we have evidenced the asymmetry caused by the presence and accretion onto the NS on the SN ejecta density. It is natural to ask if these asymmetries also appear for less compact binaries. For comparison, we show in Figure 4.2 the results of a numerical simulation for a binary with orbital period $P \approx 50$ min, in which the NS does not reach the critical mass during the entire accretion process (see Chapter 2, specifically Section 2.2). The evolution of the accretion rate and the gravitational mass of the NS in this system are shown in Figure 2.1.

In these kind of systems, all the ejecta layers passed the NS position. Thus, the total duration of the accretion process, denoted here $t_{\rm acc}$, is approximately given by the time it takes to the innermost layer of the ejecta to overcome the NS position, i.e. $t_{\rm acc} \approx a/v_{\rm inner}$, where $v_{\rm inner} = (\hat{R}_{\rm core}/R^0_{\rm star})v_{\rm star,0}$ using the homologous expansion assumption. The snapshot corresponds to a time $t = 2667$ s ≈ 44 min $\approx t_{\rm acc}/4$. To estimate the ejecta density we have chosen in this example $\Delta z = 0.08a \approx 5.3 \times 10^9$ cm. It is interesting that although the NS is in this case farther away from the CO$_{\rm core}$, it still induces a high asymmetry on the SN ejecta. We shall investigate elsewhere if this mechanism could explain the asymmetries observed in some type Ibc SNe [see, e.g., 279, 282].

4.5. X-ray Flashes (XRFs)

4.5.1. Observational feactures

In Table 2 in [246] has been listed some XRFs. Below, we listed the main general properties of these events:

- The upper limit on the energetic of the XRFs is $(7.3 \pm 0.7) \times 10^{51}$ erg as measured in GRB 110106B.
- The isotropic energies are in the range $(6.4{\pm}1.6){\times}10^{47} \lesssim E_{\rm iso} \lesssim (7.3{\pm}0.7){\times}10^{51}$ erg [see 2, 243].
- The spectral peak energies are in the range $4 \lesssim E_{\rm p,i} \lesssim 200$ keV [see 2, 243] and increase monotonically with $E_{\rm iso}$.
- The cosmological redshifts are in the range $0.0085 \leq z \leq 1.096$, with an average value of ≈ 0.43 (see Table 2 in [246]).
- The prompt emission phase has a duration ranging between $\sim 10^2$–10^4 s (see Figure 4.3) with a spectrum generally characterized by a thermal component and power-law component. The radii of the thermal emitter are in the range of 10^{10}–10^{12} cm and the temperatures vary in the range of 0.1–2 keV [see, e.g., 38], depending on the values of the binary period and separation of the progenitor systems.
- The long lasting X-ray afterglow does not exhibit any specific common late power-law behavior (see Figure 4.3).

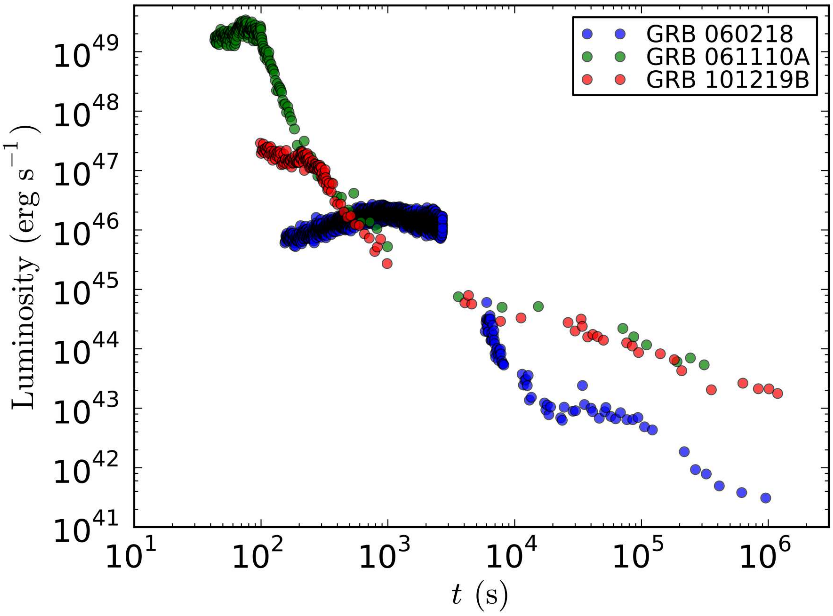

Figure 4.3.: Observed 0.3–10 keV XRT light-curves of some XRFs.

- For all XRFs at $z \lesssim 1$, an optical SN with a luminosity similar to the one of SN 2010bh [35], occurs after 10–15 days in the cosmological rest-frame.
- No high energy emission has ever been observed.

In Figure 4.3 we reproduce the rest-frame 0.3–10 keV luminosity light curves of three selected XRFs: GRB 060218 associated with SN 2006aj [38, 271], GRB 061110A [71, 72], and GRB 101219B [71, 72] associated with SN 2010ma [272].

4.5.2. Theoretical interpretation

In the IGC paradigm an XRF occurs when the CO$_{\rm core}$-NS binary separation, a, is so large (typically $a > 10^{11}$ cm, see Chapter 2) that the accretion of the SN ejecta onto the NS is not sufficient for the NS to reach $M_{\rm crit}$. In Chapter 2, we anticipate that this happen for systems with $P > P_{\rm max}$, being $P_{\rm max}$ the maximum value of the orbital period for which the NS collapses to a BH (e.g. $P_{\rm max} \approx 28$ min for a NS with initial mass of 1.4 $M_\odot$).

The hypercritical accretion of the SN ejecta onto the NS binary companion occurs at rates $< 10^{-2}\ M_\odot\ {\rm s}^{-1}$ and can last from several hundreds of seconds all the way up to $\sim 10^4$ s, until the whole SN ejecta flies beyond the NS binary orbit. The photons are trapped in the accreting material and the accretion energy is lost through a large associated neutrino emission [see, e.g., 90, 227, 239, 319, and see Chapter 3].

The resulting emission, dubbed Episode 1, exhibits a spectrum composed of a thermal component, possibly originating from the outflow within the NS atmosphere driven out by Rayleigh-Taylor convection instabilities (see section 4.3), and a power-law component. The shorter the binary period, the larger the accretion rate (see Appendix A.1) and the values of $E_{\rm iso}$ and $E_{\rm p,i}$, and correspondingly the shorter the prompt emission duration (see

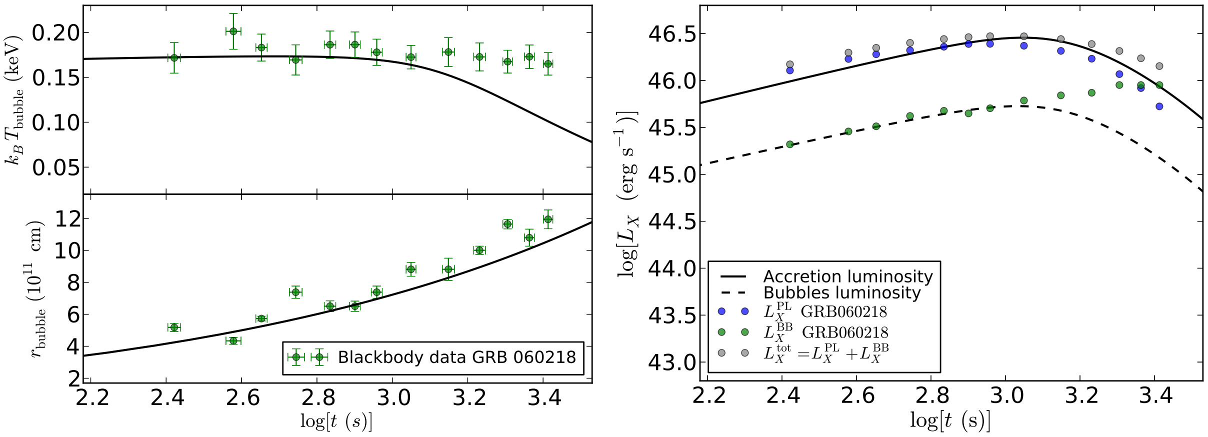

Figure 4.4.: *Left panel:* Evolution of the temperature (upper panel) and the surface radius (lower panel) of the rising entropy bubbles, compared with the thermal emission observed in GRB 060218. *Right panel:* comparison between the theoretical luminosity (accretion and rising bubbles) and the luminosity of GRB 060218. The orbital period of the system is 2.5 h and the data of GRB 060218 is taken form Campana et al. [38].

Figure 4.3). The excess of angular momentum of the system necessarily leads to a jetted emission, manifested in the power-law spectral component (see Chapter 1).

Let us apply now the model presented in Section 4.3 to the case of GRB 060218. Figure 4.4 compares the observed temperature and radius of the blackbody emission observed in GRB 060218 [38] with the temperature and surface radius evolution of the entropy bubbles in the system with a NS of initial mass $1.4\,M_\odot$, SN-progenitor of $M_{\rm ZAMS} = 15\,M_\odot$, and orbital period 2.5 h. In this example the radius expansion is consistent with an expansion law $r \approx r_0(t = t_0)^{2/5}$ and the dimensionality of the bubbles geometry is $D = 1.7$. Indeed in the IGC simulations the typical radii inferred from the evolving thermal component coincide with the observed ones of 10^{10}–10^{12} cm. In the right panel of Figure 4.4 we compare and contrast our prediction of the luminosity with the observed luminosity of GRB 060218.

In the IGC paradigm the in-state is represented by an exploding CO$_{\rm core}$ and a companion NS. The out-state is multiple system composed of a massive NS, resulting from the accretion of part of the SN ejecta onto the binary companion NS, a νNS, originating from the SN event, and the remaining part of the SN ejecta shocked by the hypercritical accretion emission of the XRF. This energy injection into the SN ejecta leads to the occurrence of a broad-lined SN Ic [*hypernova*, see, e.g., 170] with a kinetic energy larger than that of the traditional SNe Ic. The presence of ^{56}Ni in the SN ejecta leads to the observed SN emission after ≈ 10–15 days in the cosmological rest-frame which is observable for sources at $z \lesssim 1$.

Clearly the absence of hard γ-ray and GeV emissions is implicit in the nature of the hypercritical accretion process not leading to a BH and the corresponding rate of neutrino emission.

4.5.3. Influence of the Hypercritical accretion on the SN emission

In Figure 4.5 we compare and contrast the luminosity expected from the accretion process given by equation (4.1) and from the accretion-powered SN, with the observed X-ray luminosity of XRF 060218. The parameters characterizing the binary are: orbital period of 2.5 h, SN velocity $v_{\rm star,0} = 2 \times 10^9$ cm s^{-1}, a pre-supernova core obtained from the $M_{\rm ZAMS} = 20\ M_\odot$ evolution which leads to a CO$_{\rm core}$ envelope mass $\sim 4\ M_\odot$ (see table 1.1), and initial NS mass $M_{\rm NS}(t_0) = 1.4\ M_\odot$. For these binary parameters, the NS does not collapse to a BH, in agreement with the fact that XRFs, as GRB 060218, should be explained by these kind of binaries. The duration of the accretion is shorter than the one of the long-lasting X-ray emission (at times $t \sim 10^3$–10^6 s). We shall show such a long-lasting emission can be explained from the SN powered by the prompt radiation.

We now analyse the emission of the SN at early stages. Traditionally, the SN shock breaks out of the star producing a burst of X-ray emission which, in a spherically symmetric model, behaves as a sharp rise and equally fast decay as the forward shock cools. However, in our models, the SN shock has distinct asymmetries caused by the accretion onto the NS (see Figures 4.1–4.2). In addition, the X-rays emitted from this hypercritical accretion add energy to the explosion. To calculate the shock breakout luminosity, we use the simplified light-curve code described in Bayless et al. [11] and de la Rosa et al. [58]. This code assumes homologous outflow for the ejecta velocities, modelling the radiative transport using a single group diffusion scheme with prescriptions for recombination opacities and energies. Energy released in the accretion onto the NS is injected as an energy source at the base of the explosion. Because these calculations are 1-dimensional, we mimic the asymmetry in the explosion by modelling a series of spherical explosions with different densities. Each of these densities produces a different light-curve with the more massive models producing later shock breakout times.

For GRB 060218, our model assumes an initial explosion energy of 2×10^{51} erg, ranging the spherical equivalent-mass from 0.05–4 $M_\odot$. Figure 4.5 shows light-curves rising quickly at $t \lesssim 10^4$ s for the lowest mass to $\sim 10^5$ s for the 4 $M_\odot$ explosion. This maximum mass corresponds to the ejecta mass from our supernova. The corresponding CO$_{\rm core}$ mass of our progenitor is this ejecta mass plus the mass of the νNS, roughly 5.4 $M_\odot$. It is possible that the mass is slightly larger for our progenitors, and the emission from the breakout could be longer, but peak X-ray emission from shock breakout beyond a few times 10^5 s will be difficult to achieve. The observed emission would come from the sum of this full range of explosions. The close match of our models (fitted to our expected progenitor mass) to this X-ray plateau demonstrates that this sequence of shock breakouts is certainly a viable and natural explanation for this emission (see Figure 4.5).

We have shown that the X-ray plateau in the afterglow is powered almost entirely by a sequence of shock breakouts and the expanding photosphere. We turn now to the optical emission which is more complex. The optical emission can be powered by the expanding photosphere, ^{56}Ni decay and the energy deposited by the accreting NS. For GRB 060218, the light-curve in the optical and UV exhibits a double-peaked structure suggestive of multiple power sources and, using our light-curve code, we can test out different scenarios. Just like the X-ray, geometry effects will modify the optical light-curve. Here we merely

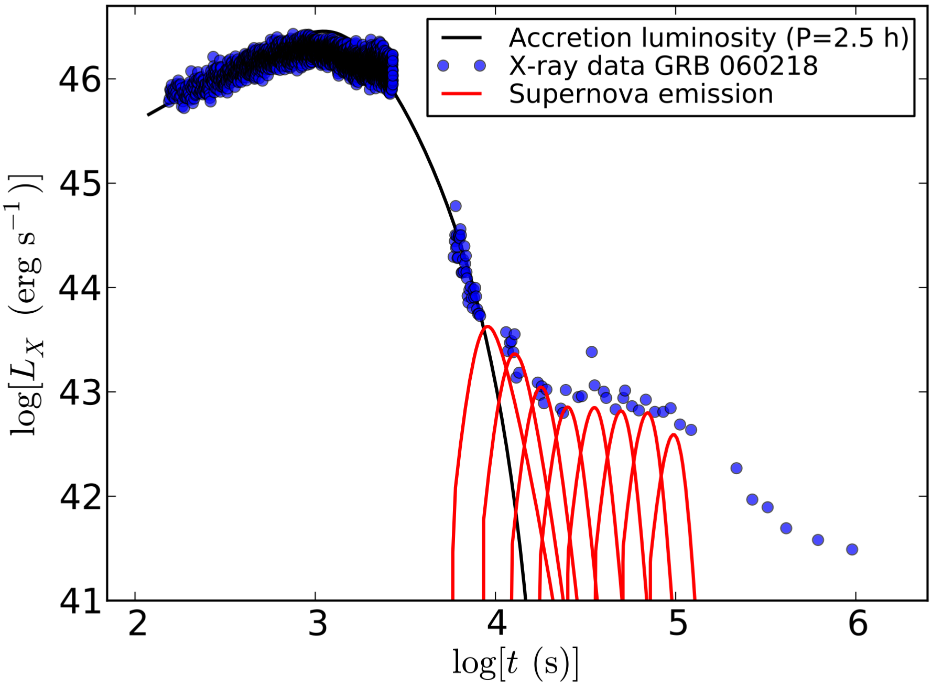

Figure 4.5.: Comparison of the accretion luminosity given by equation (4.1) and the SN luminosity with the observed X-ray luminosity of GRB 060218. The binary system has the following parameters: SN velocity $v_{0_{\rm star}} = 2 \times 10^9$ cm s^{-1}, a pre-supernova core obtained from the $M_{\rm ZAMS} = 20\ M_\odot$ evolution (see table 1.1), initial NS mass $M_{\rm NS}(t_0) = 1.4\ M_\odot$, and orbital period of 2.5 h. In this example the initial explosion energy is 2×10^{51} erg, ranging the spherical equivalent-mass from 0.05–4 $M_\odot$. It can be seen that at early times $t \lesssim 10^4$ s the luminosity is dominated by the accretion process. The SN X-ray light-curves rise quickly at $t \approx 10^4$ s for the lowest mass, to $t \sim 10^5$ s for the 4 $M_\odot$ explosion, which corresponds to total ejecta mass from our SN.

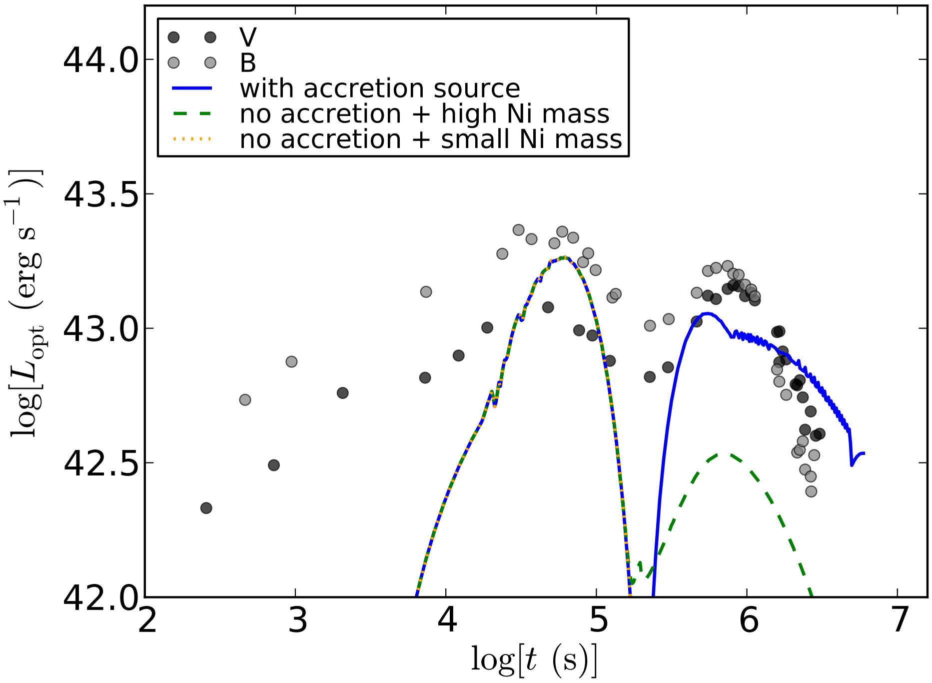

Figure 4.6.: Optical and UV luminosity of GRB 060218 [207]. The light-curve shows a double-peaked structure. The red dotted curve shows the SN optical emission without either ^{56}Ni decay or accretion energy; it can be seen that it explains only the first peak. The blue solid curve includes the energy deposition from the accretion onto the NS (which is a power source of 4×10^{46} erg s^{-1} over a 2500 s duration). This simulation reproduces both the first peak at $\sim 50,000$ s as well as the second peak at $\sim 500,000$ s. The dashed green curve shows that a second peak can also be produced without accretion power by increasing the total ^{56}Ni yield. However, even if we assume half of the total ejecta is ^{56}Ni, the produced second peak cannot explain the observational data.

probe the different emission mechanisms to determine the viability of each to explain the GRB 060218 optical light-curve.

Figure 4.6 shows the V and B band light-curves for GRB 060218 [207]. The light-curve in both bands peaks first near 50,000 s and then again at 500,000 s. Using our 1 $M_\odot$ 1D model from our X-ray emission, we simulate the V and B band light-curves. Without either ^{56}Ni decay or accretion energy, the SN explosion only explains the first peak. However, if we include the energy deposition from the accretion onto the NS (for our energy deposition, we use 4×10^{46} erg s^{-1} over a 2500 s duration), our simulations produce a second peak at roughly 500,000 s. A second peak can also be produced by increasing the total ^{56}Ni yield. However, even if we assume half of the total ejecta is ^{56}Ni, the second peak remains too dim to explain the observations.

The accretion energy in our model provides a natural explanation for the double-peaked features observed in the optical emission of GRB 060218. However, our simple model makes a series of approximations: e.g., we use gray transport, estimating the V and B emission assuming a blackbody, we assume the opacities are dominated by electron scattering, etc. Our simplified picture cannot reproduce accurately the first slowly rising part of the optical data which can be due to a combination of 1) the low-energy tail of the X-ray bubbles and 2) the geometry asymmetries which, just like for the X-rays, cause 1D effective mass ejecta to be lower along some lines of sight leading to some optical emission. The simulation of these details are out of the scope of the present article and will be the subject of future simulations. We have shown that, although approximate, the accretion mechanism can power the observed GRB 060218 light-curve.

4.6. Binary-driven Hypernovae (BdHNe)

4.6.1. Observational features

In table 3 of [236] can be found a list of BdHNe. Below we list their observational properties:

- The lower limit on the energetic of the BdHNe is $(9.2 \pm 1.3) \times 10^{51}$ erg as measured in GRB 070611.
- The observed isotropic energies are in the range $(9.2 \pm 1.3) \times 10^{51} \lesssim E_{\rm iso} \lesssim (4.07 \pm 0.86) \times 10^{54}$ erg [see 2, 243] and are in principle dependent on the NS mass.
- The spectral peak energies are in the range $0.2 \lesssim E_{\rm p,i} \lesssim 2$ MeV [see 2, 243] and increase monotonically with $E_{\rm iso}$.
- The cosmological redshifts are in the range $0.169 \leq z \leq 9.3$, with an average value of ≈ 2.42 (see Table 3 of [236].
- The prompt emission phase of BdHNe exhibits a more complex structure than that of XRFs (see Figure 4.7). Indeed three different regimes are found:

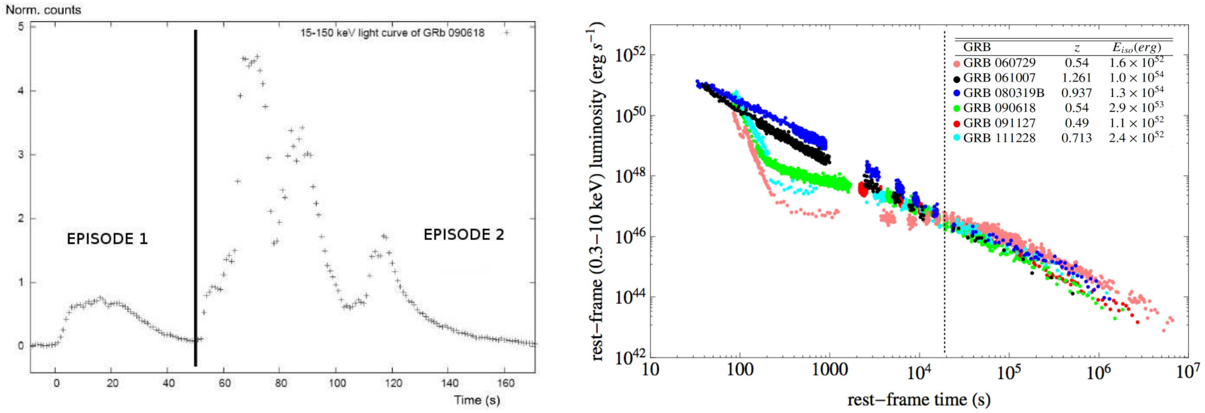

Figure 4.7.: *Left:* Count light curve of GRB 090618 obtained from Fermi GBMdetector, with a bin time of 1 s, and showing two-episode nature of the GRB. *Right:* Rest-frame 0.3-10 KeV luminosity light curve of selected BdHNe. All these sources exhibit the overlapping of the late power-law decay, outlined in [210] and a nested structured as outlines in [242]. Reproduced from [211]

a) A thermal emission with a decreasing temperature following a broken power-law behavior, and an additional non-thermal spectral component (a power-law), dominate the early emission in selected BdHNe [see, e.g., 138]. The existence of this thermal component was first identified in the GRB BATSE data by Ryde [248, 249]. It has been then shown to occur in the case of BdHNe as GRB 090618 [138], GRB 101023 [204], GRB 110709B [203], and GRB 970828 Ruffini et al. [245]. The characteristic radii inferred from the cooling thermal component are of the order of 10^9–10^{10} cm and the average expansion speed is $\sim 10^8$–10^9 cm s^{-1}.

b) This early emission is followed by the characteristic GRB emission, encompassing a thermal precursor, the P-GRB [237, 238], followed by the prompt emission [230, 232, 236].

c) The prompt emission is followed by a steep decay, then by a plateau and a late power-law decay (flare-plateau-afterglow (FPA) phase [247]). These features have been first reported in Nousek et al. [199] and Zhang et al. [320].

- The late decay has typical slopes of $-1.7 \lesssim \alpha_X \lesssim -1.3$ [210] and shows a characteristic power-law behavior both in the optical and in X-rays. When computed in the source cosmological rest-frame, the late power-law decay in X-rays exhibits new features: overlapping and nesting (see Figure 4.7). Overlapping has been proven in a sample of six BdHNe: GRBs 060729, 061007, 080319B, 090618, 091127, and 111228, [136, 210]. The nested property of the BdHNe has been discussed in Ruffini et al. [242], where it has been shown that the duration (the luminosity) of the plateau phase is inversely (directly) proportional to the energy of the GRB emission.
- For all BdHNe at $z \lesssim 1$, an optical SN with a luminosity similar to the one of SN 1998bw [95], occurs after 10–15 days in the cosmological rest-frame.
- A distinctive high energy emission observed up to 100 GeV shows a luminosity light curve following a precise power-law behavior with index ≈ -1.2 [193]. The turn-on of this GeV emission occurs after the P-GRB emission and during the prompt emission phase.

4.6.2. Theoretical interpretation

In the IGC paradigm a BdHNe occurs when the $\mathrm{CO_{core}}$-NS binary is more tightly bound ($a \lesssim 10^{11}$ cm). The larger accretion rate of the SN ejecta, e.g., $\gtrsim 10^{-2}$–10^{-1} $M_\odot$ s^{-1}, leads the companion NS to easily reach its critical mass $M_{\rm crit}$ [90, 227, and see Chapter 1], leading to the formation of a BH.

The electrodynamical conditions encountered in the final accretion phase explain the existence of a vacuum polarization process leading to the creation of an e^+e^- plasma and to the formation of a Kerr-Newman BH. For the sake of clarity and independence on the physical regime encountered, the activities of the BdHNe have been divided in a numbered set of distinct Episodes.

Episode 1 of BdHNe originates in the same hypercritical accretion process as the corresponding one of XRFs. The corresponding spectrum exhibits an expanding thermal component and a power-law function [138, 245].

Episode 2 corresponds to the GRB emission that coincides with the BH formation and leading to the vacuum polarization process and the creation of an e^+e^- plasma. For its theoretical description has been adopted the fireshell model [see 233–235]. The GRB emission occurs at Lorentz factor at the transparency of $\Gamma = 10^2$–10^3 [138, 245] and the spatial extension of the interaction of the fireshell with the circumburst medium goes all the way up to $\sim 10^{16}$–10^{17} cm, reached at the end of Episode 2 [138]. The BdHNe have $E_{\rm iso} \gtrsim 10^{52}$ erg and their $E_{p,i} \gtrsim 200$ keV is in the hard γ-ray domain.

Episode 3 in BdHNe originates from the SN ejecta [243]. In this case an extra energy injection is delivered by the interaction of the GRB outflow with the SN ejecta resulting in an isotropic energy emission of 10^{51}–10^{52} erg. This interaction produces a flare at the beginning of Episode 3 (typically at a rest-frame time of $\sim 10^2$ s) with the typical signature of an expanding thermal component in its spectrum. The radii inferred from this thermal component are $\sim 10^{12}$–10^{13} cm and their evolution reveals a mildly relativistic expansion at $\Gamma \approx 2$ [242, 243]. In particular, the X-ray flare can be modeled by considering the impact of the GRB on the SN ejecta and the propagation of the optically thick e^+e^- plasma into a medium largely baryon-contaminated (see section below).

Episode 4, as predicted in the IGC paradigm and in analogy to XRFs, corresponds to the optical SN emission observable in all BdHNe at $z \lesssim 1$ after $\approx$ 10–15 days in the cosmological rest-frame. It is remarkable that these SNe have a standard luminosity, like the one of SN 1998bw [see, e.g., 175].

Also for BdHNe the in-state is composed of an exploding $\mathrm{CO_{core}}$ and a companion NS. The out-state is again multiple system. First, there is a GRB composed of the P-GRB and its prompt emission. Then there is a newly-formed BH, produced by the hypercritical accretion of part of the SN ejecta onto the binary companion NS reaching $M_{\rm crit}$. Again, there is a νNS originating from the SN explosion. Finally, there is the remaining part of the SN ejecta shocked by the GRB emission. The energy injection into the SN ejecta from both the hypercritical accretion phase and the GRB emission leads also in this case to the occurrence of a broad-lined SN Ic [*hypernova*, see, e.g., 170] with a kinetic energy larger than that of the traditional SNe Ic.

4.6.3. Interaction of GRB on the SN ejecta in BdHNe

In Ruffini et al. [247] has been studied the early X-ray flares in the afterglow of GRBs observed by Swift-XRT. The x-ray flares only occurred in BdHNe. After analysing a sample of 16 GRBs (which have a well-determined early X-ray flare structure), they found that the X-ray flare peak luminosity in the cosmological rest frame, their duration, energy, X-ray luminosity are correlated with the GRB $E_{\rm iso}$. Additionally, it was shown that the x-ray flare occurs at radii $\sim 10^{11} - 10^{12}$ cm and expands with a mildly-relativistic Lorentz factor ($\Gamma \lesssim 4$) and a black body flux from 1% to 30% of the total GRB flux.

The possibility that the energy of the X-ray flare component originates from a fraction of the e^+e^- plasma energy interacting with the much denser medium of the SN ejecta with $10 \lesssim B \lesssim 10^2$ was also examined in [247] [see also 176]. This was done, performing hydrodynamical simulations of the expansion of an initially pure e^+e^- plasma with $\Gamma \sim 100$ through the SN ejecta using the 1-dimensional relativistic hydrodynamical (RHD) module included in the freely available PLUTO[1] code [181]. It was assumed spherical symmetry and adopted a single-fluid approach, where all the involved particle species (baryons, photons, electrons and positrons), are in local thermodynamic equilibrium (LTE).

The simulation was initialized using as initial conditions the results of the simulation showed in Figure 4.1 , that corresponds to a system where the NS reaches the critical mass and collapse to a BH. Figure 4.8 shows the SN ejecta mass that is enclosed within a cone of 5 degrees of semi-aperture angle, whose vertex is at the position of the BH at the moment of its formation (see Figure 4.1), and whose axis is along various directions measured counterclockwise with respect to the line of sight. We can see from this plots how the e^+e^- plasma engulfs different amounts of baryonic mass along different directions due to the asymmetry of the SN ejecta created by the presence of the NS binary companion and the accretion process onto it (see Section 4.4). Additionally, the initial conditions for the e^+e^- plasma were chosen consistent with those of the BdHNe. At the initial time, the e^+e^- plasma has $E_{e^+e^-} = 3.16 \times 10^{53}$ erg, a negligible baryon load and is distributed homogeneously within a region of radii on the order of 10^8–10^9 cm.

The evolution from these initial conditions leads to the formation of a shock and to its subsequent expansion until reaching the outermost part of the SN. Here, we present the results obtained in Ruffini et al. [247]. In the left panel of Figure 4.9 it is shown the radial distribution profiles of the velocity and mass density ρ_{lab} in the laboratory frame inside the SN ejecta as a function of r for $B = 200$ at two selected values of the laboratory time. The velocity distribution peaks at the shock front (with a Lorentz gamma factor $\Gamma \lesssim 4$), and behind the front it is formed a broad tail of accelerated material with $0.1 \lesssim \beta \lesssim 1$.

---

[1] http://plutocode.ph.unito.it/

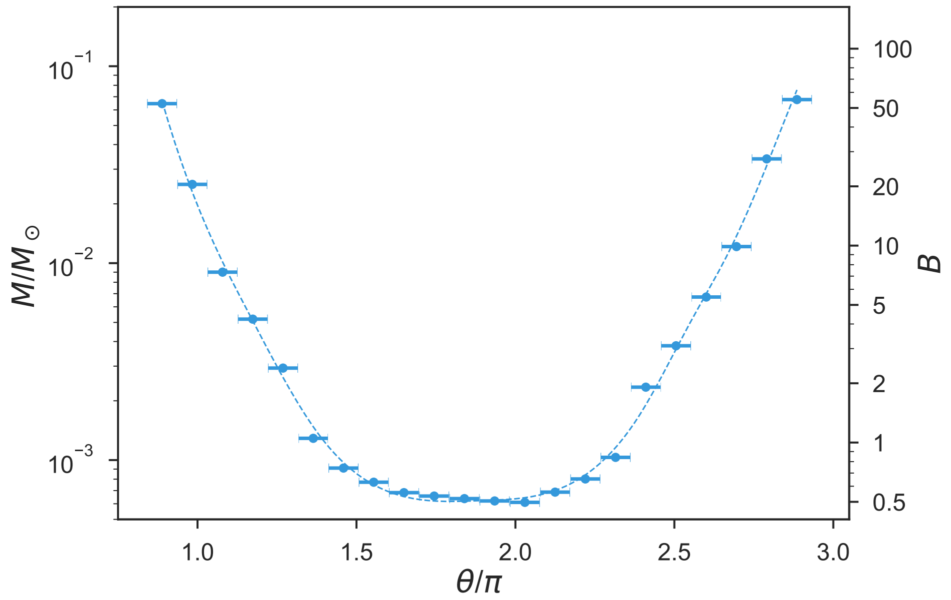

Figure 4.8.: The SN ejecta mass enclosed within a cone of 5 degrees of semi-aperture angle, whose vertex is at the position of the BH at the moment of its formation (see the lower left panel of Figure 4.1), and whose axis is along various directions measured counterclockwise with respect to the line of sight. The vertical axis on the right side gives, as an example, the corresponding value of the baryon loading B assuming a plasma energy of $E_{e^+e^-} = 3.16 \times 10^{53}$ erg.

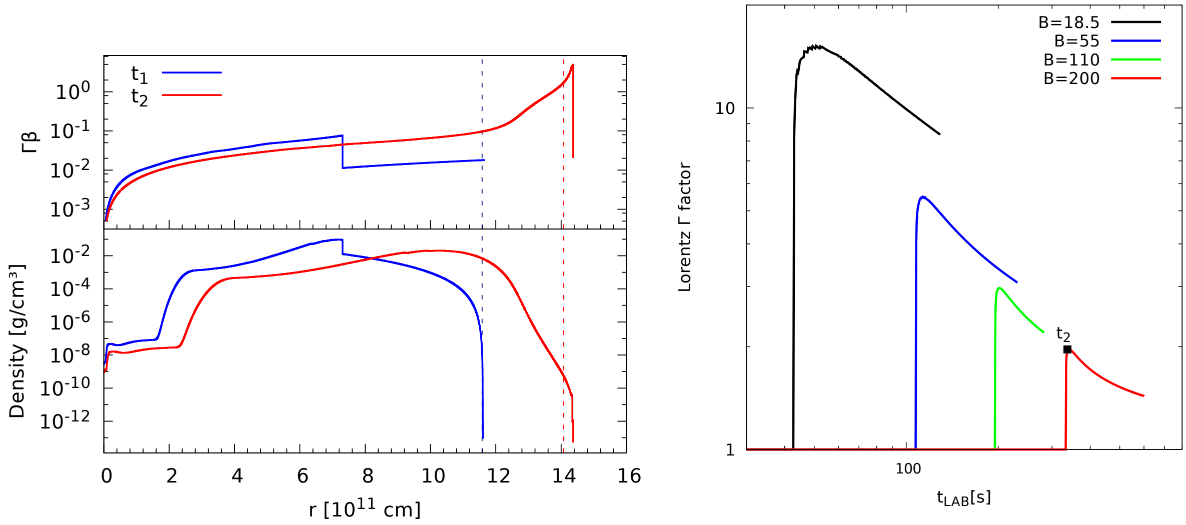

Figure 4.9.: *Left:* Distribution of the velocity inside the SN ejecta (above) and the the mass density of the SN ejecta in the laboratory frame ρ_{lab} (below) at the two fixed values of the laboratory time: t_1 (before the plasma reaches the external surface of the ejecta) and t_2 (the moment at which the plasma, after having crossed the entire SN ejecta, reaches the external surface). These particular profiles are made using a baryon load $B = 200$. The dashed vertical lines corresponds to the two values of the transparency radius R_{ph}. In particular, we see that at t_1 the shock front did not reach R_{ph} yet and the system is optically thick. *Right:* Lorentz Γ factor at the transparency radius R_{ph} as a function of the laboratory time for $E_{e^+e^-} = 3.16 \times 10^{53}$ erg and various selected values of the B parameter. Such B values correspond to the expansion of the e^+e^- plasma along various selected directions inside the remnant (see Figure 4.8). Along the red curve, corresponding to $B = 200$, there is marked the laboratory time instant t_2 represented in the right panel (at t_1 the plasma did not reach R_{ph} yet). We see that these results are in agreement with the Lorentz gamma factor $\Gamma \lesssim 4$ inferred from the thermal emission observed in the flare.
NOTE — Figures taken from Ruffini et al. [247]

The right panel of Figure 4.9 shows the Lorentz Γ factor at the transparency radius R_{ph}, namely the radius at which the optical depth τ, calculated from the observer's line of sight, is equal to 1. If we assume to have a constant cross section, τ becomes Lorentz invariant, and therefore we can compute it in laboratory coordinates in the following way:

$$\tau = \int_{R_{ph}}^{\infty} \mathrm{d}r \, \sigma_T \, n_{e^-}(r), \tag{4.7}$$

where $\sigma_T = 6.65 \times 10^{-25}$ cm^2 is the Thomson cross section, and the electron density is related to the baryon mass density by means of the formula $n_{e^-} = \rho \, \Gamma / m_P$, where m_P is the proton mass.

The relativistic expansion of an initially pure e^+e^- plasma interacting with a SN ejecta with the above-described induced asymmetries (see Figure 4.1), leads to the formation of a shock that reaches the outermost part of the ejecta with Lorentz gamma factors at the transparency radius $\Gamma(R_{ph}) \lesssim 4$. This is in striking agreement with the one inferred from the thermal component observed in the flares [see 247].

4.7. Conclusions and perspectives

In this chapter, we have studied the observational properties of the XRFs and the BdHNe within the IGC paradigm. In the XRFs, the hypercritical accretion is not sufficient to push the NS beyond its $M_{\rm crit}$ while in the BdHNe the hypercritical accretion process triggers the gravitational collapse of the NS into a BH.

We have computed the luminosity during the hypercritical accretion on the NS and shown that the presence of the NS in very compact orbit produces large asymmetries in the SN ejecta around the orbital plane (see Figures 4.1 and 4.2). These asymmetries are the combined effect of the accretion and of the action of the gravitational field of the NS on the SN layers. The SN asymmetries lead to observable effects in the SN emission.

In the case of XRFs, we have shown how the radiation during the continuous accretion process affects the SN emission both in X-rays and in the optical. The shocked material becomes transparent at different times with different luminosities along different directions owing to the asymmetry created in the SN ejecta by the orbiting and accreting NS (see Figures 4.1 and 4.2). The sequence of shock breakout luminosities are thus influenced by the asymmetries in the explosion: the light-curve produced along the more massive directions produce later shock breakout times. We have shown that the observed long-lasting, $t > t_{\rm acc}$, afterglow X-ray emission observed in XRFs can be powered by this mechanism and the early emission ($t < 10^3\, s$) is powered by the accretion luminosity. We presented a specific example of GRB 060218 (see Figure 4.5).

The X-rays emitted from the accretion add energy to the SN explosion. We have simulated the optical emission of the SN and compared and contrasted our theoretical expectation with the optical luminosity of XRF 060218 which shows a peculiar double-peaked shape.

Table 4.1.: Summary of the long GRB subclasses (XRFs, BdHNe and BH-SN) and of their observational properties. In the first three columns we indicate the long GRB subclasses and their corresponding *in-states* and *out-states*. In the following columns we list the ranges of T_{90} in the rest-frame, rest-frame spectral peak energies $E_{\mathrm{p,i}}$ and E_{iso} (rest-frame 1–10^4 keV), the isotropic energy of the X-ray data $E_{\mathrm{iso,X}}$ (rest-frame 0.3–10 keV), the isotropic energy of the GeV emission $E_{\mathrm{iso,GeV}}$ (rest-frame 0.1–100 GeV), the maximum observed redshift $z_{\max}$ and the local observed number density rate ρ_{GRB} obtained in [246]

Subclass	*In-state* (*Progenitor*)	*Out-state* (*Outcome*)	T_{90} (s)	$E_{\mathrm{p,i}}$ (MeV)	E_{iso} (erg)	$E_{\mathrm{iso,X}}$ (erg)	$E_{\mathrm{iso,Gev}}$ (erg)	$z_{\max}$	ρ_{GRB} ($\mathrm{Gpc}^{-3}\mathrm{yr}^{-1}$)
XRFs	$\mathrm{CO_{core}}$-NS	νNS-NS	~ 2–10^3	$\lesssim 0.2$	$\sim 10^{48}$–10^{52}	$\sim 10^{48}$–10^{51}	–	1.096	100^{+45}_{-34}
BdHNe	$\mathrm{CO_{core}}$-NS	νNS-BH	~ 2–10^2	~ 0.2–2	$\sim 10^{52}$–10^{54}	$\sim 10^{51}$–10^{52}	$\lesssim 10^{53}$	9.3	$0.77^{+0.09}_{-0.08}$
BH-SN	$\mathrm{CO_{core}}$-BH	νNS-BH	~ 2–10^2	$\gtrsim 2$	$> 10^{54}$	$\sim 10^{51}$–10^{52}	$\gtrsim 10^{53}$	9.3	$\lesssim 0.77^{+0.09}_{-0.08}$

REFERENCES — Ruffini et al. [246]

We have shown that without either ^{56}Ni decay or accretion energy, the SN explosion can explain only the first peak. We then showed that the inclusion of ^{56}Ni decay produces indeed a double-peaked light-curve but with a second peak which is too dim to explain the observed optical emission. This conclusion holds even adopting unphysical high amounts of ^{56}Ni mass of up to half of the ejecta mass. Instead, we demonstrated that the source of energy given by the hypercritical accretion onto the NS provides a double-peaked light-curve consistent with the observational data (see Figure 4.6). Evidence that this mechanism is also observed in additional XRFs will remain for future work.

In the case of BdHNe, the SN ejecta asymmetries are even more pronounced because this system are more compact binaries and the NS, by accretion, reaches the critical mass and collapses to a BH (see Figure 4.1). Besides the initial interaction of the SN with the radiation from the accretion process, the SN interacts with the radiation from the prompt radiation following the BH formation. The interaction of the electron-positron pairs (moving with Lorentz factor $\Gamma \sim 10^2$) with the SN material at a distance of $r \sim 10^{12}$ cm and moving at $\Gamma \sim 1$ can originate the flare observed around $t \sim 100$ s after the GRB trigger time in the X-ray data of BdHNe. We have presented the theoretical details of this process that were addressed in Ruffini et al. [247]

In Table 4.1 is resumed the main observational properties of the XRFs and BdHNe. There, we indicate the nature of their progenitors and final outcomes of their evolution of each subclass of long GRBs, their rest-frame T_{90}, their rest frame spectral peak energy $E_{\mathrm{p,i}}$ and E_{iso}, as well as the isotropic energy in X-rays $E_{\mathrm{iso,X}}$ and in GeV emission $E_{\mathrm{iso,GeV}}$, and finally their local observed number density rate. In Table 4.1 we have considered an additional subclass of long GRBs, BH-SN, based on the observation of source with energy release up to $\approx 10^{54}$, ergs (e.g. GRBs 080916C, 090902B, 110731A and 130427A). BH-SN occur in close $\mathrm{CO_{core}}$-BH binaries [233] in which the hypercritical accretion occurs onto a previously formed BH. Such BH-SN systems correspond to the late evolutionary stages of X-ray binaries as Cyg X-1 [101], or microquasars [183]. If the binary survives to the SN explosion, then the out-states of BH-SNe can be a νNS-BH or a BH-BH if the SN central remnant directly collapses to a BH. However, the latter scenario is currently ruled out by the observations of pre-SN cores which appear to have masses $< 18\,M_\odot$, very low to lead to direct BH formation [see, e.g., 266, 267, for details.].

5. Smooth Particle Hydrodynamics simulations of the Induced Gravitational Collapse scenario of long gamma-ray bursts associated with supernovae

5.1. Introduction

Until now, the study of the hypercritical accretion process during the IGC scenario has been done following the Bondi-Hoyle formalism (see Chapter 1). However, due the particular characteristics of the IGC scenario e.g its high time-variable nature, the implementation of full hydrodynamical simulations of this process becomes a necessity in order to validate the analytical estimations.

The physical picture of the IGC was first proposed in Ruffini et al. [233], formally formulated in Rueda & Ruffini [227], and then applied for the first time for the explanation of GRB 090618 in Izzo et al. [137]. The first 1-dimensional (1D) simulations of the IGC process were presented in Fryer et al. [90]. These simulations included: 1) detailed SN explosions of the $\mathrm{CO}_{\mathrm{core}}$ obtained from a 1D core-collapse SN code [84]; 2) hydrodynamic details of the hypercritical accretion process; 3) the evolution of the SN ejecta material falling into the Bondi-Hoyle accretion region all the way up to its incorporation into the NS surface. Following the Bondi-Hoyle formalism, they estimated accretion rates exceeding $10^{-3}\, M_\odot\, s^{-1}$, making highly possible that the NS reaches its critical mass and the BH formation.

Later, we presented in Becerra et al. [13] (see also Chapter 4) a first attempt of a particle-like simulation of the SN ejecta expansion under the gravitational field of the NS companion. Specifically, we described the SN matter formed by point-like particles and modeled the initial power-law density profile of the $\mathrm{CO}_{\mathrm{core}}$ by populating the inner layer with more particles and defined the initial conditions of the SN ejecta assuming an homologous velocity distribution in free expansion, i.e. $v \propto r$. The particles' trajectory were computed by solving the Newtonian equation of motion including the effects of the gravitational field of the NS companion. We 1) assumed a circular motion of the NS around the SN center; 2) implemented the changes in the NS gravitational mass owing to the accretion process via the Bondi-Hoyle formalism following Becerra et al. [14] (see Chapter 1) and

3) removed from the system the particles that cross the Bondi-Hoyle surface.

Already in Becerra et al. [13] we showed how of the asymmetric structure of the SN ejecta, produced by the presence of the accreting NS binary companion, becomes crucial for the inference of observable signatures in the GRB afterglow. In Ruffini et al. [247] we show that the $e^{+}e-$ plasma, expanding at relativistic velocities from the newborn BH site, engulfs different amounts of mass along different directions owing to the asymmetries developed in SN density profile, leading to different dynamics and consequently to different signatures for different viewing angles. The agreement of such a scenario with the observed emission from the X-ray flares in the early GRB afterglow was shown in Ruffini et al. [247].

These results point to the necessity of a detailed knowledge of the physical properties of the SN ejecta and in general of the binary system, in the 3D space and as a function of time, for the accurate inference of the consequences on the X, gamma-ray and GeV emission associated with BdHNe.

Here, we present the first 3D hydrodynamics simulations of the IGC scenario. We have used the Smooth Particles Hydrodynamics (SPH) technique as developed in the SNSPH code [89]. The SNSPH is a tree-based, parallel code that has undergone rigorous testing and has been applied to study a wide variety of astrophysical problems [e.g. 64, 91, 318]. The SPH is a mesh-free code where the fluid is represented by a set of particles, which make it to have has excellent conservative properties, i.e. energy, linear momentum, angular momentum, mass, and entropy (if no artificial viscosity operates) are all simultaneously conserved. Due to its lagrangian character, the local resolution of SPH follows the mass flow automatically, convenient to represent the large density contrasts often encountered in astrophysical problems as in the IGC scenario.

The simulation starts from the moment at which the SN shock front reaches the $\mathrm{CO}_{\mathrm{core}}$ external radius and, besides to calculate the accretion rate onto the NS companion, we also follow the evolution of the binary parameters (e.g. the binary separation, period, eccentricity) in order to determined if the final configuration becomes disrupted or not. This implies that we have introduced the gravitational effects of the remnant star, the νNS formed at the center of the SN explosion, allowing us to calculate also the accretion onto it via matter fallback.

This chapter is organized as follow. In Section 5.2 we describe the main aspects SNSPH code [89] and the algorithm applied to simulated the accretion process. In Section 5.3 we give the details on the construction of the initial binary configuration. Section 5.4 shows the results of the simulations. We have covered a wide range of initial conditions for the binary system, i.e. we have varied the $\mathrm{CO}_{\mathrm{core}}$ progenitors, the binary initial separation and SN total energy and expansion geometry. In Section 5.5 we compute the evolution of the binary stars and determine whether the stars' gravitational collapse is possible. In Section 5.6 we discuss the consequences of our results on future GRB analyses. Finally, in section 5.7 we present our conclusions and perspectives for future work. Also, in Appendix C.1 we present convergence test of the numerical simulations.

5.2. SPH formalism

We use the 3D Lagrangian hydrodynamic code SNSPH [89] to model the evolution of the binary system after the $\mathrm{CO}_{\mathrm{core}}$ collapses and the SN explosion occurs . The code follows the prescription of the SPH formalism made in Benz [16]. Basically, the fluid is divided by N particles with determined position, $\vec{r}_i$, mass, m_i, and smooth length, h_i. Physical quantities for each particle are calculated through an interpolation of the form:

$$A_i(\vec{r}_i) = \sum_j A_j \left(\frac{m_j}{\rho_j}\right) W(|\vec{r}_{ij}|, h_{ij}) \tag{5.1}$$

where $|\vec{r}_{ij}| = |\vec{r}_i - \vec{r}_j|$, $h_{ij} = (h_i + h_j)/2$ is the symmetric smooth length between particles i and j and W is the smoothing kernel, and must be defined so that:

$$\int W(\vec{r} - \vec{r}', h)\, dr' = 1\,, \quad \text{and} \quad \lim_{h \to 0} W(\vec{r} - \vec{r}', h) = \delta(\vec{r} - \vec{r}') \tag{5.2}$$

The code allows to evolve the smooth length with time with [18] :

$$dh_i/dt = -1/3(h_i/\rho_i)(d\rho_i/dt)\,. \tag{5.3}$$

Additionally, the code set limits to the total number of neighbors of each particles (we used a range $\sim 30 - 65$ neighbors). On each time step, when the number of neighbors falls above(below) these maximum(minimum) values, the particles smooth length, h_i, is lower(raise) by a configurable factor.

Then, the hydrodynamical equations of conservation of linear momentum and energy are written as:

$$\frac{d\vec{v}_i}{dt} = -\sum_{j=1}^{N} m_j \left(\frac{P_i}{\rho_i^2} + \frac{P_j}{\rho_j^2} + \Pi_{ij}\right) \vec{\nabla}_i W(r, h_{ij}) + \vec{f}_{\mathrm{g}} \tag{5.4}$$

$$\frac{du_i}{dt} = \sum_{j=1}^{N} m_j \left(\frac{P_i}{\rho_i^2} + \frac{1}{2}\Pi_{ij}\right) (\vec{v}_i - \vec{v}_j) \cdot \vec{\nabla}_i W(r, h_{ij}) \tag{5.5}$$

where $\vec{v}_i$, P_i, ρ_i and u_i are the particle velocity, pressure, density and internal energy, respectively. In order to handle shocks, an artificial viscosity term is introduced through Π_{ij} as in [187, 188]:

$$\Pi_{ij} = \begin{cases} \dfrac{-\alpha(c_i + c_j)\mu_{ij} + 0.5\beta\mu_{ij}^2}{\rho_i + \rho_j} & \text{if} \quad \vec{v}_{ij} \cdot \vec{r}_{ij} < 0 \\ 0 & \text{otherwise} \end{cases} \tag{5.6}$$

where c_i is the sound speed, $\vec{v}_{ij} = \vec{v}_i - \vec{v}_j$ and :

$$\mu_{ij} = \frac{h_{ij}\vec{ij} \cdot \vec{r}_{ij}}{|\vec{r}_{ij}|^2 + \epsilon h_{ij}^2} \tag{5.7}$$

The form for the viscosity of equation (5.6) can be interpreted as a bulk and von Neuman-Richtmyer viscosity parametrized by α and β viscosity coefficients. In the simulation is usually used $\alpha = 1.0$ and $\beta = 2.0$.

The last term of equation (5.4) refers to the fluid self-gravity force. The particles are organized in a hashed oct-tree and the gravitational force is evaluated using the multipole acceptability criterion (MAC) described in [302, 303]. The long-rage forces are replaced by the monopole terms. The gravitational potential of the SPH-particles are softening with an SPH-kernel-based smoothing [see 16, for instant]. In this approach, the SPH kernel is interpreted as a three-dimensional density distribution, and the gravity is calculated self-consistently according to this distribution.

Finally, the equation of state adopted treats the ions as a perfect-gas and takes into account the radiation pressure:

$$P = \frac{1}{3}aT^4 + n_{\rm ion}\kappa T \quad ; \quad u = aT^4 + \frac{3}{2}n_{\rm ion}\kappa T\,, \tag{5.8}$$

where $n_{\rm ion}$ is the number density of ions, T, the temperature and a the radiation constant.

The time integration is done with different methods, depending on the variable being updated. For the specific internal energy of each particle, the second-order Adams-Bashford method, a second-order method for first-order ordinary differential equations, is used:

$$u_{i+1} = u_i + \dot{u}_i\left(dt_i + \frac{dt_i^2}{2dt_{i-1}}\right) - \dot{u}_{i-1}\left(\frac{dt_i^2}{2dt_{i-1}}\right) \tag{5.9}$$

For the smoothing length, a second-order leapfrog method is used:

$$h_{i+1} = h_i + \dot{h}_i\left(\frac{dt_i + dt_{i-1}}{2}\right) \tag{5.10}$$

and position and velocity are integrated using Press method, a second-order method for second-order ordinary differential equations:

$$\dot{x}_{i+1} = \frac{x_i - x_{i-1}}{dt_{i-1}} = \ddot{x}_i\left(dt_i + \frac{dt_{i-1}}{2}\right) \tag{5.11}$$

$$x_{i+1} = x_i + (x_i - x_{i-1})\frac{dt_i}{dt_{i-1}} + \ddot{x}_i\left(\frac{dt_i(dt_i + dt_{i-1})}{2}\right) \tag{5.12}$$

For the first iteration of the simulation, it is assumed $u_{i-1} = u_i$ and $x_{i-1} = x_i - \dot{x}_i dt$.

5.2.1. Accretion Algorithm

In the simulation, the remnant of the $\rm CO_{core}$ and the NS companion are model as two point masses that only interact gravitationally with the other particles and between them.

Their equation of motion will be:

$$\frac{d\vec{v}_s}{dt} = \sum_{j=1}^{N} \frac{Gm_j}{|\vec{r}_s - \vec{r}_j|^3} (\vec{r}_j - \vec{r}_s) + \frac{GM_{s'}}{|\vec{r}_s - \vec{r}_{s'}|^3} (\vec{r}_{s'} - \vec{r}_s) \tag{5.13}$$

where subindex s and s' make reference to the stars. In the same way, each particle of the fluid will feel an additional force from the stars gravitational field:

$$\vec{f}_{s,i} = \frac{GM_s}{|\vec{r}_s - \vec{r}_i|^3} (\vec{r}_s - \vec{r}_i) \tag{5.14}$$

Additionally, these point particles can accrete other particles from the SN ejecta. Following Bate et al. [10], the conditions that a particle j has to check to be accreted by the star are:

- The particles is inside the star accretion radius, i.e :

  $$|\vec{r}_j - \vec{r}_s| < R_{\mathrm{j,acc}}\,, \quad \text{with} \quad R_{\mathrm{j,acc}} = \min\left(\xi \frac{2GM_s}{v_{js}^2 + c_j^2}\,,\, h_j\right) \tag{5.15}$$

  Usually in the simulation is used $\xi = 0.05 - 0.1$ (see section 5.5 for further details of this parameter) .

- The gravitational energy between the star and the particle is greater than its kinetic energy, i.e. :

  $$\frac{GM_s m_j}{|\vec{r}_j - \vec{r}_s|} > \frac{1}{2} m_j |\vec{v}_j - \vec{v}_s|^2 \tag{5.16}$$

- The angular momentum of the particle relative to the star is less than the one it would have in a keplerian orbit at $R_{\mathrm{j,acc}}$, i.e. :

  $$|(\vec{r}_j - \vec{r}_s) \times (\vec{v}_j - \vec{v}_s)| < \sqrt{GM_s R_{\mathrm{j,acc}}} \tag{5.17}$$

These conditions are evaluated at the beginning of every time step. The particles that fulfill them are removed from the simulation and in order to conserved the mass, linear momentum and angular momentum, we update the properties of the star as:

$$M_{\mathrm{s,new}} = M_{\mathrm{s}} + \sum_j m_j \tag{5.18}$$

$$\vec{v}_{\mathrm{s,new}} = \frac{M_s \vec{v}_s + \sum_j m_j \vec{v}_j}{M_{\mathrm{s,new}}} \tag{5.19}$$

$$L_{\mathrm{s,new}} = M_{\mathrm{s,new}} \frac{L_s \vec{v}_s + \sum_j m_j (\vec{r}_{s,j} \times \vec{v}_{s,j})}{M_{\mathrm{s}}} \tag{5.20}$$

The sum is over the particles accreted during the time step.

5.3. SPH initial setup

Our calculations include a suite of pre-SN progenitors with zero-age-main-sequence (ZAMS) masses ranging from 15 to 40 M$\odot$ obtained via the KEPLER calculations [112]. The SN explosions are simulated with the 1D core-collapse code described in Fryer et al. [84] and the multi-parameter prescriptions introduced in Fryer et al. [80] to mimic the supernova engine: the energy deposition rate and duration, the size of the convection cell above the base of the proto-NS and the time after bounce when the convective engine starts. These parameters are designed to include the uncertainties in the convection-enhanced supernova engine [see 94, 114, 191, for details].

When the shock front reach the edge of the CO$_{\rm core}$, the configuration is mapped into a 3D SPH-configuration of about 1 million particles with variable mass. This is done using weight Voronoi tessellation (WVT) as described in Diehl et al. [65].

The SPH configuration of the SN ejecta is constructed in the rotating reference frame of the progenitor star. In order to translate it to the center of mass reference frame of the initial binary system (CO$_{\rm core}$ + NS), the position and velocities of the particles are modified as follow:

$$\vec{r}_{i,new} = \mathbb{R}\vec{r}_i - \vec{r}_{\rm CO} \tag{5.21}$$

$$\vec{v}_{i,new} = \mathbb{R}\vec{v}_i - \vec{r}_i \times \vec{\Omega}_{\rm orb} - \vec{v}_{\rm CO} \tag{5.22}$$

where $\mathbb{R}$ is a rotation matrix, $\vec{r}_{\rm CO}$ and $\vec{v}_{\rm CO}$ are the position and velocity of the CO$_{\rm core}$ before the explosion and $\Omega_{\rm orb}$ is the binary orbital angular velocity, that is determined once the orbital separation and star masses are established :

$$\Omega_{\rm orb} = \sqrt{\frac{G(M_{\rm CO} + M_{\rm NS})}{a^3}} \tag{5.23}$$

with $M_{\rm CO}$ the CO$_{\rm core}$ mass and $M_{\rm NS}$ the NS mass. The equatorial plane of the binary corresponds to the x-y plane, then the initial position of the stars (NS and νNS) are on the x-axis and its motion is counter clockwise.

The minimum binary period that the system can have is given by the condition that the compactness of the CO$_{\rm core}$ is such that there is no Roche lobe overflow before the SN explosion. Then, the minimum binary separation is given by [69]:

$$\frac{R_{\rm star}}{a_{\rm orb}} = \frac{0.49q^{2/3}}{0.6q^{2/3} + \ln\left(1 + q^{1/3}\right)} \quad \text{with} \quad q = \frac{M_{\rm CO}}{M_{\rm NS}} \tag{5.24}$$

Since, we are interested in identifying the favorable conditions for which the NS companion can accrete enough mass and collapse into a BH, we will explore different initial conditions for the system. We have worked with four progenitor for the CO$_{\rm core}$ that have different ZAMS mass: $M_{\rm ZAMS}$ = 15, 25, 30 and 40 $M_\odot$. In Table 5.1 we present the main proprieties of each of these progenitors at the mapping moment: the SN mass ejected, $M_{\rm ej}$, the remnant star mass, $M_{\rm rem}$, the SN ejecta innermost radius, $R_{\rm core}$, the CO$_{\rm core}$ ra-

Table 5.1.: Proprieties of the CO$_{\rm core}$ progenitor when the forward shock has reached the star radius.

$M_{\rm ZAMS}$ ($M_\odot$)	$M_{\rm rem}$ ($M_\odot$)	$M_{\rm ej}$ ($M_\odot$)	$R_{\rm core}$ (10^8 cm)	$R_{\rm star}$ (10^9 cm)	$V_{\rm star}$ (10^8cm s^{-1})	$E_{\rm grav}$ (10^{51} erg)	m_j ($10^{-6}\,M_\odot$)
15	1.30	1.606	8.648	5.156	9.75	0.2149	0.2 – 4.4
25	1.85	4.995	2.141	5.855	5.43	1.5797	2.2 – 11.4
30^a	1.75	7.140	28.33	7.751	8.78	1.7916	1.9 – 58.9
30^b	1.75	7.140	13.84	7.830	5.21	1.5131	1.9 – 58.9
40	1.85	11.50	19.47	6.529	6.58	4.4305	2.3 – 72.3

NOTE — Each progenitor was evolved with KEPLER stellar evolution code [112] and then was exploded artificially using the 1-dimensional core-collapse code [84].
[a] $E_{\rm sn} = 1.09 \times 10^{52}$ erg
[b] $E_{\rm sn} = 2.19 \times 10^{51}$ erg

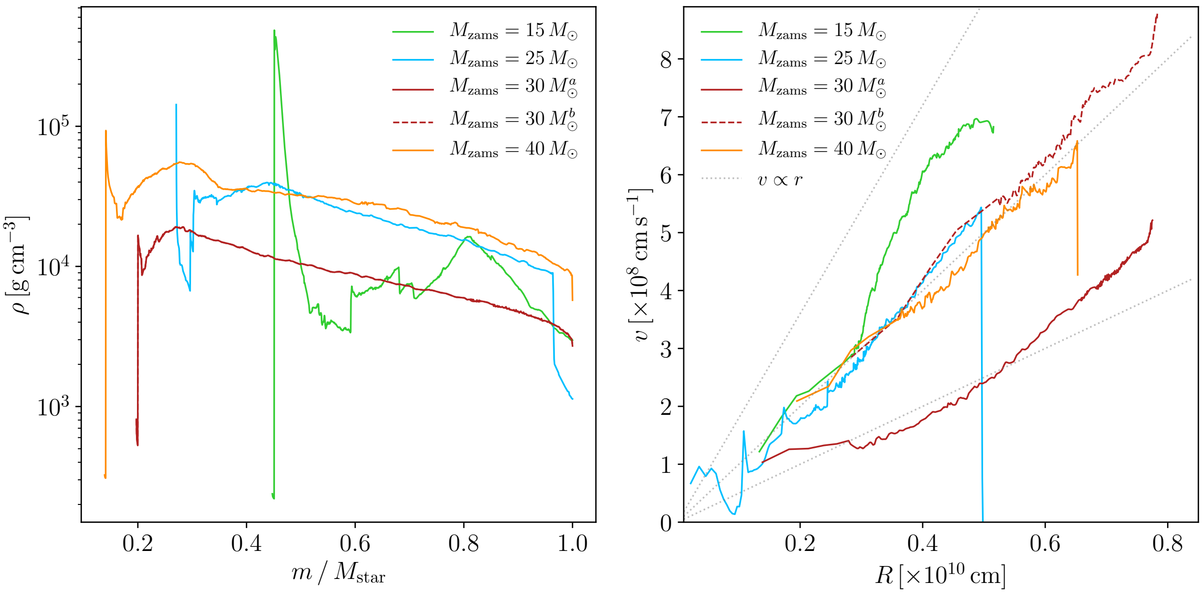

Figure 5.1.: Density (left panel) and velocity (right panel) profile of the SN ejecta when the forward shock has reached the carbon-oxygen edge for the $M_{\rm ZAMS} = 15$, 25, 30 and 40 $M_\odot$ progenitors (see Table 5.1). At this moment, the 1D simulations (with the core-collapse code used in [84]) is mapped to a 3D SPH-configuration and continue the expansion of the ejecta material.

dius when the collapse happens, $R_{\rm star}$ and the forward shock velocity, $V_{\rm star}$. In the last two columns of Table 5.1 we specify the gravitational energy of the star, $E_{\rm grav}$, and the maximum and minimum masses of the SPH particles, m_j. Figure 5.1 shows the density profile (left panel) and velocity profile (left panel) of each progenitor at the moment of the mapping to the 3D SPH-configuration (when the shock front of the explosion has reach the star surface). We have two models for the 30 $M_\odot$ progenitor, each with different SN explosion energy.

It is important to notice that we are working with progenitors that were evolved as isolated stars, i.e without taking into account that they are part of a binary system. However, as it was indicated in Fryer et al. [90], there is a 3–4 order of magnitude pressure jump between the CO$_{\rm core}$ and helium layer, this means that the star will not expand significantly when the helium layer is removed: the $\mathrm{CO_{core}}$ can be 1.5–2 times larger [see 189], then the minimum period of the system might increase by a factor of 1.8–2.8 (see Chapter 2).

The final fate of the system also will depend on the characteristics of the SN explosion. We run simulations varying the explosion energy of the SN. Rather than produce a broad range of explosion energies (as we did with the $M_{\mathrm{ZAMS}} = 30\,M_{\odot}$ progenitor), we scaled the kinetic and internal energy of the particles behind the forward shock by a factor η. In this way, the internal structure of the progenitor doesn't change, just its velocity and temperature.

In order to study the effect of an asymmetric SN explosion [see 139] we adopt a single-lobe prescription Hungerford et al. [122] following [123, 318]. Namely, the explosion is modified to a conical geometry parametrized by Θ, the opening angle of the cone, and f, the ratio of the velocities between the particles inside and outside the cone. The velocities of the SPH particles behind the forward shock are then modified as:

$$V_{\mathrm{in-cone}} = f\left[\frac{1-f^2}{2}\cos\Theta + \frac{1+f^2}{2}\right]^{-1/2} V_{\mathrm{symm}} \tag{5.25}$$

$$V_{\mathrm{out-cone}} = \left[\frac{1-f^2}{2}\cos\Theta + \frac{1+f^2}{2}\right]^{-1/2} V_{\mathrm{symm}} \tag{5.26}$$

where V_{symm} is the radial velocity of the original explosion. This prescription conserves the kinetic energy of the symmetric explosion, and to conserves the total energy of the supernova we scale the particles internal energy in the same way.

In the next section, we will present the results of our SPH-simulations.

5.4. SPH simulation results of the IGC scenario

In Table 5.2 we summarize the properties of the SN and the parameters that characterized the state of the initial binary systems with the different $\mathrm{CO_{core}}$ obtained with the progenitors of Table 5.1. We specify the η factor by which the SPH-particles velocities and internal energy are scaled, the sum of the ejecta kinetic and internal energy, $E_k + U_i$ (computed in the binary system center of mass frame), the initial orbital period $P_{\mathrm{orb,i}}$ as well as the initial binary separation, $a_{\mathrm{orb,i}}$.

For each model, we first run a simulation of the SN expansion assuming that the $\mathrm{CO_{core}}$ collapses and explodes as an isolate star, i.e. without the NS companion. In Table 5.1, we summarize the final mass of the νNS, indicated as $m_{\nu\mathrm{NS,fb}}$, and the magnitude of the νNS kick velocity, V_{kick}. This last variable comes from the linear momentum of the particles that have made fall-back and were accreted.

Table 5.2.: SPH Simulations

Model	η	$E_\mathrm{k}+U_i$ (10^{51} erg)	$p_\mathrm{orb,i}$ (s)	$a_\mathrm{orb,i}$ (10^{10} cm)	$m_{\nu\mathrm{ns,fb}}$ ($m_\odot$)	V_kick (10^4 cm/s)	$m_{\nu\mathrm{ns}}$ ($m_\odot$)	m_ns ($m_\odot$)	V_CM (10^7 cm/s)	$p_\mathrm{orb,f}$ (s)	$a_\mathrm{orb,f}$ (10^{10} cm)	e	m_bound ($M_\odot$)	bound
						$M_\mathrm{ZAMS}=15\,M_\odot$ Progenitor								
15m1p07e	0.7	1.395	395.33	1.361	1.302	3.99	1.302	2.003	4.05	1141.29	2.437	0.443	2.7×10^{-6}	yes
15m1p05e	0.5	1.101	395.33	1.361	1.303	4.83	1.303	2.006	4.02	1109.63	2.393	0.433	4.8×10^{-5}	yes
15m1p03e	0.3	0.607	395.33	1.361	1.304	18.93	1.315	2.023	3.91	953.92	2.182	0.398	6.9×10^{-4}	yes
15m1p01e	0.1	0.213	395.33	1.361	2.478	6.62	1.916	2.199	0.39	182.56	0.773	0.233	0.098	yes
15m1p005e	0.05	0.135	395.33	1.361	2.731	1.73	2.649	2.034	0.08	355.36	1.257	0.036	0.029	yes
15m2p03e	0.3	0.607	704.46	2.000	1.304	18.93	1.304	2.007	0.39	–	–	1.192	5.8×10^{-3}	no
15m2p01e	0.1	0.213	704.46	2.000	2.478	6.62	2.238	2.101	0.08	778.58	2.068	0.419	0.0759	yes
15m3p01e	0.1	0.213	1056.69	2.000	2.478	6.62	2.405	2.057	0.32	871.15	2.249	0.1032	0.0313	yes
						$M_\mathrm{ZAMS}=25\,M_\odot$ Progenitor								
25m1p1e	1.0	3.14	288.4	1.352	1.924	1.35	1.963	2.085	7.49	7011.01	8.747	0.866	0.081	yes
25m1p09e	0.9	2.84	288.4	1.352	1.935	2.97	2.013	2.162	7.17	2297.51	4.199	0.744	0.043	yes
25m1p08e	0.8	2.53	288.4	1.352	1.953	3.57	2.081	2.441	6.09	986.34	2.454	0.600	0.075	yes
25m1p07e	0.7	2.22	288.4	1.352	2.172	41.30	2.371	2.621	3.77	259.83	1.043	0.381	0.160	yes
25m2p1e	1.0	3.14	513.8	1.988	1.924	1.35	1.929	2.029	6.46	–	–	1.005	0.073	no
25m3p1e	1.0	3.14	707.8	2.605	1.924	1.35	1.924	2.024	5.76	–	–	1.086	0.025	no
25m4p1e	1.0	3.14	951.6	2.984	1.924	1.35	1.916	2.014	5.34	–	–	1.096	0.013	no
25m2p07e	0.7	2.22	513.8	1.988	2.172	41.30	2.352	2.522	3.43	602.61	1.812	0.454	0.185	yes
25m3p07e	0.7	2.22	707.8	2.605	2.172	41.30	2.178	2.320	3.25	1410.23	3.11	0.477	0.138	yes
25m5p07e	0.7	2.22	1190	3.463	2.172	41.30	2.166	2.401	3.24	1666.15	3.49	0.526	0.0051	yes
25m15p07e	0.7	2.22	3569	7.203	2.172	41.30	2.088	2.208	2.72	19288	17.41	0.639	3.4×10^{-3}	yes
25m2f20tz	1.0	3.14	288.4	1.352	1.931	1.18×10^3	2.009	2.161	7.31	2852.15	4.849	0.774	0.065	yes
25m2f20tx	1.0	3.14	288.4	1.352	1.931	1.18×10^3	1.959	2.142	7.13	8225.79	9.772	0.892	0.056	yes
25m2f20t-x	1.0	3.14	288.4	1.352	1.931	1.18×10^3	2.002	2.182	7.82	3170.17	5.209	0.801	0.054	yes
25m4f20tz	1.0	3.14	288.4	1.352	2.826	5.08×10^3	2.382	2.424	5.16	456.51	1.496	0.438	0.189	yes
25m2f40tz	1.0	3.14	288.4	1.352	2.364	5.38×10^3	2.316	2.395	5.84	529.37	1.643	0.589	0.105	yes

Model	η	$E_{\mathrm{k}} + U_i$ (10^{51} erg)	$p_{\mathrm{orb,i}}$ (s)	$a_{\mathrm{orb,i}}$ (10^{10} cm)	$m_{\nu\mathrm{ns,fb}}$ ($m_\odot$)	V_{kick} (10^4 cm/s)	$m_{\nu\mathrm{ns}}$ ($m_\odot$)	m_{ns} ($m_\odot$)	V_{CM} (10^7 cm/s)	$p_{\mathrm{orb,f}}$ (s)	$a_{\mathrm{orb,f}}$ (10^{10} cm)	e	m_{bound} ($M_\odot$)	bound
$M_{\mathrm{ZAMS}} = 30\,M_\odot$ Progenitor - exp 1														
30m1p1ea	1.0	8.43	363.8	1.667	1.756	40.80	1.757	2.007	9.67	–	–	1.701	0.0	no
30m1p07ea	0.7	5.95	363.8	1.667	1.755	39.36	1.758	2.015	9.58	–	–	1.647	9.6×10^{-4}	no
30m1p05ea	0.5	4.26	363.8	1.667	1.758	96.20	1.764	2.031	9.46	–	–	1.501	0.012	no
30m1p03ea	0.3	2.59	363.8	1.667	2.178	3.93×10^3	1.869	2.455	7.79	6090.81	8.137	0.852	0.168	yes
30m2p03ea	0.3	2.59	648.23	2.449	2.178	3.93×10^3	1.837	2.192	7.21	–	–	1.095	0.0854	no
$M_{\mathrm{ZAMS}} = 30\,M_\odot$ Progenitor - exp 2														
30m1p1eb	1.0	3.26	363.8	1.667	4.184	141.30	3.675	2.382	3.59	727.929	2.209	0.5686	0.331	yes
30m1p12eb	1.2	3.91	363.8	1.667	2.462	147.79	2.515	2.376	5.86	2764.53	5.0092	0.733	0.133	yes
30m2p12eb	1.2	3.91	623.27	2.410	2.462	147.79	2.621	2.228	4.85	9425.47	11.3017	0.848	0.029	yes
30m1p2eb	2.0	6.45	363.8	1.667	1.771	13.89	1.783	2.077	9.50	–	–	1.447	5.7×10^{-3}	no
30m1p31eb	3.14	10.02	363.8	1.667	1.766	5.21	1.768	2.017	9.95	–	–	1.712	6.5×10^{-4}	no
$M_{\mathrm{ZAMS}} = 40\,M_\odot$ Progenitor														
40m1p1e	1.0	10.723	209.54	1.295	1.871	176.43	1.874	2.119	13.68	–	–	1.845	0.038	no
40m1p09e	0.9	9.670	209.54	1.295	1.872	141.38	1.881	2.274	13.35	–	–	1.538	0.027	no
40m1p08e	0.8	8.618	209.54	1.295	1.873	242.93	1.886	2.545	12.52	–	–	1.276	0.016	no
40m1p07e	0.7	7.506	209.54	1.295	1.879	464.82	2.095	3.033	10.12	5157.3	7.7118	0.881	0.051	yes
40m1p06e	0.6	6.513	209.54	1.295	6.568	69.73	3.784	3.209	4.57	145.31	0.792	0.612	1.053	yes
40m1p05e	0.5	5.145	209.54	–	–	0.91	5.430	3.642	–	3.586	0.339	0.243	1.250	yes
40m2p1e	1.0	10.723	373.47	1.295	1.871	176.43	1.873	2.046	10.79	–	–	2.194	6.13×10^{-3}	no
40m2p07e	0.7	7.506	373.47	1.295	1.879	464.82	2.064	2.755	8.757	264493	104.26	0.984	0.078	yes
40m4p07e	0.7	7.506	746.95	3.022	1.879	464.82	1.959	2.507	7.799	–	–	1.1804	0.0744	no
40m2p06e	0.6	6.513	373.47	1.295	6.568	69.73	5.581	2.961	2.58	347.329	1.523	0.648	0.509	yes

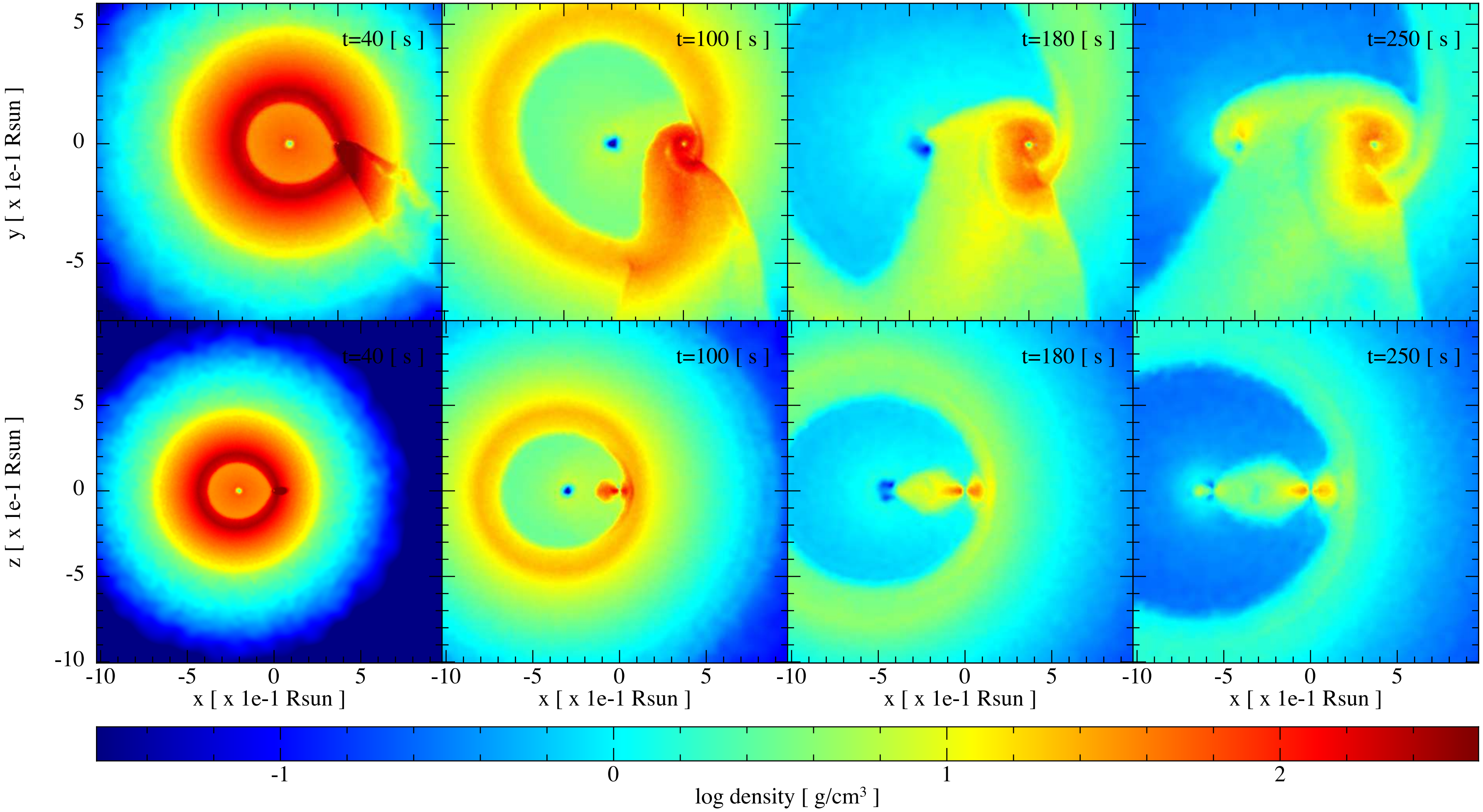

Figure 5.2.: Snapshots of the SPH simulation of the IGC scenario. The initial binary system is formed by a $\mathrm{C}_{\mathrm{core}}$, which progenitor is a $M_{\mathrm{ZAMS}} = 25\,M_{\odot}$ and a $2\,M_{\odot}$ NS with an initial orbital period of around 5 min (Model 25M1p1e of table 5.2). In the upper panel is shown the surface density on the binary equatorial plane, at different times of the simulation, while the lower panel corresponds to the plane transversal to the binary orbital plane. The reference system was rotated and translated in a way that the x-axis is along the line that joins the binary stars and the origin of the reference system is at the NS position. At $t = 40$ seconds (first frame from left to right), it sees that the particles captured by the NS have formed a kind of tail behind it, then this particles star to circularized around the NS and a kind of thick disk can be seen at $t = 100$ seconds (second frame from left to right). The material captured by the gravitational field of the NS companion is also attracted by the νNS and start to be accreted by it as can be seen at $t = 180$ second (third frame). After around one initial orbital period, at $t = 250$ seconds, around the both stars have been form a kind of disk structure. The νNS is along the x-axis at: -2.02, -2.92, -3.73 and -5.64 for $t = 40$, 100, 180 and 250 s, respectively.

NOTE — This figure and all the snapshots figures where done with the SNSPLASH visualization program [217]

Then, we run simulations of the SN expansion with the $\mathrm{CO}_{\mathrm{core}}$ as part of a binary system with a $2\,M_\odot$ NS as companion. In Table 5.2 we summarize the parameters that characterized the final outcomes of these simulations: the νNS final mass, $m_{\nu\mathrm{NS}}$, the NS companion final mass, m_{NS}, the velocity of the final binary system center-of-mass, period, V_{CM}, the final orbital period, $P_{\mathrm{orb,f}}$, the major semi-axis and eccentricity of the final system orbit, $a_{\mathrm{orb,f}}$ and e_f, respectively, and the amount of mass bounded to the binary stars when the simulation was stopped, m_{bound}.In the final column of Table 5.2, we have specified if the system remains bound as a new binary system or if it is disrupted in the explosion.

5.4.1. Canonical model: $25\,M_{\mathrm{ZMAS}}$ progenitor

We are going to take the $25\,M_{\mathrm{ZMAS}}$ progenitor star for the $\mathrm{CO}_{\mathrm{core}}$ and a $2\,M_\odot$ NS as our canonical initial binary system in order to describe the main features of the simulation while the SN expands with the NS companion presence, (model 25m1p1e of Table 5.2). This binary system has a minimum orbital period of about 4.86 minutes, that corresponds to a binary separation of 1.34×10^{10} cm. Later, we will change one by one the initial conditions and compare the outcomes with the ones of this canonical system.

Figure 5.2 shows snapshots of the mass density in the x-y plane, the binary equatorial plane (upper panel) and x-z plane (lower panel) at different time of the simulation. In the plot, the reference system has been rotated and translated in a way that the x-axis is along the line that joins the stars of the binary system (νNS-NS) and the origin is at the NS companion position. In general, when the SN starts to expand, the faster outermost particles of the SN will pass almost without being disturbing by the NS gravitational field. The slower-moving material is gravitational capture by the NS, initially formig a tail and ultimately forming a thick disk around it. In addition, there are particles from the innermost layers of the SN-ejecta, that do not have enough kinetic energy to scape, leading fallback accretion onto the νNS. Then, at some point, the material that have been capture by the NS companion start to be also attracted by the νNS and being accreted by it.

To confirm the formation of the disk around the NS companion, in Figure 5.3 has been calculated the angular velocity profile with respect the NS companion position at different times and for two different directions: the line that joins the binary stars with the νNS in the $-x$ direction labeled as $\theta = 0$; and the line perpendicular to this last on the orbital binary plane, labeled as $\theta = \pi/2$. The angular velocity of the particles closed to the NS companion ($r/a_0 < 0.25$) superpose the keplerian angular velocity. This confirms the estimations from analytical approximations made in [14, see also Chapter 1], where it was shown that the SN ejecta have enough angular momentum to circularize around the NS before being accreted. Figure 5.4 shows the mass accretion rate as a function of simulation time on the binary system stars: the NS companion (red line), on the νNS (blue line), also called the fallback accretion rate, and the sum of both mass accretion rate (green line). Either the fallback accretion rate or the NS accretion rate are much greater that the Eddigton limit. The NS is allowed to accrete at this high rate by the emission of neutrinos at its surface via e^+e^- pair annihilation that is the most efficient neutrino emission process at the density and temperature conditions developed [see 13, and Chapter 3 for more

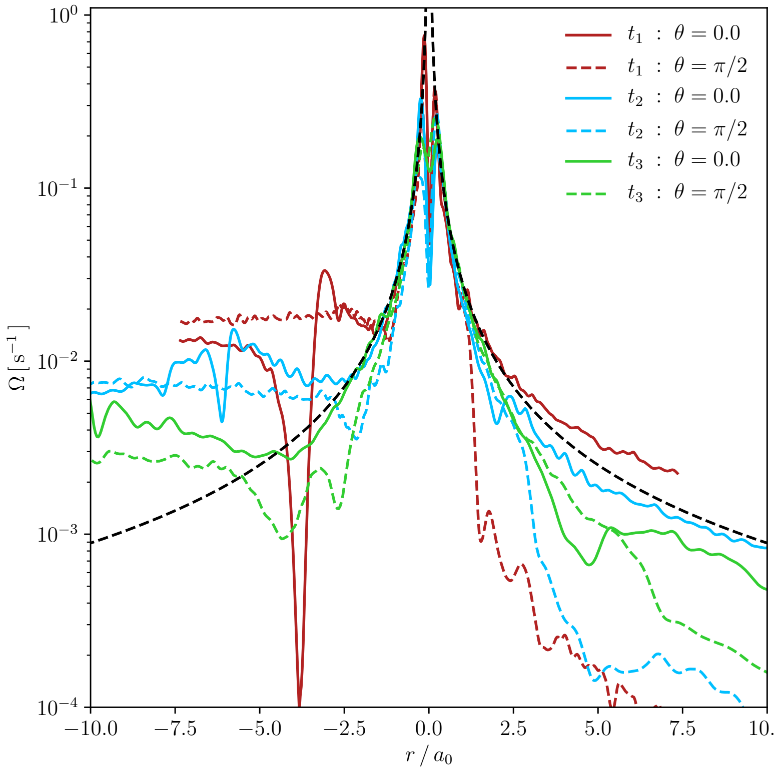

Figure 5.3: Angular velocity profiles of the SN material closed to the NS companion at three different times: $t_1 = 140.0$ s, $t_2 = 280.0$ s, $t_3 = 599.9$ s. The label $\theta = 0$ corresponds to the line that joins the binary stars and the label $\theta = \pi/2$ is the line perpendicular to this last and lies on the equatorial binary system. Close to the NS, the angular velocity approaches the keplerian angular velocity (black line). This suggests that before been accreted the particles will have enough angular momentum to circularize around the star a form a kind of thick disk. The minimum of the solid line in the $-x$ direction indicates the position of the νNS: at -3.01, -5.04 and -10.49 for t_1, t_2 and t_3 respectively.

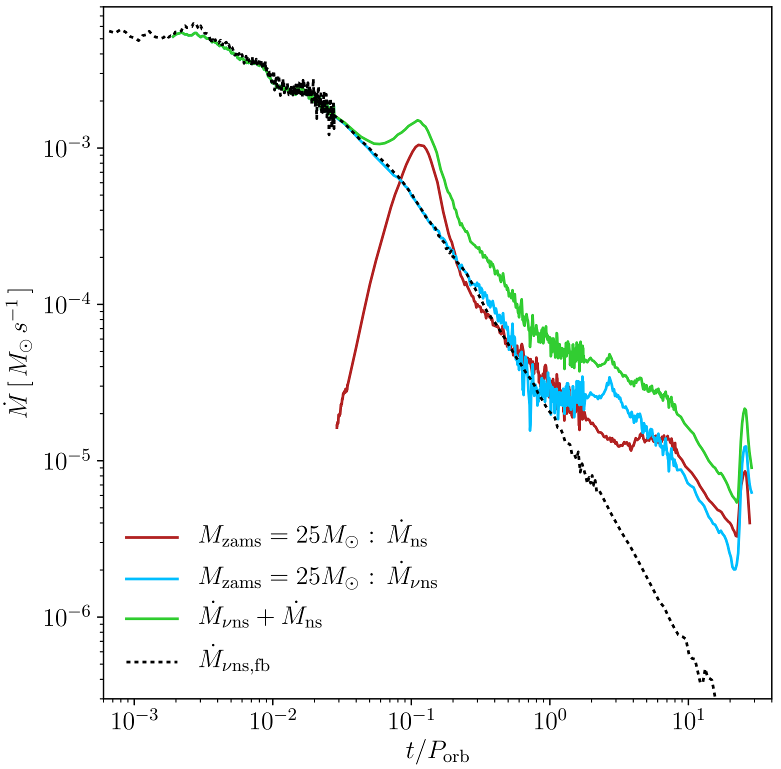

Figure 5.4: Mass-accretion rate on the NS (red line) and the νNS (blue line) during the SPH simulation of the expansion of the SN ejecta. In green line is the sum of both accretion rates. The initial binary system is the same as the one of Figure 5.2. The dotted black line corresponds to the fallback mass accretion on the ν-NS when the $\rm CO_{core}$ collapses in an single-star configuration, i.e. without the presence of the NS companion.

details]. This allows the matter to cool enough fast to be incorporated to the star and therefore, to evolve the star masses, we can add the mass of the particles that fulfill the accretion conditions (see Section 5.2 and equations 5.20). As we have shown the SN ejecta might transport a high amount of angular momentum and form a thick disk around the NS before accretion take place. There, the densities and temperatures are not high enough to cool the matter by neutrino emission and outflows might occur [see, e.g., 22, 60, 147].

Up to 25 % of the infalling matter can be ejected in strong outflows removing much of the system angular momentum [79, 86]. This means that the mass-accretion rate calculated here might overstimate the actual accretion rate onto the star but up to a factor of order unity. It is also important to notice that the accretion rate depends directly on the value adopted for the ξ parameter in equation (5.15). For this simulation, we adopted $\xi = 0.1$. In the next section, we are going to vary this parameter and establish the influence of it on the system final fate.

As we anticipated, we have also run the simulation of the SN ejecta expansion without the NS companion, in order to calculate the fallback accretion rate (black line in Figure 5.4) and compare it with the accretion rate onto the νNS in the binary simulation. At the beginning of the simulation, there is no different between both accretion rates: an almost flatter high accretion phase at early time and then a decline proportional to $t^{-5/3}$ [60, 324]. However, at around $t/P_{\rm orb} \approx 1.0$, there is a jump in the fallback accretion rate of the binary simulation, that can be associated to the time at which the νNS start to accrete the material decelerated by the NS companion. The high early time accretion rate calculated here, is due to the fallback of those particles that did not have enough kinetic energy to escape from the νNS gravitational field. This can occur, either because after the forward shock is launched, the proto-NS cools and contracts, sending a rarefaction wave to the ejecta, that decelerates it [51], or because the SN shock is smoothly decelerated when it goes outward pushing the star material out [78, 313].

5.4.2. SN explosion energy

In the following, we start to change systematically the initial parameters that will affect the fate of the final configuration. We will do it one by one, in order to determinate the most favorable conditions that increases the accretion rate on the NS companion and could induced its collapse. Figure 5.5 shows the mass accretion rate onto the NS and onto the νNS for different energies of the SN explosion, with the same progenitor star for the $\mathrm{CO}_{\rm core}$: the $M_{\rm ZAMS} = 25\, M_\odot$ of Table 5.1. As was explained in Section 5.3, in these simulations we scale the kinetic energy and the internal energy by a factor η (i.e. the velocities of the particles were multiplied by $\sqrt{\eta}$) once we map the 1D exploded configurations to the 3D one. As expected, the total mass accreted by the NS companion is lager for low energetic SN than for high energetic ones, and then more favorable to the collapse of the NS (see models from 25m1p1e to 25m1p07e in Table 5.2). On the other hand, the energy of the SN explosion needs to be high enough, otherwise a considerable part of the ejected mass causes fallback and can instead induce the collapse of the νNS to a BH. This is a novel and alternative possibility not considered in the original version of the IGC scenario [see, e.g., 90, 227]. Additionally, the energy of the SN explosion seems to do not have a big influence on magnitud of the peak of the mass-accretion rate but do have on its shape. The NS companion acretes more mass in the weakest SN explosion ($\eta = 0.7$) because the accretion rate it maintains almost constant for a longer time than in the strongest explosion ($\eta = 1$) where a clear peak appears.

As we did before, we calculate now for these explosions the fallback accretion rate onto the νNS for the isolate progenitors and compare and contrast it with its binary system

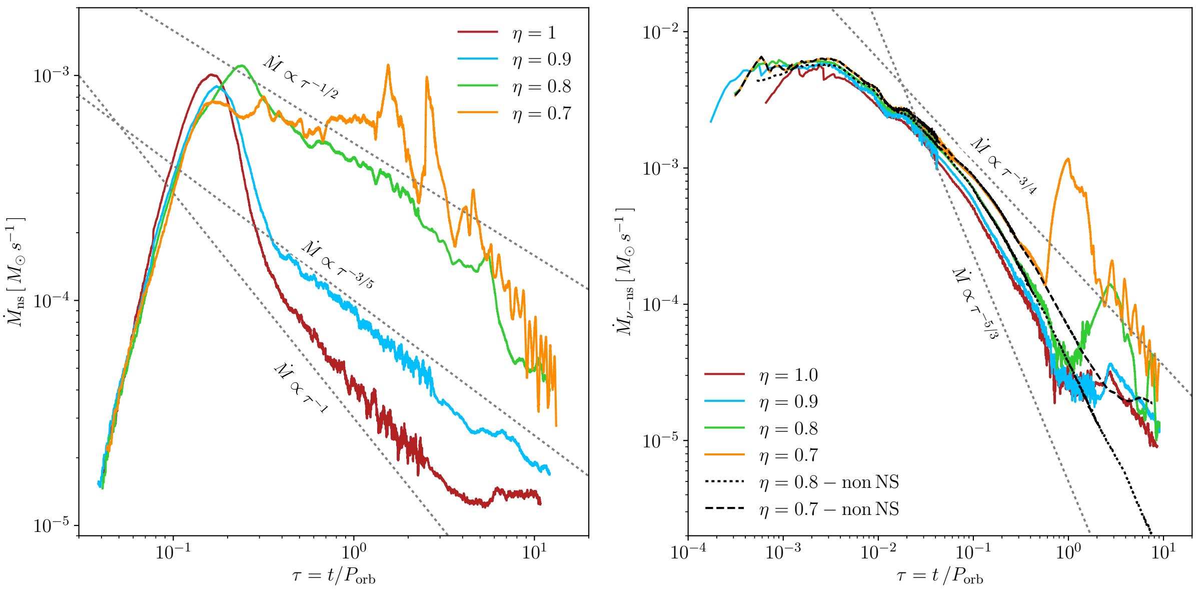

(a) NS mass accretion rate

(b) νNS mass accretion rate

Figure 5.5.: Mass-acretion rate onto the NS (left panel) and onto the νNS (right panel) in the IGC scenario. The initial binary system is the same as the one of Figure 5.4 but the SN energy has been varied scaling the kinetic and internal energy of the SPH particles by a factor $\eta < 1$. The accretion rate on the NS presents a peak for the most energetic SN, while in the weaker ones this peak is flattened, i.e. the accretion happens at a nearly constant rate for a longer time, making the star to increase its mass faster. At early time, the fallback accretion rate onto the νNS is nearly independent of the SN energy, although the late bump induced by the accretion of the material gravitational capture by the NS companion is stronger for the weakest explosions.

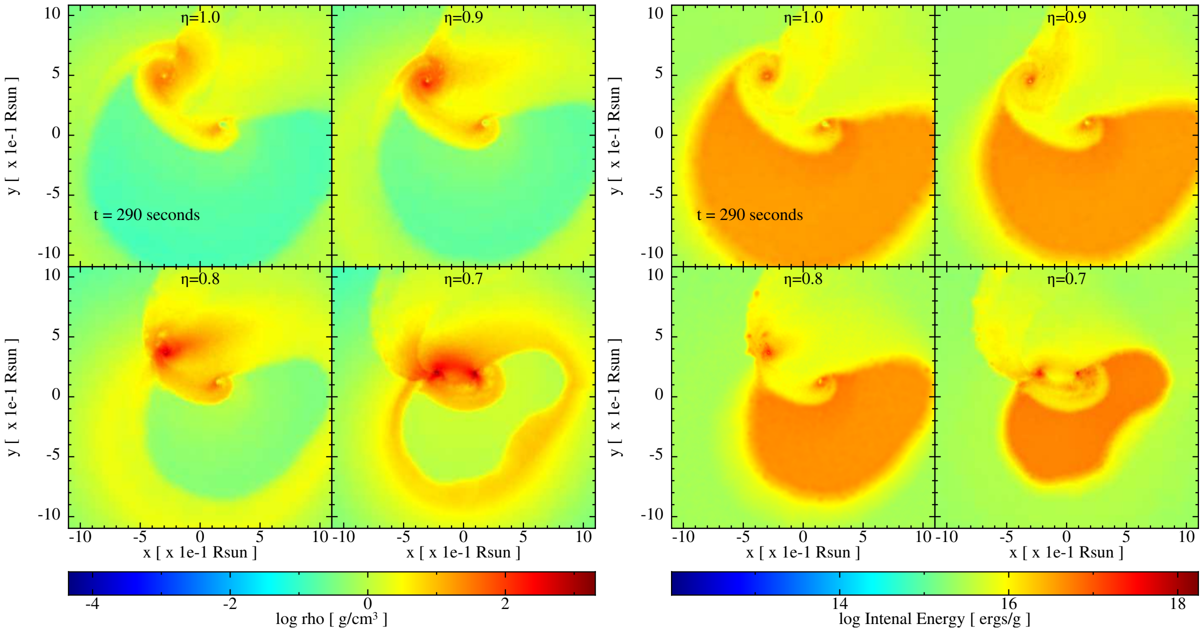

(a) Surface density

(b) Surface specific internal energy

Figure 5.6.: Snapshots of the mass density (left panel) and the specific internal energy (right panel) on the equatorial plane after 290.0 s from the beginning of the SPH simulation (around one orbital period of the initial binary system). The initial binary system parameters are the same as the one represented in Figure 5.2 but the SN explosion energy has been scaled by a factor η shown at the upper side of each panel (these simulations correspond to models 25M1p1e with $\eta = 1$, 25M1p09e with $\eta = 0.9$, 25M1p08e with $\eta = 0.8$ and 25M1p07e with $\eta = 0.7$ of Table 5.2). The accretion onto the νNS as the NS companion is higher for the weaker SN explosions, then the star masses increase faster and the final orbital period of the system shortens. In these explosion also the amount of mass accreted by the νNS is larger.

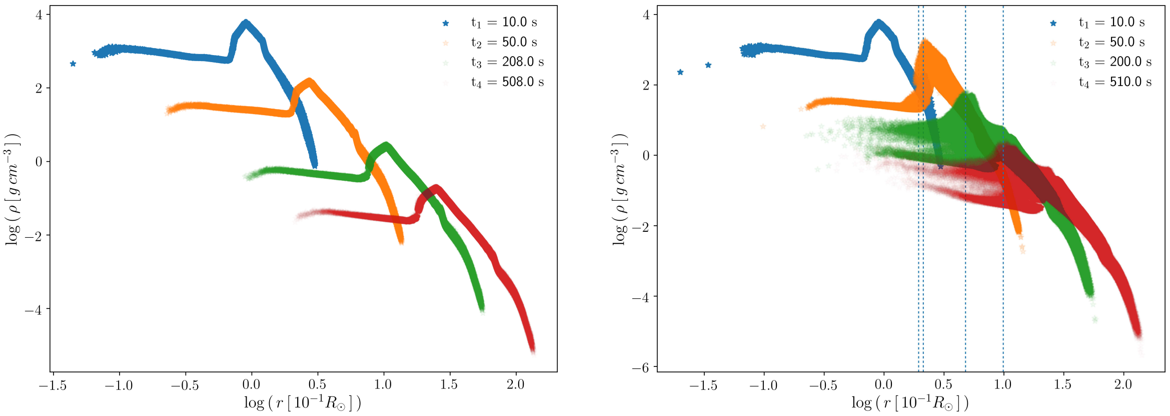

(a) Single star ($\eta = 1.0$)

(b) Binary system ($\eta = 1.0$)

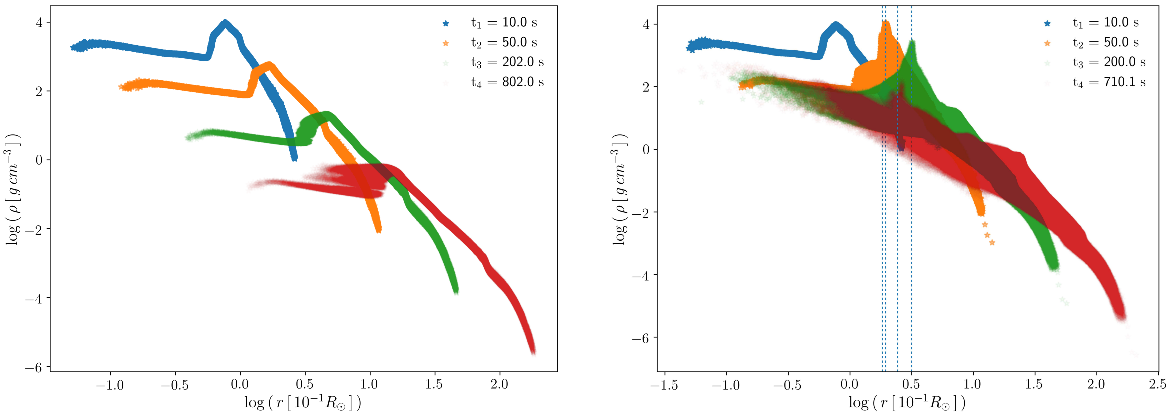

(c) Single star ($\eta = 0.7$)

(d) Binary system ($\eta = 0.7$)

Figure 5.7.: Density profile evolution of the SN ejecta material after the core collapse of the CO$_{\rm core}$ of a $M_{\rm ZAMS} = 25\,M_\odot$ progenitor. The r coordinate is measure from the νNS position. The plots at the left panel corresponds to the evolution of the SN in a single star system while the ones at the right panel the CO$_{\rm core}$ belongs to a binary system with a NS companion of $2\,M_\odot$ and an initial binary separation of 1.36×10^{10} cm. The blue-dotted lines indicate the position of the NS companion. The SN energy of the upper plots is 1.56×10^{51} erg (Model 25M1p1e of Table 5.2) and for the lower plots the SN energy is 6.4×10^{50} erg (Model 25M1p07e of Table 5.2). For isolated SN explosions (or for very wide binaries), the density of the SN ejecta would approximately follow the homologous evolution as is seen in the left panel plots. But, for explosions occurring in close binaries with compact companions (as it's the case of the IGC progenitors), the SN ejecta is subjected to a strong gravitational field which produces an accretion process on the NS companion and a deformation of the supernova fronts closer to the accreting NS companion, as in seen in the right panel plots.

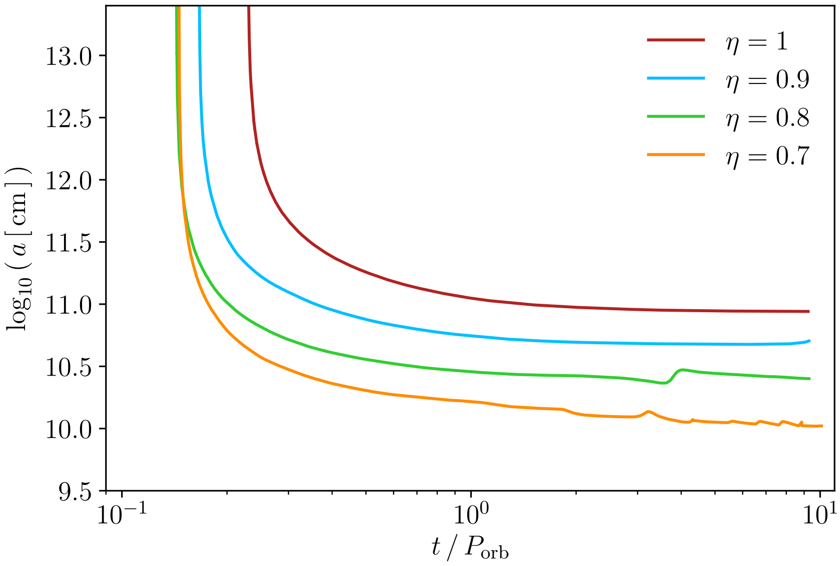

Figure 5.8.: Evolution of the semi-major axis of the νNS-NS binary system. The initial configuration is a binary system formed by the $\mathrm{CO_{core}}$ of a $M_{\rm ZAMS} = 25\,M_\odot$ progenitor and a NS of $2\,M_\odot$ with an initial binary period of approximately 5 min. The $\mathrm{CO_{core}}$ collapses and undergoes a SN explosion ejecting around $5M_\odot$ and leaving a proto-NS of $1.85M_\odot$ (see Table 5.1). Not all the material ejected in the SN leaves the binary system. Some part of this material fallback and is accreted by the νNS while, some other part is accreted by the NS companion. The final binary configuration can remain bound even when the system lost most of the half of its initial total mass.

counterpart. The right panel of Figure 5.5 shows the evolution of the mass accretion rate on the νNS. The black lines correspond to the single progenitors simulations for the scale factors $\eta = 0.8$ and $\eta = 0.7$. The accretion rate peaks at an early time and then decays as $t \propto t^{-5/3}$ [45]. For the binary simulations (color lines) a late peak on the fallback accretion rate is produced from the accretion of the material captured by the gravitational field of the NS companion. This is higher and even early for low energetic supernova (around one order of magnitude for the less energetic explosion ($\eta = 0.7$).

For these simulations, Figure 5.6 shows snapshots of the mass density and the specific internal energy on the equatorial plane after about one orbital period of the initial configuration (~ 5 min). Each panel corresponds to a different value of the η parameter: $\eta = 1.0$ and $\eta = 0.9$ for the left and right upper panels, $\eta = 0.8$ and $\eta = 0.7$ for the left and right bottom panels. The asymmetries of the interior ejecta layer are more pronounced for the less energetic explosion. The orbital period of the final configuration shortens with the decreases of the SN energy, i.e with the accretion of mass by the binaries stars. For example, the accretion onto the νNS and onto the NS companion is around 20% and 16%, respectively, more efficient for the weakest explosion ($\eta = 0.7$) with respect to the strongest one ($\eta = 1$), and the final orbital period is almost 90% shorter that the one of the final system from the most energetic explosion (see Table 5.2).

In order to compare the SN evolution in the single and binary simulations, in Figure 5.7 we show the SN density profile seen from the νNS at different times and for two different SN energies (models 25M1p1e and 25M1p07e of Table 5.2). The left-side plots correspond to the explosion of the $\mathrm{CO_{core}}$ of the $M_{\rm ZAMS} = 25\,M_\odot$ progenitor of Table 5.1, while the right size plots shows its binary counterpart with a $2\,M_\odot$ NS companion. For the isolated SN explosions, the SN ejecta density profiles evolve approximately following an homologous evolution keeping its spherical symmetry around the explosion center. For the explosions occurring in the close binaries, the NS companion gravitational field induced asymmetries in the SN fronts closer to it, that will be more pronounced for the low energetic explosions (see also Figure 5.6). We have shown that these asymmetries lead to observational effects both in the supernova optical emission and in the GRB X-ray afterglow [see 13, 247, and Chapter 4].

We have also studied the evolution of the binary parameters during the SN expansion. Figure 5.8 shows the evolution of the binary semi-major axis with time for the same cases of Fig. 5.5. In these simulations, that correspond to the minimum orbital period of the initial binary system ($\sim$ 5 mins), independently on the SN energy, the post-explosion system remains bound. This occurs even if the system loses more than the half of its total initial mass. For example, for the $\eta = 1$ case, the mass loss in the system is around $4.82\,M_\odot$, namely about 54.7 % of its total initial mass.

If we were to assume that the ejected mass in the SN explosion leaves the system instantaneously, the semi-major axis of the post-explosion system, a, is given by $a/a_0 = (M_0 - \Delta M)/(M_0 - 2a_0\Delta M/r)$, where M_0 and a_0 is the total mass and the semi-major axis of the initial binary system, ΔM is the mass ejected in the SN and r is the star separation at the moment of the explosion [116]. Then, binaries with circular initial orbits become unbound after a SN event if more than half of its total initial mass is lost. However, as it was shown in Fryer et al. [88], in the IGC scenario the mass loss can not be considered instantaneous because the binary initial periods are of the same order than the time it takes for the slowest SN layer to reach the NS companion. For example, the innermost layers of the $25\,M_\odot$ progenitor have a velocity of the order of 10^8 cm s^{-1} so they reach the NS initial position in a time $\sim$ 100 s, nearly 2/5 of the initial binary period. Moreover, it has to be considered that either the νNS or the NS companion will accrete mass and momentum from the SN ejecta, and this will reduce the system mass loss.

5.4.3. Initial binary period

We continue the exploration of the parameter space of the initial binary configurations by running simulations with different values of the initial orbital period. Figure 5.9 shows the mass-accretion rate onto the NS companion for three different initial orbital periods: 4.8 min, 8.1 min and 11.8 min, and for two different SN energies: the canonical explosion (with $\eta = 1$) and the $\eta = 0.7$ modified explosion. For the canonical SN model, an increment of about 1.7 times in the orbital period, changes the fate of the post-explosion binary system, leading to an unbound final configuration. While, for the less energetic explosion, the system remains bounded in all scenarios in which we have increased the initial binary period (up to $\approx$ 60.0 mins, i.e. $\approx$ 12 times the minimum orbital period). For the two explosion energies, the accretion rate seems to scale with the initial binary period of the configuration and follow the same power law at the late times of the accretion process.

Figure 5.10 shows snapshots, at two different times, of the mass density on the orbital

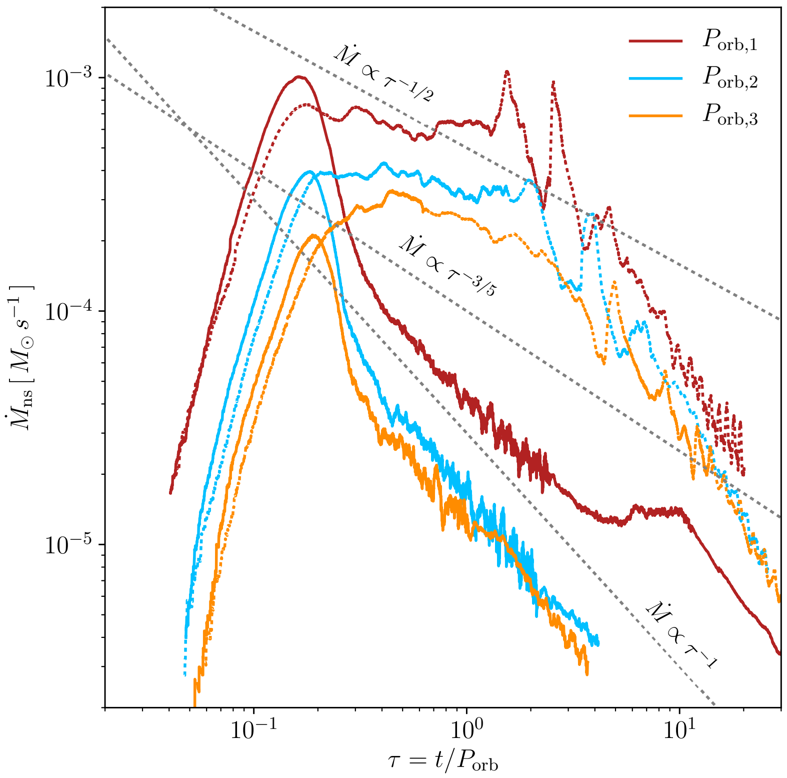

Figure 5.9: Mass-accretion rate onto the NS companion in the IGC scenario. Different colors correspond to different initial orbital period: $P_{\rm orb,1} = 4.8$ min (red line), $P_{\rm orb,1} = 8.1$ min (blue line), $P_{\rm orb,1} = 11.8$ min (orange line). The other parameters that characterize the initial binary system are the same as in Figure 5.4. The solid lines correspond to a SN energy of 1.57×10^{51} ergs, while the dotted ones corresponds to a lower SN energy of 6.5×10^{50} ergs. It can be seen that the mass accretion rate scales with the binary orbital period.

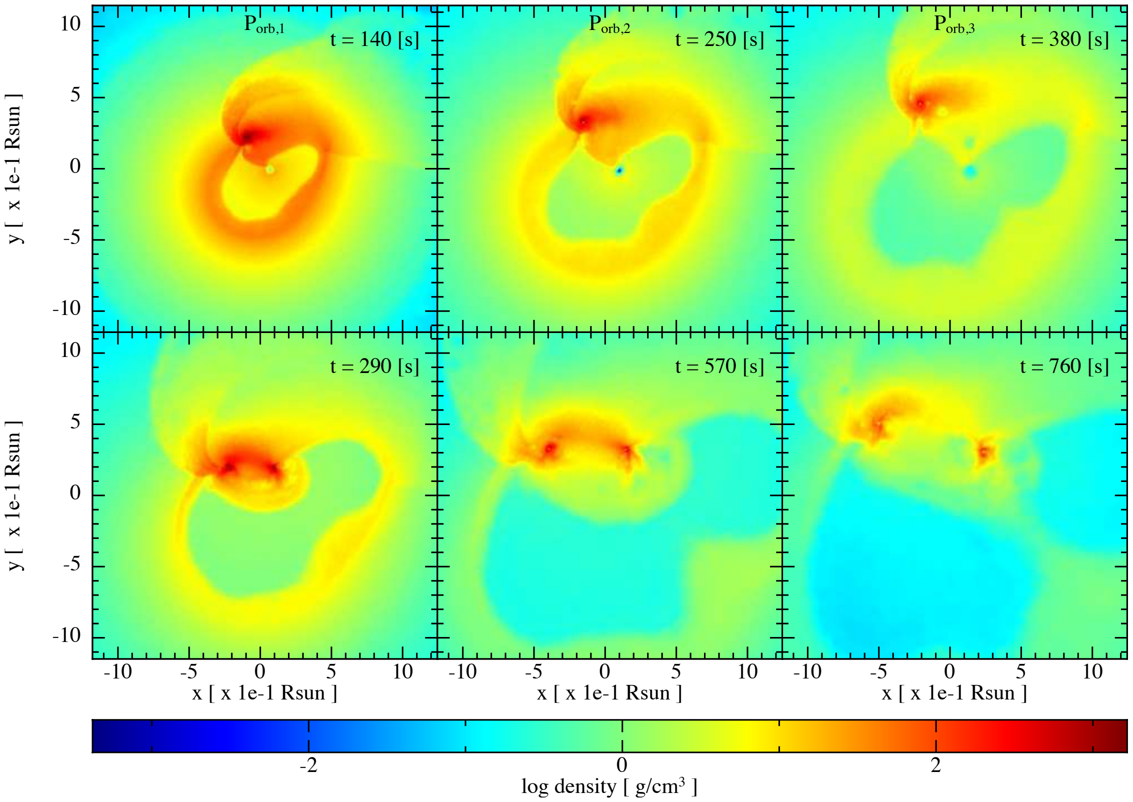

Figure 5.10.: Snapshots of the density surface on the equatorial plane for systems with three different initial binary period. The initial binary system is formed by the $\mathrm{CO_{core}}$ of the $M_{\rm ZAMS} = 25\,M_\odot$ progenitor (see Table 5.1) and a $2\,M_\odot$ NS. The SN energy has been reduced to 6.5×10^{50} erg , scaling the particles velocity and the internal energy by a factor $\eta = 0.7$. The periods of the labels are $P_{\rm orb,1} = 4.8$ min, $P_{\rm orb,1} = 8.1$ min and $P_{\rm orb,1} = 11.8$ min that correspond to Models 25M1p07e, 25M3p07de and 25M2p07e of Table 5.2, respectively.

plane for the same initial binary periods of Figure 5.9 and the modified explosion with $\eta = 0.7$. The system looks like is evolving self similarly with the increase of the binary period.

5.4.4. Asymmetric SN expansion

We now explore how a SN explosion with an asymmetry blastwave affects the evolution of the system. With the parameters $f = 2.0$ (ratio between the in-cone and the out-cone velocities) and $\Theta = 20.0$ (cone amplitude) of equations (5.25) and (5.26), we have performed simulations with the direction of the lobe in the z-axis (perpendicular to the equatorial binary plane) and in the $+x$-axis (directed to the NS companion) and $-x$-axis (opposed to the NS companion). Additionally, we explore the dependence with the opening angle and the ratio velocities, running simulations with $f = 4.0$ and with $\Theta = 40.0$ (see Table 5.2). Figure 5.11 shows the accretion rate onto the NS companion for these simulations. We can see that the introduction of asymmetries in the SN expansion velocity increases the accretion rate on the NS companion as well as the fallback accretion rate onto the νNS. This is expected because, in order to conserved the SN energy explosion, we increased the velocities of the particles inside the cone while we decreased the velocities of the particles out-side it, then these slower particles are more probably captured by the accreting stars. The direction of the lobe does not introduce appreciable changes in the evolution of the accretion rate or the final star masses as it does when the parameters f or Θ are increased.

Figure 5.12 showns snapshots of the mass density for the simulations of the asymmetric SN expansion. As it was previously done, the reference system was rotated and translated in the way that its center corresponds to the NS companion position and the x-axis joins the binary stars. Contrary to the symmetric cases, the binary orbital plane change after the SN ejecta if the lobe of the explosion is directed outside the equatorial plane of the initial binary. For example, for $f = 2.0$, the final orbital plane makes an angle of 2.55° with respect to the initial orbital plane and for $f = 4.0$, this angle grows up to 11.5° . However, either for the symmetry or the asymmetry explosion, the magnitude of the velocity of the center-of-mass of the final binary system remains around $100 - 800\,\mathrm{km/s}$. The kick velocities giving in Table 5.2 are consequence to the accretion of the linear momentum from the accreted particles and the gravitational attraction that the ejecta material do on the νNS [140]. Another source for the NS kick velocity can be due to the anisotropic emission of the neutrino during the star collapse [21, 87, 309].

5.4.5. $\mathrm{CO_{core}}$ progenitor mass

Finally, we have varied the progenitor of the $\mathrm{CO_{core}}$. Figure 5.13 shows the mass-accretion rate onto the NS companion for all the progenitors listed in Table 5.1. In Table 5.2 we summarize the results for these simulations, and additionally we have run more simulations with each of this progenitors changing the SN energy and the initial binary separation. We now presents the salient properties of these simulations.

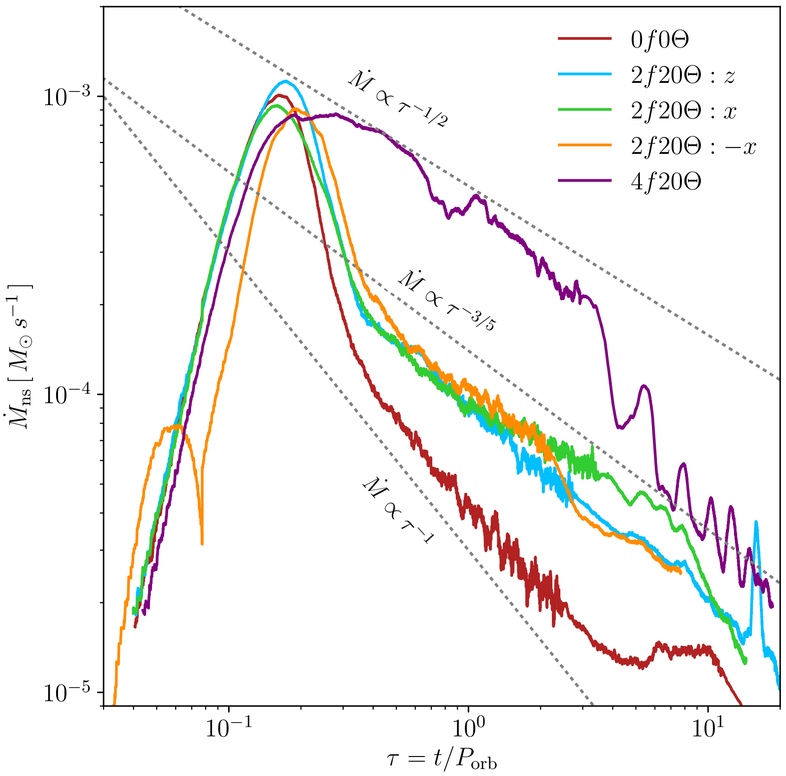

Figure 5.11: Mass-accretion rate onto the NS companion introducing a conical geometry for the SN velocity profile of the $M_{\rm ZAMS} = 25\,M_\odot$ progenitor (see Table 5.1). The parameter of the initial binary system are the same as the one for Figure 5.4. The cone was opened along the z-axis (perpendicular to the orbital plane-blue and purple lines) and along the x-axis (on the orbital plane-green and orange lines). Since the SN energy is conserved, the introduction of the asymmetry reduces the particles velocity and increases the accretion rate.

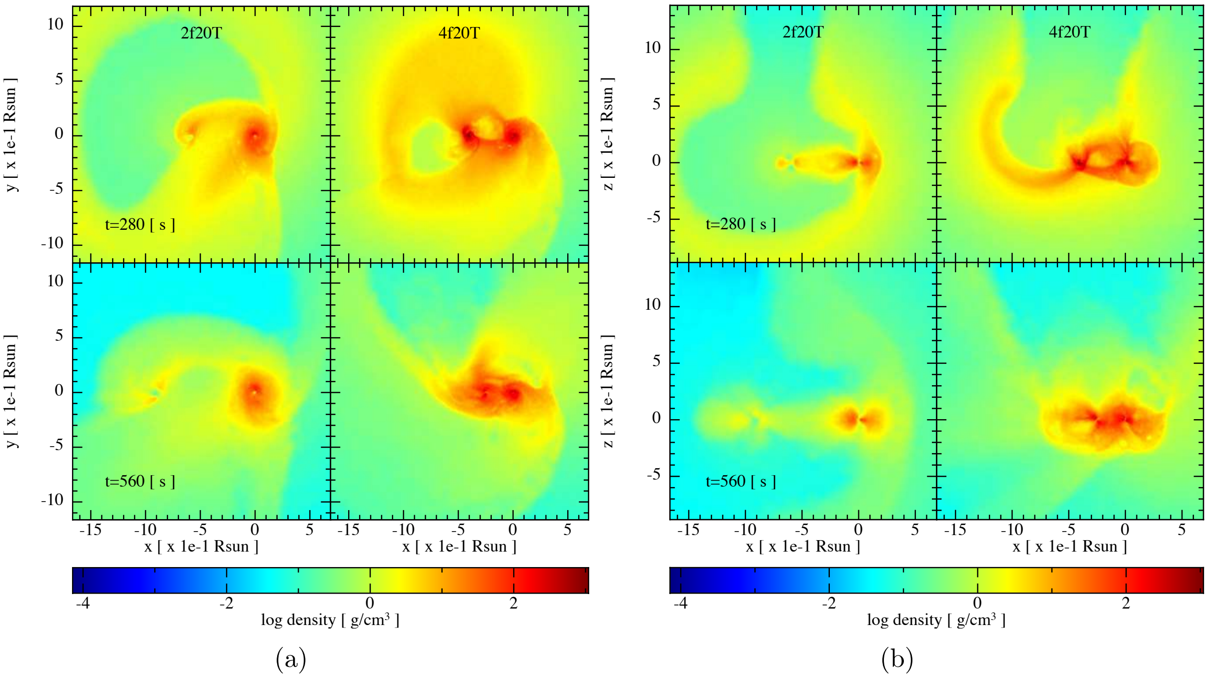

(a)

(b)

Figure 5.12.: Snapshots of the surface density on the binary equatorial plane (left panel) and the plane orthogonal to it (right panel). The reference system have been rotated and translated in a way that the x-axis becomes directed in the line that joins the binary stars and its origin is at the NS companion. The initial binary system is the same as the one represented in Figure 5.2 but the SN velocity profile has been modified to a conical geometry following equations (5.25) and (5.26). In all the cases, the cone opens along the z-axis. The left frames of each plot have parameters $f = 2.0$ and $\Theta = 20.0$ (Model 25m2f20tz of Table 5.2) while the right ones have $f = 4.0$ and $\Theta = 20.0$ (Model 25m4f20tz of Table 5.2). If the lobe of the explosion is directed outside of the initial orbital plane, as in here, the orbital plane of the final configuration changes. For the $f = 2.0$, the final orbital plane makes an angle of 2.55° with respect to the initial orbital plane and for $f = 4.0$, this angle grows up to 11.5°

The $15\,M_\odot$ ejects just around $1.6\,M_\odot$, then the energy of the SN explosion need to be low (in the order of 10^{50} ergs) and the binary system enough compact, in order to have a significant accretion on the NS companion. However, if the SN energy is considerably reduced, most of the SN material will do fallback onto the νNS. For example, scaling the SN kinetic energy and internal energy by $\eta = 0.05$, almost 80% of the SN ejecta is accreted by the νNS, while scaling by a parameter $\eta = 0.1$, the accreted material via fallback is reduced to the 30%. It is important to point out that, if the initial orbital period is increased by a factor of 1.7, the amount of ejecta mass that can not escape to the νNS gravitational field grows to the 55%. Namely, the presence of a close NS companion could avoid the collapse of the νNS in the weak explosion cases.

For the $30\,M_\odot$ progenitor, we worked with two simulated explosions with different energies, one almost one order of magnitude stronger than the other. For the lowest energetic explosion, $E_{\rm sn,1}$, a significant amount of mass is making fallback, then the collapse due to the hypercritical accretion on the νNS is more probable than the one of the NS companion. On the other hand, the velocities of the stronger energetic explosion, $E_{\rm sn,2}$, are so high that almost all the SN ejecta surpass the NS companion without being captured by it, and the final configuration of νNS and NS become unbound. For these explosions, the ration between the total SN energy and the kinetic energy is 0.45 and 0.81, respectively.

We have performed more simulations scaling the energy of these two explosions, and summarized their results in Table 5.2. In these cases, we can evaluate how accurate is our alternative path of changing the explosion energy by just scaling the velocities and the internal energy of the SPH-particles instead of re-run new simulations of the $\rm CO_{core}$ collapse and bounce of the shock. Figure 5.14 shows the density profile at around the same time for the two explosions of the $30\,M_\odot$ progenitor and their respective simulations with the scaled SN energy. In general, the internal radius of the low energetic explosion is about two times smaller that the one of the high energetic explosion (see Figure 5.1). These will increased the material that will make fallback in the single star as well as in the binary system simulations, even when the scaled energy of the explosion become comparable.

Finally, we used a $40\,M_\odot$ as the progenitor of the $\rm CO_{core}$. Since, this progenitor ejects around $11\,M_\odot$ in the SN, the energy of the explosion needs to be low to make the final configuration remains bounded and also for the NS companion to be able to accrete enough mass to collapse. If we used a factor $\eta = 0.7$ to reduce the SPH-particles velocity and internal energy, we see that the amount of mass accreted by the νNS is low but the mass accreted by the NS-companion could make it to induced its collapse. Instead, for $\eta = 0.5$, more of the ejecta make fallback accretion and onto the νNS.

Fryer et al. [90] performed a 1D numerical simulation of the $\rm CO_{core}$ collapse, bounce and explosion and was estimated the accretion rate on the NS companion using the Bondi-Hoyle-Lyttleton formalism [27, 28, 121]. In these simulation, at the beginning of the accretion process, there is a burst in the accretion rate, growing up to the $10^{-1}\,\rm M_\odot/s$, that is two order of magnitude greater than the accretion rate that we are obtaining with the SPH simulation. However the total time of the accretion process is much shorter in those simulations that the one presented here, making the amount of mass accreted

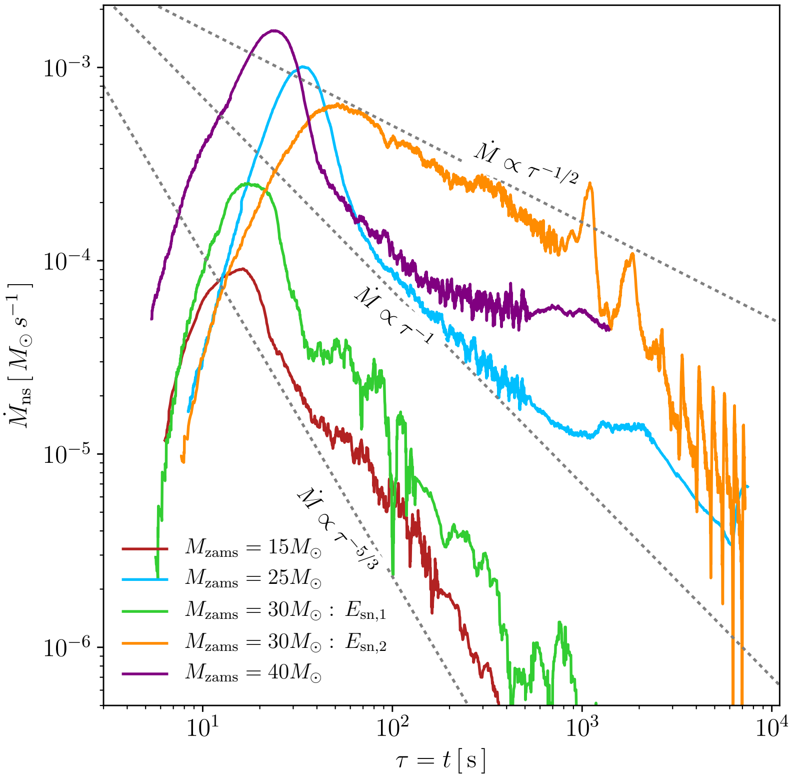

Figure 5.13: Mass-accretion rate onto the NS companion using the explosion of all the $\mathrm{CO_{core}}$ progenitors resumed in Table 5.1. The NS companion has an initial mass of $2\,M_\odot$ and the orbital period is close to the minimum period that the system can have in order that there is not Roche Overflow before the collapse of the $\mathrm{CO_{core}}$: 6.5 min, 4.8 min, 6.0 min and 4.4 min for the $M_{\rm ZAMS} = 15$, 25, 30 and $40\,M_\odot$ progenitors, respectively.

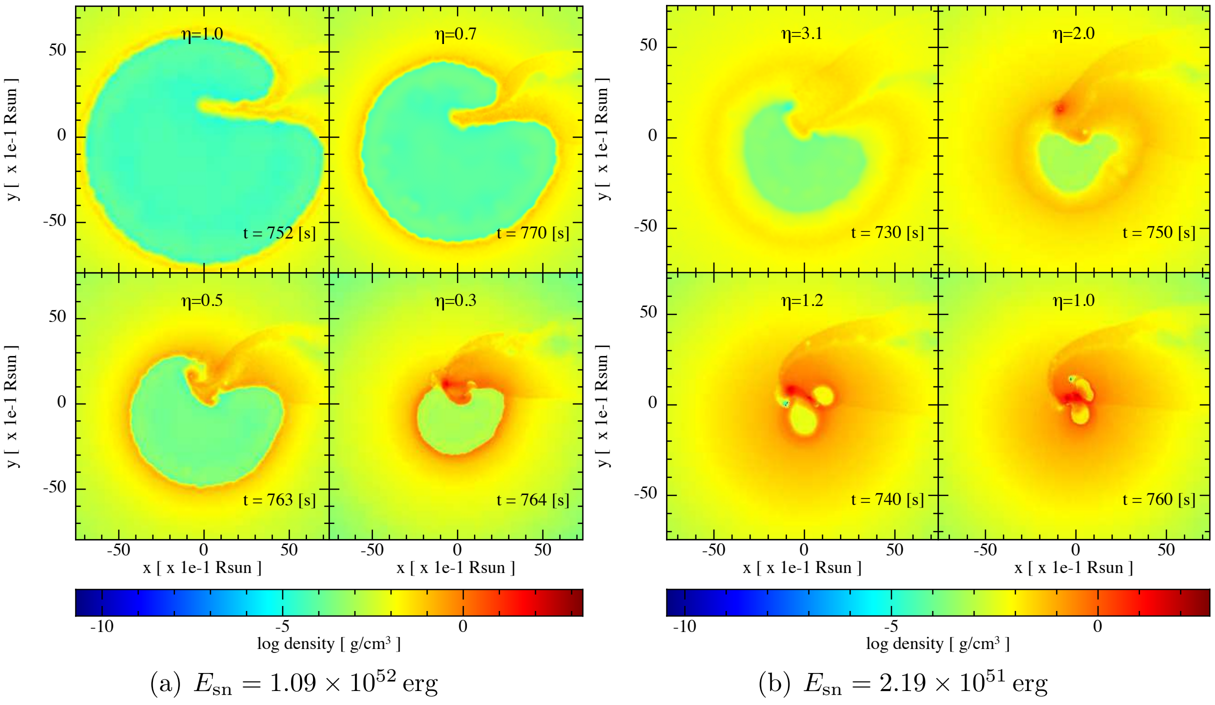

(a) $E_{\rm sn} = 1.09 \times 10^{52}$ erg

(b) $E_{\rm sn} = 2.19 \times 10^{51}$ erg

Figure 5.14.: Snapshots of the mass density on the binary equatorial plane. The initial binary system is formed by the $\mathrm{CO_{core}}$ of the $M_{\rm ZAMS} = 30\,M_\odot$ progenitor and a $2\,M_\odot$ NS with a orbital period of around 6 min. We have simulated the collapse and bounce of the $30\,M_\odot$ progenitor with two different SN energy as is specified in the left and right panel labels. We show the simulations scaling the SN energy of these two explosions by a factor η (specified in the upper part of each frame). In general, the internal radius of the low energetic explosion is about two times smaller that the one of the high energetic explosion (see Figure 5.1). This increases the fallback on the νNS and the region closed to the binary system becomes denser.

by the NS companion comparable between the simulations. This discrepancy is a direct consequence of the increase of dimension of the simulation. While the 1D simulation is stopped when the SN innermost layer reach the NS and doesn't take into account the angular momentum of the particles with respect to the accreting star, the 3D simulation can go beyond this point because there are particles that remains bounded to the NS in a kind of disk structure, and the star continues the accretion process.

5.5. Evolution and collapse of the NS companion

We turn now to the issue of evaluating whether the NS companion collapses or not to a BH due to the accretion of SN material. For this, we need both to study how the NS gravitational mass and angular momentum evolve with time, and to set a value to the NS critical mass. As a first approximation, we assume that the NS evolves from an equilibrium configuration to the next, using the uniformly rotating NS equilibrium configurations in Cipolletta et al. [49, 50]. These configurations were constructed using the public code RNS [276] to solve the axisymmetric Einstein equations for three selected relativistic mean-field nuclear matter (EOS) models: NL3, GM1 and TM1.

Here, we will follow the formalism we have exposed in Chapter 1. The evolution of the NS gravitational mass is given by equation (1.35). As a matter of convenience, we will rewrite here:

$$\dot{M}_{\rm ns} = \left(\frac{\partial M_{\rm ns}}{\partial M_b}\right)_{J_{\rm ns}} \dot{M}_b + \left(\frac{\partial M_{\rm ns}}{\partial J_{\rm ns}}\right)_{M_b} \dot{J}_{\rm ns} \tag{5.27}$$

The relation between NS baryonic mass M_b and the NS gravitational mass $M_{\rm ns}$ for a rotating NS including the effects of rotation in general relativity can be found in Appendix A.2.

The mass and angular momentum of the accreted particles add to the baryonic mass and the angular momentum of the NS, thus we can integrate equation (5.27) and follow the evolution of the gravitational mass of both the νNS and the NS companion. The NS can accrete mass until it reaches an instability limit: the mass shedding limit or the secular axisymmetric instability (see Chapter 1 and Appendix A.2).

In the left panel of Figure 5.15 we show the track followed by the NS companion (solid line) and the νNS (dashed line) in the $M_{\rm star}$-$j_{\rm star}$ plane for the $25\,M_{\rm zmans}$ progenitor of the CO$_{\rm core}$, for two different SN explosion energies (models 25M1p1e and 25M1p07e of Table 5.2). For the system with the stronger SN explosion, the νNS and the NS companion reaches the mass-shedding limit at $t = 21.66\,$min with $1.93\,M_\odot$ and $t = 20.01\,$min with $2.055\,M_\odot$, respectively. For the less energetic SN explosion this occurs early, at $t = 5.51\,$min with $2.04\,M_\odot$ for the νNS, and at $t = 2.91\,$min with $2.09\,M_\odot$ for the NS companion. The dotted line shows the continuation of the integration of equation (5.27) for all the simulation time. For the NS companion, there is a decreasing of angular momentum. This occurs because there is a change in the direction of rotation of the accreted particles with respect to one of the accreting NS star.

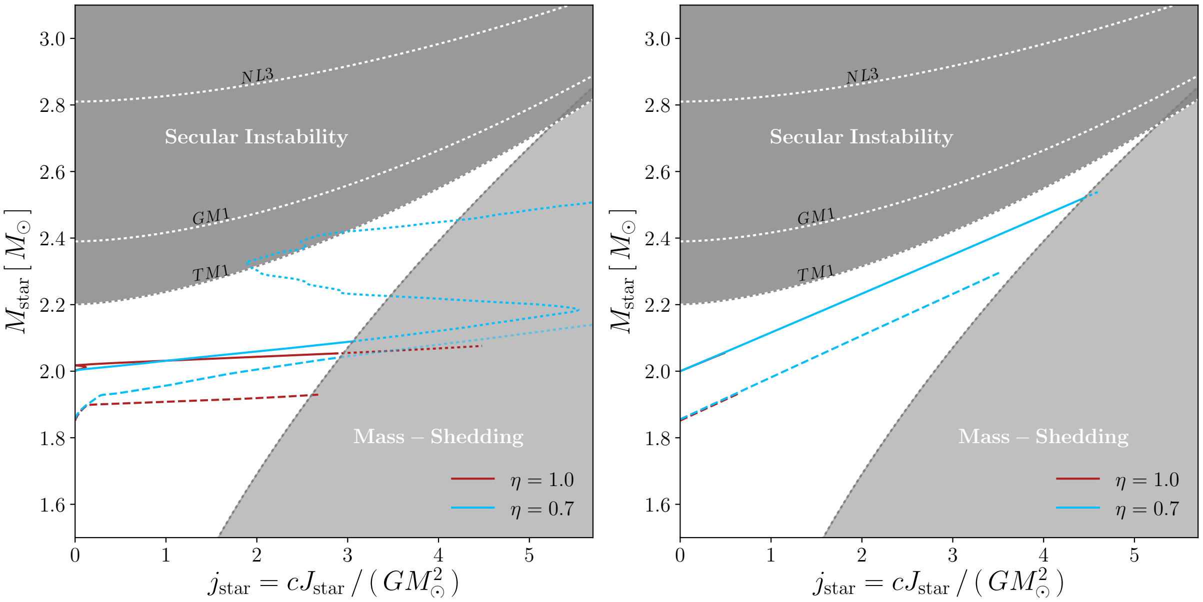

Figure 5.15.: Evolution of the νNS (dashed line) and the NS companion (solid line) in the mass-dimensionless angular momentum ($M_{\rm star}$-$j_{\rm star}$) plane. The mass of the particles accreted contributed to the star baryonic mass. In the left plot we adopt that the star accretes all the particles angular momentum. In the right plot we adopt that the star accretes from a disk-like structure, namely that the angular momentum evolution is dictated by the disk-accretion torque (see text for details). In this example the initial binary system is formed by the $\rm CO_{core}$ of the $25\,M_\odot$ progenitor and a $2\,M_\odot$ NS with an orbital period of about 5 min. The red lines correspond to a SN explosion of 1.57×10^{51} erg, while for the blue line the explosion energy has been scaled by a factor $\eta = 0.7$, leading to 6.5×10^{50} erg.

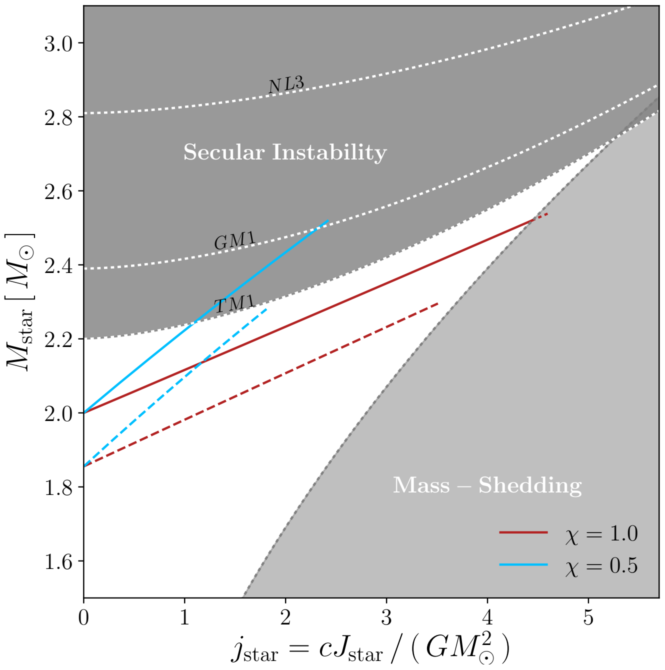

Figure 5.16.: Evolution of the νNS (dashed line) and the NS companion (solid line) in the mass-dimensionless angular momentum ($M_{\rm star}$-$j_{\rm star}$) plane. The angular momentum evolution is dictated by the disk-accretion torque given by Equation (5.29), where we have introduced the efficiency parameter, $\chi \leq 1$, that accounts for angular momentum losses between the disk and the stellar surface. The initial binary system is formed by the $\rm CO_{core}$ of the $25\,M_\odot$ progenitor and a $2\,M_\odot$ NS with an orbital period of about 5 min. The SN explosion energy has been scaled by $\eta = 0.7$ (Model 25M1p07e of table 5.2).

Since we are assuming that the angular momentum of the accreted particles is totally transferred to the NS, even the accretion of a little amount of mass might bring it soon to the mass-shedding limit (see Figure 5.15). However, we see in the simulations that kind of disk is form around the NS, then before they being actually accreted, they circularize and loose angular momentum owing to the friction force developed in the disk. In this picture, we need to integrate equation (5.27) assuming that the star angular momentum evolution is given by the disk accretion torque, as was done in Chapter 1:

$$\dot{J}_{\rm ns} = l(R_d)\dot{M}_b \tag{5.28}$$

with $l(R_d)$ being the specific angular momentum of the particles at the disk interior radius, R_d. The disk interior radius will given by the last circular orbit around the NS, see equation (1.39).

In the right panel of Figure 5.15 we show the evolution of the νNS and the NS companion in the $M_{\rm star}$-$j_{\rm star}$, for the same models that the ones of the left panel. In this case, we have integrated equation (5.27) with equation (5.28), assuming again, that the particle mass sums to the star baryonic mass and the disk viscous time scale is smaller that the accretion time scale, i.e we used the mass accretion rate obtained from the SPH simulations. In this cases, only the NS companion for the less energetic SN simulation reaches the mass-shedding limit.

We have assumed until now a totally efficient transfer of angular momentum of the particles from the inner disk to the NS surface. However, angular momentum losses (e.g., by accretion outflows) should be taken into account. We model these losses introducing a parameter for the efficiency of the angular momentum transfer, $\chi \leq 1$ [see e.g. 13, and Chapters 1 and 2], defined as:

$$\dot{J}_{\rm ns} = \chi\, l(R_d)\dot{M}_b. \tag{5.29}$$

In Figure 5.16 we compare the evolutionary path on the mass-dimensionless angular momentum plane for two values of the efficiency parameter, $\chi = 0.5$ and $\chi = 1.0$. It can be seen that angular momentum losses make the star to reach the secular instability limit, namely the critical mass to collapse to a BH, instead of the mass-shedding limit. This result is in agreement with the results presented in Becerra et al. [13, 14].

Table 5.5 lists the total angular momentum of the particles accreted by the binary stars, $L_{\rm tot}$, as well as the accreted mass, $M_{\rm star}$ and accreted angular momentum, $j_{\rm star} = cJ_{\rm star}/(GM_\odot^2)$ of the star when it crosses the stability region (if it does), or when the simulation was stopped. We show the results for two selected values of the angular mosentum transfer efficiency parameter, $\chi = 1$ and 0.5. In the case of a totally efficient transfer of angular momentum ($\chi = 1.0$) the mass-shedding limit is reached first by the stars, while if it is assumed angular momentun losses by adopting a lower value for χ parameter, the stars reach first the secular axisymmetry instability. For low energetic SN explosion, it is more probable that the νNS arrive to the mass-shedding limit. This is the case for the less energetic explosion of the $M_{\rm ZAMS} = 15\,M_\odot$ progenitor, the $30\,M_\odot$ and also the $40\,M_\odot$ ones. On the other hand, there are few cases in which the NS companion arrives first to the mass-shedding limit. The one in which the progenitor of the CO$_{\rm core}$ is the

Table 5.5.: Final state of the νNS and the NS companion

		νNS							NS						
			$\chi = 0.5$			$\chi = 1.0$				$\chi = 0.5$			$\chi = 1.0$		
$\mathrm{CO_{core}}$	Model	$L_{\rm tot}$	$M_{\nu\rm NS}$	$j_{\nu\rm NS}$	Fate	$M_{\nu\rm NS}$	$j_{\nu\rm NS}$	Fate	$L_{\rm tot}$	$M_{\rm NS}$	$j_{\rm NS}$	Fate	$M_{\rm NS}$	$j_{\rm NS}$	Fate
$M_{\rm zams}$		$c/(GM_\odot^2)$	$M_\odot$	$c/(GM_\odot^2)$		$M_\odot$	$c/(GM_\odot^2)$		$c/(GM_\odot^2)$	$M_\odot$	$c/(GM_\odot^2)$		$M_\odot$	$c/(GM_\odot^2)$	
$15\,M_\odot$	15m1p07e	0.027	1.302	0.007	Stb	1.302	0.008	Stb	0.085	2.004	0.009	Stb	2.002	0.018	Stb
	15m1p05e	0.069	1.303	0.009	Stb	1.303	0.016	Stb	0.323	2.004	0.019	Stb	2.004	0.037	Stb
	15m1p03e	0.019	1.315	0.041	Stb	1.315	0.077	Stb	0.362	2.023	0.101	Stb	2.023	0.204	Stb
	15m2p03e	0.091	1.303	0.08	Stb	1.303	0.017	Stb	0.579	2.006	0.026	Stb	2.006	0.056	Stb
	15m1p01e	13.63	1.815	1.571	Stb	1.636	1.874	M-sh	19.373	2.157	0.701	Stb	2.159	1.377	Stb
	15m2p01e	38.38	2.077	2.534	Stb	1.639	1.892	M-sh	12.533	2.080	0.35	Stb	2.080	0.693	Stb
	15m3p01e	30.95	1.759	1.377	Stb	1.862	3.253	M-sh	2.004	2.045	1.197	Stb	2.045	0.388	Stb
$25M_\odot$	25m1p1e	3.469	1.931	0.321	Stb	1.933	0.627	Stb	4.746	2.055	0.2467	Stb	2.056	0.497	Stb
	25m2p1e	1.779	1.912	0.242	Stb	1.914	0.472	Stb	1.927	2.022	0.099	Stb	2.022	0.198	Stb
	25m3p1e	1.085	1.912	0.229	Stb	1.912	0.399	Stb	1.944	2.018	0.0813	Stb	2.019	0.1639	Stb
	25m1p09e	6.243	1.982	0.513	Stb	1.983	1.010	Stb	6.538	2.127	0.584	Stb	2.129	1.187	Stb
	25m1p08e	7.331	2.038	1.449	Stb	2.031	1.365	Stb	9.870	2.258	1.242	Sc-in	2.348	3.576	Stb
	25m1p07e	18.146	2.284	1.826	Stb	2.289	3.434	Stb	8.491	2.246	1.105	Sec-in	2.528	4.506	M-sh
	25m2p07e	19.51	2.250	1.663	Stb	2.265	3.215	Stb	9.908	2.252	1.135	Sc-in	2.426	3.648	Stb
	25m3p07e	21.34	2.214	1.476	Stb	2.226	2.812	Stb	17.292	2.004	2.246	Sc-in	2.425	3.638	Stb
$30\,M_\odot$ [a]	30m1p1ea	0.077	1.756	0.021	Stb	1.756	0.044	Stb	0.059	2.006	0.026	Stb	2.006	0.052	Stb
	30m1p07ea	0.954	1.758	0.032	Stb	1.758	0.062	Stb	0.366	2.012	0.053	Stb	2.012	0.106	Stb
	30m1p05ea	1.828	1.764	0.053	Stb	1.764	0.107	Stb	4.073	2.028	0.125	Stb	2.028	0.251	Stb
	30m1p03ea	3.560	1.842	0.3494	Stb	1.843	0.692	Stb	33.083	2.246	2.358	Sc-in	2.356	3.532	Stb
	30m2p03ea	4.266	1.821	0.267	Stb	1.821	0.522	Stb	36.161	2.151	0.7006	Stb	2.154	1.426	Stb
$30\,M_\odot$ [b]	30m1p1eb	64.935	2.379	2.614	Sc-in	2.215	3.507	M-sh	19.995	2.244	1.099	Sc-in	2.307	2.634	Stb
	30m1p12eb	28.432	2.362	2.541	Stb	2.200	3.392	M-sh	33.681	2.244	1.100	Sc-in	2.304	2.606	Stb
	30m2p12eb	26.508	2.397	2.807	Sc-in	2.162	3.297	M-sh	23.922	2.1801	0.802	Stb	2.1827	1.572	Stb
	30m1p2eb	2.819	1.777	0.106	Stb	1.777	0.196	Stb	7.846	2.061	0.271	Stb	2.061	0.546	Stb
	30m1p31eb	0.721	1.766	0.0611	Stb	1.766	0.105	Stb	1.6715	2.014	0.062	Stb	2.014	0.122	Stb
$40\,M_\odot$	40m1p1e	1.125	1.874	0.081	Stb	1.873	0.132	Stb	11.504	2.056	0.2453	Stb	2.056	0.4918	Stb
	40m1p09e	2.189	1.875	0.087	Stb	1.875	0.164	Stb	25.669	2.236	1.097	Stb	2.236	2.247	Stb
	40m1p08e	3.468	1.879	0.105	Stb	1.879	0.199	Stb	30.146	2.254	1.22	Sc-in	2.405	4.060	M-sh
	40m1p07e	9.963	2.042	0.7631	Stb	2.042	1.486	Stb	34.074	2.243	1.09	Sc-in	2.526	4.491	M-sh
	40m2p07e	9.6264	2.023	0.689	Stb	2.024	1.343	Stb	42.97	2.245	1.100	Sc-in	2.522	4.458	M-sh
	40m4p07e	10.333	1.942	0.342	Stb	1.942	0.652	Stb	27.474	2.246	1.129	Sc-in	2.4135	3.6104	Stb
	40m1p06e	171.063	2.310	1.948	Sc-in	2.338	3.857	M-sh	63.31	2.244	1.098	Sc-in	2.529	4.518	M-sh
	40m2p06e	121.594	2.318	1.987	Sc-in	2.331	3.793	M-sh	45.944	2.244	1.096	Sc-in	2.527	4.506	M-sh
	40m1p05e	11.593	2.316	1.197	Sc-in	2.338	3.861	M-sh	5.434	2.133	0.588	Stb	2.134	1.158	Stb

NOTE—Stb: stable configuration; M-sh: mass-shedding limit; Sc-in: secular axisymmetric instability.

[a] $E_{\rm sn} = 1.09 \times 10^{52}$ erg

[b] $E_{\rm sn} = 2.19 \times 10^{51}$ erg

$M_{\rm ZAMS} = 25 M_\odot$ star, the SN energy was scaled with $\eta = 0.7$, and the orbital binary period is the shortest one. Also, when the progenitor of the $\mathrm{CO_{core}}$ is a $M_{\rm ZAMS} = 40\,M_\odot$ star and the SN energy was scaled with $\eta = 0.8$, $\eta = 0.7$ and $\eta = 0.6$.

Notice that in the case with $\eta = 0.8$ and $\chi = 1$ the NS companion arrives to the mass-shedding limit, and with $\chi = 0.5$ arrives to the secular instability limit, but the final system is unbound after the SN ejecta leave the system. This contradicts the results in Fryer et al. [88] where was concluded that almost the 100% of the final binary systems NS-BH produced in the BdHNe will remain bound, after following the evolution of the binary parameter in the IGC scenario. However there was studied progenitors with ejecta masses up to $8\,M_\odot$ and the $M_{\rm ZAMS} = 40\,M_\odot$ has $\approx 11\,M_\odot$ of ejected mass, making the accretion on the NS becomes higher to maintain the system bound.

We turn now to analyse the relevance of the ξ-parameter of equation (5.15) on the mass-accretion rate onto the star. Until now, we have assumed a value $\xi = 0.1$ for this parameter. A larger value of ξ results in higher accretion rates: it allows a bigger gravitational capture radius and then more particles can be accreted by the star. In this way, a $\xi = 1.0$, the maximum value that ξ can have, will establish an upper limit for the mass accretion rate onto the star. We can also establish a lower limit for the accretion rate, if we allow the star just accretes the particle which angular momentum is equals or smaller that the angular momentum that a particle orbiting the star would have at the last circular orbit. An equivalent condition is to adopt a varying ξ parameter that equals the capture radius to the radius of the last stable orbit, $r_{\rm ISCO}$. But, since the $r_{\rm ISCO}$ for the NS is of the order of the NS radius, i.e. ~ 10 km, we will need to increase considerably the number of particles to be able to resolve the NS surface.

We have re-run the SPH simulations adopting different values for ξ, for the initial binary system formed by the $\rm CO_{core}$ of the $M_{\rm ZAMS} = 25\,M_\odot$ and a $2\,M_\odot$ binary system with an orbital period of about 5 min. In Figure 5.17 we show the accretion rate on the NS companion for $\xi = 1.0$, 0.5 and 0.1. The label $\xi = \xi_{j_{\rm isco}}$ corresponds to the case in which the star just accretes the particles which angular momentum is smaller that the angular momentum of the last stable orbit. The late mass-accretion rate of the simulations with $\xi = \xi_{j_{\rm isco}}$ and $\xi = 0.5$ and 1.0 fall almost with the same power law, $\dot{M} \propto t^{5/3}$. Also, for the same simulation, in Figure 5.18 show snapshots of the density surface at the binary equatorial plane at two different times.

The simulation with $\xi = 1.0$ and $\xi = 0.5$ gives greater peaks for the mass accretion rate. This is expected since in these cases the NS capture radius is larger, the star cleans up its surrounding and produces, at later times, a quickly dropping accretion rate. Comparing this simulation with the one with $\xi = 0.1$, we can deduce that there is a delay time between the particles are gravitational captured by the star and the time it is actually accreted by it. We should expect that the simulation with $\xi_{j_{\rm isco}}$ give a better resolution of the disk around the NS companion. However, the artificial viscosity used in the code was introduced in order to resolve shocks and does not model the disk viscosity [119]. Then, we are seeing that the particles that circularize around the star, at some point scape from the NS gravitational field, making the mass-accretion rate to drop (see figure 5.18). In Table 5.6 we summarize the parameters that characterize the final state of the NS companion as well as the final binary system. We have re-run simulation with the $M_{\rm ZAMS}$ =25, 30 and 40 $M_\odot$ progenitors of the $\rm CO_{core}$.

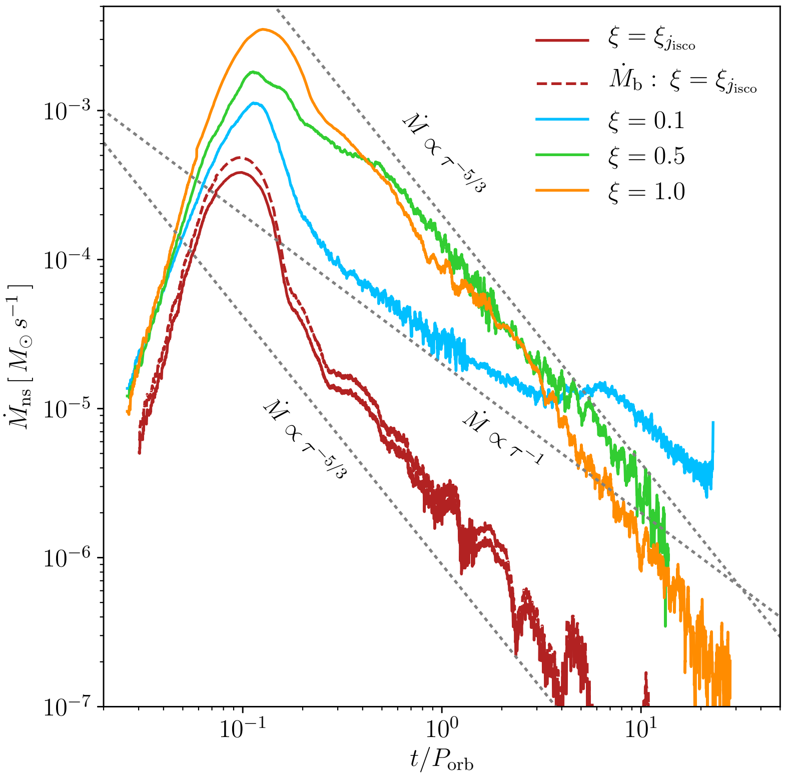

Figure 5.17: Mass-accretion rate onto the NS companion adopting different values for the ξ parameter of equation (5.15). This parameter controls the size of the particle capture radius. A value $\xi = 1.0$ establish an upper limit on the mass-accretion rate. We also defined a lower limit on the accretion (red line), allowing to the star just accreted those particles that have an angular momentum smaller that the angular momentum of the last stable orbit. The initial binary configuration is the one of Figure 5.4.

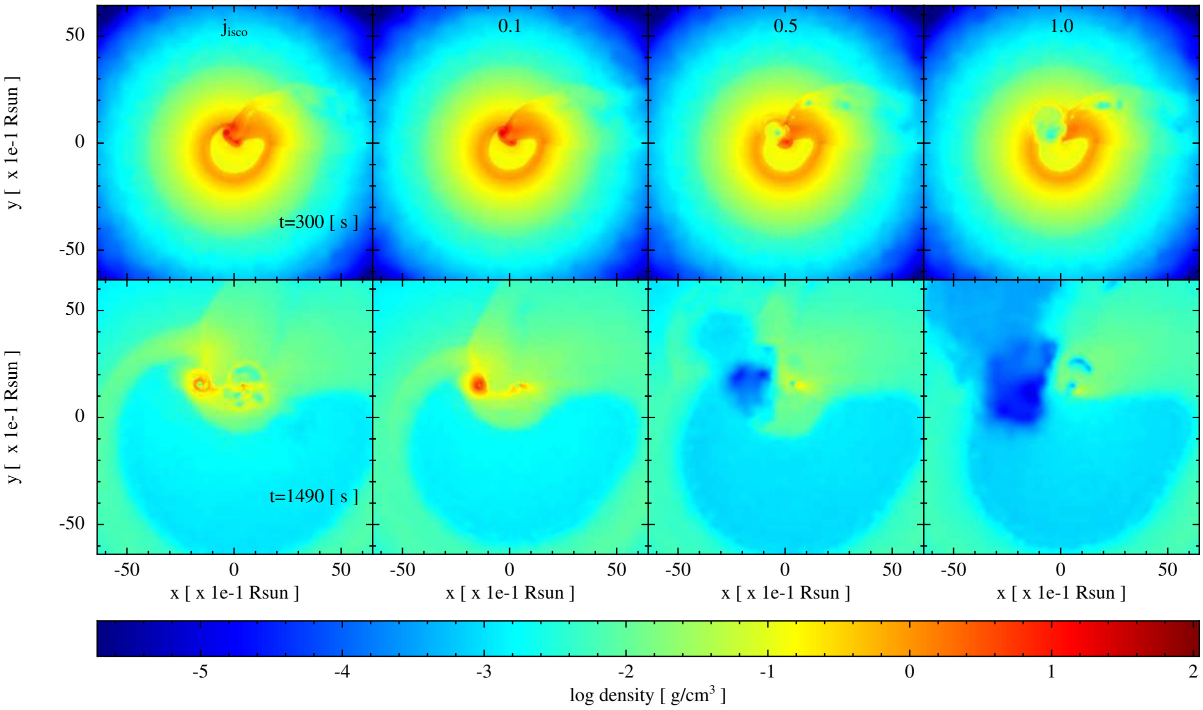

Figure 5.18.: Snapshots of the surface density mass. The initial binary system is form by the $\mathrm{CO_{core}}$ of a $M_\mathrm{ZAMS} = 25M_\odot$ progenitor and a $2M_\odot$ NS with an initial orbital period of around 5 min. For the plots in upper panel have been past around one orbital period of the initial binary system, 300 seconds, and for the plots of the bottom panel, the time correspond to about 24 minutes from the beginning of the simulation. The vertical panels correspond to different values for the ξ parameter in equation 5.15, from the second to the fourth it is: 0.1, 0.5 and 1.0. In the simulation label j_isco have been allow the star accretes just the particles that has an angular momentum smaller than the one it has in the star last stable orbit.

Table 5.6.: NS companion final state

Progenitor $M_{\rm ZAMS}$	η	ξ	$\Delta M_{\rm acc}$ $M_\odot$	$\Delta l_{\rm acc}$ $c/(GM_\odot^2)$	$m_{\rm bound}$ $M_\odot$	$a_{\rm orb}$ 10^{10} cm
$25M_\odot$	1.0	$j_{\rm isco}$	0.011	0.0097	0.00238	14.96
		0.1	0.078	4.746	0.081	8.11
		0.5	0.171	31.921	4.97×10^{-3}	9.78
		1.0	0.211	42.148	1.31×10^{-3}	48.87
	0.7	$j_{\rm isco}$	0.049	0.087	0.077	1.724
		0.1	0.659	7.765	0.1603	1.021
		1.0	0.633	225.64	4.53×10^{-3}	1.575
$30M_\odot$	2.0	0.1	0.077	7.846	5.6×10^{-3}	–
	2.0	1.0	0.172	22.166	5.3×10^{-4}	–
$40M_\odot$	0.8	0.1	0.457	30.147	0.0165	–
	0.8	1.0	0.545	56.835	7.03×10^{-3}	–

5.6. Consequences on GRB analysis

We have recently addressed in Ruffini et al. [247] the essential role of X-ray flares in differentiating and act as separatrix between the BdHN model and the collapsar-fireball model of GRBs [310]. Previous works show that gamma-ray spikes in the prompt emission occur at 10^{15}–10^{17} cm from the GRB site with Lorentz factor $\Gamma \sim 10^2$–10^3. Instead, the analysis of the thermal emission of the X-ray flares in the early (source rest-frame times $t \sim 10^2$ s) afterglow of long GRBs, shows that they occur at radii $\sim 10^{12}$ cm and expand mildly-relativistically with $\Gamma \lesssim 4$ [247]. These model independent observations are in contrast with an ultra-relativistic expansion all the way from the GRB prompt emission to the afterglow, as traditionally adopted in the majority of the GRB literature.

Based on the SN ejecta profiles obtained in our previous simulations of BdHNe [13], we have shown in Ruffini et al. [247] [see also 176] that, within the BdHN model, the collision of the initial e^+e^- plasma of the GRB with the SN ejecta occurs at 10^{10} cm and reaches transparency at 10^{12} cm with $\Gamma \lesssim 4$. This result shows the agreement of the BdHN scenario with the X-ray flares observations.

The new set of 3D simulations presented in this work serves to perform new simulations of the dynamics of the e^+e- plasma, relativistically expanding from the newborn BH and impacting onto the SN ejecta, then expanding as a baryon-loaded plasma all the way to the reach of transparency. This process will have different signatures along the different directions around the newborn BH in view of the SN density asymmetries, both along the orbital plane itself or between it and the orthogonal ones. Our results show that, indeed, there is a region of poor baryon pollution created by the accretion process where the e^+e^- plasma can reach ultra-relativistic velocities with $\Gamma \sim 10^2$–10^3 that explains the prompt emission being emitted at 10^{15}–10^{17} cm from the GRB site. The analysis of the expansion of the e^+e^--baryon plasma along all the other directions will be essential for the explanation of the additional light-curve and spectral properties of the X-ray flares, of the gamma-ray flares, as well as of the GeV emission of BdHNe (Aimuratov, et al., to be submitted).

On the other hand, we have evaluated in our simulations if the binary holds gravitationally bound or it becomes unbound by the SN explosion. Therefore, we are determining the space of initial binary and SN explosion parameters leading to the formation of νNS-NS or νNS-BH binaries. This topic is of relevance for the connection between long and short GRBs and their relative density rate and will be the subject of forthcoming works.

5.7. Conclusions and perspectives

We have performed the first full numerical 3D simulations of the IGC scenario: in a $\mathrm{CO_{core}}$-NS binary system, the $\mathrm{CO_{core}}$ collapses and explodes in a SN triggering a hypercritical accretion process onto the NS companion. The initial conditions for the simulations were constructed as follows. The $\mathrm{CO_{core}}$ stars are evolved using the KEPLER evolution code [112] until the conditions for the collapse are met. Then, the stars are exploded with the 1D core-collapse code [84]. When the forward SN shock reaches the stellar radius, we map the explosion to a 3D-SPH configuration and continue the evolution of the SN expansion with a NS binary companion using the SNSPH code [89].

We followed the evolution of the SN ejecta, including their morphological structure, under the action of the gravitational field of both the new NS νNS and the NS companion. We estimated the accretion rate onto both stars with the aid of Equation (5.27). The baryonic mass-accretion rates are calculated from the mass of the SPH particles accreted. We have seen a formation of a kind of disk around the NS companion from the simulations (e.g. see Figure 5.2), the angular momentum rate are determined assuming the particles are accreted from the last stable orbit.

We determined the fate of the binary system for a wide parameter space including different $\mathrm{CO_{core}}$ masses (see table 5.1), orbital periods and SN explosion geometry and energies. We evaluate, for selected nuclear EOS of NSs, if the accretion process leads the NSs either to the mass-shedding limit, or to the secular axisymmetric instability for gravitational collapse to a BH, or to a more massive, fast rotating, but stable NS. We assess if the binary holds gravitationally bound or it becomes unbound by the SN explosion. With this information we determined the space of initial binary and SN explosion parameters leading to the formation of νNS-NS or νNS-BH binaries.

In order to generate a high accretion rate on the NS companion, we have shown that the energy of the SN explosion needs to be high enough, otherwise the particles will not be able to escape from the νNS gravitational field, i.e. a considerable amount of gas will do fallback inducing the collapse of νNS instead of the NS companion. On the other hand, we have shown that the SN energy can not be so high, in this case the SN ejecta will pass the NS companion being almost unperturbed by the NS gravitational field. Weak SNe does not produce an appreciable increment in the NS accretion-rate but it longer the time of the accretion at high rate making the total accreted mass to be larger for the weaker SN explosions.

In general, the probability that the binary system after the SN event becomes disrupted decreases with the accretion of mass by the binary stars. Then, for the most massive progenitors of the $\mathrm{CO_{core}}$ (e.g. $M_{\rm ZAMS} = 40\,M_\odot$) and the wider binary initial configurations, we expect that the binaries will be disrupted when the $\mathrm{CO_{core}}$ collapses and the SN is launched. This can be easily explained since the initial binary period scales the accretion rate, tighter orbits developed higher accretions, and a massive progenitor will eject more mass in the SN.

Finally, we discussed in section 5.6 some of the consequences of our simulations in the analysis of long GRBs. Recent results on the thermal emission of the X-ray flares in the early (source rest-frame times $t \sim 10^2$ s) afterglow of long GRBs show that they occur at radii $\sim 10^{12}$ cm and expand mildly-relativistically with $\Gamma \lesssim 4$. This was shown to be agreement with the BdHNe of the IGC scenario [see 247, and section 5.6 above for details]: the e^+e^- plasma of the GRB, relativistically expanding from the newborn BH, collides with the SN ejecta at distances of the order of 10^{10} cm, to then reach transparency at 10^{12} cm with $\Gamma \lesssim 4$. The 3D simulations presented in this work will be essential to explore the dynamics of the e^+e^- plasma along all spatial directions and to estimate, as a function of the viewing angle, the light-curve and spectral properties of BdHNe.

These 3D numerically simulations constitute a step forward in the understanding of the IGC scenario. However, there are many aspects that could be implement in the SPH code in future studies. In other to reduce the uncertainties on the ξ parameter, the simulation of accretion process could be improved if the physics needed to model the disc formed around the NS companion are introduced, e.g. an α-viscosity formalism. On the other hand, in these simulations, we have modeled the binary star as point particles. If they can be modelled as 3D objects, would be possible to follow the particles until its incorporation on the star and study also the hydrodynamics closed to the NS surface as well as study the structure evolution of the accreting stars.

6. The Spin Evolution of Fast-Rotating, Magnetized Super-Chandrasekhar White Dwarfs in the Aftermath of White Dwarf Mergers

6.1. Introduction

Type Ia supernovae (SNe Ia) are one of the most energetic explosive events in the cosmos. Since there is a well established relationship between their intrinsic brightnesses and the shapes of their light curves [206] and, moreover, because they are so luminous that they can be detected at very large distances, SNe Ia can be used as as standardizable cosmological candles. This has opened a new era in cosmology, and has enabled us to measure the acceleration of the universe [205, 225]. Additionally, SNe Ia play an important role in modern cosmology, since they allow us to probe the fundamental physical theories underlying dark energy – see, for instance, [305] for a recent review on this interesting topic.

Nevertheless, despite the importance of SNe Ia, we still do not know the nature of their progenitor systems. Actually, this has remained a long-standing mystery for various decades. We do know that the outburst is driven by the explosion of a carbon-oxygen white dwarf in a binary system, but we do not know the precise mechanism that destabilizes the white dwarf. Several hypothesis have been put forward over the years, and most likely SNe Ia may have a diversity of progenitors. In the following we superficially describe the possible evolutionary channels leading to a SN Ia. In the so-called single-degenerate channel (SD) a white dwarf in a binary system accretes matter from a non-degenerate companion, and explodes as it approaches the Chandrasekhar limiting mass – see, for instance, [109] for a recent discussion. In the double-degenerate scenario (DD) two white dwarfs members of a close binary system lose angular momentum and energy through the radiation of gravitational waves, and a merger occurs [124, 304]. Another possible scenario is the core-degenerate scenario (CD). Within this formation channel a hot core is formed at the end of the common envelope phase of the binary system [142, 162], and the merger of the core of the asymptotic giant branch (AGB) star and a secondary white dwarf powers the explosion – see [8] for a simulation of the merger process. Another recently proposed pathway is the white dwarf-white dwarf collisional scenario, in which two white dwarfs collide – see [7] for a recent summary of the relevant literature on the subject. Despite some attractive features of this scenario, it has been shown that it can only account for at most a few per cent of all SNe Ia [125]. Each of these formation channels has its own advantages and drawbacks, and in some cases these are severe. Currently, one of the most favored ones is the DD channel, because it provides adequate answers to two important observational facts, namely the absence of hydrogen in the nebular phase [158], and the delay time distribution [288]. Consequently, we focus on it.

Smoothed Particle Hydrodynamics (SPH) simulations of the coalescence of binary white dwarfs show that a prompt explosion is not always the result of the interaction during the dynamical phase of the merger [164, 317]. Only those binary systems in which both the secondary and primary stars are massive enough lead to a SN Ia outburst. Actually, the parameter space for violent mergers is very narrow [201, 254], and only when two carbon-oxygen white dwarfs of masses larger than $\sim 0.8\, M_\odot$ merge the result of the dynamical phase is a prompt explosion. Within this theoretical framework, the dynamical phase of the merger is followed by a second phase in which the material of the debris region can be accreted and possibly lead to a SN Ia explosion.

The existing simulations of the coalescence of binary white dwarfs [17, 54, 164, 220, 325] show that the final result of the coalescence consists of a central white dwarf made of the undisrupted primary star and a hot, convective corona made of about half of the mass of the disrupted secondary. This central remnant is surrounded by a heavy Keplerian disk, made of the rest of the mass of the disrupted secondary, since little mass is ejected from the system during the merger episode. The rapidly-rotating, hot corona is convective and an efficient $\alpha\omega$ dynamo can produce magnetic fields of up to $B \approx 10^{10}$ G [96]. Recent two-dimensional magneto-hydrodynamic simulations of post-merger systems confirm the growth of the white dwarf magnetic field after the merger [141, 326]. Thus, the role of magnetic fields in the aftermath of the dynamical merger needs to be explored. This is precisely the aim of the present work, as very few studies [15, 141, 153] of the post-merger evolution including magnetism has been done so far. On the other hand, there are few works that explore the evolution of the post-merger systems but without considering the effects of the central remnant magnetic-field – see, e.g., [317], [293], [262], and [259].

This chapter is organized as follows. In Section 6.2 we explain the model of the evolution of the post-merger system. In particular, we describe the torques that act on the central remnant (Section 6.2.1), the structure of the rotating central white dwarf (Section 6.2.2), and its thermal evolution (Section 6.2.3). In Section 6.3 we present the prescriptions adopted to model the accretion rate on the central star. In Section 6.4 we present our choice of initial conditions. Later, in Section 6.5, we discuss extensively the results of our simulations for two prescriptions to compute the accretion rate. Specifically, in Section 6.5.1 we discuss the case in which the accretion rate is obtained employing the cooling timescale, while in Section 6.5.2 we present the results obtained when it is computed using the viscous timescale. Finally, in Section 6.6 we compare with previous works and in Section 6.7 we summarize our major findings, we elaborate on their significance and we present our concluding remarks.

6.2. Numerical setup for the post-merger evolution

Numerical simulations of binary white dwarf mergers indicate that in those cases in which a violent merger does not occur the merged configuration has three distinct regions [17, 54, 106, 164, 220, 325]. First, a central white dwarf that rotates as a rigid solid. On top of it a hot, differentially-rotating, convective corona can be found. This corona is made of matter accreted from the disrupted secondary star. The mass of this region is about half of the mass of the secondary white dwarf. Finally, surrounding these two regions there is a rapidly rotating Keplerian disk, which is made of the rest of the material of the disrupted secondary, since only a small amount of mass is ejected from the system during the coalescence. The evolution of the post-merger configuration depends, naturally, on the mass of the central remnant, which is made of the primary white dwarf and the hot corona, and on the properties of the surrounding disk.

Before entering into details it is important to discuss some timescales, which are relevant to adopt a reasonable approximation for the evolution of the system. The post-merger configuration formed in the coalescence has a clear hierarchy of timescales. First comes the dynamical timescale $t_{\rm dyn} \sim \Omega^{-1}$, being Ω the rotation velocity. This timescale is typically of the order of a few seconds. Next in order of magnitude is the viscous timescale, $t_{\rm visc}$, of the Keplerian disk. This timescale governs the transport of disk mass inwards and of angular momentum outwards. The viscous phase of the evolution is normally followed using the Shakura-Sunyaev α prescription [260]. Adopting typical values van Kerkwijk et al. [293] found that $t_{\rm visc}$ ranges between 10^3 and 10^4 s. However, for the merger remnants studied here we find that the viscous timescales could be significantly shorter, typically 1 s – see Section 6.3.2 . These viscous timescales are a little longer, but of the same order, of the dynamical timescale of the post-merger Super-Chandrasekar WD studied here ($t_{\rm dyn} \sim 0.2 - 0.3\,$s, see Section 6.2.2). Finally, in this set of characteristic times is the thermal timescale of the merger product, $t_{\rm th}$, which is typically much longer and will be discussed in detail for every simulation.

In the following we first discuss the interactions between the remnant and the disk in order to identify the torque that acts on the central remnant and model the evolution of its angular momentum. Then we present how we model the structure of the rotating white dwarf central remnant, as well as its thermal evolution. The fate of the white dwarf depends crucially on the accretion rate in the post-merger phase. Thus, we consider two very different physical scenarios to determine the accretion rate onto the central remnant. In the first of them the accretion rate is determined by the viscous time-scale, whereas in the second scenario the accretion rate is governed by thermal time-scale. These will be discussed in Section 6.3.

6.2.1. Torques on the central remnant

The most commonly employed model of disk evolution is that of Ghosh & Lamb [99]. This model was later improved by Wang [298], and Wang [299]. Within this model the magnetic field of the remnant penetrates the disk in a broad transition zone as a result of the Kelvin-Helmholtz instabilities, turbulent diffusion and magnetic field reconnection. Furthermore, the material of the disk corotates with the star only in a narrow region, and reaches its surface channeled by the magnetic field lines. We assume that the magnetic field of the remnant penetrates the disk up to approximately the Alfvén radius [57]:

$$R_{\rm mag} = \left(\frac{\mu_{\rm WD}^2}{\dot{M}_{\rm disk}\sqrt{2GM_{\rm WD}}}\right)^{2/7}, \tag{6.1}$$

where $\mu_{\rm WD} = B_{\rm WD}R_{\rm WD}^3$ is the magnetic moment of the star, $B_{\rm WD}$ its magnetic field, and $\dot{M}_{\rm disk}$ is the mass flow through the inner radius of the disk, R_0.

The angular momentum per unit mass entering into the magnetosphere of the white dwarf through the inner radius is $l_0 = R_0^2\Omega_{\rm K}^0$, where

$$\Omega_{\rm K}^0 = \left(\frac{GM_{\rm WD}}{R_0^3}\right)^{1/2} \tag{6.2}$$

is the Keplerian angular velocity at R_0. This material is channeled by the magnetic field onto the surface of the remnant. Thus, the resulting spin-up torque on the star due accretion of disk matter is given by:

$$T_{\rm acc} = \xi_{\rm acc}\dot{M}_{\rm WD}R_0^2\Omega_{\rm K}(R_0), \tag{6.3}$$

where $\dot{M}_{\rm WD} = \varepsilon\dot{M}_{\rm disk}$ is the mass accretion rate on the white dwarf, ε measures how efficient accretion is, and $\xi_{\rm acc}$ is a parameter that accounts for the deceleration of the accreted matter in the inner region of the disk. The values adopted for these two parameters will be discussed below. If the star rotates faster than the matter at the inner disk radius, the centrifugal barrier blocks this material. Hence, it cannot reach the surface of the newly born white dwarf. This matter is therefore ejected from the system. This happens when the inner edge of the disk moves beyond the corotation radius, that is beyond the distance at which the disk rotates with the same angular velocity of the central object:

$$R_{\rm co} = \left(\frac{GM_{\rm WD}}{\Omega_{\rm WD}^2}\right)^{1/3}. \tag{6.4}$$

When $R_0 > R_{\rm co}$, the system enters into the dubbed *propeller regime* [126]. During this phase, the material reaching the magnetosphere is ejected with higher specific angular momentum that the one it had previously, thus resulting in a spin-down torque acting on the star. This torque is given by [178]:

$$T_{\rm prop} = \sqrt{GM_{\rm WD}R_0}\dot{M}_{\rm disk}\left(1-\omega_{\rm f}\right), \tag{6.5}$$

In this expression we have introduced the so-called *fastness parameter*:

$$\omega_{\rm f} = \Omega_{\rm WD}/\Omega_{\rm K}(R_0) = (R_0/R_{\rm co})^{3/2} \tag{6.6}$$

The rotating magnetic field of the star originates an induced electric field that results in a wind. The wind fills the magnetosphere and corotates with the star [102]. At the light-cylinder, $R_{\rm lc} = c/\Omega_{\rm WD}$, the corotation velocity reaches the speed of light, delimiting the region within which corotation of the magnetosphere is enforced. At larger distances, the field lines become open. For the spin-down torque due to electromagnetic energy losses in a force-free magnetosphere, $T_{\rm dip}$, we adopt the result of [273]:

$$T_{\rm dipole} = k_1 \frac{\mu_{\rm WD}^2 \Omega_{\rm WD}^3}{c^3}(1 + k_2 \sin^2\theta), \tag{6.7}$$

with $k_1 = 1 \pm 0.05$ and $k_2 = 1 \pm 0.1$, and θ is the angle between the magnetic moment and the rotation axis of the star.

Finally, an additional torque, $T_{\rm mag}$, results from the interaction of the disk with the magnetic field of the white dwarf. According to Ghosh & Lamb [99], matter of the disk moving in the magnetic field of the white dwarf generates currents that confine the stellar field inside the disk. The magnetic field threading the disk is $\vec{B}_{\rm disk} = \eta \vec{B}_{\rm WD}^{\rm p}$, where $\vec{B}_{\rm WD}$ is the magnetic field of the white dwarf, $\vec{B}_{\rm WD}^{\rm p}$ is its projection on the plane of the disk, and $\eta \leq 1$ is the screening coefficient which accounts for the effect of currents in the partially diamagnetic disk induced by the stellar field. In particular, the poloidal field induces an azimuthal current due to the radial motion of the plasma, that partially screens the stellar magnetic field. Also, the relative motion between the disk and the star magnetosphere generates a toroidal field, B_ϕ. In the simulations, we have considered that the growth of B_ϕ is limited by diffusive decay due to turbulent mixing within the disk [299]. Following the analytical formulation of Wang [301], the magnetic torque acting on the central star due to its interaction with the disk is given by:

$$T_{\rm mag} = \frac{\Gamma \eta^2 \mu_{\rm WD}^2}{R_0^3}\left[\frac{2h}{R_0}(1-\omega_f)\sin^2\theta + \frac{\cos^2\theta}{3}(1-2\omega_f)\right], \tag{6.8}$$

with $h \ll 1$ the thickness of the disk, and $\Gamma \simeq 1$ is a parameter that characterizes the steepness in the vertical transition from Keplerian rotation inside the disk to corotation with the star at the top of the disk. In the derivation of equation (6.8), the magnetic field of the white dwarf has been approximated as a dipole and it was assumed that the rotating axis of the star is perpendicular to the plane of the disk. Note that this expression generalizes the models of Wang [298, 299].

Based on this, the post-merger evolution of the angular momentum of the white dwarf is the result of the combined effect of the dipole radiation torque, $T_{\rm dipole}$, the accretion torque, $T_{\rm acc}$, the disk-interaction torque, $T_{\rm disk}$, and the propeller torque $T_{\rm prop}$:

$$\dot{J}_{\rm WD} = \begin{cases} T_{\rm acc} & R_{\rm WD} > R_0 \\ \\ T_{\rm acc} + T_{\rm dipole} + T_{\rm mag} & R_{\rm WD} < R_0 \wedge \omega_{\rm f} \leq 1 \\ \\ T_{\rm dipole} + T_{\rm prop} & R_{\rm WD} < R_0 \wedge \omega_{\rm f} > 1 \end{cases} \tag{6.9}$$

In the simulations presented here we assumed that the inner disk radius is the Alfvén radius.

6.2.2. Rotating white dwarf configurations

We follow the evolution of the spin of the post-merger remnant calculating at every timestep the new stable rotating configuration with mass, $M_{\rm WD} + \delta M$, and angular momentum, $J_{\rm WD}+\delta J$, adopting the slow rotation approximation [110, 111]. We also assumed that the central remnant product of the merger rotates as a rigid body, as predicted by detailed SPH simulations [164]. The equation of state of the white dwarf is assumed to be that of a zero temperature degenerate electron gas [42], to which we add the corresponding contribution of ions.

The region of stability of uniformly rotating white dwarfs is bound by the secular axisymmetric instability limit, the mass-shedding or Keplerian limit, and the inverse β-decay instability limit, that for pure carbon is $3.49 \times 10^{10}\,{\rm g\,cm}^3$ [30, 226].

Figure 6.1 shows the mass-central density relation for the general relativistic uniformly rotating white dwarfs: the static, Keplerian, secular axisymmetric instability and inverse β-decay sequences enclose the stability region. The mass-shedding, or Keplerian, limit is reached when the angular velocity of the star equals the Keplerian velocity of a particle orbiting at the equator, namely when the centrifugal and gravitational forces are balanced. In this situation matter at the surface of the star is marginally bound to it. Hence, small perturbations result in mass loss until the star becomes either stable again or arrives to a dynamical instability point [263, 275]. If the white dwarf crosses the β-decay instability limit, electrons are captured by nuclei. Since the principal contribution to the pressure of the star comes from electrons, electron captures reduce the pressure, leading to an instability [253]. The secular axisymmetric instability arises because the star is unstable with respect to axisymmetric perturbations. In a first phase, the star is expected to evolve quasi-stationarily with the instability growth timescale, which depends on the time required for angular momentum to be redistributed either by viscous dissipation, or by the emission of gravitational waves [43]. This timescale is typically long compared to the dynamical timescale [30], except in the non-rotating case where they are equal, because in this case there is no angular momentum to be redistributed. Eventually, when the star crosses the dynamical instability limit, gravitational collapse takes place [275]. A sufficient (but not necessary) condition for the onset of secular instability can be obtained using the turning-point method Friedman et al. [76]. This method considers a sequence of uniformly rotating models of a given (constant) angular momentum. The secular axisymmetric instability sets in at the density of the turning-point:

$$\left(\frac{\partial\, M(\rho_c, J)}{\partial\, \rho_c}\right)_J = 0. \tag{6.10}$$

Finally, the maximum mass of static configurations is the Chandrasekhar limiting mass $M_{\rm max} = M_{\rm Ch} \approx 1.4\,M_\odot$, while the maximum mass of rotating white dwarfs lies on the Keplerian sequence $M_{\rm max}^{J\neq 0} = 1.52\,M_\odot$. The configurations with mass between $M_{\rm max}^{J=0} < M_{\rm WD} < M_{\rm max}^{J\neq 0}$ are called super-Chandrasekhar white dwarfs, and are metastable since they are supported by rotation. As the angular momentum of the star varies the central white dwarf necessarily evolves towards one of the previously described instability limits (mass-shedding or secular axisymmetric instability).

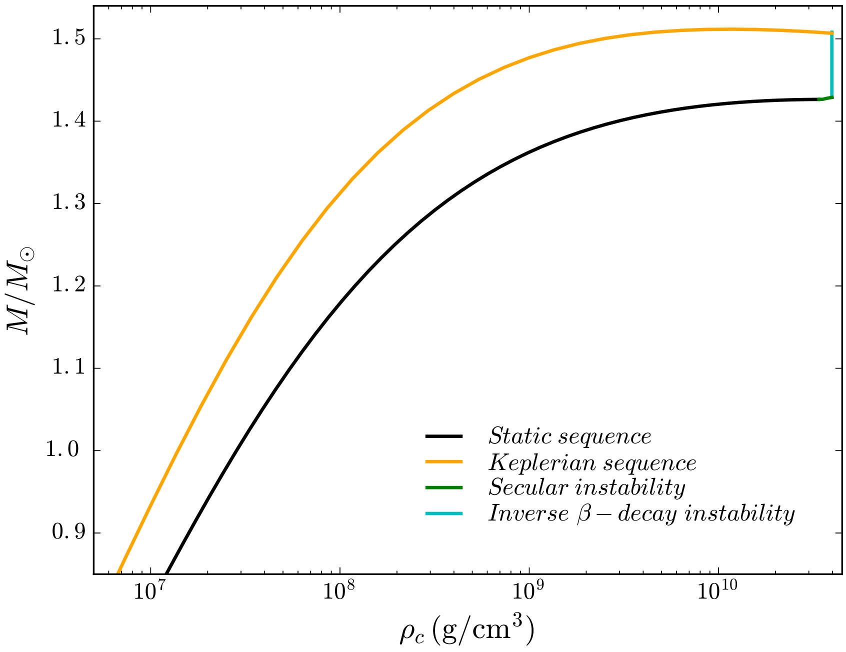

Figure 6.1: Instability lines of rotating white dwarfs in the diagram of mass versus central density. The stability region is delimited by the static sequence (black line), the Keplerian sequence (orange line), the line of secular instability (green line), and the inverse β-decay line (blue).

6.2.3. Temperature of the central remnant

We turn now to the thermal evolution of the central white dwarf remnant. We have seen above in sections 6.2.1 and 6.2.2, and we shall see below from the energy balance and transport equations, that the structure and thermal evolution of the white dwarf depend crucially on the accretion rate, which is set by the disk physics. In section 6.3 we analyze the evolution and fate of the post-merger system for two physical prescriptions to set the accretion rate. In the first case the infall rate is driven by the disk angular-momentum transport (viscous) timescale which, owing to its shortness for the present binary parameters, leads to highly super-Eddington rates. It has been argued in the literature that the dissipation required to produce such very short viscous timescales might heat the disk to the point of carbon ignition [see, e.g., 186]. Such effects are not accounted for in the disk model we adopt in this work. In order to account for the possibility that the disk self-regulate avoiding very high accretion rates, we evaluate a second case in which the matter infall is driven by the cooling timescale. We show that this assumption leads to infall rates near the Eddington limit value.

The thermal evolution of an accreting white dwarf has been studied by many authors [196, 250, 317]. The main goal of most of these works was to establish whether the conditions that may lead to a type Ia supernova were reached. For instance, in a pioneering work Nomoto & Iben [196] found that for accretion rates larger than a critical value $\dot{M}_{\rm crit} \approx 2\times 10^{-6}\,M_\odot\,{\rm yr}^{-1}$, the outer layers of the star are heated by mass accretion, while heat conduction and neutrino emission cool it. This results in a thermal inversion near the surface of the star, and ultimately leads to an off-center carbon ignition. Saio & Nomoto [250] followed the subsequent evolution of the star and determined that carbon is burned in the entire white dwarf, being the final outcome an oxygen-neon white dwarf. However, these works only considered non-rotating configurations and constant accretion rates. More recently, Yoon et al. [317] studied the viscous evolution of remnants of white dwarf mergers introducing the effects of rotation but did not consider the effects of the magnetic field of the white dwarf. The post-merger object was modeled as a differentially rotating white dwarf with a cold core and a hot envelope accreting mass from a surrounding Keplerian disk at a constant rate. This allowed them to compute the conditions under which the off-center ignition can be avoided for the case in which the magnetic field is not taken into account

We have explained above (see Sect. 6.2.1) how the rotation rate of the merged remnant evolves due to the interaction of the magnetic field and the disk, and which are the equilibrium configurations of the the rotating white dwarf. However, during the course of the evolution the temperature of the white dwarf also changes due to accretion from the disk, which heats the white dwarf interior. This, in turn, may trigger a type Ia supernova explosion. In order to assess this possibility, we follow the evolution of the interior temperature of the post-merger central white dwarf in an approximate way, which is described next.

The equation of energy conservation reads:

$$\frac{dL}{dm} = \epsilon_{\rm nuc} - \epsilon_\nu + T\dot{s}, \tag{6.11}$$

where m is the mass coordinate (i.e., the mass enclosed within the radial distance r), L is the luminosity, T the temperature, s the specific entropy, and $\epsilon_{\rm nuc}$ and ϵ_ν are the energy release and energy loss per unit mass by nuclear reactions and neutrino emission, respectively.

For carbon-oxygen white dwarfs, thermonuclear energy is essentially released by two nuclear reactions:

$$\begin{aligned} {}^{12}\mathrm{C} + {}^{12}\mathrm{C} &\rightarrow {}^{20}\mathrm{Ne} + \alpha + 4.62\,\mathrm{MeV}, && (6.12)\\ {}^{12}\mathrm{C} + {}^{12}\mathrm{C} &\rightarrow {}^{23}\mathrm{Na} + \mathrm{p} + 2.24\,\mathrm{MeV}, && (6.13) \end{aligned}$$

with nearly the same probability. We adopted the carbon fusion reaction rates of Gasques et al. [97], which are valid for all regimes of ρ and T, that is from the thermonuclear regime to the pynonuclear regime. For the neutrino energy losses, we used the analytical fits of Itoh et al. [128], which consider electron-positron pair annihilation ($e^-e^+ \rightarrow \nu\bar{\nu}$), photo-neutrino emission ($e + \gamma \rightarrow e\nu\bar{\nu}$), plasmon decay ($\gamma \rightarrow \nu\bar{\nu}$), and electron-nucleus bremsstrahlung [$e(Z,A) \rightarrow e(Z,A)\nu\bar{\nu}$]. As it will be discussed in below, the dominant channel for neutrino losses in the central regions is electron-nucleus bremsstrahlung, while in the outer layers, emission of neutrinos is dominated by plasmon decay.

The energy flux is given by:

$$\frac{dT}{dr} = -\frac{3}{16\sigma}\frac{\kappa\rho}{T^3}\frac{L}{4\pi r^2}, \tag{6.14}$$

where σ is the Stephan-Boltzmann constant and κ is the opacity, which can be written as:

$$\frac{1}{\kappa} = \frac{1}{\kappa_{\rm cond}} + \frac{1}{\kappa_{\rm rad}}, \tag{6.15}$$

with $\kappa_{\rm rad}$ and $\kappa_{\rm cond}$ the Rosseland mean radiative opacity and the conductive opacity, respectively. In the white dwarf core degeneracy is so high that the most efficient transport mechanism is conduction. Hence, the opacity is dominated by the first term. We adopted the thermal conductivity of Itoh et al. [130, 134], whereas for the radiative opacity we used Kramer's law, $\kappa_{\rm rad} = 4.34 \times 10^{24} \rho T^{-3.5}$ cm^2 g^{-1}.

The change of entropy with time can be obtained from:

$$T\dot{s} = c_v \dot{T} - \left[\frac{P}{\rho^2} - \left(\frac{\partial u}{\partial \rho}\right)_T\right]\dot{\rho} \tag{6.16}$$

where u is the specific internal energy and c_v the specific heat capacity at constant volume. The first term of the right-hand side of Eq. (6.16) corresponds to the release of the internal energy, while the second term accounts for the change of gravitational potential energy due to the expansion or compression of the configuration.

To evaluate the term in square brackets in Eq. (6.16) we considered a fully ionized non-ideal electron-ion plasma, taking into account the ion-ion and the ion-electron Coulomb interactions, and also the exchange-correlation corrections of electrons. We note that for super-Chandrasekhar white dwarfs both Coulomb corrections and quantum effects are important. The importance of Coulomb corrections is measured by the Coulomb coupling parameter $\Gamma = Z^2 e^2/(aT)$, where $a = (3/(4\pi n_i)^{1/3}$ is the mean interaction distance and n_i the ion number density. At $\Gamma \lesssim 1$ the ions behave as a gas, at $\Gamma > 1$ as a strongly coupled Coulomb liquid, while crystallization occurs at $\Gamma \approx 175$. Quantum effects become important at temperatures smaller than $T_{\rm p} = \hbar\omega_{\rm p}/k_{\rm B}$, where $\omega_{\rm p} = (4\pi Z^2 e^2 n_i/m_i)^{1/2}$ is the ion plasma frequency. Finally, we used analytical fits to the heat capacity obtained from the free energy computed by Chabrier & Potekhin [41] and Potekhin & Chabrier [216].

Following Nomoto [194], we obtained the density change by adopting the white dwarf mass coordinate, $q_{\rm WD} \equiv m/M_{\rm WD}$, as the independent variable:

$$\dot{\rho} = \left[\left(\frac{\partial \rho}{\partial M_{\rm WD}}\right)_{q_{\rm WD}} - \frac{q_{\rm WD}}{M_{\rm WD}}\left(\frac{\partial \rho}{\partial q_{\rm WD}}\right)_{M_{\rm WD}}\right]\dot{M}_{\rm WD} \tag{6.17}$$

This equation explicitly provides the contribution of the global structural changes as well as the contribution of the internal distribution of density to the thermal evolution during the accretion process.

The post-merger evolution of the system is computed assuming that the central white dwarf evolves in a sequence of stable configurations (see Sect.6.2.2). To calculate the evolution of the temperature, at each time step we integrate Eqs. (6.11) and (6.14) using Eqs. (6.16) and (6.17).

In order to integrate Eqs. (6.11) and (6.14), a set of boundary conditions at the surface of the star must be adopted. We treat the material accreted in each interval time as a thin envelope surrounding the star. Following Townsley & Bildsten [289], we assume that the accreted material enters on top of the shell and pushes down the existing material deeper into the star. Then, the local heat equation becomes:

$$T\left(\frac{\partial}{\partial t}+v_r\frac{\partial}{\partial r}\right)s \approx T v_r\frac{\partial s}{\partial r}=\frac{dL}{dm}-(\epsilon_{\rm nuc}-\epsilon_\nu) \tag{6.18}$$

where $v_r = \dot{M}_{\rm WD}/(4\pi r^2\rho)$ is the velocity of the material given by mass conservation. We constructed static envelopes for each stable configuration with total mass $M_{\rm WD}$ and radius $R_{\rm WD}$, integrating Eqs. (6.14) and (6.18).

To analyze if the newly formed white dwarf reaches during its evolution the conditions suitable to produce a type Ia we adopted the following procedure. We first require as a necessary condition that the white dwarf crosses the ignition curve, i.e. the curve in the $\log\rho - \log T$ plane where the nuclear energy released becomes larger than the neutrino emissivity, $\epsilon_{\rm nuc} = \epsilon_\nu$. For temperatures and densities beyond this curve nuclear energy production exceeds neutrino losses and the star is heated, possibly leading to a supernova outburst. Additionally, we require that burning proceeds in an almost instantaneous way. The characteristic time $\tau_{\rm CC}$ of nuclear reactions is:

$$\tau_{\rm CC}=\frac{\epsilon_{\rm nuc}}{\dot{\epsilon}_{\rm nuc}}\approx\epsilon_{\rm nuc}\left(\dot{T}\frac{\partial\epsilon_{\rm nuc}}{\partial T}\right)^{-1}=c_p\left(\frac{\partial\epsilon_{\rm nuc}}{\partial T}\right)^{-1}, \tag{6.19}$$

where c_p is the specific heat at constant pressure. If this characteristic timescale becomes shorter that the dynamical timescale

$$\tau_{\rm dyn}^{-1}=\sqrt{24\pi G\rho}, \tag{6.20}$$

the star reaches the thermodynamic conditions necessary to explode as a type Ia supernova.

6.3. Mass accretion rate on the central remnant

As mentioned before, the accretion rate onto the post-merger central remnant can be computed in two different ways. Within the first approximation, the accretion rate is set by the thermal state of the envelope of the white dwarf [317]. Within the second one the central remnant accretes mass from a thin Keplerian disk and its evolution is given by the viscous time-scale – see [293] but also [141]. Since, due to the lack of full numerical analyses of this process with realistic physical ingredients, it is not yet clear which one of these treatments is more appropriate, we will calculate the evolution of the central white dwarf remnant adopting both prescriptions and we will discuss the differences between both sets of calculations. In both cases we are interested in determining the long-term evolution central white dwarf taking into account the interaction between the disk and the magnetic field resulting from the merger. To handle this problem, we adopt a simplified picture of the post-merger system consisting of a magnetized rotating white dwarf surrounded by a thin Keplerian disk.

6.3.1. Accretion rate set by the thermal timescale

As discussed by Yoon et al. [317], the assumption that the accretion timescale is set by the viscous time-scale given by the Shakura-Sunyaev α prescription could be inappropriate to estimate the accretion timescale onto the newly-formed white dwarf since the structure of the merged system deviates from a central, point-like mass surrounded by a thin disk that is the central assumption adopted within the α-formalism. Yoon et al. [317] argued that under these conditions the relevant timescale might be the cooling timescale of the low density envelope between the central object and the disk. If the relevant timescale is the cooling timescale of the envelope of the post-merger white dwarf, the accretion rate will be given by:

$$\dot{M}_{\rm WD} = \frac{M_{\rm disk}}{\min(\tau_\nu, \tau_{\rm thermal})} \tag{6.21}$$

where $M_{\rm disk}$ is the total mass of the disk, and τ_ν and $\tau_{\rm thermal}$ are the neutrino cooling time and the thermal time on the envelope of the white dwarf, respectively. These two timescales are given by:

$$\tau_\nu = \frac{c_{\rm v}}{\epsilon_\nu} T_S \bigg|_S , \tag{6.22}$$

and

$$\tau_{\rm thermal} = \frac{3}{64\sigma}\left(\int_{\Delta r}\left(\frac{\kappa c_v}{T^3}\right)^{1/2}\rho\, dr\right)^2 , \tag{6.23}$$

[113, 208], where c_v is the heat capacity at constant volume, κ is the opacity, ϵ_ν is the energy release by the neutrino emission and Δr delimits the region of interest – see Sect. 6.2.3 for a discussion of the thermal properties of the white dwarf.

For the values typical of the post-merger white dwarf ($\rho = 10^6$ g/cm^3 and $T = 10^8$ K), the neutrino luminosity will be $L_\nu \sim 10^2\, L_\odot$ and the thermal energy will be of $U \sim 10^{48}$ erg. At the beginning of the simulations the neutrino cooling timescale is about $\tau_\nu \sim 6 \times 10^5$ yr while the thermal timescale is $\tau_{\rm thermal} \sim 10^6$ yr. Then, the initial accretion rate is about $\dot{M}_{\rm WD} \sim 10^{-7}\, M_\odot$ yr^{-1}, close to the Eddington limit.

6.3.2. Accretion rate set by the viscous timescale

Numerical simulations – see, e.g., [17], Lorén-Aguilar et al. [164] and [55] – show that the disk product of the coalescence of two white dwarfs of unequal masses is not thin, although it is not thick either. Specifically, Lorén-Aguilar et al. [164] found that the thickness of the newly formed disk is $H \sim 5.0 \times 10^{-3}\ R_\odot$, while the typical size is $R_{\rm disk} \sim 0.2\ R_\odot$ – see their Table 1. Hence, $H/R_{\rm disk} \simeq 0.025$. Thus, assuming that the disk is thin is not an extreme assumption and, in the worst of the situations, it can be considered as a limiting case. Obviously, the other limiting case is to assume that the disk is thick. Here we assume that the disk is thin, and we postpone the study of a thick disk to a forthcoming publication.

For a thin, Keplerian accretion disk, the evolution of the surface mass density, Σ, is given by the diffusion equation:

$$\frac{\partial \Sigma}{\partial t} = \frac{3}{r}\frac{\partial}{\partial r}\left[r^{1/2}\frac{\partial}{\partial r}\left(\nu \Sigma r^{1/2}\right)\right], \tag{6.24}$$

where ν is the turbulent kinematic viscosity. To describe the time evolution of the disk we use one of the three self-similar solutions of Eq. (6.24) found by Pringle [218]. These solutions are obtained for an opacity parametrized as $\kappa = \kappa_0 \rho^a T^b$. Within this approximation mass is accreted onto the central white dwarf, but the angular momentum of the disk is conserved, $J_{\rm disk} = J_0$, because the outer edge of the disk moves outwards – see Eq. (6.26). In a general case $J_{\rm disk}$ would not be conserved because there is a trade-off of angular moment between the disk and the central white dwarf. However, since the angular moment of the white dwarf, $J_{\rm WD}$, is much smaller than that of disk, this solution is accurate enough for the purpose of estimating the accretion rate onto the white dwarf. Actually, we have checked that at all times $J_{\rm WD}/J_{\rm disk} < 0.1$ in our simulations.

Within this approximation mass flows at the inner disk boundary at a rate

$$\dot{M}_{\rm disk} = \frac{(\beta-1)M_0}{t_{\rm visc}}\left(1+\frac{t}{t_{\rm visc}}\right)^{-\beta}, \tag{6.25}$$

and the disk outer radius evolves as

$$R_{\rm out} = r_0\left(1+\frac{t}{t_{\rm visc}}\right)^{2\beta}, \tag{6.26}$$

where M_0 and J_0 are, respectively, the initial mass and angular momentum of the disk, $j_0 = J_0/M_0$, $r_0 = 3.88\, j_0^2/(GM_0)$, and β is a constant that depends on the opacity regime. Here we have adopted a bound-free opacity ($\beta = 5/4$). In equations (6.25) and (6.26), $t_{\rm visc}$ is a constant of the model related to the disk viscous time scale at early times. It can be shown [70] that the viscous timescale is then determined by M_0 and j_0:

$$t_{\rm visc} = 9.82\times 10^9 \frac{j_0^{25/7}}{M_{\rm WD}^{10/7} M_0^{3/7}}\left(\frac{\sigma}{\alpha^8 \kappa_0}\right)^{1/7}\left(\frac{\bar{\mu} m_p}{\kappa_B}\right)^{15/14} \tag{6.27}$$

where m_p is the proton mass and μ the mean molecular weight. Adopting $\alpha = 0.1$ for the viscosity parameter [260] gives:

$$t_{\rm visc} \simeq 10.9\left(\frac{j_0}{10^{18}\,{\rm cm^2\,s^{-1}}}\right)^{25/7}\left(\frac{M_0}{0.1\,M_\odot}\right)^{3/7}\,{\rm s}, \tag{6.28}$$

This solution has been employed to describe debris disks around massive black holes formed by tidal disruption of stars [39] and in supernova fallback disks around young neutron stars [44]. This formulation was also used in Külebi et al. [153] to study the long-term evolution of the disk interaction of magnetized white dwarf resulting from white dwarf mergers that do not develop prompt explosion conditions.

We obtain that the initial conditions of the merged system are such that $t_{\rm visc} \sim 0.2 - 0.8$ s (see Table 6.1). This, in turn, results in accretion rates at early times $\dot{M}_{\rm WD} = M_0/t_{\rm visc} \sim$

$10^{-1}\,M_\odot$ s^{-1} and initial disk outer-radius $R_{\rm out} \sim 0.1 R_\odot$. However, for times longer than $t_{\rm visc}$, the accretion rate drops one order of magnitude and, after 10^2 s, the accretion is $10^{-4}\,M_\odot$ s^{-1}.

In the above equations the disk viscous timescale, $t_{\rm visc}$, is a constant. It is clear from Equation. (6.27) that it is a good approximation for low infall rates because the specific angular momentum would not change appreciably. The above estimate of the accretion rate shows that this is not the present case so we have checked the effect of the assumption of the constancy of $t_{\rm visc}$ on the evaluation of $\dot{M}_{\rm disk}$ as follows. First we compute the accretion rate using Equation (6.25) keeping $t_{\rm visc}$ constant and then allowing it to increase with time owing to the mass loss by the disk. We found that the increase of $t_{\rm visc}$ would lower $\dot{M}_{\rm disk}$ at most by 10% during the evolution. This result assure us about our assumption of a constancy of the viscous timescale on the estimate of the infall rate at the inner disk radius.

6.4. Initial conditions

We compute the post-merger initial configuration assuming that both mass and angular momentum are conserved during the merger. This is a reasonable assumption, since SPH simulations show that very little mass is ejected from the system. Moreover, little angular momentum is carried away by the unbound material, since its velocity is mostly radial. A rough estimate of the degree to which mass and angular momentum are conserved is $J_{\rm ej}/J \sim M_{\rm ej}/M \sim 10^{-3}$ [54, 164]. Consequently, the orbital angular momentum of the coalescing white dwarfs is invested in spinning up the primary white dwarf and in the angular momentum of the rapidly rotating disk.

If the spin angular momentum of the merging white dwarfs is neglected, the total angular momentum just before the merger is:

$$J_{\rm sys} = q\sqrt{\frac{G M_2^3 (R_1 + R_2)}{(1+q)}} \tag{6.29}$$

where (M_1, R_1) and (M_2, R_2) are, respectively, the masses and radii of the merging stars, and $q = M_2/M_1$ is the mass ratio of the original binary system. Figure 6.2 shows the contours of constant angular momentum and of constant total mass in the plane defined by M_1 and M_2. Given an initial total mass and angular momentum of the remnant, $(M_{\rm WD}, J_{\rm WD})$, and an initial disk mass, M_0, we computed the initial angular momentum of the disk, J_0, assuming that the central remnant rotates as a rigid body. To do this we considered that just before the mass transfer episode the orbital separation was such that the secondary was about to fill its Roche lobe, for which we adopted the expression of [69], which is in all the cases close to $R_1 + R_2$. This is the same to say that the merger episode begins when both stars are in contact. We also took into account that according to detailed SPH simulations of the merger process roughly half of the mass of the secondary star goes to form the disk, whereas the rest of the material is directly accreted onto the primary component of the binary system [164].

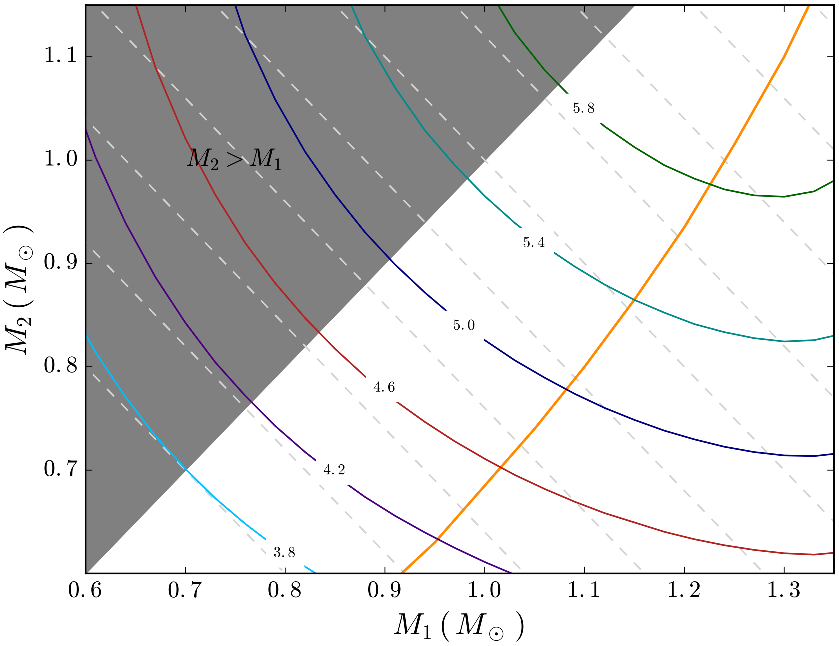

Figure 6.2: Parameter space of the initial white dwarf binary system. Solid lines are contours of constant total angular momentum, labeled in units of 10^{50} g cm^2 s^{-1}. The gray, dotted straight lines are contours of constant total mass, from $1.4\,M_\odot$ to $2.6\,M_\odot$, in steps of $0.1\,M_\odot$. The shaded area corresponds to configuration with $q > 1$. The orange line corresponds to location of the system when the secondary is filling its Roche lobe ($R_2 = R_{\rm L}$).

Nevertheless, given the exploratory nature of the simulations presented here, we did not constrain ourselves to the values obtained in the SPH simulations, and we adopted different values for the mass of the remnant and for the mass of the disk. Since a rigidly rotating white dwarf can support a maximum angular momentum $\lesssim 10^{50}$ g cm^2 s $^{-1}$ [30], angular momentum conservation implies that a substantial fraction of the angular momentum of the binary system goes to the Keplerian disk.

Also, we mention that detailed SPH simulations of non-symmetric white dwarf mergers show that as the less massive white dwarf is disrupted and part of its matter is accreted onto the primary star, the accreted mass is compressed and heated. Thus, for all the cases studied here we have assumed an inverse initial temperature profile. Specifically, we adopted initial temperature profiles similar to those resulting from detailed SPH simulations.

In Table 6.1 we list the initial masses of the stars of the original binary system – columns 2 and 3, respectively – as well as the initial conditions for the models presented in this work. The top section of this table lists the characteristics of the models for which the accretion rate was computed employing the cooling timescale, while the bottom section summarizes the most relevant information of those models computed employing the accretion rate given by the viscous timescale. Note that the mass of the rapidly rotating central white dwarf $M_{\rm WD}$ of all these simulations (listed in column 4) is the same. Since we are modeling white dwarfs as rigidly rotating configurations, only two parameters are needed to determine the remaining characteristics of the merged configuration. Thus, we decided to vary the initial angular velocity $\Omega_{\rm WD}$ and the mass of the disk M_0. These two quantities are listed in columns 8 and 5, respectively. For a super-Chandrasekhar white dwarf of $1.45\,M_\odot$, the minimum angular velocity for the gravitational stability to set in is around 2.03 rad s^{-1}. Note that the angular velocities adopted here are in all cases larger than this value. Once the angular velocity of the white dwarf is known we determine its total angular momentum, $J_{\rm WD}$, which is listed in column 9 of the table, and the radius of the white dwarf, $R_{\rm WD}$, listed in the sixth column. The adopted magnetic field $B_{\rm WD}$

of the white dwarf is given in column 7. The rest of columns of Table 6.1 list the initial angular momentum J_0 (column 10) of the disk, the efficient parameter ε (column 11), that is relevant for estimating the mass accretion rate, the viscous timescale $t_{\rm visc}$, and the cooling timescale of the disk $t_{\rm cool}$ (columns 12 and 13).

In our simulations the magnetic field of the remnant was kept fixed at $B_{\rm WD} = 10^9$ G, a representative value of the magnetic field resulting from the stellar dynamo originated during the coalescence [96]. For the typical values found in the SPH simulations of merging white dwarfs the magnetic field can be as high as $\sim 10^{10}$ G, depending if the dynamo is saturated. However, we decided to adopt a conservative value as a reference magnetic field, 10^9 G. However, we also computed some models with various magnetic field strengths, ranging from 10^6 to 10^9 G. An important point which is worth emphasizing is that for the simulations presented here we assumed that during the merging process an ordered global dipole field is produced. However, this is not guaranteed – see, for instance, the discussion in the conclusions of [259].

6.5. Results

Since the evolution of the post-merger system depends critically on the adopted prescription for the mass accretion rate onto the central white dwarf resulting from the coalescence of the binary system, we discuss the results obtained using the accretion rates described in Sections 6.3.2 and 6.3.1 separately. We first discuss the results obtained using an accretion rate set by the cooling timescale, and subsequently we present the results obtained when the viscous timescale is employed. However, before going into the details a cautionary remark is in order. In particular, we emphasize that small variations in the values of the parameters adopted for the different simulations presented below can lead to substantially different outcomes.

6.5.1. Accretion rate set by the cooling timescale

To start with we discuss our reference model. This is model A in Table 6.1. For this model we adopted a magnetic field $B = 10^9$ G. We note that during the early phases of the evolution of the post-merger remnant the dominant cooling mechanism of the external layers of the central white dwarf is neutrino emission. Therefore, the initial relevant timescale to compute the accretion rate is $\dot{M}_{\rm WD} = M_{\rm WD}/\tau_\nu \sim 10^{20}$ g s^{-1}. This accretion rate is of the order of the Eddington limit. However, in our calculations the evolution of the model is followed self-consistently. That is, we computed the mass accretion rate with the cooling timescale provided by the evolution – see below.

For this model, the magnetospheric radius is $R_{\rm mag} = 0.062\,R_\odot$ and the corotation radius is $R_{\rm co} = 0.0039\,R_\odot$. Thus, $R_{\rm mag} > R_{\rm co} > R_{\rm WD}$, so the dipole radiation torque and the propeller torque drive the evolution of the spin of the remnant. Under these conditions the central object does not accrete matter. To illustrate the evolution, Figure 6.3 shows

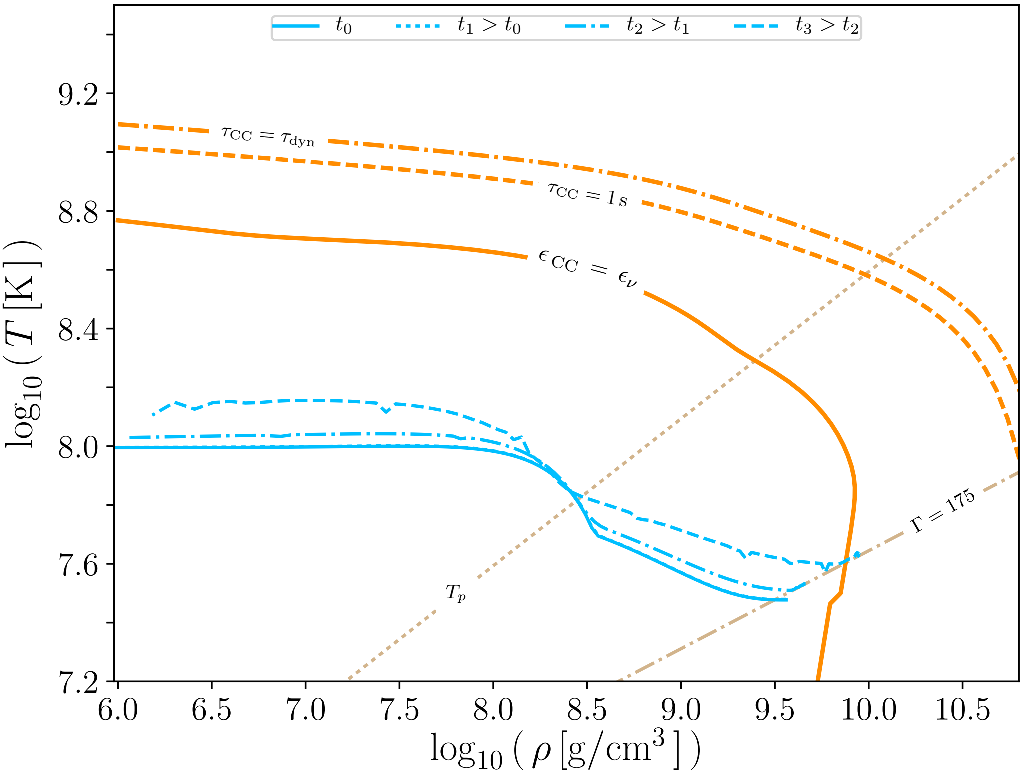

Figure 6.3.: Temperature-density profiles of the central white dwarf at different times of the evolution for model A. This model was computed assuming $B = 10^9$ G and an accretion rate set by the cooling timescale. We also show the carbon ignition line, labeled as $\epsilon_{\rm CC} = \epsilon_\nu$, and two carbon burning timescales $\tau_{\rm CC} = \tau_{\rm dyn}$ and $\tau_{\rm CC} = 1\,\rm s$. In these panels the crystallization curve is labeled as $\Gamma = 175$, and the plasma temperature as $T_{\rm p}$. The configuration at t_1 have a temperature profile almost equal to the initial one. At t_2 and t_3, it heats at the center as well at the surface.

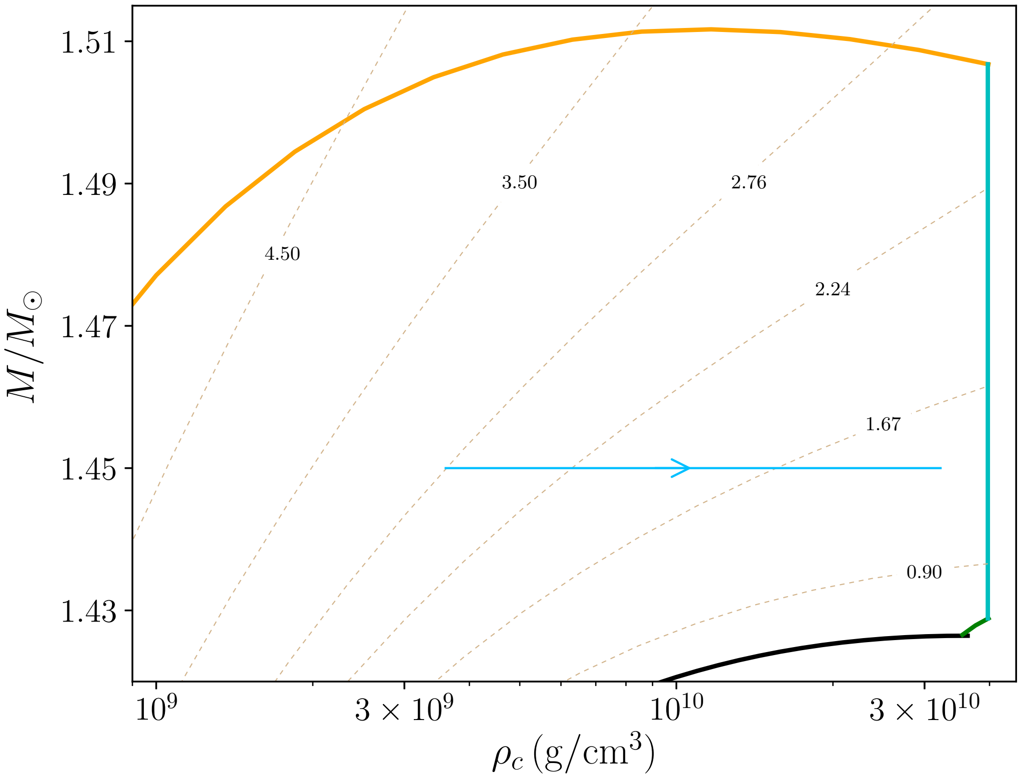

Figure 6.4.: Evolution of model A in the mass-central density plane. The colors of the lines indicating the regions of the various instabilities discussed here are the same shown in Figure 6.1. Also shown are the contours of constant angular momentum (dotted lines).

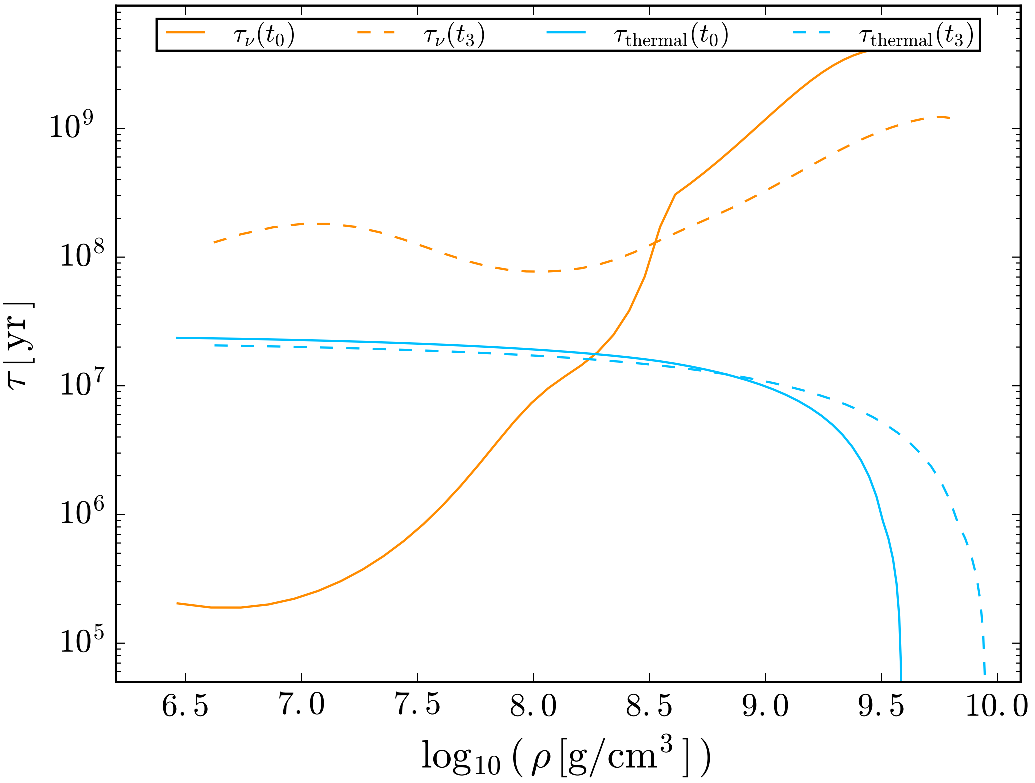

Figure 6.5.: Run of the neutrino and thermal timescales in the interior of model A at selected times, see text for details.

some temperature profiles at selected times. In particular, we show these profiles at times t_0 – corresponding to the beginning of the evolution, solid line – at a time just before the central white dwarf reaches explosive conditions – time $t = t_3$, long dashed line – and at two intermediate stages – times t_1 and t_2, short dashed line and dashed-dotted line, respectively. As can be seen in this figure, during the entire evolution both the central regions and the outer layers of the white dwarf are compressed and heated. These two regions of the white dwarf are separated by the line at which the temperature of the nearly isothermal core equals the plasma temperature, $T_{\rm P}$. This behavior is a consequence of the torques acting on the white dwarf. The acting torques brake the white dwarf, decreasing its angular velocity. As a consequence, the centrifugal force decreases and the gravitational force dominates. Thus, to balance the enhanced gravity the density increases, so does the temperature. Ultimately, the center of the star reaches the thermodynamic conditions needed to burn carbon explosively. These conditions are illustrated in this figure by the curves $\epsilon_{\rm nuc} = \epsilon_\nu$, $\tau_{\rm CC} = \tau_{\rm dyn}$ and $\tau_{\rm CC} = 1$ s. This occurs at time 40.8 yr, just before these regions reach the beta-decay instability limit, and when the central regions of the star are already crystallizing. Figure 6.4 displays the evolution of model A in the mass-central density plane. As can be seen, the evolutionary track corresponds to pure compression, and no matter is accreted. Note as well that carbon in the central regions of the star is ignited before the inverse β-decay instability is reached.

Figure 6.5 shows the run of the neutrino and thermal timescales in the white dwarf interior of model A at two relevant times, namely at times $t = t_0$ and $t = t_3$, as previously defined. As can be seen, for $t = t_0$ neutrinos cool the external layers of the star, while in the internal regions thermal diffusion is the dominant transport mechanism.

Table 6.1.: Parameters of the simulations of post-merger remnants.

Model	M_1 $[M_\odot]$	M_2 $[M_\odot]$	$M_{\rm WD}$ $[M_\odot]$	M_0 $[M_\odot]$	$R_{\rm WD}$ $[R_\odot]$	$B_{\rm WD}$ [G]	$\Omega_{\rm WD}$ $[{\rm rad\,s^{-1}}]$	$J_{\rm WD}$ $[{\rm g\,cm^2\,s^{-1}}]$	J_0 $[{\rm g\,cm^2\,s^{-1}}]$	ε $[-]$	$t_{\rm visc}$ [s]	$t_{\rm cool}$ [yr]
A	1.12	0.78	1.45	0.45	0.0026	10^9	3.00	2.79×10^{49}	5.86×10^{50}	0.1	0.745	2.26×10^4
B	1.12	0.78	1.45	0.45	0.0026	10^6	3.00	2.79×10^{49}	5.86×10^{50}	0.1	0.745	2.26×10^4
C	1.12	0.78	1.45	0.45	0.0026	10^7	3.00	2.79×10^{49}	5.86×10^{50}	0.1	0.745	2.26×10^4
D	1.12	0.78	1.45	0.45	0.0026	10^8	3.00	2.79×10^{49}	5.86×10^{50}	0.1	0.745	2.26×10^4
E	1.12	0.78	1.45	0.45	0.0026	10^9	3.00	2.79×10^{49}	5.86×10^{50}	0.1	0.745	2.26×10^4
F	1.12	0.78	1.45	0.65	0.0026	10^9	3.00	2.79×10^{49}	5.86×10^{50}	0.1	0.253	2.26×10^4
G	1.12	0.78	1.45	0.45	0.0026	10^6	3.00	2.79×10^{49}	5.86×10^{50}	0.1	0.745	2.26×10^4
H	1.12	0.78	1.45	0.45	0.0026	10^9	3.00	2.79×10^{49}	5.86×10^{50}	0.5	0.745	2.26×10^4
I	1.12	0.78	1.45	0.45	0.0039	10^9	2.30	4.56×10^{49}	5.69×10^{50}	0.1	0.668	2.79×10^3
J	1.12	0.78	1.45	0.45	0.0034	10^9	2.50	3.87×10^{49}	5.76×10^{50}	0.1	0.697	5.66×10^3
K	1.12	0.78	1.45	0.45	0.0032	10^9	2.60	3.60×10^{49}	5.78×10^{50}	0.1	0.709	7.79×10^3
L	1.12	0.78	1.45	0.45	0.0030	10^9	2.70	3.35×10^{49}	5.83×10^{50}	0.1	0.719	1.05×10^4
M	1.12	0.78	1.45	0.45	0.0029	10^9	2.80	3.14×10^{49}	5.68×10^{50}	0.1	0.729	1.38×10^4
N	1.12	0.78	1.45	0.45	0.0028	10^9	2.85	2.93×10^{49}	5.68×10^{50}	0.1	0.665	1.57×10^4
O	1.12	0.78	1.45	0.45	0.0028	10^9	2.90	2.93×10^{49}	5.68×10^{50}	0.1	0.737	1.78×10^4
P	1.12	0.78	1.45	0.45	0.0022	10^9	3.50	2.24×10^{49}	5.86×10^{50}	0.1	0.769	5.34×10^4
Q	1.12	0.78	1.45	0.45	0.0017	10^9	4.50	1.75×10^{49}	5.96×10^{50}	0.1	0.793	8.79×10^4

Table 6.2.: Outcome and evolutionary times of the post-merger remnants for several values of the magnetic field strength and initial angular velocity.

Model	$B_{\rm WD}$ [G]	$\Delta\, t$ [yr]							Outcome
$\Omega_{\rm WD}$ $[{\rm s^{-1}}]$		2.3	2.5	2.6	2.7	2.8	2.9	3.0	
A	10^9	5.50×10^1	4.68×10^1	4.33×10^1	4.02×10^1	4.71×10^1	6.95×10^1	4.08×10^1	Center
B	10^6	4.00×10^3	8.81×10^3	6.39×10^3	5.27×10^3	5.63×10^3	3.65×10^3	4.94×10^3	Off-center
C	10^7	2.81×10^4	3.95×10^4	2.09×10^4	1.66×10^4	1.34×10^4	1.59×10^4	1.50×10^4	Center
D	10^8	9.29×10^2	7.96×10^2	7.39×10^2	8.92×10^2	8.31×10^2	7.76×10^2	5.61×10^2	Center

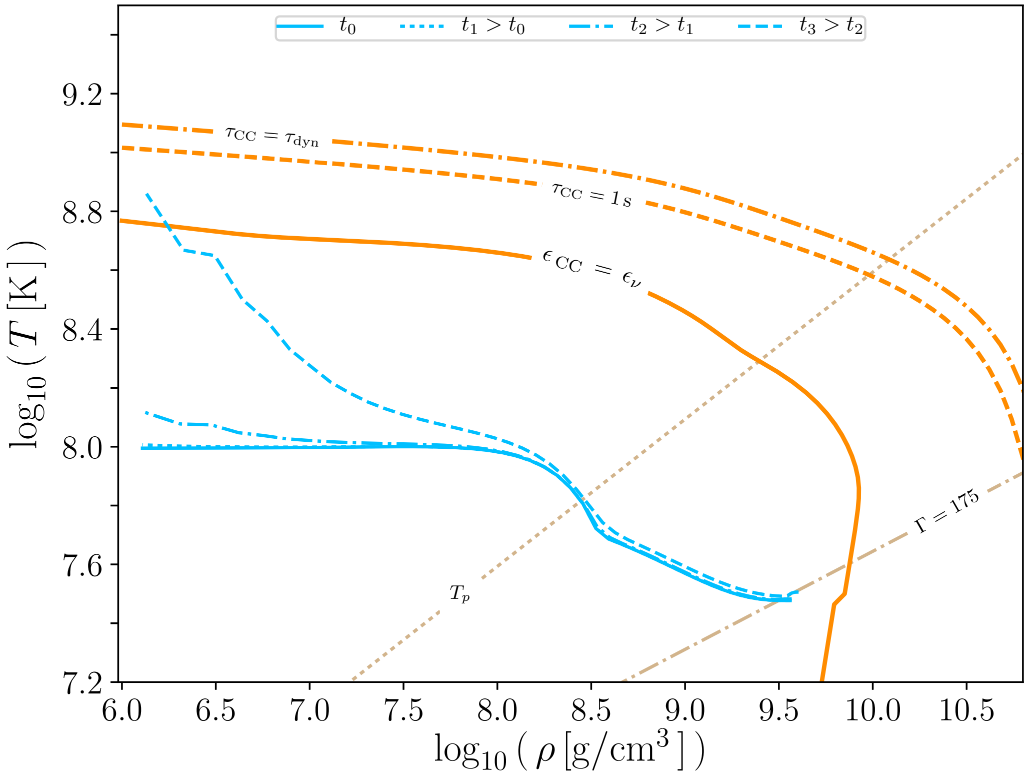

Figure 6.6.: Same as Figure 6.3 but for the case in which a modest magnetic field, $B = 10^6$ G, is adopted. This is model B in Table 6.1.

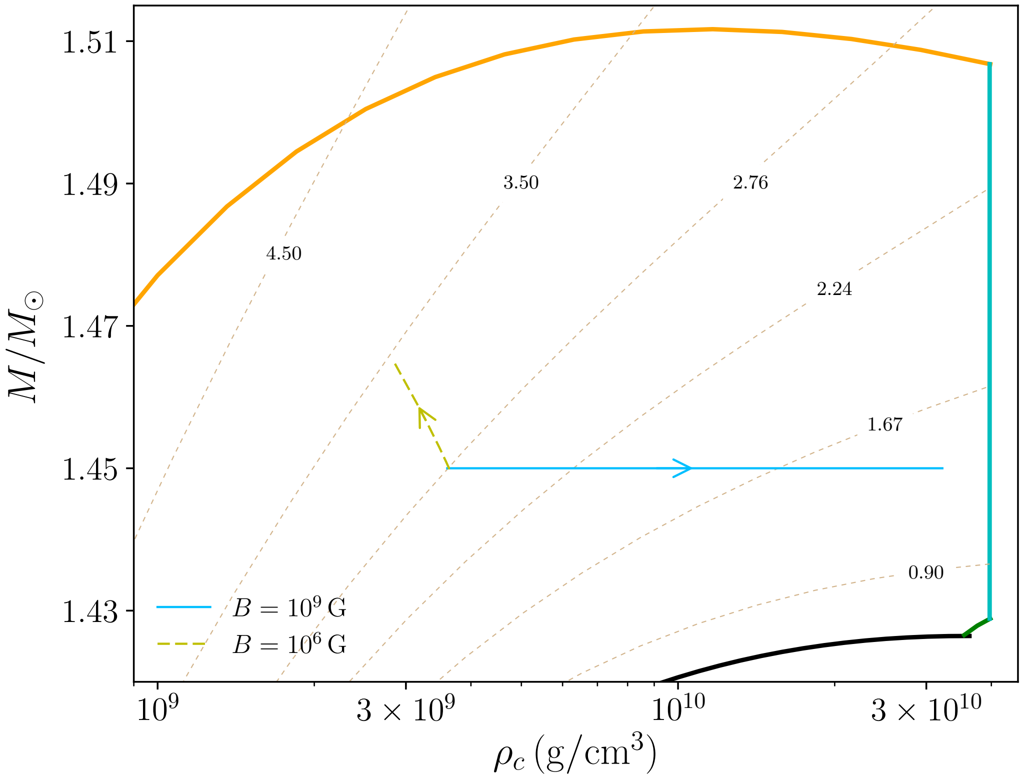

Figure 6.7.: Same as Figure 6.4 but have been added the case in which a modest magnetic field, $B = 10^6$ G, is adopted (yellow line). This is model B in Table 6.1.

At time t_3 the relevant cooling timescale in the outer layers of the white dwarf is no longer the neutrino timescale, but the thermal timescale. Actually, it is important to realize that in the dense inner core of the white dwarf the shorter timescale is always the thermal timescale. Thus, Figure 6.5 clearly shows that the cooling timescale must be computed self-consistently along the evolution of the remnant to obtain physically sound results. We emphasize that although this plot illustrates these timescales for model A, our calculations demonstrate that this is a representative case, and that for all the models listed in the top section of Table 6.1 the run of these timescales is similar.

To study the dependence of the evolution of the merged configuration on the magnetic field we ran a suite of models with varying strengths of the magnetic field. These are models B, C and D in Table 6.1, for which we adopted magnetic field strengths $B = 10^6$, 10^7 and 10^8 G, respectively, keeping unchanged the rest of the parameters of model A. For the sake of conciseness we only discuss model B, which corresponds to the smallest magnetic field strength, 10^6 G.

Figure 6.6 shows the evolution of the remnant at different times for this model. These times were selected using the same criteria we used previously, and the line coding is the same. In this case $R_{\rm mag} < R_{\rm WD}$ and the central white dwarf can accrete matter from the disk. Under these conditions we find that accretion onto the white dwarf heats the outer layers of the star, while the temperature of its core remains almost unchanged. Ultimately the very outer layers of the white dwarf are heated to such an extent that carbon is ignited off-center. However, an inspection of Figure 6.7, which shows the evolution in the mass-central density plane, reveals that actually the central regions of the star expand slightly. This again is due to the acting torques, that spin-up the white dwarf.

We found that if the magnetic field of the white dwarf is higher than 3.84×10^6 G, the magnetospheric radius is larger than the co-rotation radius. Thus, in this case the central remnant does not accrete more material after the merger, so the propeller torque and the dipole radiation torque drive the evolution of its spin rate. On the other hand, if the magnetic field is lower than 1.88×10^6 G, the magnetospheric radius is smaller than the white dwarf radius. Hence, the central white dwarf accretes material. Consequently, in this case the evolution of the rotation rate is driven by the accretion torque. Thus, for these initial conditions the magnetic field determines the accretion rate and the evolution of the star.

To further study the dependence of these results on the input parameters, we also analyzed the dependence on the initial angular velocity. In Table 6.2 we list the times at which the post-merger central star reaches the conditions suitable for a explosion to occur, for several magnetic field strengths (models A to D) and initial angular velocities. Clearly, the duration of this phase as well as the final outcome depend sensitively on value of the adopted magnetic field, and to a lesser extent on the initial angular velocity.

6.5.2. Accretion rate set by viscous timescale

In the previous section we have assumed that the accretion rate on the white dwarf is given by the shorter timescale of the cooling mechanisms. In this section we present the results for the case in which the white dwarf accretes material at a rate set by the viscous timescale of the Keplerian disk.

For the sake of definiteness in the following we discuss in detail, with the help of Figures 6.8 and 6.9, the time evolution of model E, which is similar to model A, the only difference being that in this case the accretion rate is computed adopting the viscous timescale, while the rest of initial conditions and assumptions are the exactly the same. Furthermore, for this model we study two possibilities for the efficiency parameter $\xi_{\rm acc}$ in equation (6.3). The first of these possibilities corresponds to the case in which $\xi_{\rm acc} = 1.0$, that is, when matter is accreted on the remnant with the Keplerian velocity at the inner disk radius. The second one corresponds to the case in which matter is accreted on the remnant with the Keplerian velocity at the surface of the remnant, which we label as $\xi_{\rm acc} = \xi_{\rm WD}$ in the figures discussed below. Shortly after the merger, due to the high accretion rates, $R_{\rm mag} < R_{\rm WD}$ – see the top panel of Figure 6.8. Hence, the only torque acting on the white dwarf is that resulting from accretion. For the set of parameters of model E, the initial accretion rate onto the white dwarf given by equation (6.25) is large, even if a efficiency of $\varepsilon = 0.1$ is adopted, $\dot{M}_{\rm WD} \sim 0.01\, M_\odot$ s^{-1}. Consequently, the mass of the white dwarf rapidly increases during this phase. However, its central density only increases in the case in which matter is accreted with the Keplerian velocity of the remnant – blue line in Figure 6.9 – whereas in the case in which $\xi_{\rm acc} = 1.0$ – green line in this figure – the central density of the white dwarf decreases.

The evolution of the central density of the remnant is the result of an intricate trade-off between the increase in mass, the change in the rotation period due to the acting torque, and the evolution of the moment of inertia of the remnant. The increase in mass of the remnant alone clearly would result in an increase of the central density. The change in the rotation speed due to the acting torque – which tends to increase the angular velocity – would result in a decrease of the central density, as the centrifugal force increases. Finally, since $I \propto M_{\rm WD} R_{\rm WD}^2$, as the mass of the white dwarf increases due to accretion, the moment of inertia would increase. However, since the mass-radius relationship for rotating white dwarfs depends crucially on the angular velocity, the radius of the remnant, hence I, ultimately depends on the acting torque. Furthermore, for super-Chandrasekhar white dwarfs the slope of the mass-radius relationship is very steep. Consequently small changes in the mass can induce large variations of the radius of the remnant. The interplay between these factors is rather complex, but in general terms we find that the evolution of the moment of inertia is dominated by the variation of the radius of the remnant.

It is then clear that the crucial parameter that dictates the evolution of the central density of the remnant is $\xi_{\rm acc}$. Specifically, when $\xi_{\rm acc} = 1.0$ is adopted the remnant is spun-up very rapidly by the acting torque – as it is shown in the bottom panel of Figure 6.8 – its radius increases notably – see the top panel of this figure – the moment of inertia increases markedly, and the central density first decreases. On the contrary, if matter is accreted onto the surface of the white dwarf with the same angular velocity of the remnant,

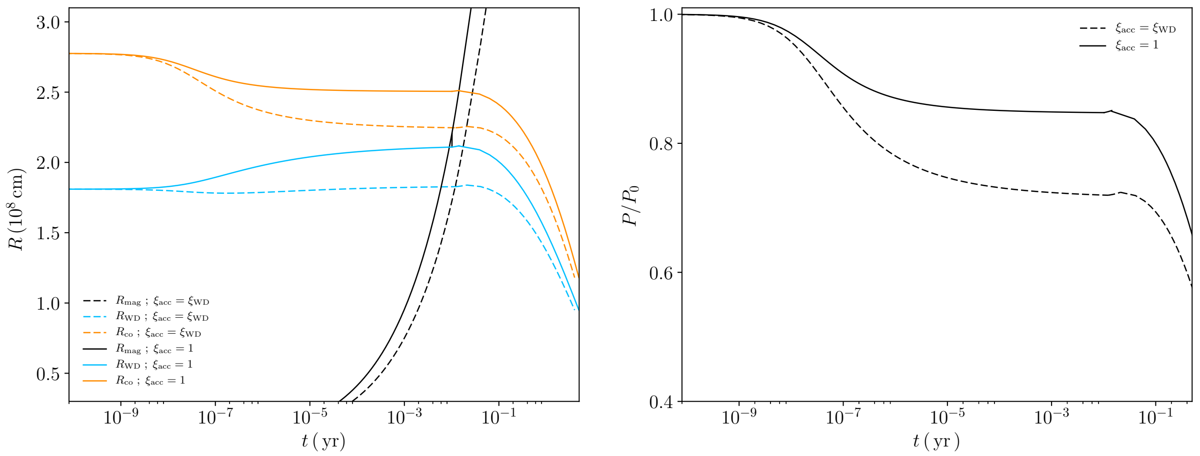

Figure 6.8.: The left panel shows the evolution of the radius of the remnant, $R_{\rm WD}$, the corotation radius $R_{\rm co}$, and the magnetospheric radius, $R_{\rm mag}$ for model E, while the right panel shows the evolution of the rotation period of the central white dwarf.

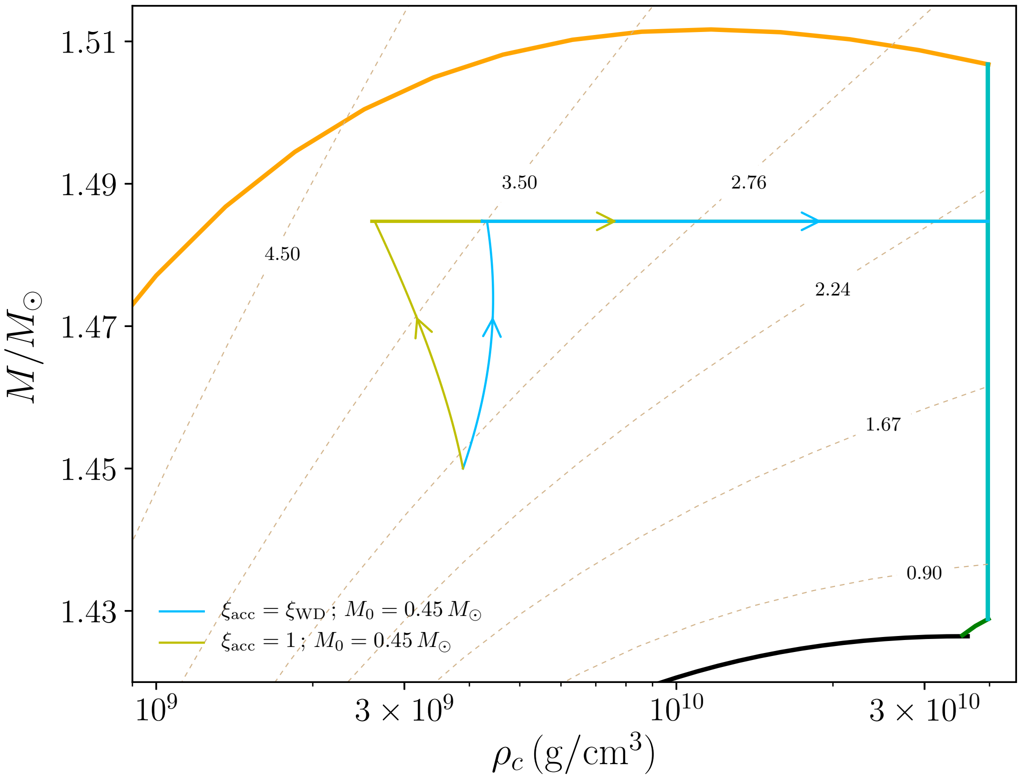

Figure 6.9.: Evolutionary tracks in the mass-density plane for model E for two assumptions about the value of $\xi_{\rm acc}$, and $\varepsilon = 0.1$.

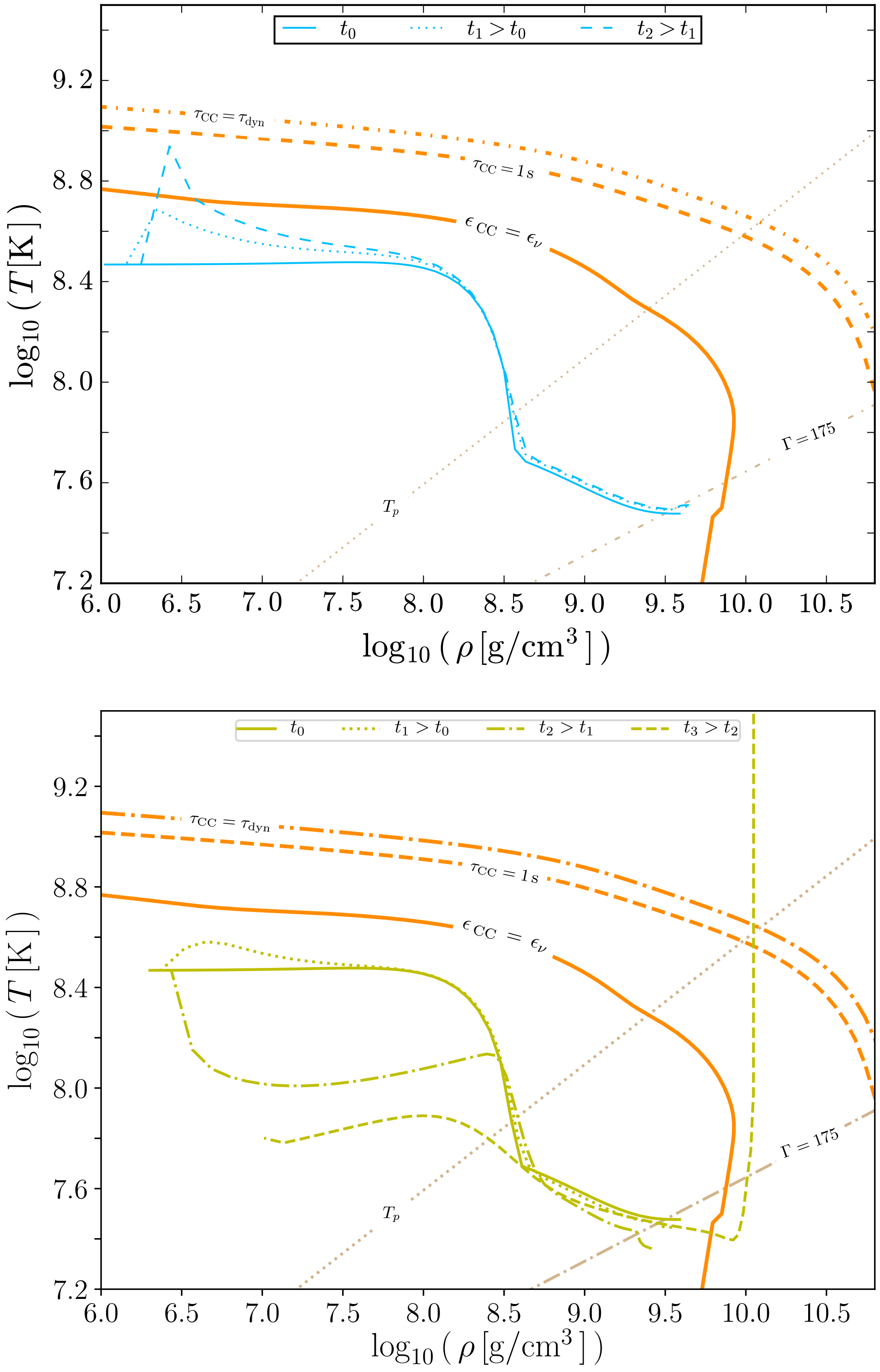

Figure 6.10.: Temperature-density profiles of the central white dwarf at different times of the evolution for model E. The left panel shows the model with $\xi = \xi_{acc}$, while the right panel displays the model for which $\xi = 1$ is adopted. Time t_1 corresponds to a time shortly after accretion from the disk starts (short dashed line), t_2 is the time at which the merged remnant enters into the propeller phase and accretion stops (dashed line), and t_3 is a time just before the post-merger object crosses the beta-instability limit (long dashed line).

the acting torque is considerably smaller, the moment of inertia remains approximately constant, the radius of the remnant decreases, and the central density increases steadily. In both cases, once the magnetic radius becomes larger than the radius of the white dwarf ($R_{\rm WD} < R_{\rm mag} < R_{\rm co}$), the dipole and the disk-interaction torques drive the evolution of the remnant – the top panel of Figure 6.8 clearly depicts this. When this happens, the fastness parameter of the white dwarf is ~ 0.8. Consequently, shortly after ($\lesssim 0.5\,{\rm yr}$), the remnant reaches a fastness parameter $\omega_{\rm f} = 1$, and the evolution is driven by the propeller torque. At this point of the evolution, accretion from the disk stops. Consequently, the moment of inertia of the remnant decreases considerably, the rotation period decreases as well, and the white dwarf contracts. Hence, the central density increases rapidly (see the top panel of Figure 6.8). All this sequence of events ultimately leads the remnant to cross the line of inverse β-decay instability. It is interesting to note that the mass of the remnant when it crosses the instability line does not depend on the adopted valued of $\xi_{\rm acc}$. This will depend on the mass accretion rate on the white draft, and consequently on the adopted efficient parameter ξ. The $\xi_{\rm acc}$ is directly related to the change of angular momentum. Then $\xi_{\rm acc}$ and ξ plays different role in the evolution of the post-merger configuration, although its effect will be combined as can be see in equation (6.3).

We now pay attention to thermal evolution of the post-merger remnant of model E. Figure 6.10 shows several temperature-density profiles at selected times after the merger took place. The top panel of this figure shows the case in which $\xi = \xi_{\rm acc}$ is adopted, whereas the bottom panel corresponds to the case in which $\xi = 1$ is employed. The initial temperature profiles are shown as a solid blue and green lines in Figure 6.10, respectively. In both cases, during the first evolutionary phases the large accretion rates discussed earlier heat the outer layers of the star. However, neutrino emission also plays a significant role. When $\xi = \xi_{\rm acc}$ is adopted compressional work exceeds neutrino emission, and thus an off-center temperature peak rapidly grows. In particular, the temperature profile peaks at $\log \rho \sim 6.54$. As time passes by, the peak temperature increases, and ultimately the outer layers of the white dwarf reach the thermodynamic conditions needed to ignite carbon explosively.

On the contrary, when $\xi = 1.0$ is adopted (bottom panel of Figure 6.10) the evolution is more complex. In this case accretion first heats the outer layers of the central white dwarf, but neutrino cooling dominates. Hence, after a short time interval the entire central white dwarf cools to a temperature smaller than the initial one. Time t_2 is the time at which accretion stops. Thus, for times longer than t_2 the evolution of the star is driven by angular momentum looses by dipole emission. Eventually, at time t_3 carbon is ignited at the center of the white dwarf.

Sensitivity of the results to the free parameters

We first compare the evolution when different masses of the disk are adopted, keeping the mass of the remnant fixed. With this in mind, in Figure 6.11 we show the evolutionary tracks of model F and compare them with those of model E. This model corresponds to a final post-merger remnant of mass $1.45\,M_{\odot}$ and an initial disk mass $0.65\,M_{\odot}$, whereas the rest of the parameters of the model were not varied – see Table 6.1. Additionally, as we did for model E we also studied two possibilities. The first of these corresponds to an accretion efficiency parameter $\xi_{\rm acc} = 1.0$, whereas for the second one we assumed that at the inner disk radius the accreted material has the angular velocity of the white dwarf, $\xi_{\rm acc} = \xi_{\rm WD}$. Note that, in the case in which $\xi_{\rm acc} = 0.1$ is adopted, the evolution of this model is very similar to the one of model E, but arrive to the mass-shedding limit in the accretion phase. When $\xi_{\rm acc} = \xi_{\rm WD}$ is chosen, the remnant also crosses the line of inverse β-decay instability. The only difference is that for model F, which has a disk considerably more massive, more mass is accreted before the remnant crosses the instability line. Hence, the remnant has a larger mass in the propeller phase, and the line of β-decay instability is crossed when the white dwarf is more massive.

Next, we analyze the influence on the evolution of the strength of the magnetic field, as we did previously for those models in which the accretion rate is computed using the cooling timescale. We do this comparison adopting a very low value for the magnetic field strength, $B = 10^6$ G – model G in Table 6.1, the same value adopted in Sect. 6.5.1. The results of this analysis are shown in Figure 6.12. As can be seen the differences between the evolution of models E and G are minor. Thus, we conclude that for the typical values of the magnetic field strength originated in the merger of two white dwarfs, the evolution of these models is not significantly affected by the adopted magnetic field. This can be explained from the fact that, at early times in the viscous timescale prescription, the mass and angular momentum of the WD post-merger evolution is dominated by the accretion torque and the effect of the magnetic field is neglected until the magnetospheric radius equals the WD one. It is in this initial phase when more significant accretion of mass by the central star occurs. Since, the accretion timescale in this scenarios is so short, the evolution of the magnetospheric radius is dominated by the change of the mass accretion rate.

Another free parameter of our formulation is ε, which we recall measures how efficient accretion is. All the calculations presented until now have been performed adopting $\varepsilon = 0.1$. However, since the accreted mass depends significantly on the precise value of this free parameter it is important to assess its impact on the results. We now study the sensitivity of our calculations to the value adopted for it. To this end we conducted an additional set of simulations in which we adopted $\varepsilon = 0.5$. This is model H in Table 6.1. In Figure 6.13 we compare the results of these calculations with those of model E. As it could be expected, this parameter turns out to be critical, since it controls how efficient accretion is. Consequently, when $\varepsilon = 0.5$ is adopted the remnant evolves towards the mass-shedding limit instead of crossing the β-instability line. We consider model E as a reasonable guess, although keeping in mind that larger values of ε cannot be discarded “a priori”, and therefore could alter the evolution of the remnant.

Naturally, another key ingredient of our approach is the initial angular velocity of the central white dwarf, $\Omega_{\rm WD}$. Figure 6.14 shows the evolutionary tracks for different values of the initial angular velocity of the post-merger remnant, keeping unchanged the rest of initial conditions of model E – models I to Q in Table 6.1 (dashed lines) – and we compare them with the evolutionary sequence of model E, our reference model for this prescription for the accretion rate (solid lines). As can be seen, the model with the smallest initial angular velocity – namely that with initial angular velocity 2.30 $\mathrm{rad\,s^{-1}}$, model I – reaches the mass-shedding limit during the accretion phase. Furthermore, for

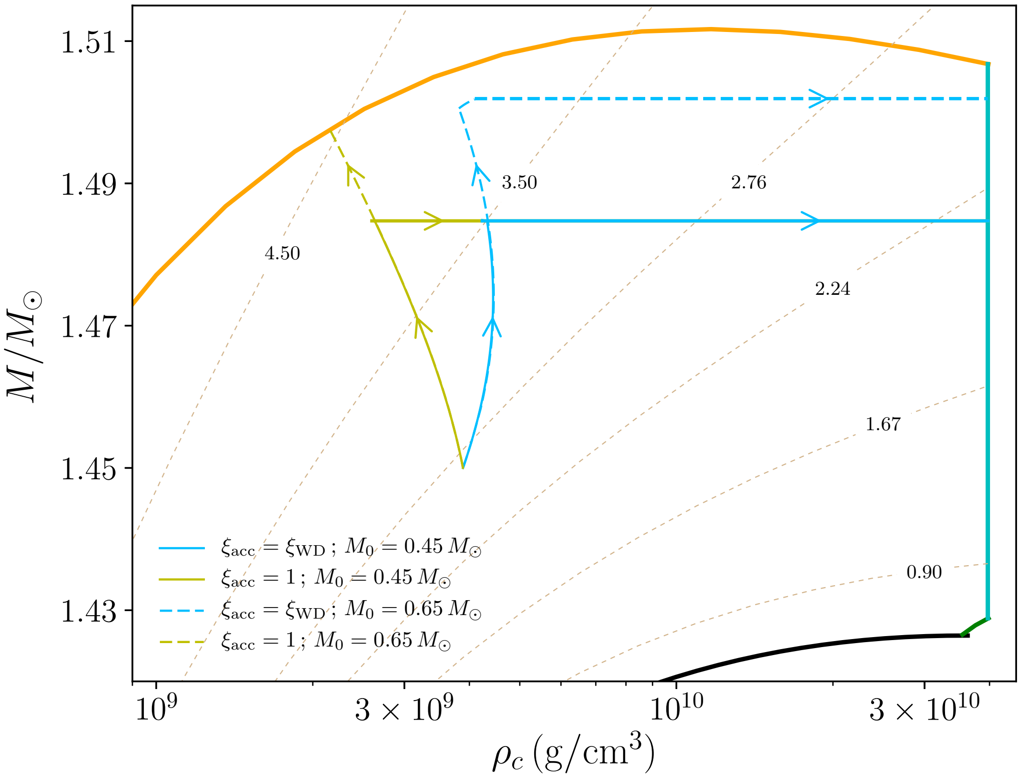

Figure 6.11.: Same as Figure 6.9. We compare models E (solid lines) and F (dashed lines) for two different disk initial mass, $0.45\,M_\odot$ and $0.65\,M_\odot$, respectively.

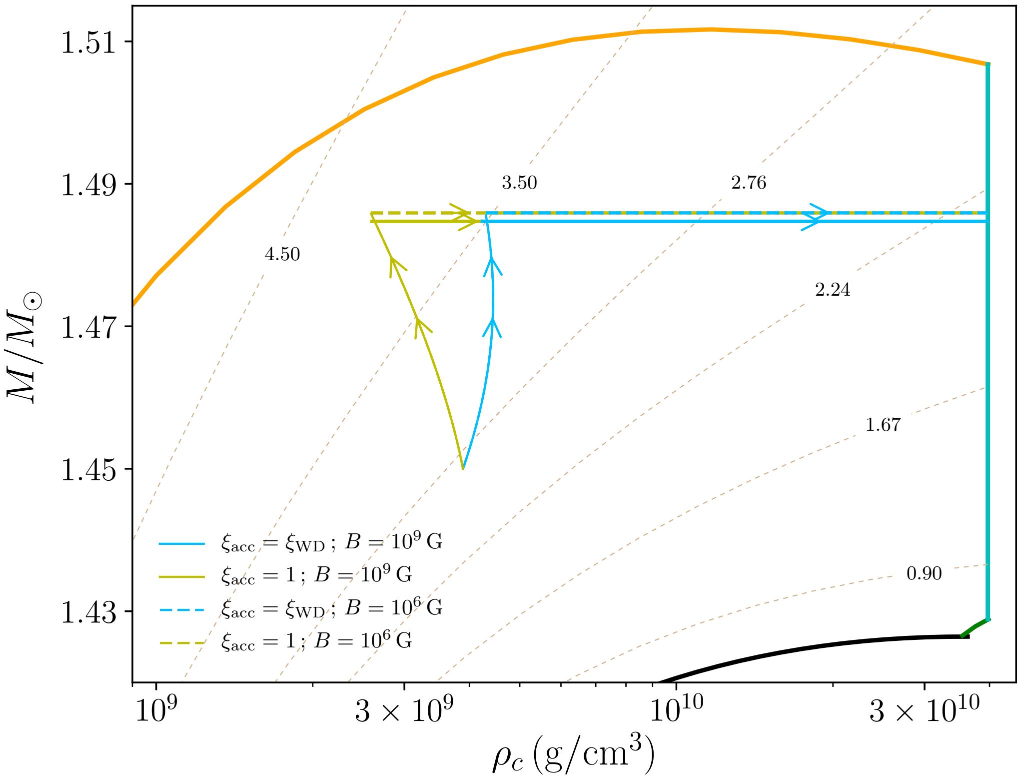

Figure 6.12.: Same as Figure 6.9. We compare models E (solid lines) and G (dashed lines) for two different values of the WD magnetic field, 10^9 G and 10^6 G, respectively.

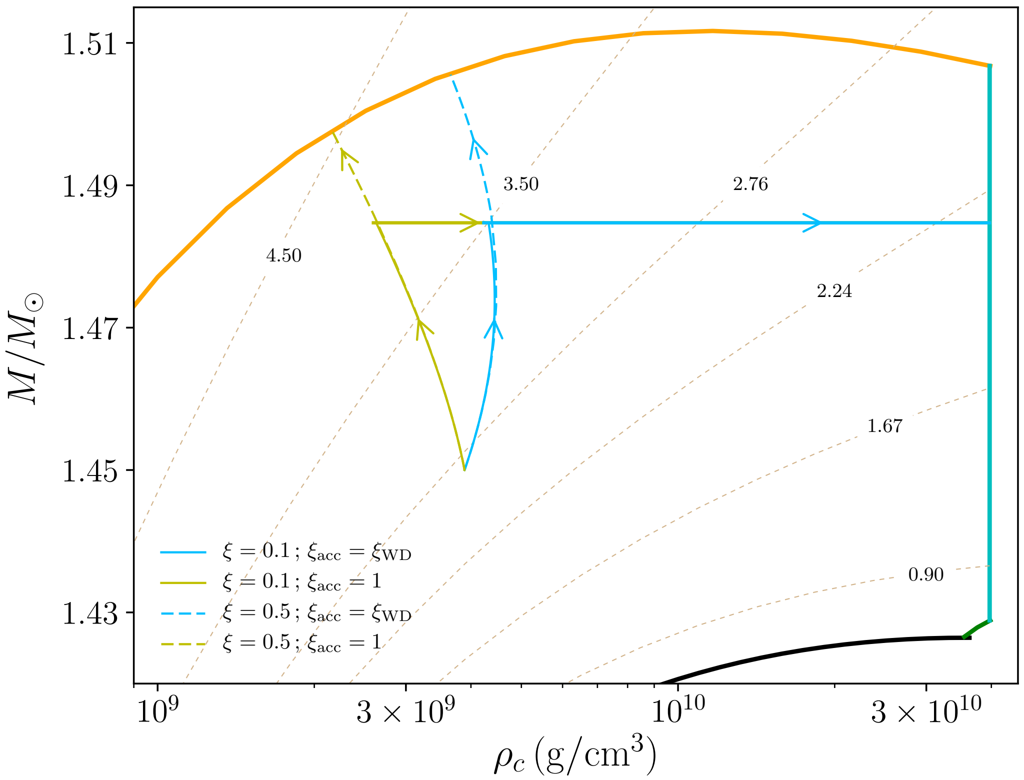

Figure 6.13.: Same as Figure 6.9 for two values of the accretion efficiency parameter, $\varepsilon = 0.1$ (solid lines) and 0.5 (dashed lines), models E and H, respectively.

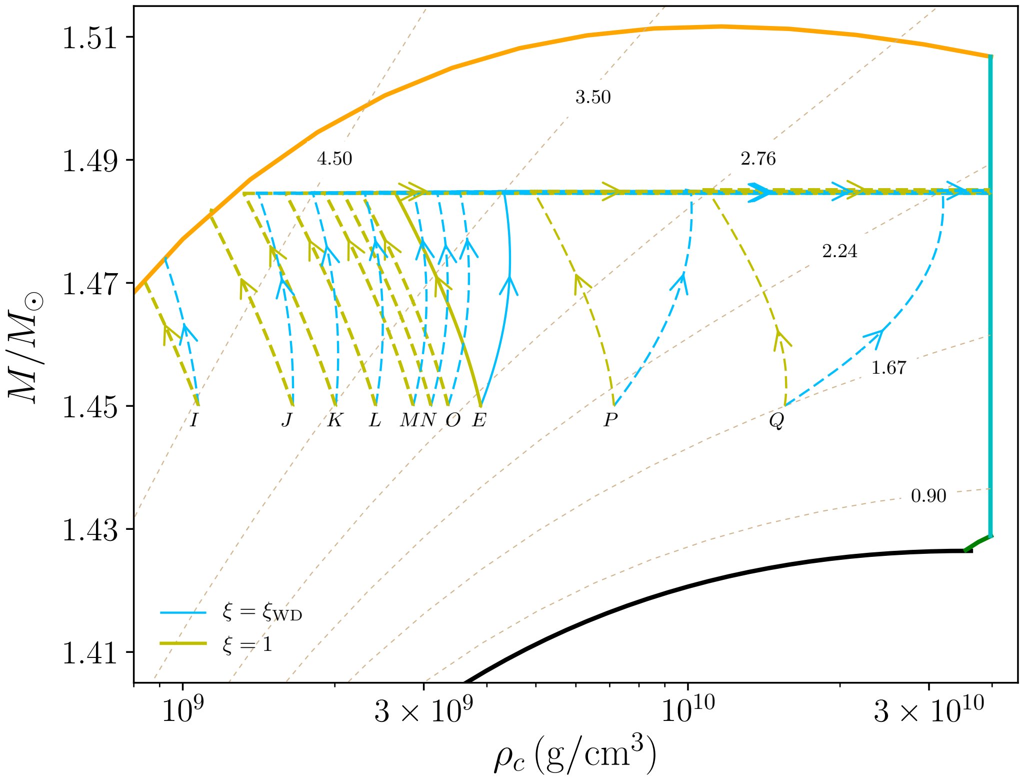

Figure 6.14.: Same as Figure 6.9 for several values of the initial angular velocity, models I to P in Table 6.1, compared to our reference case, for which the initial angular velocity is $\Omega_{\rm WD} = 3.00$ (model E). From left to right the initial angular velocities of the remnant are $\Omega_{\rm WD} = 2.30$, 2.50, 2.60, 2.70, 2.80, 2.85, 2.90, 3.50, and $4.50\,{\rm s}^{-1}$.

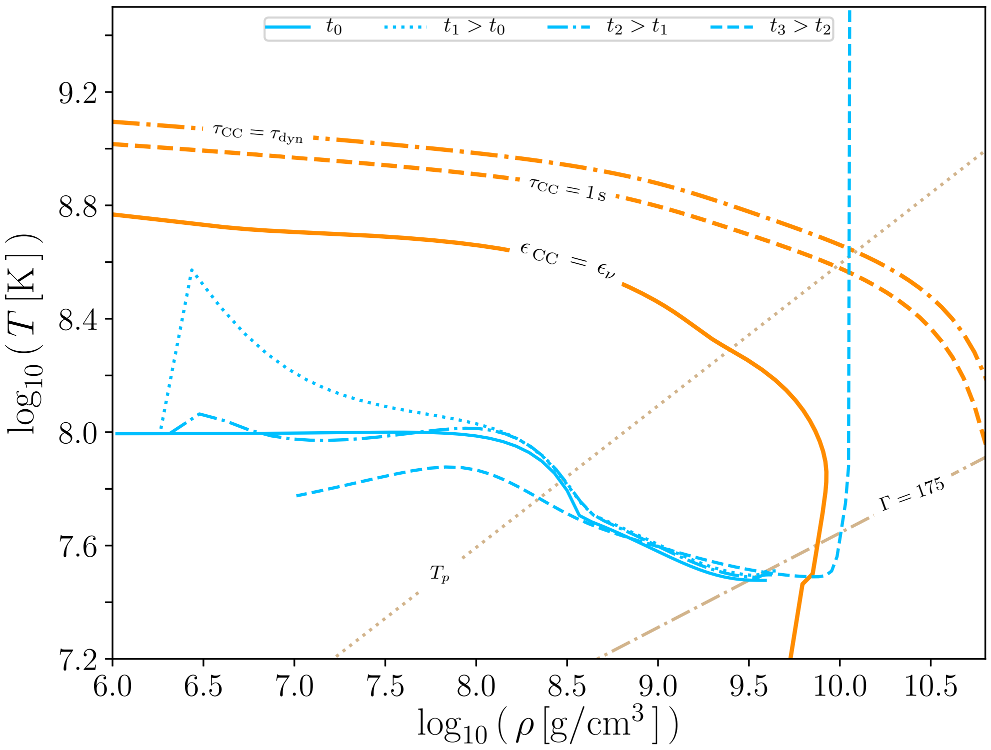

Figure 6.15.: Same as Figure 6.10 for the case in which the initial temperature of model E is smaller. For the sake of conciseness we only display the model for which $\xi = 1$ is adopted.

this model the central density decreases, irrespective of the value adopted for $\xi_{\rm acc}$. Model J, for which we adopted $\Omega_{\rm WD} = 2.50\,\mathrm{rad\,s^{-1}}$, only reaches the mass-shedding limit if $\xi_{\rm acc} = 1.0$, otherwise it reaches the β instability region. The rest of the models do not cross the mass-shedding instability line. Note as well that for model J, as it occurs for model I, the central density decreases, independently of the value adopted for $\xi_{\rm acc}$. For model K the central density decreases if $\xi_{\rm acc} = 1.0$ and increases otherwise. This is also true for models with even faster rotation rates.

Additionally, to take into account the effects of the initial temperature for the case in which $\xi = \xi_{\rm acc}$ is adopted we computed a model in which the initial configuration corresponds to a white dwarf in which the external layers have a temperature sizably smaller, namely 10^8 K, than that of our standard case – that is, model E – which was computed adopting a temperature of the external layers 3×10^8 K. The evolution of this additional model is shown in Figure 6.15, and it is markedly different different from that of model E. Specifically, when the adopted temperature is 10^8 K, the external layers of the white dwarf are initially heated by the accreted material, as it happens also for model E. However, in this case neutrino cooling (basically dominated by neutrino bremsstrahlung) is so strong that the remnant cools rapidly and eventually carbon is ignited at the center of the star, when the central regions have already crystallized.

Evolutionary times

Finally, we study the time needed to reach the instability lines, Δt. We have shown before that the most important parameter that determines the evolution of the system is the initial period of the system. In the top panel of Figure 6.16 the dependence of Δt on the initial period of the rotating white dwarf resulting from the merger is displayed, for our two choices for the value of $\xi_{\rm acc}$. Clearly, the larger the period is, the longer Δt is. This is the natural consequence of the smaller initial centrifugal force.

The second important parameter that determines the duration of this evolutionary phase is the strength of the magnetic field of the remnant. We showed before that the value of $B_{\rm WD}$ has little effect on the outcome of the post-merger system – see Figure 6.12. Notwithstanding, $B_{\rm WD}$ influences considerably Δt. This occurs because the larger $B_{\rm WD}$ is, the larger is the magnetospheric radius. Thus, we expect that large values of $B_{\rm WD}$ would result in substantially smaller values of Δt. To illustrate this in a quantitative manner, in the bottom panel of Figure 6.16 the total time needed to reach the instability region is plotted as a function of the surface magnetic field of the remnant. As can be seen, the evolution of the systems is indeed faster for large magnetic field strengths. This behavior is natural since for large magnetic field strengths the central remnant is more tightly coupled with the surrounding Keplerian disk. Consequently, the accretion phase is shorter. In addition, in this panel we also show (using a solid, red line) the time it takes to the remnant to become unstable when only magnetic dipole braking is considered. Since in this case, there is no accretion, the star will evolve in a constant mass sequence. From equation (6.7), we obtained:

$$\Delta\, t = \frac{c^3}{2B_{\rm WD}^2}\int_{J_{\rm WD,0}}^{J_{{\rm WD},f}} \frac{dJ_{\rm WD}}{\Omega_{\rm WD}^3 R_{\rm WD}^6} \tag{6.30}$$

It's easily to see that $\Delta\, t$ is inversely proportional to the square of the magnetic field. Clearly, the evolution of the system is always much faster when all the torques acting on the remnant are correctly taken into account. Furthermore, it is important to realize that the evolution is even faster when matter is accreted onto the surface of the remnant with the Keplerian velocity. Finally, note as well that when $\xi_{\rm acc} = 1.0$ is adopted, moderately longer durations of the post-merger phase, when compared with the case in which the accreted matter has the Keplerian velocity at the surface of the remnant, are obtained.

6.6. Comparison with previous works

A detailed study of the evolution of the remnant of white dwarf mergers started with the work of Yoon et al. [317]. They mapped the final configuration of the SPH simulations of the merger of a 0.9–0.6 $M_\odot$ binary into a 1-D stellar evolution hydrodynamic code and follow its forward evolution. Their merger remnant is represented by a cold and slowly rotating rigid core surrounding by a hot and rapid rotating envelope with a Keplerian disk around it. They allowed the accretion from the disk by a constant accretion rate (of the order of the Eddington limit) and include a prescription for the transport of angular

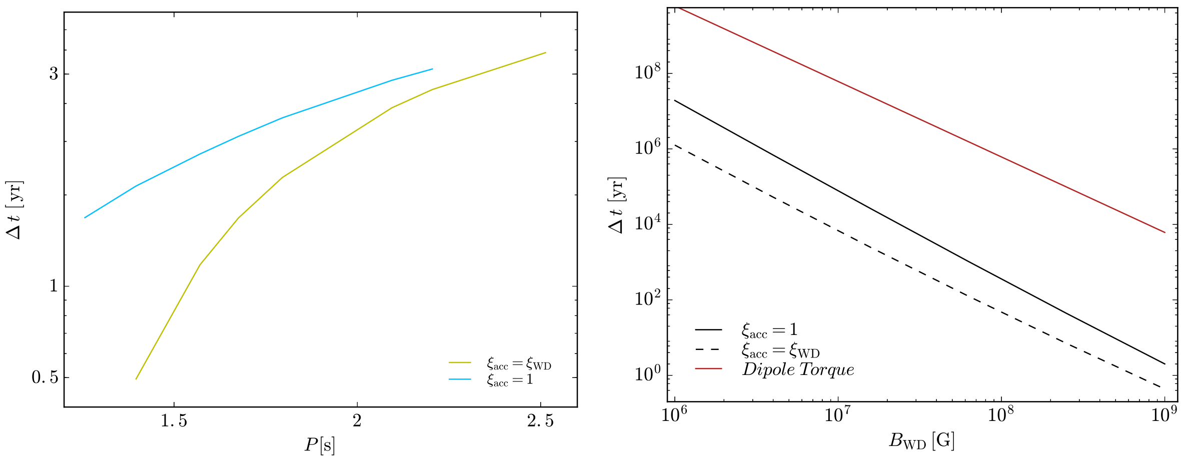

Figure 6.16.: Left panel: time necessary to reach the instability line as a function of of the initial period of the remnant. Right panel: time necessary to reach the instability line as a function the magnetic field of the remnant.

momentum with timescales of the order of the thermal timescale. They conclude that a off-center carbon ignition can be avoided if the transport angular momentum timescale is greater that the cooling timescale by neutrino emission and the accretion rate on the star is slow enough, i,e, $\dot{M}_{\rm WD} < 5 \times 10^{-6}$–$10^{-5}\,M_\odot$ yr^{-1}. We improved this approach allowing the mass-accretion rate to vary with time, consistently with the white dwarf thermal evolution. Additionally, we introduced a framework for evolution of the angular momentum of the post-merger white dwarf including the torque that acts on the star taking into account the magnetic field effect of the central white dwarf on the evolution of the post-merger configuration. We have found that strong magnetic fields, $B_{\rm WD} > 10^7$ G can also avoid an off-center carbon ignition.

van Kerkwijk et al. [293] estimated the post-merger evolution based on the results of the SPH simulations of [164] and concluded that the accretion occurs in a shorter timescale ($\sim$ 10 h), causinga compression of the white dwarf core, with a consequent increase of its temperature until it reaches the carbon-ignition runaway leading to a delayed explosion. However, they focus on mass-symmetric white dwarf mergers (0.6–0.6 $M_\odot$) in which the two white dwarfs are disrupting and the final remnant configuration has a temperature profile that peaks at the center.

A different approach was presented in Shen et al. [262] and in Schwab et al. [258, 259]. In these works it was argued that, due to the differential rotation of the system, after the dynamical phase of the merger the magneto-rotational instability becomes effective, and that in a viscous timescale 10^4 s (orders of magnitude shorter than the thermal timescale $\sim 10^4$ yr) the angular momentum of the tidally disrupted white dwarf can be redistributed in the surface of the central star, leading to a rotating configuration with a hot envelope and with almost all the mass of the secondary star. These works also computed the thermal evolution of the post-merger remnant characterized with a timescale of the order of 10^3–10^4 yr. Schwab et al. [259] studied the merger of a $0.9 - 0.6\,M_\odot$ white dwarf binary, and [258, 259] extended the initial conditions parameter space but the evolution of post-merger configuration in presence of a magnetic field of the central white dwarf was not there considered. These configurations spin down during the viscous evolution, while our super-Chandrasekhar remnants spin up during all the evolution, even in the case of angular momentum losses.

There are two works considering the effect of the magnetic field during the dynamical timescale of the merger [326] and in the viscous timescale of the post-merger evolution [141]. In these works, the evolution of the system magnetic field is followed in a different fashion with respect to our approach, since we have adopted a dipole magnetic field with constant magnitude and inclination angle. Assuming as initial condition the remnant of the merger of a 0.6–0.6 $M_\odot$ carbon-oxygen white dwarf binary from the SPH simulation of Lorén-Aguilar et al. [164], Ji et al. [141] evolves the system for 3×10^4 s with the FLASH code in a 2D axisymmetric cylindrical Eulerian grid. They introduced a weak poloidal magnetic field and showed that the magneto-rotational instability developed in the disk leads to a rapid growth of its magnetic field, the spin down of the white dwarf remnant and its magnetization to field strengths around $\sim 2 \times 10^8$ G. They computed an effective magnetic Shakura-Sunyaev parameter of the order of $\langle \alpha_m \rangle \sim 0.01$, a value one order of magnitude smaller than the α we adopted here. They found that the white dwarf magnetic field varies with time, indicating a disordered interior magnetic field. At the end of the simulation the magnetic field toroidal component is 1.5 times bigger than the poloidal one. In our model we have assumed a dipole magnetic field aligned with the white dwarf rotation axis. In this case, the magnetic field, has no toroidal component. However, the simulations of Ji et al. [141] have limited resolution and the field strength are affected by numerical resistivity. In addition, in these magneto-hydrodynamics simulations the disk lost almost 90% of its initial mass, with 82% of it accreted by the white dwarf remnant and the rest going into outflows of which about $10^{-3} M_\odot$ are ejected and unbound to the system. The central white dwarf spins down, losing angular momentum due to the development of Maxwell stresses at the white dwarf boundary. A directed comparison is difficult, since we have studied super-Chandrasekhar white dwarf with initial angular velocity one order of magnitude higher than the one studied by Ji et al. [141] ($\Omega_{\rm WD,0} = 0.03$ s^{-1}). However, one difference is that in our model the white dwarf first gain angular momentum due to the mass accretion, and then due to the magnetic torque loses it.

Zhu et al. [326] simulated the merger of a 0.625–0.65 $M_\odot$ carbon-oxygen white dwarf binary giving to each white dwarf a dipole seed magnetic field with the moving-mesh code AREPO [274]. They found that during the merger dynamics, the magnetic field were too weak to have an effect in the evolution, obtaining a final remnant composed by a degenerate core with a thermally supported envelope surrounding by a rotationally supported disk. This configuration is similar to the one obtained in the SPH simulations [325]. However, the remnant magnetic field has a complex structure with a volume average field strength $> 10^{10}$ G in the core, with both poloidal and toroidal components.

In Table 6.3 is summarized the main features of the post-merger evolution studied in this paper and the comparison with the ones of the works discussed above. We specified the binary mass of the merger configurations studied, the post-merger configurations after the merger (for the works of [293, 317, 325]) or after the viscous evolutions of the system (for the work of [141, 259, 262]), the magnitude and configuration of the central remnant magnetic field (if it is considered). In the last column, we specified if the central remnant developed conditions for an off center or center carbon ignition.

Table 6.3.: Comparison with previous works (B_t/B_p : ratio of the toroidal to the poloidal field strength. E_{Bt}/E_B : ratio of the toroidal to the total magnetic energy).

Work	Merger Configuration	Post-merger configurations	Magnetic field	Magnetic field configuration	Carbon Ignition
Yoon et al. [317]	$0.9\,M_\odot - 0.6\,M_\odot$ $0.9\,M_\odot - 0.7\,M_\odot$ $1.0\,M_\odot - 1.0\,M_\odot$	slowly rotating cold core ($0.6\,M_\odot$) with a rapidly rotating hot envelope ($0.5\,M_\odot$) + a Keplerian disc ($0.4\,M_\odot$)	-	-	Center/off-center ignition
van Kerkwijk et al. [293]	$0.6\,M_\odot - 0.6\,M_\odot$ C/O WD	rapidly rotating WD + thick disk	-	-	Center ignition
Shen et al. [262]	$0.6\,M_\odot - 0.9\,M_\odot$ C/O WD	WD ($\sim 0.9\,M_\odot$) with a hot, slowly rotating and radially extended envelope supported by thermal pressure ($\sim 0.6\,M_\odot$)	-	-	Off-center ignition that lead a high mass O/Ne WD
Schwab et al. [259] / Schwab et al. [258]	$0.6\,M_\odot - 0.9\,M_\odot$ $0.9\,M_\odot - 1.2\,M_\odot$ C/O WD	WD with a thermally supported envelope ($1.5\,M_\odot$)	-	-	Off-center ignition that leads an O/Ne WD
Ji et al. [141]	$0.6\,M_\odot - 0.6\,M_\odot$ C/O WD	rotating WD ($0.96\,M_\odot$) surrounding by a hot corona ($0.04\,M_\odot$) + thick disk ($0.2\,M_\odot$)	2×10^8 G	$\frac{B_t}{B_p} \sim 1.5$	Center Ignition
Zhu et al. [325]	$0.625\,M_\odot$-$0.65\,M_\odot$ C/O WD	WD ($0.64\,M_\odot$) surrounded by thermally supported hot envelope ($0.42\,M_\odot$) + disk ($0.21\,M_\odot$)	4×10^{10} G	$\frac{E_{Bt}}{E_B} = 0.6$	-
This work	$0.78\,M_\odot$-$1.12\,M_\odot$ C/O WD	$1.45\,M_\odot$ rigidly rotating super-Chandrasekhar WD + $0.45\,M_\odot$ thin Keplerian disk	$[10^6, 10^9]$ G	Poloidal	Center/off center ignition

6.7. Conclusions

The evolution of the remnant of the merger of a binary white dwarf is still an open problem. Detailed hydrodynamical simulations show that the product of the merger consists of a central white dwarf that rotates as a rigid body, surrounded by a hot, rapidly rotating corona – which has been proven to produce large magnetic fields – and a Keplerian disk. In this paper we studied the evolution of metastable, magnetized super-Chandrasekhar white dwarfs formed in the aftermath of the merger of close binary systems made of two white dwarfs.

Our simulations take into account the magnetic torques acting on the star, accretion from the Keplerian disk, and the threading of the magnetic field lines through the disk – therefore improving previous calculations of this kind. Furthermore, in our computations – at odds with previous efforts – we employ a mass-radius relationship for rotating white dwarfs. Also, our calculations incorporate the thermal evolution of the white dwarf. All in all, the set of calculations presented here relies on solid physical grounds. However, there are assumptions in our model that might be relaxed in forthcoming works. For instance, to allow a non-zero inclination angle between the spin axis and the orientation of the dipole magnetic field and its evolution with time. Also, the post-merger central remnant rotates differentially between the core and the corona, while we have adopted a totally rigid central remnant. Thus the model can be improved by implementing a transport mechanism for the angular momentum in the interior of the central white dwarf remnant.

Furthermore, our simulations were performed using two different prescriptions for the mass accretion rate on the central white dwarf. In a first set of simulations we adopted an accretion rate set by cooling timescale of the Keplerian disk, whereas in the second suite of models the adopted accretion rate was computed using the viscous timescale of the disk. These two prescriptions for the accretion rate cover a very large range of values, and therefore allow us to investigate the possible outcomes of the evolution of these systems in a quite generic way.

Finally, we also explored the effects of the adopted set of initial parameters. These include the mass of the remnant star, its radius, angular velocity, and moment of inertia, as well as the strength of the magnetic field. We showed that the timescale in which the newly formed white dwarf evolves to reach the thermodynamical conditions for carbon be burned explosively, or to reach the Keplerian mass-shedding, secular axisymmetric instability or inverse beta decay instability depends crucially on all these parameters.

We showed that in most of our models carbon reactions are highly efficient in heating the interior of the remnant, with timescales shorter than the dynamical time. This can happen both in the outer layers or at the center of the newly formed white dwarf, depending on the initial conditions of the white dwarf and on the efficiency of mass accretion and angular momentum evolution (see Fig. 6.10). In most cases, the time it takes to the star to reach explosive conditions is shorter than the one needed to reach the inverse beta-decay instability or the secular instability, which lead to gravitational collapse. Hence, we conclude that the central white dwarf can reach conditions for a delayed explosion for a sufficiently broad set of initial conditions. Whether carbon is ignited at the center of is burned off-center depends crucially on the magnetic field strength and is almost independently of the post-merger WD initial angular velocity. Our simulations show that when the magnetic field is weak carbon is ignited off-center, while central explosions are the outcome when a ordered global strong dipole magnetic field is produced in the hot, rapidly rotating convective corona formed in the aftermath of white dwarf mergers. Naturally, this depends on whether the stellar dynamo is saturated or not.

In summary, spinning, magnetized, super-Chandrasekhar white dwarfs, resulting from the merger of two less massive white dwarfs that do not produce a Type Ia supernova in a violent merger can produce a delayed explosion, provided that the remnant is massive enough and a strong magnetic field is produced during the merger.

A. Appendix for Chapter I

A.1. Analytic approximation for the peak accretion rate

We can see from Figure 1.3 that the shorter(smaller) the orbital period(separation) the higher the peak accretion rate $\dot{M}_{\rm peak}$ and the shorter the peak time, $t_{\rm peak}$. Indeed, we can derive such a feature from simple arguments. The accretion rate given by equation (1.1) increases for higher densities and lower velocities, so we should expect as indeed shown in Figure 1.3, it increases with time as the inner ejecta layers, which are denser and slower [see equations (1.5) and (1.3)], reach and passed the accretion region. The accretion rate starts to peak at the passage of the innermost densest layer, $r_{\rm inner}$, through the capture region. Such a layer moves with velocity $v_{\rm inner} = (r_{\rm inner}/R_{0_{\rm star}})v_{0_{\rm star}}$ as given by the homologous expansion assumption.

Thus, the accretion rate peaks around the peak time:

$$t_{\rm peak} = \frac{a - R_{\rm cap}}{v_{\rm inner}} = \frac{(a - R_{\rm cap})\ R_{0_{\rm star}}}{r_{\rm inner} v_{0_{\rm star}}}, \tag{A.1}$$

namely the time when $r_{\rm inner}$ reaches the capture region which is located at a distance $r = a - R_{\rm cap}$ from the $\mathrm{CO}_{\rm core}$ center. The radius $r_{\rm inner}$ is the maximum of the density profile (1.7), namely the root of the equation:

$$r_{\rm inner} - R_{0_{\rm star}} + R_{0_{\rm star}} m \ln\left(\frac{r_{\rm inner}}{\hat{R}_{\rm core}}\right) = 0, \tag{A.2}$$

where we recall $\hat{R}_{\rm core} \approx 0.31 R_{\rm core}$. Since $r_{\rm inner} \approx \hat{R}_{\rm core}$, we can obtain the approximate solution:

$$r_{\rm inner} \approx \varsigma R_{\rm core}, \qquad \varsigma \equiv \frac{R_{0_{\rm star}}}{R_{\rm core}} \frac{1 + m}{1 + m(R_{0_{\rm star}}/\hat{R}_{\rm core})}. \tag{A.3}$$

Since $v_{\rm inner} < v_{\rm orb}$, we can approximate the relative velocity as given only by the orbital one, i.e. $v_{\rm rel} \approx v_{\rm orb}$, and within this approximation, the capture radius reduces to $R_{\rm cap} \approx (2M_{\rm NS}/M)a$. Then, equation (A.1) becomes

$$t_{\rm peak} \approx \left(1 - \frac{2M_{\rm NS}}{M}\right)\left(\frac{GM}{4\pi^2}\right)^{1/3}\left(\frac{R_{0_{\rm star}}}{\varsigma R_{\rm core}}\right)\frac{P^{2/3}}{v_{0_{\rm star}}}. \tag{A.4}$$

We can now evaluate equation (1.1) at the above $t = t_{\rm peak}$ and applying the same

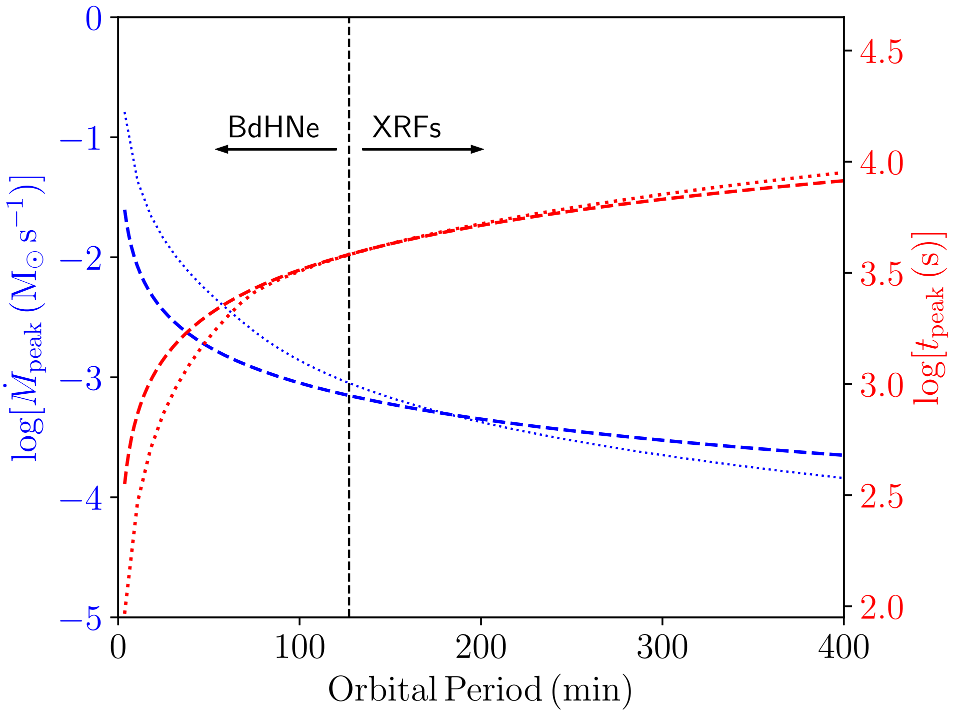

Figure A.1.: Peak accretion rate ($\dot{M}_{\rm peak}$, blue curves and left y-scale) and peak time ($t_{\rm peak}$, red curves and right y-scale) as a function of the orbital period. The dashed curves give the analytic peak accretion rate and time (A.5) and (A.4), respectively, while the dotted curves correspond to the values obtained from the numerical integration of the equations in Sec. 1.2. This example corresponds to the following binary parameters: a CO core from the $M_{\rm ZAMS} = 20\ M_\odot$ progenitor of Table 1.1, an initial NS mass $2.0\ M_\odot$, and a velocity of the outermost ejecta layer $v_{\rm star,0} = 2\times10^9$ cm s^{-1}. For these parameters we have $\eta \approx 0.41$ from equation (A.3). The black dashed vertical line marks the maximum orbital period (for these system parameters, $P_{\rm max} \approx 127$ min) for which the NS reaches, by accretion, the critical mass and collapses to a BH (see Figure 2.2 in Section 2.2). We recall that within the IGC interpretation systems with $P < P_{\rm max}$ lead to BdHNe while systems with $P > P_{\rm max}$ lead to XRFs.

approximations, we obtain for the peak accretion rate

$$\dot{M}_{\rm peak} \approx 2\pi^2 \frac{(2M_{\rm NS}/M)^{5/2}}{(1-2M_{\rm NS}/M)^3}\eta^{3-m}\frac{\rho_{\rm core}\,R_{\rm core}^3}{P}, \tag{A.5}$$

where we recall $M = M_{\rm CO} + M_{\rm NS}$ is the total binary mass, being $M_{\rm CO} = M_{\rm env} + M_{\nu{\rm NS}}$ the total mass of the CO$_{\rm core}$ given by the envelope mass and the central iron core mass leading to the formation of the νNS.

Figure A.1 shows the behavior of equations (A.5) and (A.4) as a function of the orbital period and compare them with the corresponding values obtained from the numerical integration of the accretion equations presented in Section 1.2. This example is for the binary parameters: a CO$_{\rm core}$ from the $M_{\rm ZAMS} = 20\ M_\odot$ progenitor of Table 1.1, an initial NS mass $2.0\ M_\odot$, and a velocity of the outermost ejecta layer $v_{\rm star,0} = 2\times10^9$ cm s^{-1}. For these parameters, $\varsigma \approx 0.41$ from equation (A.3). It can be seen that the accuracy of the above simple analytic formulas increases for the systems with $P > P_{\rm max}$. This is expected since, as we have mentioned, only for these systems the innermost ejecta layers passed the NS position. In systems with $P < P_{\rm max}$, the NS collapses to a BH before the passage of the innermost layers. In those cases, the maximum accretion rate is not reached at the passage of $r_{\rm inner}$ but at the passage of a layer located at $r_{\rm max} > r_{\rm inner}$, hence with velocity $v_{\rm max} = v(r = r_{\rm max}) > v_{\rm inner}$, and thus $v_{\rm max} \gtrsim v_{\rm orb}$. In any case, it is clear the above formulas for $\dot{M}_{\rm peak}$ and $t_{\rm peak}$ remain valid to obtain typical (order-of-magnitude) estimates of the accretion process in these binaries. The consistency of the numerical and analytic results (within their range of validity) shown here serves as well as an indicator of the reliability of the numerical results.

A.2. Uniformly Rotating Neutron Star Structure

The contents of this appendix are based on the work of Cipolletta et al. [49]. The interior and exterior metric of a uniformly rotating NS can be written in the form of the stationary axisymmetric spacetime metric

$$ds^2 = -e^{2\nu}dt^2 + e^{2\psi}(d\phi - \omega dt)^2 + e^{2\lambda}(dr^2 + r^2 d\theta^2), \tag{A.6}$$

where ν, ψ, ω and λ depend only on variables r and θ. It is useful to introduce the variable $e^{\psi} = r\sin(\theta)Be^{-\nu}$, being again $B = B(r, \theta)$. The energy-momentum tensor of the NS interior is given by

$$T^{\alpha\beta} = (\varepsilon + P)u^{\alpha}u^{\beta} + Pg^{\alpha\beta}, \tag{A.7}$$

where ε and P denote the energy density and pressure of the fluid, and u^{α} is the fluid 4-velocity. Thus, with the metric given by equation (A.6) and the energy-momentum tensor given by equation (A.7), one can write the field equations as (setting $\zeta = \lambda + \nu$):

$$\nabla \cdot (B\nabla\nu) = \frac{1}{2}r^2\sin^2\theta B^3 e^{-4\nu}\nabla\omega \cdot \nabla\omega + 4\pi B e^{2\zeta - 2\nu}\left[\frac{(\varepsilon + P)(1 + v^2)}{1 - v^2} + 2P\right], \tag{A.8}$$

$$\nabla \cdot \left(r^2\sin^2\theta B^3 e^{-4\nu}\nabla\omega\right) = -16\pi r\sin\theta B^2 e^{2\zeta - 4\nu}\frac{(\varepsilon + P)v}{1 - v^2}, \tag{A.9}$$

$$\nabla \cdot (r\sin(\theta)\nabla B) = 16\pi r\sin\theta B e^{2\zeta - 2\nu}P, \tag{A.10}$$

$$\begin{aligned}
\zeta_{,\mu} = & - \Bigg\{\left(1 - \mu^2\right)\left(1 + r\frac{B_{,r}}{B}\right)^2 + \left[\mu - \left(1 - \mu^2\right)\frac{B_{,r}}{B}\right]^2\Bigg\}^{-1}\Bigg[\frac{1}{2}B^{-1}\big\{r^2 B_{,rr} \\
& - \left[\left(1 - \mu^2\right)B_{,\mu}\right]_{,\mu} - 2\mu B_{,\mu}\big\}\Bigg\{-\mu + \left(1 - \mu^2\right)\frac{B_{,\mu}}{B}\Bigg\} + r\frac{B_{,r}}{B}\Bigg[\frac{1}{2}\mu + \mu r\frac{B_{,r}}{B} \\
& + \frac{1}{2}\left(1 - \mu^2\right)\frac{B_{,\mu}}{B}\Bigg] + \frac{3}{2}\frac{B_{,\mu}}{B}\left[-\mu^2 + \mu\left(1 - \mu^2\right)\frac{B_{,\mu}}{B}\right] - \left(1 - \mu^2\right)r\frac{B_{,\mu r}}{B}\left(1 + r\frac{B_{,r}}{B}\right) \\
& - \mu r^2(\nu_{,r})^2 - 2\left(1 - \mu^2\right)r\nu_{,\mu}\nu_{,r} + \mu\left(1 - \mu^2\right)(\nu_{,\mu})^2 - 2\left(1 - \mu^2\right)r^2 B^{-1}B_{,r}\nu_{,\mu}\nu_{,r} \\
& + \left(1 - \mu^2\right)B^{-1}B_{,\mu}\left[r^2(\nu_{,r})^2 - \left(1 - \mu^2\right)(\nu_{,\mu})^2\right] + \left(1 - \mu^2\right)B^2 e^{-4\nu}\Bigg\{\frac{1}{4}\mu r^4(\omega_{,r})^2 \\
& + \frac{1}{2}\left(1 - \mu^2\right)r^3\omega_{,\mu}\omega_{,r} - \frac{1}{4}\mu\left(1 - \mu^2\right)r^2(\omega_{,\mu})^2 + \frac{1}{2}\left(1 - \mu^2\right)r^4 B^{-1}B_{,r}\omega_{,\mu}\omega_{,r} \\
& - \frac{1}{4}\left(1 - \mu^2\right)r^2 B^{-1}B_{,\mu}\left[r^2(\omega_{,r})^2 - \left(\mu^2\right)(\omega_{,\mu})^2\right]\Bigg\}\Bigg],
\end{aligned} \tag{A.11}$$

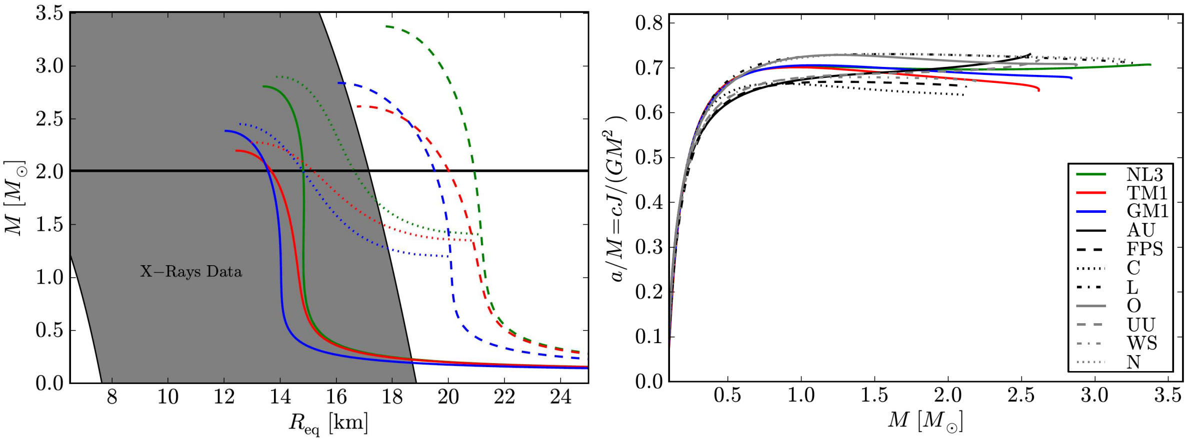

Figure A.2.: *Left:* Mass versus equatorial radius for the TM1 (red line), GM1 (blue line) and NL3 (green line) EOS. It's represented the static sequence (solid line), rotating sequence at the faster observed pulsar (PSR J1748-2446ad) spin frequency, $f = 716$ Hz [115] (dotted line) and the keplerian sequence (dashed line) of NS configurations. The shadow region represents observational limits on the NS radius derived from NS x-ray emission. *Right:* Dimensionless angular momentum, $a/M \equiv cJ/(GM^2)$, in function of the NS mass. The NS configurations correspond to the keplerian sequence for various EOS.
NOTE—Pictures taken from Cipolletta et al. [49]

where, in the equation for $\zeta_{,\mu}$, we introduced $\mu \equiv \cos(\theta)$.

We can integrate numerically the above Einstein equations once a relation between ε and P is given, namely an equation of state (EOS). The NS interior is made of a core and a crust. The core of the star has densities higher than the nuclear value, $\rho_{\rm nuc} \approx 3 \times 10^{14}$ g cm^{-3}, and it is composed by a degenerate gas of baryons (e.g. neutrons, protons, hyperons) and leptons (e.g. electrons and muons). The crust, in its outer region ($\rho \leq \rho_{\rm drip} \approx 4.3 \times 10^{11}$ g cm^{-3}), is composed of ions and electrons, and in the so-called inner crust ($\rho_{\rm drip} < \rho < \rho_{\rm nuc}$), there are also free neutrons that drip out from the nuclei. For the crust, we adopt the Baym-Pethick-Sutherland (BPS) EOS [12]. For the core, we here adopt modern models based on relativistic mean-field (RMF) theory, which have Lorentz covariance, intrinsic inclusion of spin, a simple mechanism of saturation for nuclear matter, and they do not violate causality. We use an extension of the formulation of Boguta & Bodmer [26] with a massive scalar meson (sigma) and two vector meson (omega and rho) mediators, and possible interactions between them.

With the knowledge of the EOS we can compute equilibrium configurations integrating the above equations for suitable initial conditions, for instance central density and angular momentum (or angular velocity) of the star. Then, after integrating the Einstein equations, properties of the NS can be obtained for the given central density and angular momentum such as the total gravitational mass, the total baryon mass, polar and equatorial radii, moment of inertia, quadrupole moment, etc. In Figure A.2 is shown the mass-radius relations for the three EOS study in Cipolletta et al. [49]. These three representative EOS satisfy the astrophysical constraint of leading to a NS critical mass larger than the heaviest massive NS observed, PSR J0348+0432, with $M = 2.01 \pm 0.04\, M_\odot$ [3]. For the present problem of accretion onto the NS, as we have mentioned in Chapter 1, an important relation to be obtained from the NS equilibrium properties, is the one between the total baryon rest-mass, M_b, and the gravitational mass, $M_{\rm NS}$, namely the gravitational binding energy of the NS; see equation (1.35). For non-rotating configurations, Cipolletta

Table A.1.: Critical mass and corresponding radius for selected parametrizations of nuclear EOS

EOS	$M_{\rm crit}^{J=0}$	$R_{\rm crit}^{J=0}$	$M_{\rm max}^{J\neq 0}$	$R_{\rm max}^{J\neq 0}$	p	k	f_K	$M_{\rm min}^{j=0}$	c_1	c_2
	$(M_\odot)$	(km)	$(M_\odot)$	(km)			(kHz)	$(M_\odot)$		
NL3	2.81	13.49	3.38	17.35	1.68	0.006	1.34	1.68	0.225	0.94
GM1	2.39	12.56	2.84	16.12	1.69	0.011	1.49	1.57	0.238	0.94
TM1	2.20	12.07	2.62	15.98	1.61	0.017	1.40	1.61	0.238	0.94

NOTE — In the eighth column it is also reported the rotation frequency of the critical mass configuration in the rotating case. This value corresponds to the frequency of the last configuration along the secular axisymmetric instability line, i.e the configuration that intersects the Keplerian mass-shedding sequence.
REFERENCES — Cipolletta et al. [49]

et al. [49] obtained an EOS-independent relation:

$$\frac{M_b}{M_\odot} = \frac{M_{\rm NS}}{M_\odot} + \frac{13}{200}\left(\frac{M_{\rm NS}}{M_\odot}\right)^2 . \tag{A.12}$$

For the non-zero angular momentum configurations we are interested at, Cipolletta et al. [49] obtained

$$\frac{M_b}{M_\odot} = \frac{M_{\rm NS}}{M_\odot} + \frac{13}{200}\left(\frac{M_{\rm NS}}{M_\odot}\right)^2 \left(1 - \frac{1}{130} j_{\rm NS}^{1.7}\right), \tag{A.13}$$

where $j_{\rm NS} \equiv c J_{\rm NS}/(G M_\odot^2)$. This formula is accurate within an error of 2% and it correctly generalizes the above equation (A.12), approaching it in the limit $j_{\rm NS} \to 0$. This relation has been shown to be very accurate also in the description fo the binding energy of other EOS model including hyperonic and hybrid ones [20].

The NS can accrete mass until it reaches a region of instability. There are two main instability limits for rotating NSs, namely the mass-shedding or Keplerian limit, and the secular axisymmetric instability. Cipolletta et al. [49] shows that along the mass-shedding sequence, the NS has the maximum possible angular momentum: $J_{\rm NS,max} = 0.7\, G\, M_{\rm NS}^2\, /\, c$ (see Figure A.2). Cipolletta et al. [49] also shows that the critical NS mass along the secular instability line, is approximately given by:

$$M_{\rm NS}^{\rm crit} = M_{\rm NS}^{J=0}(1 + k j_{\rm NS}^p)\,, \tag{A.14}$$

where the parameters k and p depends on the nuclear EOS (see Table A.1). These formulas fit the numerical results with a maximum error of 0.45%. It can be checked that the latter is, as expected, below the 3.2 $M_\odot$ critical mass upper bound by Rhoades & Ruffini [224].

Finally, if the NS is accreting from a disk, the angular momentum gained by the star will depend on the specific angular momentum of the particles at the inner disk radius will. The inner radius of the disk is given by the last stable orbit, $r_{\rm lso}$, in the case in which it is located outside the NS, otherwise it equals the NS equatorial radius, $R_{\rm NS}$. Cipolletta et al. [50] obtained a fitting function of the minimum NS mass, $M_{\rm min}$, for which given a value of the angular momentum one has $r_{\rm lso} \geq R_{\rm NS}$:

$$\frac{M_{\rm min}}{M_\odot} = \frac{M_{\rm min}^{j=0}}{M_\odot} + c_1 j^{c_2} \tag{A.15}$$

where $M_{\rm min}^{j=0}$, c_1 and c_2 are dimensionless constants that will depend of the EOS (see Table A.1).

In addition to the above relations, we have used in this work an analytic formula, equation (1.39) obtained by Cipolletta et al. [50], which gives us the angular momentum of the mostly bound circular orbit around a uniformly rotating NS, as a function of the NS mass and angular momentum. Such a relation has allowed us to perform the simulations of the evolution of the accreting NS in a semianalytic fashion, including dynamically the feedback of the increase of the NS mass and angular momentum into the exterior geometry.

B. Appendix for Chapter III

B.1. Electron-positron pair anhilation process

In this Appendix, following Yakovlev et al. [316] we going to analyse the process of neutrino-pair emission due to the annihilation of electron-positron pairs:

$$e^{+} + e^{-} \rightarrow \nu + \bar{\nu}\,. \tag{B.1}$$

We wiill adopt the units $\hbar = c = \kappa_B = 1$. This process is most efficient in the low-density and high-temperature plasma, where rhe positron fraction is the highest. In a strongly degenerate electron plasma, the process is suppressed because of the negligibly small positron fraction.

The pair annihilation is the simplest neutrino process described by one four-tail Feynman diagram. The interaction hamiltonian is:

$$\hat{H} = \frac{G_F}{\sqrt{2}} J_\alpha l^\alpha \ , \tag{B.2}$$

with

$$l^\alpha = \bar{\psi}'_\nu \gamma^\alpha (1 + \gamma^5) \psi_\nu \quad \text{and} \qquad J^\alpha = \bar{\psi}'_e \gamma^\alpha (C_V + C_A \gamma^5) \psi_e \tag{B.3}$$

where l^α and $J = (J^0, \vec{J})$ are the neutrino weak and the weak electron-positron 4-currents, respectively, γ^α and γ^5 are the Dirac matrices, ψ_ν, ψ'_ν, ψ_e and ψ'_e are the neutrino , antineutrino, electron and positron wave fuctions, repectively , and $\bar{\psi}_\nu$ denotes the Dirac conjugate. The weak electron current consistes of the vector and axial-vector terms containing the vector and axial-vector constants, C_V and C_A, respectively. Emision of electron neutrinos, $\nu_e\bar{\nu}_e$, goes via either charged and neutral electroweak currents, and the amplitudes of both reactions channels are summed coherently: $C_{Ve} = 2\sin^2\theta_W + 0.5$ and $C_{Ae} = 0.5$. Emission of the muon, $\nu_\mu\bar{\nu}_\mu$, and tau, $\nu_\tau\bar{\nu}_\tau$ neutrinos can only go through neutral electroweak currents, so: $C_{V\mu} = C_{V\tau} = 2\sin^2\theta_W - 0.5$ and $C_{A\mu} = C_{V\mu} = -0.5$.

The wave functions are taken in the form:

$$\psi_\nu = \frac{u_\nu}{\sqrt{2\epsilon_\nu}} \mathrm{e}^{ip_\nu x} \quad ; \quad \psi'_\nu = \frac{u'_\nu}{\sqrt{2\epsilon'_\nu}} \mathrm{e}^{-ip'_\nu x} \quad ; \quad \psi_e = \frac{u_e}{\sqrt{2\epsilon_e}} \mathrm{e}^{-ip_e x} \quad ; \quad \psi'_e = \frac{u'_e}{\sqrt{2\epsilon'_e}} \mathrm{e}^{ip'_e x} \tag{B.4}$$

where $x = (t, \vec{r})$ is the 4-vector of time-space coordinate, $p_\nu = (\epsilon_\nu, \vec{p_\nu})$, $p'_\nu = (\epsilon'_\nu, \vec{p_\nu}\,')$, $p_e = (\epsilon_e, \vec{p_e})$ and $p'_e = (\epsilon'_e, \vec{p_e}\,')$ are the particles 4-momentum, while u_ν and u'_ν are the standard bispinors and $\bar{u}_e u_e = \bar{u}'_e u'_e = 2m_e$.

The general expresion for the neutrino emissibity, $\epsilon_{e^-e^+}$, is:

$$\epsilon_{e^-e^+} = (2\pi)^4 \frac{G_F^2}{2} \sum_{\nu} \int \frac{d\vec{p}_e}{(2\pi)^3} \frac{d\vec{p}_e{}'}{(2\pi)^3} \frac{d\vec{p}_\nu}{(2\pi)^3} \frac{d\vec{p}_\nu{}'}{(2\pi)^3} (\epsilon_\nu + \epsilon'_\nu) f_e f'_e \delta^{(4)}(p_e + p'_e - p_\nu - p'_\nu) \mathcal{L}^{\alpha\beta} \mathcal{J}_{\alpha\beta} \tag{B.5}$$

where f_e and f'_e are the Fermi-Dirac distribution of the electron and positron and the sumation is over all neutrino flavors. The last term of equation (B.5) is equals to:

$$\begin{aligned} \mathcal{L}^{\alpha\beta} \mathcal{J}_{\alpha\beta} &= \frac{4}{\epsilon_e \epsilon'_e \epsilon_\nu \epsilon'_\nu} [(p_e p_\nu)(p'_e p'_\nu)(C_V + C_A)^2 \\ &\quad + (p_e p'_\nu)(p'_e p_\nu)(C_V - C_A)^2 + m_e^2 (C_V^2 - C_A^2)(p_\nu p'_\nu)] \end{aligned} \tag{B.6}$$

When equation (B.5) is integrated over $d\vec{p}_\nu$ and $d\vec{p}_\nu{}'$ with the Lenard indentity, the final pair anihilation emissivity reduces to:

$$\epsilon_{e^-e^+} = (2\pi)^4 \frac{G_F^2 m_e^4}{3(2\pi)^7} \int d\vec{p}_e d\vec{p}_e{}' \sigma_D \, f_e f'_e \frac{\epsilon_e + \epsilon'_e}{\epsilon_e \epsilon'_e} \tag{B.7}$$

whit σ_D the Dicus cross section [63]:

$$\sigma_D = C_+^2 \left(1 + 3 \frac{p_e \cdot p'_e}{m_e^2} + 2 \frac{(p_e \cdot p'_e)^2}{m_e^4} \right) + 3 C_-^2 \left(1 + \frac{p_e \cdot p'_e}{m_e^2} \right) \tag{B.8}$$

where $C_+^2 = \sum_\nu (C_V^2 + C_A^2)$ and $C_-^2 = \sum_\nu (C_V^2 - C_A^2)$. The emissivity for any selected neutrino flavor can be obtained recalculating $C_\pm^2$. In a streihgforward way, the information about the neutrino and antineutrino can be calculated from the integral, in standard physical units:

$$\varepsilon^m = \frac{2 G_F^2 (m_e c^2)^4}{3 (2\pi\hbar)^7 (\hbar c)^3} \int f_e f'_e \frac{\epsilon_e^m + \epsilon_e'^m}{\epsilon_e \epsilon'_e} \sigma_D d\vec{p}_e d\vec{p}_e{}' \tag{B.9}$$

Then $\epsilon_{e^-e^+} = \varepsilon^1$, while the number emissivity is $n = \varepsilon^0$. Also, the neutrinos or antirneutrino energy moments are: $\langle E_{\nu(\bar{\nu})} \rangle = \varepsilon^m / \varepsilon^0$. For a relativistic, non-degenerate plasma ($\kappa_B T > 2 m_e c^2$ and $1 > \eta_{e^\pm}$), the last equation can be approximated with a very good accuracy by:

$$\varepsilon^m \approx \frac{2 G_F^2 (\kappa_B T)^{8+m}}{9 \pi^5 \hbar \, (\hbar c)^9} C_+^2 \left[\mathcal{F}_{m+1}(\eta_{e^+}) \mathcal{F}_1(\eta_{e^-}) + \mathcal{F}_{m+1}(\eta_{e^-}) \mathcal{F}_1(\eta_{e^+}) \right] \tag{B.10}$$

where $\mathcal{F}_k(\eta) = \int_0^\infty dx \, x^k / (1 + \exp(x - \eta))$.

C. Appendix for Chapter V

C.1. SPH convergence test

In this Appendix we will evaluate the convergence of the SPH simulation of the IGC scenario. To this task, we have done numerical experiment varying the number of the particles of the simulation with which we model the SF ejecta material for the different progenitors of the $\mathrm{CO_{core}}$ (see Table 5.1).

We did simulations with $\sim$ 1, 1.5, 2 and 3 millions particles with different progenitors and with different values of the ξ parameter that determines the size of the particles radius capture (see equation (5.15)). We have resumed the results of these simulations in Table C.1. We compared the final accreted mass and angular momentum of the binary stars: the νNS and the NS companion, the final orbital period and final eccentricity of the orbit. We also report the relative error of these quantities taking as the reference values the ones of the simulation with around 1 million of particles.

In Figure C.1 is shown profiles of the density on the binary orbital plane and along different direction, taking the NS companion as the center of the reference frame. In Figure C.2, it's also shown the mass accretion rate on the νNS and the NS companion. Finally, in Figure C.3, it's presented the flux of mass and angular momentum on the NS companion at two different distances from it: $0.02\,R_{\odot}$ and at r_{cap}, defined as the maximum particles radius capture between the particles accreted by the NS in each iteration. All these figures corresponds to the simulation of an initial binary system forms by the $\mathrm{CO_{core}}$ of the $M_{\mathrm{ZAMS}}25\,M_{\odot}$ progenitor (see Table 5.1) and a $2\,M_{\odot}$ NS with an initial orbital period of ≈ 2 min.

Table C.1.: Convergence study of the SPH simulation of the IGC scenario. For each simulation, in the four first columns is shown the progenitor of the $\mathrm{CO}_{\mathrm{core}}$, the number of particles used in the simulation, the η factor with which was scaled the kinetic and internal energy of the SPH-particles in order to mimic an weaker ($\eta < 1$) or stronger ($\eta > 1$) SN explosion and the ξ parameter that determines the size of the particles capture radius. In the following columns it's shown the final mass and angular momentum of the νNS and the NS companion as well as the period and eccentricity of the final binary system orbit. For each of these values is shown the relative errors with respect to the 1 million particles simulation

Progenitor M_{ZAMS}	N million	η	ξ	$m_{\nu ns}$ ($M_\odot$)	$\mathrm{Er}(m_{\nu ns})$	$L_{\nu ns}$ ($10^{51}\,\mathrm{g\,cm^2\,/\,s}$)	$\mathrm{Er}(L_{\nu ns})$	m_{ns} ($M_\odot$)	$\mathrm{Er}(m_{\mathrm{ns}})$	L_{ns} ($10^{51}\,\mathrm{g\,cm^2\,/\,s}$)	$\mathrm{Er}(L_{\mathrm{ns}})$	$p_{\mathrm{orb,f}}$ (s)	$\mathrm{Er}(p_{\mathrm{orb}})$	e	$\mathrm{Er}(e)$
$25M_\odot$	1.0	1.0	0.1	1.964		3.478		2.078		3.288		6298.29		0.860	
	1.5			1.951	0.0066	3.522	0.0127	2.064	0.0067	3.323	0.0106	8274.54	0.3137	0.883	0.0267
	2.0			1.943	0.0106	3.455	0.0066	2.065	0.0063	3.250	0.0115	7868.58	0.2493	0.880	0.0232
	3.0			1.935	0.0147	3.482	0.0012	2.051	0.0129	3.292	0.0012	10744.9	0.706	0.897	0.0430
	1.0	1.0	0.5	1.915		3.627		2.126		3.255		9843.52		0.892	
	1.5			1.906	0.0046	3.434	0.053	2.099	0.0126	3.118	0.0428	14031.1	0.4254	0.923	0.0348
	2.0			1.900	0.0078	3.499	0.035	2.102	0.0112	3.155	0.0307	12871.2	0.3075	0.913	0.0235
	1.0	1.0	1.0	1.937		3.669		2.209		3.217		91557.2		0.979	
	1.5			1.926	0.0056	3.119	0.1499	2.189	0.0091	2.745	0.1467	25489.6	0.7215	0.962	0.0174
	2.0			1.919	0.0092	3.461	0.0566	2.179	0.0135	3.047	0.0528	145340.6	0.5874	0.985	0.0061
$30M_\odot$ [1]	1.0	2.0	0.1	1.783		4.499		2.077		3.861		–		1.44	
	2.0			1.772	0.0061	4.451	0.0106	2.043	0.0164	3.859	0.00051	–		1.50	0.0416
	1.0	2.0	1.0	1.781		4.087		2.172		3.351		–		1.38	
	2.0			1.769	0.0067	4.614	0.1289	2.115	0.0262	3.859	0.1550	–		1.55	0.1096
$40M_\odot$	1.0	1.0	0.1	1.875		4.419		2.124		3.902		–		1.84	
	2.0			1.869	0.0032	4.276	0.0323	2.069	0.0259	3.862	0.0102	–		2.00	0.0869

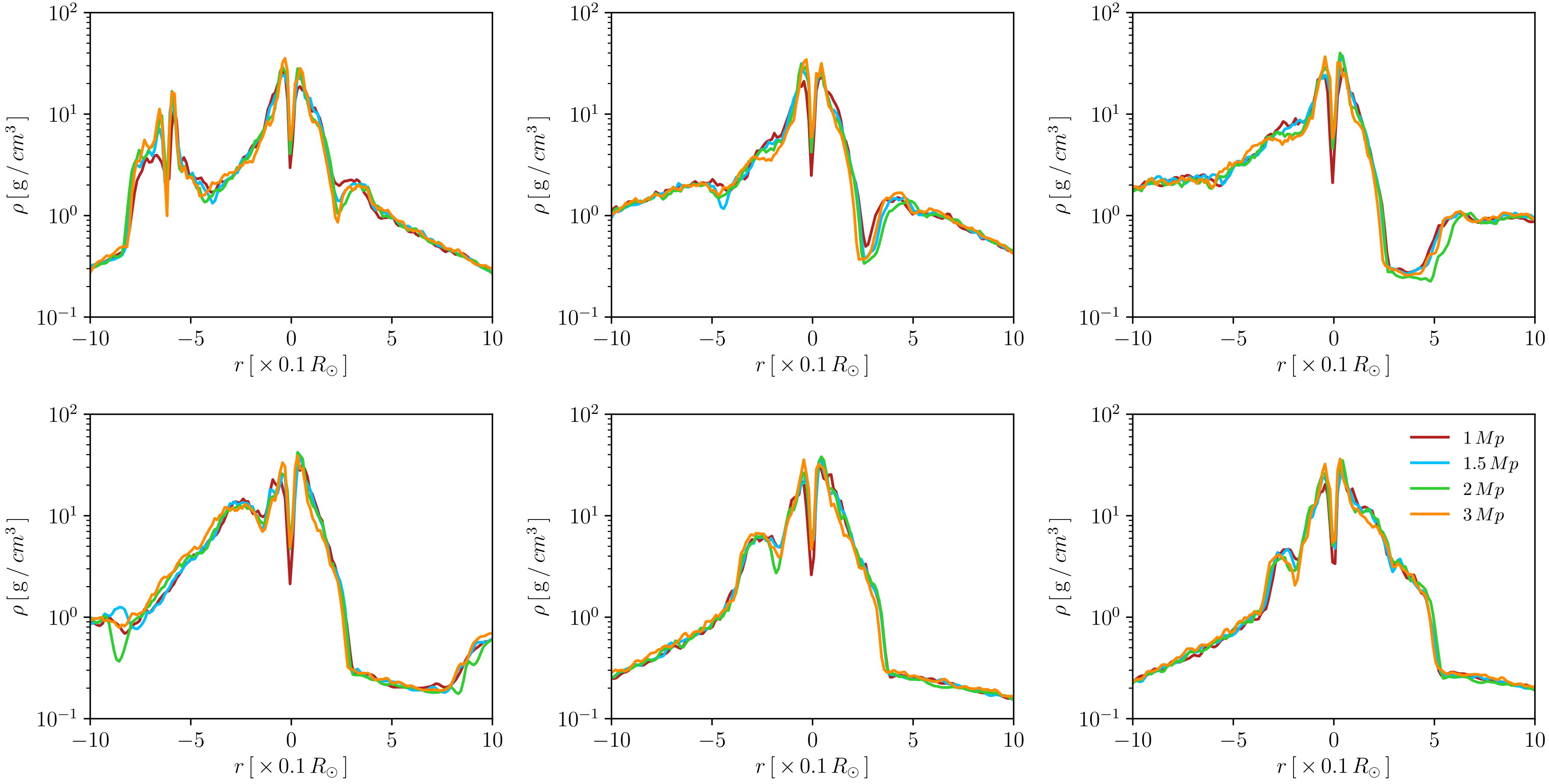

Figure C.1.: Density along different directions θ on the orbital binary system plane (νNS-NS). From left to right of upper panel: $\theta = 0.0$, $\pi/6$ and $\pi/3$ and in the bottom panel $\theta = \pi/2$, $2\pi/3$ and $5\pi/6$. The center of the reference system is on the NS position and the νNS is on the $-x$ axis. The θ direction if measured from the $+x$ axis. The initial binray system is form by the $\mathrm{CO}_{\mathrm{core}}$ of the $M_{\mathrm{ZAMS}} = 25\,M_\odot$ progenitor and a $2\,M_\odot$ NS in a orbital period of about 5 min. Different colors correspond to different number of particles: 1 million (red line), 1.5 million (blue line), 2 million (green line) and 3 million (orange line.

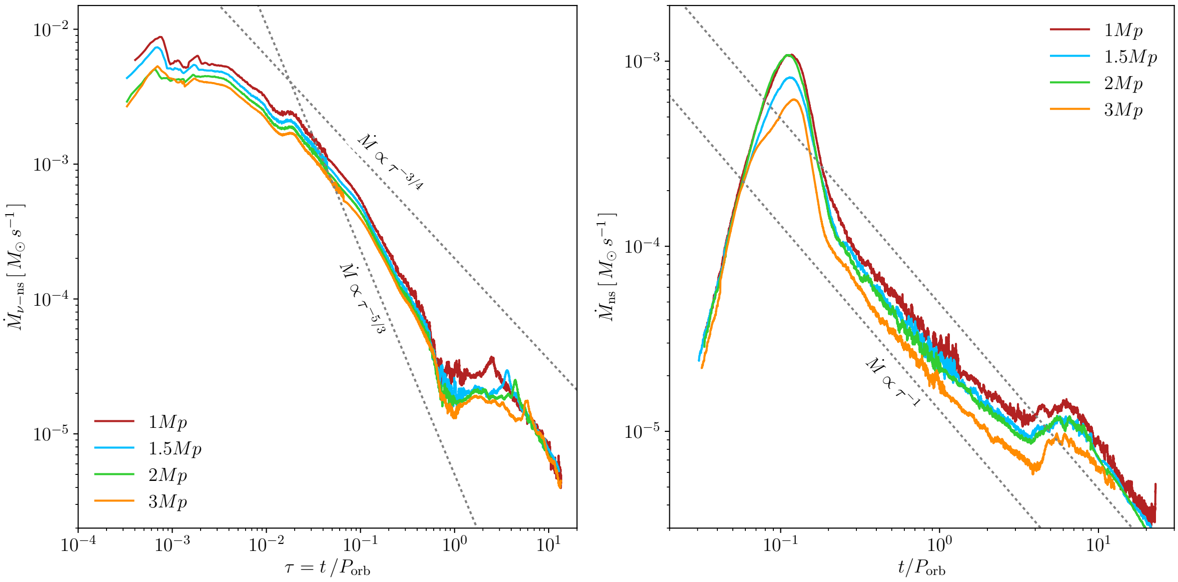

(a) νNS

(b) NS

Figure C.2.: Mass accretion rate on the nuNS (left panel) and the NS companion (right panel) for different number of particles modeling the SN expansion in the simulation. The initial binary period is the same as in Figure C.1

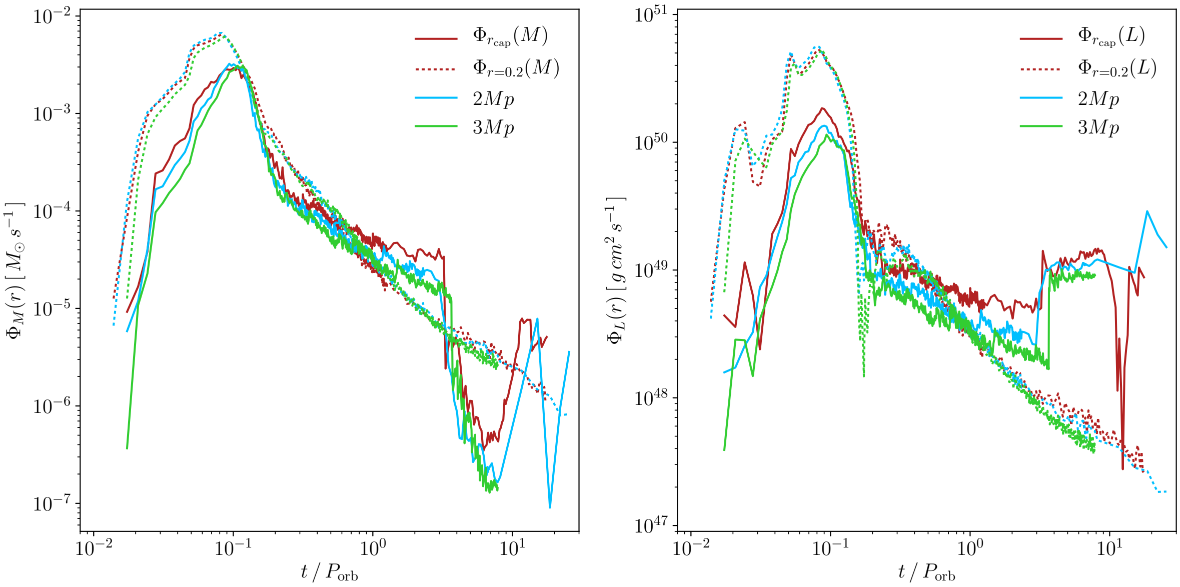

(a) Mass flux

(b) Angular momentum flux

Figure C.3.: Mass (left panel) and angular momentum flux (right panel) thought spheres of radius $r = 0.2\,R_\odot$ and $r = R_{\rm cap}$ with the NS in the center. The $R_{\rm cap}$ surface is defined as the maximum particle radius capture between the particles accreted by the NS in each iteration. The initial binary period is the same as in Figure C.1

List of Figures

List of Tables

Bibliography

[1] Abe, K., Abe, T., Aihara, H., et al., Letter of Intent: The Hyper-Kamiokande Experiment — Detector Design and Physics Potential —, ArXiv e-prints. 2011

[2] Amati, L., & Della Valle, M., Measuring Cosmological Parameters with Gamma Ray Bursts, International Journal of Modern Physics D, 22, 1330028. 2013

[3] Antoniadis, J., Freire, P. C. C., Wex, N., et al., A Massive Pulsar in a Compact Relativistic Binary, Science, 340, 448. 2013

[4] Anzer, U., Boerner, G., & Monaghan, J. J., Numerical studies of wind accretion, A&A, 176, 235. 1987

[5] Armitage, P. J. 2009, Astrophysics of Planet Formation (Cambridge University Press)

[6] Atwood, W. B., Abdo, A. A., Ackermann, M., et al., The Large Area Telescope on the Fermi Gamma-Ray Space Telescope Mission, ApJ, 697, 1071. 2009

[7] Aznar-Siguán, G., García-Berro, E., Lorén-Aguilar, P., José, J., & Isern, J., Detonations in white dwarf dynamical interactions, MNRAS, 434, 2539. 2013

[8] Aznar-Siguán, G., García-Berro, E., Lorén-Aguilar, P., Soker, N., & Kashi, A., Smoothed particle hydrodynamics simulations of the core-degenerate scenario for Type Ia supernovae, MNRAS, 450, 2948. 2015

[9] Barthelmy, S. D., Baumgartner, W. H., Cummings, J. R., et al., GRB 120422A: Swift-BAT refined analysis., GRB Coordinates Network, Circular Service, No. 13246, #1 (2012), 13246. 2012

[10] Bate, M. R., Bonnell, I. A., & Price, N. M., Modelling accretion in protobinary systems, MNRAS, 277, 362. 1995

[11] Bayless, A. J., Even, W., Frey, L. H., et al., The Effects on Supernova Shock Breakout and Swift Light Curves Due to the Mass of the Hydrogen-rich Envelope, ApJ, 805, 98. 2015

[12] Baym, G., Pethick, C., & Sutherland, P., The Ground State of Matter at High Densities: Equation of State and Stellar Models, ApJ, 170, 299. 1971

[13] Becerra, L., Bianco, C. L., Fryer, C. L., Rueda, J. A., & Ruffini, R., On the Induced Gravitational Collapse Scenario of Gamma-ray Bursts Associated with Supernovae, ApJ, 833, 107. 2016

[14] Becerra, L., Cipolletta, F., Fryer, C. L., Rueda, J. A., & Ruffini, R., Angular Momentum Role in the Hypercritical Accretion of Binary-driven Hypernovae, ApJ, 812, 100. 2015

[15] Beloborodov, A. M., Magnetically powered outbursts from white dwarf mergers, MNRAS, 438, 169. 2014

[16] Benz, W. 1990, in Numerical Modelling of Nonlinear Stellar Pulsations Problems and Prospects, ed. J. R. Buchler, 269

[17] Benz, W., Cameron, A. G. W., Press, W. H., & Bowers, R. L., Dynamic mass exchange in doubly degenerate binaries. I - 0.9 and 1.2 solar mass stars, ApJ, 348, 647. 1990

[18] Benz, W., Thielemann, F.-K., & Hills, J. G., Three-dimensional hydrodynamical simulations of stellar collisions. II - White dwarfs, ApJ, 342, 986. 1989

[19] Bethe, H. A., & Brown, G. E., Evolution of Binary Compact Objects That Merge, ApJ, 506, 780. 1998

[20] Bhattacharyya, S., Bombaci, I., Bandyopadhyay, D., Thampan, A. V., & Logoteta, D., Millisecond radio pulsars with known masses: Parameter values and equation of state models, New Astronomy, 54, 61. 2017

[21] Bisnovatyi-Kogan, G. S., Asymmetric neutrino emission and formation of rapidly moving pulsars, Astronomical and Astrophysical Transactions, 3, 287. 1993

[22] Blandford, R. D., & Begelman, M. C., On the fate of gas accreting at a low rate on to a black hole, MNRAS, 303, L1. 1999

[23] Blandford, R. D., & Payne, D. G., Hydromagnetic flows from accretion discs and the production of radio jets, MNRAS, 199, 883. 1982

[24] Blandford, R. D., & Znajek, R. L., Electromagnetic extraction of energy from Kerr black holes, MNRAS, 179, 433. 1977

[25] Bloom, J. S., Kulkarni, S. R., Djorgovski, S. G., et al., The unusual afterglow of the γ-ray burst of 26 March 1998 as evidence for a supernova connection, Nature, 401, 453. 1999

[26] Boguta, J., & Bodmer, A. R., Relativistic calculation of nuclear matter and the nuclear surface, Nuclear Physics A, 292, 413. 1977

[27] Bondi, H., On spherically symmetrical accretion, MNRAS, 112, 195. 1952

[28] Bondi, H., & Hoyle, F., On the mechanism of accretion by stars, MNRAS, 104, 273. 1944

[29] Boshkayev, K., Quevedo, H., & Ruffini, R., Gravitational field of compact objects in general relativity, Phys. Rev. D, 86, 064043. 2012

[30] Boshkayev, K., Rueda, J. A., Ruffini, R., & Siutsou, I., On General Relativistic Uniformly Rotating White Dwarfs, ApJ, 762, 117. 2013

[31] Boshkayev, K. A., Quevedo, H., Abutalip, M. S., Kalymova, Z. A., & Suleymanova, S. S., Geodesics in the field of a rotating deformed gravitational source, International Journal of Modern Physics A, 31, 1641006. 2016

[32] Bowers, R. L., & Wilson, J. R., A numerical model for stellar core collapse calculations, ApJSS, 50, 115. 1982

[33] Bromberg, O., Nakar, E., Piran, T., & Sari, R., Short versus Long and Collapsars versus Non-collapsars: A Quantitative Classification of Gamma-Ray Bursts, ApJ, 764, 179. 2013

[34] Brown, G. E., Lee, C.-H., Wijers, R. A. M. J., & Bethe, H. A., Evolution of black holes in the galaxy, Phys. Rep., 333, 471. 2000

[35] Bufano, F., Pian, E., Sollerman, J., et al., The Highly Energetic Expansion of SN 2010bh Associated with GRB 100316D, ApJ, 753, 67. 2012

[36] Burrows, A., & Hayes, J., Pulsar Recoil and Gravitational Radiation Due to Asymmetrical Stellar Collapse and Explosion, Physical Review Letters, 76, 352. 1996

[37] Burrows, A., & Thompson, T. A., Neutrino-Matter Interaction Rates in Supernovae: The Essential Microphysics of Core Collapse, ArXiv Astrophysics e-prints. 2002

[38] Campana, S., Mangano, V., Blustin, A. J., et al., The association of GRB 060218 with a supernova and the evolution of the shock wave, Nature, 442, 1008. 2006

[39] Cannizzo, J. K., Lee, H. M., & Goodman, J., The disk accretion of a tidally disrupted star onto a massive black hole, ApJ, 351, 38. 1990

[40] Cano, Z., Wang, S.-Q., Dai, Z.-G., & Wu, X.-F., The Observer's Guide to the

Gamma-Ray Burst Supernova Connection, Advances in Astronomy, 2017, 8929054. 2017

[41] Chabrier, G., & Potekhin, A. Y., Equation of state of fully ionized electron-ion plasmas, Phys. Rev. E, 58, 4941. 1998

[42] Chandrasekhar, S., The Maximum Mass of Ideal White Dwarfs, ApJ, 74, 81. 1931

[43] —, The Evolution of the Jacobi Ellipsoid by Gravitational Radiation, ApJ, 161, 571. 1970

[44] Chatterjee, P., Hernquist, L., & Narayan, R., An Accretion Model for Anomalous X-Ray Pulsars, ApJ, 534, 373. 2000

[45] Chevalier, R. A., Neutron star accretion in a supernova, ApJ, 346, 847. 1989

[46] —, Neutron star accretion in a stellar envelope, ApJ, 411, L33. 1993

[47] Chornock, R., Berger, E., Levesque, E. M., et al., Spectroscopic Discovery of the Broad-Lined Type Ic Supernova 2010bh Associated with the Low-Redshift GRB 100316D, ArXiv e-prints. 2010

[48] Christodoulou, D., & Ruffini, R., Reversible Transformations of a Charged Black Hole, Phys. Rev. D, 4, 3552. 1971

[49] Cipolletta, F., Cherubini, C., Filippi, S., Rueda, J. A., & Ruffini, R., Fast rotating neutron stars with realistic nuclear matter equation of state, Phys. Rev. D, 92, 023007. 2015

[50] —, Last stable orbit around rapidly rotating neutron stars, Phys. Rev. D, 96, 024046. 2017

[51] Colgate, S. A., Neutron-Star Formation, Thermonuclear Supernovae, and Heavy-Element Reimplosion, ApJ, 163, 221. 1971

[52] Costa, E., Frontera, F., Heise, J., et al., Discovery of an X-ray afterglow associated with the γ-ray burst of 28 February 1997, Nature, 387, 783. 1997

[53] Cox, J. P. 1968, Principles of stellar structure - Vol.1: Physical principles; Vol.2: Applications to stars (New York: Gordon and Breach, 1968)

[54] Dan, M., Rosswog, S., Brüggen, M., & Podsiadlowski, P., The structure and fate of white dwarf merger remnants, MNRAS, 438, 14. 2014

[55] Dan, M., Rosswog, S., Guillochon, J., & Ramirez-Ruiz, E., Prelude to A Double Degenerate Merger: The Onset of Mass Transfer and Its Impact on Gravitational Waves and Surface Detonations, ApJ, 737, 89. 2011

[56] Dasgupta, B., & Dighe, A., Collective three-flavor oscillations of supernova neutrinos, Phys. Rev. D, 77, 113002. 2008

[57] Davidson, K., & Ostriker, J. P., Neutron-Star Accretion in a Stellar Wind: Model for a Pulsed X-Ray Source, ApJ, 179, 585. 1973

[58] de la Rosa, J., Roming, P., Pritchard, T., & Fryer, C., Characterizing Mid-ultraviolet to Optical Light Curves of Nearby Type IIn Supernovae, ApJ, 820, 74. 2016

[59] Della Valle, M., Supernovae and Gamma-Ray Bursts: A Decade of Observations, International Journal of Modern Physics D, 20, 1745. 2011

[60] Dexter, J., & Kasen, D., Supernova Light Curves Powered by Fallback Accretion, ApJ, 772, 30. 2013

[61] Dezalay, J.-P., Barat, C., Talon, R., et al. 1992, in American Institute of Physics Conference Series, Vol. 265, American Institute of Physics Conference Series, ed. W. S. Paciesas & G. J. Fishman, 304–309

[62] Di Matteo, T., Perna, R., & Narayan, R., Neutrino Trapping and Accretion Models for Gamma-Ray Bursts, ApJ, 579, 706. 2002

[63] Dicus, D. A., Stellar Energy-Loss Rates in a Convergent Theory of Weak and Electromagnetic Interactions, Phys. Rev. D, 6, 941. 1972

[64] Diehl, S., Fryer, C., & Herwig, F. 2008, in Astronomical Society of the Pacific Conference Series, Vol. 391, Hydrogen-Deficient Stars, ed. A. Werner & T. Rauch, 221

[65] Diehl, S., Rockefeller, G., Fryer, C. L., Riethmiller, D., & Statler, T. S., Generating Optimal Initial Conditions for Smoothed Particle Hydrodynamics Simulations, PASA, 32, e048. 2015

[66] Dominik, M., Belczynski, K., Fryer, C., et al., Double Compact Objects. I. The Significance of the Common Envelope on Merger Rates, ApJ, 759, 52. 2012

[67] Done, C., Gierliński, M., & Kubota, A., Modelling the behaviour of accretion flows in X-ray binaries. Everything you always wanted to know about accretion but were afraid to ask, A&AR, 15, 1. 2007

[68] Edgar, R., A review of Bondi-Hoyle-Lyttleton accretion, New Astronomy Reviews, 48, 843. 2004

[69] Eggleton, P. P., Approximations to the radii of Roche lobes, ApJ, 268, 368. 1983

[70] Ertan, Ü., Ekşi, K. Y., Erkut, M. H., & Alpar, M. A., On the Evolution of Anomalous X-ray Pulsars and Soft Gamma-ray Repeaters with Fall Back Disks, ApJ, 702, 1309. 2009

[71] Evans, P. A., Beardmore, A. P., Page, K. L., et al., An online repository of Swift/XRT light curves of γ-ray bursts, A&A, 469, 379. 2007

[72] —, Methods and results of an automatic analysis of a complete sample of Swift-XRT observations of GRBs, MNRAS, 397, 1177. 2009

[73] Fesen, R. A., & Gunderson, K. S., Optical Spectroscopy and Imaging of the Northeast Jet in the Cassiopeia A Supernova Remnant, ApJ, 470, 967. 1996

[74] Fogli, G. L., Lisi, E., Mirizzi, A., & Montanino, D., Probing supernova shock waves and neutrino flavour transitions in next-generation water Cherenkov detectors, J. Cosm. Astropart. Phys., 4, 002. 2005

[75] Frail, D. A., Kulkarni, S. R., Nicastro, L., Feroci, M., & Taylor, G. B., The radio afterglow from the γ-ray burst of 8 May 1997, Nature, 389, 261. 1997

[76] Friedman, J. L., Ipser, J. R., & Sorkin, R. D., Turning-point method for axisymmetric stability of rotating relativistic stars, ApJ, 325, 722. 1988

[77] Fruchter, A. S., Levan, A. J., Strolger, L., et al., Long γ-ray bursts and core-collapse supernovae have different environments, Nature, 441, 463. 2006

[78] Fryer, C. L., Mass Limits For Black Hole Formation, ApJ, 522, 413. 1999

[79] —, Neutrinos from Fallback onto Newly Formed Neutron Stars, ApJ, 699, 409. 2009

[80] Fryer, C. L., Andrews, S., Even, W., Heger, A., & Safi-Harb, S., Parameterizing the Supernova Engine and its Effects on Remnants and Basic Yields, ArXiv e-prints. 2017

[81] Fryer, C. L., Belczynski, K., Ramirez-Ruiz, E., et al., The Fate of the Compact Remnant in Neutron Star Mergers, ApJ, 812, 24. 2015

[82] Fryer, C. L., Belczynski, K., Wiktorowicz, G., et al., Compact Remnant Mass Function: Dependence on the Explosion Mechanism and Metallicity, ApJ, 749, 91. 2012

[83] Fryer, C. L., Benz, W., & Herant, M., The Dynamics and Outcomes of Rapid Infall onto Neutron Stars, ApJ, 460, 801. 1996

[84] Fryer, C. L., Benz, W., Herant, M., & Colgate, S. A., What Can the Accretion-Induced Collapse of White Dwarfs Really Explain?, ApJ, 516, 892. 1999

[85] Fryer, C. L., & Heger, A., Core-Collapse Simulations of Rotating Stars, ApJ, 541, 1033. 2000

[86] Fryer, C. L., Herwig, F., Hungerford, A., & Timmes, F. X., Supernova Fallback: A Possible Site for the r-Process, ApJ, 646, L131. 2006

[87] Fryer, C. L., & Kusenko, A., Effects of Neutrino-driven Kicks on the Supernova Explosion Mechanism, ApJSS, 163, 335. 2006

[88] Fryer, C. L., Oliveira, F. G., Rueda, J. A., & Ruffini, R., Neutron-Star-Black-Hole Binaries Produced by Binary-Driven Hypernovae, Physical Review Letters, 115, 231102. 2015

[89] Fryer, C. L., Rockefeller, G., & Warren, M. S., SNSPH: A Parallel Three-dimensional Smoothed Particle Radiation Hydrodynamics Code, ApJ, 643, 292. 2006

[90] Fryer, C. L., Rueda, J. A., & Ruffini, R., Hypercritical Accretion, Induced Gravitational Collapse, and Binary-Driven Hypernovae, ApJ, 793, L36. 2014

[91] Fryer, C. L., & Warren, M. S., Modeling Core-Collapse Supernovae in Three Dimensions, ApJ, 574, L65. 2002

[92] —, The Collapse of Rotating Massive Stars in Three Dimensions, ApJ, 601, 391. 2004

[93] Fryer, C. L., Woosley, S. E., & Hartmann, D. H., Formation Rates of Black Hole Accretion Disk Gamma-Ray Bursts, ApJ, 526, 152. 1999

[94] Fryer, C. L., & Young, P. A., Late-Time Convection in the Collapse of a 23 M_{solar} Star, ApJ, 659, 1438. 2007

[95] Galama, T. J., Vreeswijk, P. M., & van Paradijs et al., J., An unusual supernova in the error box of the γ-ray burst of 25 April 1998, Nature, 395, 670. 1998

[96] García-Berro, E., Lorén-Aguilar, P., Aznar-Siguán, G., et al., Double Degenerate Mergers as Progenitors of High-field Magnetic White Dwarfs, ApJ, 749, 25. 2012

[97] Gasques, L. R., Afanasjev, A. V., Aguilera, E. F., et al., Nuclear fusion in dense matter: Reaction rate and carbon burning, Phys. Rev. C, 72, 025806. 2005

[98] Gehrels, N. 2004, in American Institute of Physics Conference Series, Vol. 727, Gamma-Ray Bursts: 30 Years of Discovery, ed. E. Fenimore & M. Galassi, 637–641

[99] Ghosh, P., & Lamb, F. K., Accretion by rotating magnetic neutron stars. II - Radial and vertical structure of the transition zone in disk accretion, ApJ, 232, 259. 1979

[100] Ghosh, P., Pethick, C. J., & Lamb, F. K., Accretion by rotating magnetic neutron stars. I - Flow of matter inside the magnetosphere and its implications for spin-up and spin-down of the star, ApJ, 217, 578. 1977

[101] Giacconi, R., & Ruffini, R., eds. 1978, Physics and astrophysics of neutron stars and black holes

[102] Goldreich, P., & Julian, W. H., Pulsar Electrodynamics, ApJ, 157, 869. 1969

[103] Goodman, J., Dar, A., & Nussinov, S., Neutrino annihilation in Type II supernovae, ApJ, 314, L7. 1987

[104] Grefenstette, B. W., Harrison, F. A., Boggs, S. E., et al., Asymmetries in core-collapse supernovae from maps of radioactive ^{44}Ti in CassiopeiaA, Nature, 506, 339. 2014

[105] Greiner, J., Peimbert, M., Esteban, C., et al., Redshift of GRB 030329., GRB Coordinates Network, 2020. 2003

[106] Guerrero, J., García-Berro, E., & Isern, J., Smoothed Particle Hydrodynamics simulations of merging white dwarfs, A&A, 413, 257. 2004

[107] Guetta, D., & Della Valle, M., On the Rates of Gamma-Ray Bursts and Type Ib/c Supernovae, ApJ, 657, L73. 2007

[108] Gursky, H., & Ruffini, R., eds. 1975, Astrophysics and Space Science Library, Vol. 48, Neutron stars, black holes and binary X-ray sources; Proceedings of the Annual Meeting, San Francisco, Calif., February 28, 1974

[109] Han, Z., & Podsiadlowski, P., The single-degenerate channel for the progenitors of Type Ia supernovae, MNRAS, 350, 1301. 2004

[110] Hartle, J. B., Slowly Rotating Relativistic Stars. I. Equations of Structure, ApJ, 150, 1005. 1967

[111] Hartle, J. B., & Thorne, K. S., Slowly Rotating Relativistic Stars. II. Models for Neutron Stars and Supermassive Stars, ApJ, 153, 807. 1968

[112] Heger, A., & Woosley, S. E., Nucleosynthesis and Evolution of Massive Metal-free Stars, ApJ, 724, 341. 2010

[113] Henyey, L., & L'Ecuyer, J., Studies in Stellar Evolution. VIII. The Time Scale for the Diffusion of Energy in the Stellar Interior, ApJ, 156, 549. 1969

[114] Herant, M., Benz, W., Hix, W. R., Fryer, C. L., & Colgate, S. A., Inside the supernova: A powerful convective engine, ApJ, 435, 339. 1994

[115] Hessels, J. W. T., Ransom, S. M., Stairs, I. H., et al., A Radio Pulsar Spinning at 716 Hz, Science, 311, 1901. 2006

[116] Hills, J. G., The effects of sudden mass loss and a random kick velocity produced in a supernova explosion on the dynamics of a binary star of arbitrary orbital eccentricity - Applications to X-ray binaries and to the binary pulsars, ApJ, 267, 322. 1983

[117] Hjorth, J., & Bloom, J. S. 2012, The Gamma-Ray Burst - Supernova Connection, ed. C. Kouveliotou, R. A. M. J. Wijers, & S. Woosley, 169–190

[118] Hobbs, G., Lorimer, D. R., Lyne, A. G., & Kramer, M., A statistical study of 233 pulsar proper motions, MNRAS, 360, 974. 2005

[119] Hosono, N., Saitoh, T. R., & Makino, J., A Comparison of SPH Artificial Viscosities and Their Impact on the Keplerian Disk, ApJSS, 224, 32. 2016

[120] Houck, J. C., & Chevalier, R. A., Steady spherical hypercritical accretion onto neutron stars, ApJ, 376, 234. 1991

[121] Hoyle, F., & Lyttleton, R. A., The effect of interstellar matter on climatic variation, Proceedings of the Cambridge Philosophical Society, 35, 405. 1939

[122] Hungerford, A. L., Fryer, C. L., & Rockefeller, G., Gamma Rays from Single-Lobe Supernova Explosions, ApJ, 635, 487. 2005

[123] Hungerford, A. L., Fryer, C. L., & Warren, M. S., Gamma-Ray Lines from Asymmetric Supernovae, ApJ, 594, 390. 2003

[124] Iben, Jr., I., & Tutukov, A. V., Supernovae of type I as end products of the evolution of binaries with components of moderate initial mass (M not greater than about 9 solar masses), ApJSS, 54, 335. 1984

[125] Ilkov, M., & Soker, N., The number of progenitors in the core-degenerate scenario for Type Ia supernovae, MNRAS, 428, 579. 2013

[126] Illarionov, A. F., & Sunyaev, R. A., Why the Number of Galactic X-ray Stars Is so Small?, A&A, 39, 185. 1975

[127] Itoh, N., Adachi, T., Nakagawa, M., Kohyama, Y., & Munakata, H., Neutrino energy loss in stellar interiors. III - Pair, photo-, plasma, and bremsstrahlung processes, ApJ, 339, 354. 1989

[128] Itoh, N., Hayashi, H., Nishikawa, A., & Kohyama, Y., Neutrino Energy Loss in

Stellar Interiors. VII. Pair, Photo-, Plasma, Bremsstrahlung, and Recombination Neutrino Processes, ApJSS, 102, 411. 1996

[129] Itoh, N., & Kohyama, Y., Neutrino-pair bremsstrahlung in dense stars. I - Liquid metal case, ApJ, 275, 858. 1983

[130] Itoh, N., Kohyama, Y., Matsumoto, N., & Seki, M., Electrical and thermal conductivities of dense matter in the crystalline lattice phase, ApJ, 285, 758. 1984

[131] —, Neutrino-pair bremsstrahlung in dense stars. III - Low-temperature quantum corrections in the liquid metal phase, ApJ, 280, 787. 1984

[132] —, Neutrino-pair bremsstrahlung in dense stars. IV - Phonon contributions in the crystalline lattice phase, ApJ, 285, 304. 1984

[133] Itoh, N., Matsumoto, N., Seki, M., & Kohyama, Y., Neutrino-pair bremsstrahlung in dense stars. II - Crystalline lattice case, ApJ, 279, 413. 1984

[134] Itoh, N., Mitake, S., Iyetomi, H., & Ichimaru, S., Electrical and thermal conductivities of dense matter in the liquid metal phase. I - High-temperature results, ApJ, 273, 774. 1983

[135] Iwamoto, K., Nomoto, K., Hoflich, P., et al., Theoretical light curves for the type IC supernova SN 1994I, ApJ, 437, L115. 1994

[136] Izzo, L., Pisani, G. B., Muccino, M., et al. 2013, in EAS Publications Series, Vol. 61, EAS Publications Series, ed. A. J. Castro-Tirado, J. Gorosabel, & I. H. Park, 595–597

[137] Izzo, L., Rueda, J. A., & Ruffini, R., GRB 090618: a candidate for a neutron star gravitational collapse onto a black hole induced by a type Ib/c supernova, A&A, 548, L5. 2012

[138] Izzo, L., Ruffini, R., Penacchioni, A. V., et al., A double component in GRB 090618: a proto-black hole and a genuinely long gamma-ray burst, A&A, 543, A10. 2012

[139] Janka, H.-T., Explosion Mechanisms of Core-Collapse Supernovae, Annual Review of Nuclear and Particle Science, 62, 407. 2012

[140] Janka, H.-T., & Mueller, E., Neutron star recoils from anisotropic supernovae., A&A, 290, 496. 1994

[141] Ji, S., Fisher, R. T., García-Berro, E., et al., The Post-merger Magnetized Evolution of White Dwarf Binaries: The Double-degenerate Channel of Sub-Chandrasekhar Type Ia Supernovae and the Formation of Magnetized White Dwarfs, ApJ, 773, 136. 2013

[142] Kashi, A., & Soker, N., A circumbinary disc in the final stages of common envelope and the core-degenerate scenario for Type Ia supernovae, MNRAS, 417, 1466. 2011

[143] Kato, S., Fukue, J., & Mineshige, S. 2008, Black-Hole Accretion Disks — Towards a New Paradigm — (Kyoto University Press)

[144] Keil, M. T., Raffelt, G. G., & Janka, H.-T., Monte Carlo Study of Supernova Neutrino Spectra Formation, ApJ, 590, 971. 2003

[145] Klebesadel, R. W. 1992, The durations of gamma-ray bursts, ed. C. Ho, R. I. Epstein, & E. E. Fenimore, 161–168

[146] Klebesadel, R. W., Strong, I. B., & Olson, R. A., Observations of Gamma-Ray Bursts of Cosmic Origin, ApJ, 182, L85. 1973

[147] Kohri, K., Narayan, R., & Piran, T., Neutrino-dominated Accretion and Supernovae, ApJ, 629, 341. 2005

[148] Kohyama, Y., Itoh, N., & Munakata, H., Neutrino energy loss in stellar interiors. II - Axial-vector contribution to the plasma neutrino energy loss rate, ApJ, 310, 815. 1986

[149] Kohyama, Y., Itoh, N., Obama, A., & Hayashi, H., Neutrino energy loss in stellar interiors. 6. Axial vector contribution to the plasma neutrino energy-loss rate for strongly degenerate electrons, ApJ, 431, 761. 1994

[150] Kouveliotou, C., Meegan, C. A., Fishman, G. J., et al., Identification of two classes of gamma-ray bursts, ApJ, 413, L101. 1993

[151] Kovacevic, M., Izzo, L., Wang, Y., et al., A search for Fermi bursts associated with supernovae and their frequency of occurrence, A&A, 569, A108. 2014

[152] Krolik, J. H. 1998, Active Galactic Nuclei: From the Central Black Hole to the Galactic Environment (Princeton: Princeton University Press)

[153] Külebi, B., Ekşi, K. Y., Lorén-Aguilar, P., Isern, J., & García-Berro, E., Magnetic white dwarfs with debris discs, MNRAS, 431, 2778. 2013

[154] Kulkarni, A. K., & Romanova, M. M., Analytical hotspot shapes and magnetospheric radius from 3D simulations of magnetospheric accretion, MNRAS, 433, 3048. 2013

[155] Landau, L. D., & Lifshitz, E. M. 1959, Fluid mechanics (Oxford: Pergamon Press, 1959)

[156] Leach, R. W., & Ruffini, R., On the Masses of X-Ray Sources, ApJ, 180, L15. 1973

[157] Lee, H. K., Brown, G. E., & Wijers, R. A. M. J., Issues Regarding the Blandford-Znajek Process as a Gamma-Ray Burst Inner Engine, ApJ, 536, 416. 2000

[158] Leonard, D. C., Constraining the Type Ia Supernova Progenitor: The Search for Hydrogen in Nebular Spectra, ApJ, 670, 1275. 2007

[159] Leonard, D. C., Filippenko, A. V., Barth, A. J., & Matheson, T., Evidence for Asphericity in the Type IIN Supernova SN 1998S, ApJ, 536, 239. 2000

[160] Liang, E., Zhang, B., Virgili, F., & Dai, Z. G., Low-Luminosity Gamma-Ray Bursts as a Unique Population: Luminosity Function, Local Rate, and Beaming Factor, ApJ, 662, 1111. 2007

[161] Liu, T., Zhang, B., Li, Y., Ma, R.-Y., & Xue, L., Detectable MeV neutrinos from black hole neutrino-dominated accretion flows, Phys. Rev. D, 93, 123004. 2016

[162] Livio, M., & Riess, A. G., Have the Elusive Progenitors of Type Ia Supernovae Been Discovered?, ApJ, 594, L93. 2003

[163] Long, M., Romanova, M. M., & Lovelace, R. V. E., Locking of the Rotation of Disk-Accreting Magnetized Stars, ApJ, 634, 1214. 2005

[164] Lorén-Aguilar, P., Isern, J., & García-Berro, E., High-resolution smoothed particle hydrodynamics simulations of the merger of binary white dwarfs, A&A, 500, 1193. 2009

[165] Lyman, J. D., Bersier, D., James, P. A., et al., Bolometric light curves and explosion parameters of 38 stripped-envelope core-collapse supernovae, MNRAS, 457, 328. 2016

[166] MacFadyen, A. I., & Woosley, S. E., Collapsars: Gamma-Ray Bursts and Explosions in "Failed Supernovae", ApJ, 524, 262. 1999

[167] MacFadyen, A. I., Woosley, S. E., & Heger, A., Supernovae, Jets, and Collapsars, ApJ, 550, 410. 2001

[168] MacLeod, M., & Ramirez-Ruiz, E., Asymmetric Accretion Flows within a Common Envelope, ApJ, 803, 41. 2015

[169] —, On the Accretion-fed Growth of Neutron Stars during Common Envelope, ApJ, 798, L19. 2015

[170] Maeda, K., & Nomoto, K., Bipolar Supernova Explosions: Nucleosynthesis and Implications for Abundances in Extremely Metal-Poor Stars, ApJ, 598, 1163. 2003

[171] Maeda, K., Kawabata, K., Mazzali, P. A., et al., Asphericity in Supernova Explosions from Late-Time Spectroscopy, Science, 319, 1220. 2008

[172] Matheson, T., Garnavich, P. M., Stanek, K. Z., et al., Photometry and Spectroscopy of GRB 030329 and Its Associated Supernova 2003dh: The First Two Months, ApJ, 599, 394. 2003

[173] Meegan, C. A., Fishman, G. J., Wilson, R. B., et al., Spatial distribution of gamma-ray bursts observed by BATSE, Nature, 355, 143. 1992

[174] Melandri, A., Pian, E., Ferrero, P., et al., The optical SN 2012bz associated with the long GRB 120422A, A&A, 547, A82. 2012

[175] Melandri, A., Pian, E., D'Elia, V., et al., Diversity of gamma-ray burst energetics vs. supernova homogeneity: SN 2013cq associated with GRB 130427A, A&A, 567, A29. 2014

[176] Melon Fuksman, J. D., Becerra, L., Bianco, C. L., et al. 2018, in European Physical Journal Web of Conferences, Vol. 168, European Physical Journal Web of Conferences, 04009

[177] Mendez, M., Clocchiatti, A., Benvenuto, O. G., Feinstein, C., & Marraco, H. G., SN 1987A - A linear polarimetric study, ApJ, 334, 295. 1988

[178] Menou, K., Esin, A. A., Narayan, R., et al., Black Hole and Neutron Star Transients in Quiescence, ApJ, 520, 276. 1999

[179] Metzger, B. D., Thompson, T. A., & Quataert, E., Proto-Neutron Star Winds with Magnetic Fields and Rotation, ApJ, 659, 561. 2007

[180] Metzger, M. R., Djorgovski, S. G., Kulkarni, S. R., et al., Spectral constraints on the redshift of the optical counterpart to the γ-ray burst of 8 May 1997, Nature, 387, 878. 1997

[181] Mignone, A., Zanni, C., Tzeferacos, P., et al., The PLUTO Code for Adaptive Mesh Computations in Astrophysical Fluid Dynamics, ApJSS, 198, 7. 2012

[182] Mikheev, S. P., & Smirnov, A. I., Resonant amplification of neutrino oscillations in matter and solar-neutrino spectroscopy, Nuovo Cimento C Geophysics Space Physics C, 9, 17. 1986

[183] Mirabel, I. F., & Rodríguez, L. F., Microquasars in our Galaxy, Nature, 392, 673. 1998

[184] Misiaszek, M., Odrzywołek, A., & Kutschera, M., Neutrino spectrum from the pair-annihilation process in the hot stellar plasma, Phys. Rev. D, 74, 043006. 2006

[185] Mizuno, Y., Yamada, S., Koide, S., & Shibata, K., General Relativistic Magnetohydrodynamic Simulations of Collapsars: Rotating Black Hole Cases, ApJ, 615, 389. 2004

[186] Mochkovitch, R., & Livio, M., The coalescence of white dwarfs and type I supernovae - The merged configuration, A&A, 236, 378. 1990

[187] Monaghan, J. J., Smoothed particle hydrodynamics, annurev, 30, 543. 1992

[188] —, Smoothed particle hydrodynamics, Reports on Progress in Physics, 68, 1703. 2005

[189] Moriya, T., Tominaga, N., Tanaka, M., et al., Fallback Supernovae: A Possible Origin of Peculiar Supernovae with Extremely Low Explosion Energies, ApJ, 719, 1445. 2010

[190] Munakata, H., Kohyama, Y., & Itoh, N., Neutrino energy loss in stellar interiors, ApJ, 296, 197. 1985

[191] Murphy, J. W., Dolence, J. C., & Burrows, A., The Dominance of Neutrino-driven Convection in Core-collapse Supernovae, ApJ, 771, 52. 2013

[192] Narayan, R., Piran, T., & Kumar, P., Accretion Models of Gamma-Ray Bursts, ApJ, 557, 949. 2001

[193] Nava, L., Vianello, G., Omodei, N., et al., Clustering of LAT light curves: a clue to the origin of high-energy emission in gamma-ray bursts, MNRAS, 443, 3578. 2014

[194] Nomoto, K., Accreting white dwarf models for type I supernovae. I - Presupernova evolution and triggering mechanisms, ApJ, 253, 798. 1982

[195] Nomoto, K., & Hashimoto, M., Presupernova evolution of massive stars., Phys. Rep., 163, 13. 1988

[196] Nomoto, K., & Iben, Jr., I., Carbon ignition in a rapidly accreting degenerate dwarf - A clue to the nature of the merging process in close binaries, ApJ, 297, 531. 1985

[197] Nomoto, K., Yamaoka, H., Pols, O. R., et al., A carbon-oxygen star as progenitor of the type Ic supernova 1994I, Nature, 371, 227. 1994

[198] Nomoto, K. I., Iwamoto, K., & Suzuki, T., The evolution and explosion of massive binary stars and Type Ib-Ic-IIb-IIL supernovae., Phys. Rep., 256, 173. 1995

[199] Nousek, J. A., Kouveliotou, C., Grupe, D., et al., Evidence for a Canonical Gamma-Ray Burst Afterglow Light Curve in the Swift XRT Data, ApJ, 642, 389. 2006

[200] Paczyński, B., Are Gamma-Ray Bursts in Star-Forming Regions?, ApJ, 494, L45. 1998

[201] Pakmor, R., Kromer, M., Röpke, F. K., et al., Sub-luminous type Ia supernovae from the mergers of equal-mass white dwarfs with mass ˜0.9M$_{solar}$, Nature, 463, 61. 2010

[202] Patrignani, C., & Particle Data Group, Review of Particle Physics, Chinese Physics C, 40, 100001. 2016

[203] Penacchioni, A. V., Ruffini, R., Bianco, C. L., et al., GRB 110709B in the induced gravitational collapse paradigm, A&A, 551, A133. 2013

[204] Penacchioni, A. V., Ruffini, R., Izzo, L., et al., Evidence for a proto-black hole afnd a double astrophysical component in GRB 101023, A&A, 538, A58. 2012

[205] Perlmutter, S., Aldering, G., Goldhaber, G., et al., Measurements of Ω and Λ from 42 High-Redshift Supernovae, ApJ, 517, 565. 1999

[206] Phillips, M. M., The absolute magnitudes of Type IA supernovae, ApJ, 413, L105. 1993

[207] Pian, E., Mazzali, P. A., Masetti, N., et al., An optical supernova associated with the X-ray flash XRF 060218, Nature, 442, 1011. 2006

[208] Piersanti, L., Gagliardi, S., Iben, Jr., I., & Tornambé, A., Carbon-Oxygen White Dwarfs Accreting CO-rich Matter. I. A Comparison between Rotating and Nonrotating Models, ApJ, 583, 885. 2003

[209] Piran, T., The physics of gamma-ray bursts, Reviews of Modern Physics, 76, 1143. 2004

[210] Pisani, G. B., Izzo, L., Ruffini, R., et al., Novel distance indicator for gamma-ray bursts associated with supernovae, A&A, 552, L5. 2013

[211] Pisani, G. B., Ruffini, R., Aimuratov, Y., et al., On the Universal Late X-Ray Emission of Binary-driven Hypernovae and Its Possible Collimation, ApJ, 833, 159. 2016

[212] Pontecorvo, B., Mesonium and Antimesonium, Soviet Journal of Experimental and Theoretical Physics, 6, 429. 1958

[213] —, Neutrino Experiments and the Problem of Conservation of Leptonic Charge, Soviet Journal of Experimental and Theoretical Physics, 26, 984. 1968

[214] Popham, R., Woosley, S. E., & Fryer, C., Hyperaccreting Black Holes and Gamma-Ray Bursts, ApJ, 518, 356. 1999

[215] Postnov, K. A., & Yungelson, L. R., The Evolution of Compact Binary Star Systems, Living Reviews in Relativity, 17, 3. 2014

[216] Potekhin, A. Y., & Chabrier, G., Equation of state of fully ionized electron-ion plasmas. II. Extension to relativistic densities and to the solid phase, Phys. Rev. E, 62, 8554. 2000

[217] Price, D. J. 2011, SPLASH: An Interactive Visualization Tool for Smoothed Particle Hydrodynamics Simulations, Astrophysics Source Code Library

[218] Pringle, J. E. 1974, PhD thesis, , Univ. Cambridge, (1974)

[219] Proga, D., MacFadyen, A. I., Armitage, P. J., & Begelman, M. C., Axisymmetric Magnetohydrodynamic Simulations of the Collapsar Model for Gamma-Ray Bursts, ApJ, 599, L5. 2003

[220] Raskin, C., Scannapieco, E., Fryer, C., Rockefeller, G., & Timmes, F. X., Remnants of Binary White Dwarf Mergers, ApJ, 746, 62. 2012

[221] Rawls, M. L., Orosz, J. A., McClintock, J. E., et al., Refined Neutron Star Mass Determinations for Six Eclipsing X-Ray Pulsar Binaries, ApJ, 730, 25. 2011

[222] Rees, M., Ruffini, R., & Wheeler, J. A. 1974, Black holes, gravitational waves and cosmology: an introduction to current research

[223] Reichart, D. E., Observations and Theoretical Implications of GRB 970228, ApJ, 485, L57. 1997

[224] Rhoades, C. E., & Ruffini, R., Maximum Mass of a Neutron Star, Physical Review Letters, 32, 324. 1974

[225] Riess, A. G., Filippenko, A. V., Challis, P., et al., Observational Evidence from Supernovae for an Accelerating Universe and a Cosmological Constant, Astron. J., 116, 1009. 1998

[226] Rotondo, M., Rueda, J. A., Ruffini, R., & Xue, S.-S., Relativistic Feynman-Metropolis-Teller theory for white dwarfs in general relativity, Phys. Rev. D, 84, 084007. 2011

[227] Rueda, J. A., & Ruffini, R., On the Induced Gravitational Collapse of a Neutron Star to a Black Hole by a Type Ib/c Supernova, ApJ, 758, L7. 2012

[228] Ruffini, R. 2015, in Thirteenth Marcel Grossmann Meeting: On Recent Developments in Theoretical and Experimental General Relativity, Astrophysics and Relativistic Field Theories, ed. K. Rosquist, 242–314

[229] Ruffini, R., Black holes, supernovae and gamma ray bursts, Astronomy Reports, 59, 591. 2015

[230] Ruffini, R., Bernardini, M. G., Bianco, C. L., et al. 2005, in American Institute of Physics Conference Series, Vol. 782, XIth Brazilian School of Cosmology and Gravitation, ed. M. Novello & S. E. Perez Bergliaffa, 42–127

[231] Ruffini, R., Bernardini, M. G., Bianco, C. L., et al. 2006, in The Tenth Marcel Grossmann Meeting. Proceedings of the MG10 Meeting held at Brazilian Center for Research in Physics (CBPF), Rio de Janeiro, Brazil, 20-26 July 2003, Eds.: Mário Novello; Santiago Perez Bergliaffa; Remo Ruffini. Singapore: World Scientific Publishing, in 3 volumes, ISBN 981-256-667-8 (set), ISBN 981-256-980-4 (Part A), ISBN 981-256-979-0 (Part B), ISBN 981-256-978-2 (Part C), 2006, XLVIII + 2492 pp.: 2006, p.369, ed. M. Novello, S. Perez Bergliaffa, & R. Ruffini, 369

[232] Ruffini, R., Bianco, C. L., Chardonnet, P., Fraschetti, F., & Xue, S.-S., On the

Structures in the Afterglow Peak Emission of Gamma-Ray Bursts, ApJ, 581, L19. 2002

[233] Ruffini, R., Bianco, C. L., Fraschetti, F., Xue, S.-S., & Chardonnet, P., On a Possible Gamma-Ray Burst-Supernova Time Sequence, ApJ, 555, L117. 2001

[234] —, On the Interpretation of the Burst Structure of Gamma-Ray Bursts, ApJ, 555, L113. 2001

[235] —, Relative Spacetime Transformations in Gamma-Ray Bursts, ApJ, 555, L107. 2001

[236] Ruffini, R., Bianco, C. L., Xue, S.-S., et al., On the Instantaneous Spectrum of Gamma-Ray Bursts, International Journal of Modern Physics D, 13, 843. 2004

[237] Ruffini, R., Salmonson, J. D., Wilson, J. R., & Xue, S.-S., On the pair electromagnetic pulse of a black hole with electromagnetic structure, A&A, 350, 334. 1999

[238] —, On the pair-electromagnetic pulse from an electromagnetic black hole surrounded by a baryonic remnant, A&A, 359, 855. 2000

[239] Ruffini, R., & Wilson, J., Possibility of Neutrino Emission from Matter Accreting into a Neutron Star, Physical Review Letters, 31, 1362. 1973

[240] Ruffini, R., Bernardini, M. G., Bianco, C. L., et al. 2008, in Proceedings of The Eleventh Marcel Grossmann Meeting On Recent Developments in Theoretical and Experimental General Relativity, Gravitation and Relativistic Field Theories. Held 23-29 July 2006 Berlin, Germany. Published by World Scientific Publishing Co. Pte. Ltd., ed. H. Kleinert, R. T. Jantzen, & R. Ruffini, 368–505

[241] Ruffini, R., Izzo, L., Muccino, M., et al., Induced gravitational collapse at extreme cosmological distances: the case of GRB 090423, A&A, 569, A39. 2014

[242] Ruffini, R., Muccino, M., Bianco, C. L., et al., On binary-driven hypernovae and their nested late X-ray emission, A&A, 565, L10. 2014

[243] Ruffini, R., Wang, Y., Enderli, M., et al., GRB 130427A and SN 2013cq: A Multi-wavelength Analysis of An Induced Gravitational Collapse Event, ApJ, 798, 10. 2015

[244] Ruffini, R., Muccino, M., Kovacevic, M., et al., GRB 140619B: a short GRB from a binary neutron star merger leading to black hole formation, ApJ, 808, 190. 2015

[245] Ruffini, R., Izzo, L., Bianco, C. L., et al., Induced gravitational collapse in the BATSE era: The case of GRB 970828, Astronomy Reports, 59, 626. 2015

[246] Ruffini, R., Rueda, J. A., Muccino, M., et al., On the Classification of GRBs and Their Occurrence Rates, ApJ, 832, 136. 2016

[247] Ruffini, R., Wang, Y., Aimuratov, Y., et al., Early X-Ray Flares in GRBs, ApJ, 852, 53. 2018

[248] Ryde, F., The Cooling Behavior of Thermal Pulses in Gamma-Ray Bursts, ApJ, 614, 827. 2004

[249] —, Is Thermal Emission in Gamma-Ray Bursts Ubiquitous?, ApJ, 625, L95. 2005

[250] Saio, H., & Nomoto, K., Evolution of a merging pair of C + O white dwarfs to form a single neutron star, A&A, 150, L21. 1985

[251] Sakamoto, T., Barthelmy, S. D., Baumgartner, W. H., et al., GRB 100316D: Swift-BAT refined analysis., GRB Coordinates Network, Circular Service, No. 10511, #1 (2010), 10511. 2010

[252] Salam, A. 1968, Elementary Particle Physics (Stockholm: Almqvist and Wiksells)

[253] Salpeter, E. E., Energy and Pressure of a Zero-Temperature Plasma., ApJ, 134, 669. 1961

[254] Sato, Y., Nakasato, N., Tanikawa, A., et al., A Systematic Study of Carbon-Oxygen

White Dwarf Mergers: Mass Combinations for Type Ia Supernovae, ApJ, 807, 105. 2015

[255] Scheck, L., Kifonidis, K., Janka, H.-T., & Müller, E., Multidimensional supernova simulations with approximative neutrino transport. I. Neutron star kicks and the anisotropy of neutrino-driven explosions in two spatial dimensions, A&A, 457, 963. 2006

[256] Scheck, L., Plewa, T., Janka, H.-T., Kifonidis, K., & Müller, E., Pulsar Recoil by Large-Scale Anisotropies in Supernova Explosions, Physical Review Letters, 92, 011103. 2004

[257] Schreier, E., Levinson, R., Gursky, H., et al., Evidence for the Binary Nature of Centaurus X-3 from UHURU X-Ray Observations., ApJ, 172, L79. 1972

[258] Schwab, J., Quataert, E., & Kasen, D., The evolution and fate of super-Chandrasekhar mass white dwarf merger remnants, MNRAS, 463, 3461. 2016

[259] Schwab, J., Shen, K. J., Quataert, E., Dan, M., & Rosswog, S., The viscous evolution of white dwarf merger remnants, MNRAS, 427, 190. 2012

[260] Shakura, N. I., & Sunyaev, R. A., Black holes in binary systems. Observational appearance., A&A, 24, 337. 1973

[261] Shapiro, S. L., & Lightman, A. P., Black holes in X-ray binaries - Marginal existence and rotation reversals of accretion disks, ApJ, 204, 555. 1976

[262] Shen, K. J., Bildsten, L., Kasen, D., & Quataert, E., The Long-term Evolution of Double White Dwarf Mergers, ApJ, 748, 35. 2012

[263] Shibata, M., Baumgarte, T. W., & Shapiro, S. L., Stability and collapse of rapidly rotating, supramassive neutron stars: 3D simulations in general relativity, Phys. Rev. D, 61, 044012. 2000

[264] Shimizu, T., Yamada, S., & Sato, K., Axisymmetric neutrino radiation and the mechanism of supernova explosions, ApJ, 432, L119. 1994

[265] Sibgatullin, N. R., & Sunyaev, R. A., Energy Release on the Surface of a Rapidly Rotating Neutron Star during Disk Accretion: A Thermodynamic Approach, Astronomy Letters, 26, 772. 2000

[266] Smartt, S. J., Progenitors of Core-Collapse Supernovae, annurev, 47, 63. 2009

[267] —, Observational Constraints on the Progenitors of Core-Collapse Supernovae: The Case for Missing High-Mass Stars, PASA, 32, e016. 2015

[268] Smith, N., Mass Loss: Its Effect on the Evolution and Fate of High-Mass Stars, annurev, 52, 487. 2014

[269] Smith, N., Li, W., Filippenko, A. V., & Chornock, R., Observed fractions of core-collapse supernova types and initial masses of their single and binary progenitor stars, MNRAS, 412, 1522. 2011

[270] Soderberg, A. M., Kulkarni, S. R., & Frail, D. A., GRB 031203: variable radio source., GRB Coordinates Network, 2483. 2003

[271] Soderberg, A. M., Kulkarni, S. R., Nakar, E., et al., Relativistic ejecta from X-ray flash XRF 060218 and the rate of cosmic explosions, Nature, 442, 1014. 2006

[272] Sparre, M., Sollerman, J., Fynbo, J. P. U., et al., Spectroscopic Evidence for SN 2010ma Associated with GRB 101219B, ApJ, 735, L24. 2011

[273] Spitkovsky, A., Time-dependent Force-free Pulsar Magnetospheres: Axisymmetric and Oblique Rotators, ApJ, 648, L51. 2006

[274] Springel, V., E pur si muove: Galilean-invariant cosmological hydrodynamical simulations on a moving mesh, MNRAS, 401, 791. 2010

[275] Stergioulas, N., Rotating Stars in Relativity, Living Reviews in Relativity, 6, 3. 2003

[276] Stergioulas, N., & Friedman, J. L., Comparing models of rapidly rotating relativistic stars constructed by two numerical methods, ApJ, 444, 306. 1995

[277] Svensson, K. M., Levan, A. J., Tanvir, N. R., Fruchter, A. S., & Strolger, L.-G., The host galaxies of core-collapse supernovae and gamma-ray bursts, MNRAS, 405, 57. 2010

[278] Tagliaferri, G., Malesani, D., Chincarini, G., et al., GRB 031203: spectoscopic evidence for a 1998bw-like SN., GRB Coordinates Network, 2545. 2004

[279] Tanaka, M., Kawabata, K. S., Maeda, K., et al., Spectropolarimetry of the Unique Type Ib Supernova 2005bf: Larger Asymmetry Revealed by Later-Phase Data, ApJ, 699, 1119. 2009

[280] Tananbaum, H., Gursky, H., Kellogg, E. M., et al., Discovery of a Periodic Pulsating Binary X-Ray Source in Hercules from UHURU, ApJ, 174, L143. 1972

[281] Tanvir, N. R., Levan, A. J., Fruchter, A. S., et al., A 'kilonova' associated with the short-duration γ-ray burst GRB 130603B, Nature, 500, 547. 2013

[282] Taubenberger, S., Valenti, S., Benetti, S., et al., Nebular emission-line profiles of Type Ib/c supernovae - probing the ejecta asphericity, MNRAS, 397, 677. 2009

[283] Tauris, T. M., Langer, N., Moriya, T. J., et al., Ultra-stripped Type Ic Supernovae from Close Binary Evolution, ApJ, 778, L23. 2013

[284] Tauris, T. M., Langer, N., & Podsiadlowski, P., Ultra-stripped supernovae: progenitors and fate, MNRAS, 451, 2123. 2015

[285] Tauris, T. M., & van den Heuvel, E. P. J. 2006, Formation and evolution of compact stellar X-ray sources, ed. W. H. G. Lewin & M. van der Klis, 623–665

[286] Tavani, M., Euclidean versus Non-Euclidean Gamma-Ray Bursts, ApJ, 497, L21. 1998

[287] Toropina, O. D., Romanova, M. M., & Lovelace, R. V. E., Bondi-Hoyle accretion on to a magnetized neutron star, MNRAS, 420, 810. 2012

[288] Totani, T., Morokuma, T., Oda, T., Doi, M., & Yasuda, N., Delay Time Distribution Measurement of Type Ia Supernovae by the Subaru/XMM-Newton Deep Survey and Implications for the Progenitor, PASJ, 60, 1327. 2008

[289] Townsley, D. M., & Bildsten, L., Theoretical Modeling of the Thermal State of Accreting White Dwarfs Undergoing Classical Nova Cycles, ApJ, 600, 390. 2004

[290] Tubbs, D. L., & Schramm, D. N., Neutrino Opacities at High Temperatures and Densities, ApJ, 201, 467. 1975

[291] Uribe, J. D., Becerra, L., Guzzo, M. M., et al., Neutrino Oscillations within the Induced Gravitational Collapse Paradigm of Long Gamma-Ray Bursts, ApJ, 852, 120. 2018

[292] Usov, V. V., Millisecond pulsars with extremely strong magnetic fields as a cosmological source of gamma-ray bursts, Nature, 357, 472. 1992

[293] van Kerkwijk, M. H., Chang, P., & Justham, S., Sub-Chandrasekhar White Dwarf Mergers as the Progenitors of Type Ia Supernovae, ApJ, 722, L157. 2010

[294] van Paradijs, J., Groot, P. J., Galama, T., et al., Transient optical emission from the error box of the γ-ray burst of 28 February 1997, Nature, 386, 686. 1997

[295] von Kienlin, A., GRB 130427A: Fermi GBM observation., GRB Coordinates Network, Circular Service, No. 14473, #1 (2013), 14473. 2013

[296] Wang, L., Wheeler, J. C., Li, Z., & Clocchiatti, A., Broadband Polarimetry of

Supernovae: SN 1994D, SN 1994Y, SN 1994ae, SN 1995D, and SN 1995H, ApJ, 467, 435. 1996

[297] Wang, Y.-M., Spin-reversed accretion as the cause of intermittent spindown in slow X-ray pulsars, A&A, 102, 36. 1981

[298] —, Disc accretion by magnetized neutron stars - A reassessment of the torque, A&A, 183, 257. 1987

[299] —, On the Torque Exerted by a Magnetically Threaded Accretion Disk, ApJ, 449, L153. 1995

[300] —, Location of the Inner Radius of a Magnetically Threaded Accretion Disk, ApJ, 465, L111. 1996

[301] —, Torque Exerted on an Oblique Rotator by a Magnetically Threaded Accretion Disk, ApJ, 475, L135. 1997

[302] Warren, M. S., & Salmon, J. K. 1993, in Proceedings of the 1993 ACM/IEEE Conference on Supercomputing (New York: ACM), 12–21

[303] Warren, M. S., & Salmon, J. K., A portable parallel particle program, Computer Physics Communications, 87, 266. 1995

[304] Webbink, R. F., Double white dwarfs as progenitors of R Coronae Borealis stars and Type I supernovae, ApJ, 277, 355. 1984

[305] Weinberg, D. H., Mortonson, M. J., Eisenstein, D. J., et al., Observational probes of cosmic acceleration, Phys. Rep., 530, 87. 2013

[306] Weinberg, S., A Model of Leptons, Physical Review Letters, 19, 1264. 1967

[307] Wilson, R. E., The Limiting Mass of Centaurus X-3, ApJ, 174, L27. 1972

[308] Wolfenstein, L., Neutrino oscillations in matter, Phys. Rev. D, 17, 2369. 1978

[309] Woosley, S. E. 1987, in IAU Symposium, Vol. 125, The Origin and Evolution of Neutron Stars, ed. D. J. Helfand & J.-H. Huang, 255–270

[310] Woosley, S. E., Gamma-ray bursts from stellar mass accretion disks around black holes, ApJ, 405, 273. 1993

[311] Woosley, S. E., & Bloom, J. S., The Supernova Gamma-Ray Burst Connection, annurev, 44, 507. 2006

[312] Woosley, S. E., Heger, A., & Weaver, T. A., The evolution and explosion of massive stars, Reviews of Modern Physics, 74, 1015. 2002

[313] Woosley, S. E., & Weaver, T. A., The Evolution and Explosion of Massive Stars. II. Explosive Hydrodynamics and Nucleosynthesis, ApJSS, 101, 181. 1995

[314] Xing, Z.-z., Properties of CP violation in neutrino-antineutrino oscillations, Phys. Rev. D, 87, 053019. 2013

[315] Xu, D., de Ugarte Postigo, A., Leloudas, G., et al., Discovery of the Broad-lined Type Ic SN 2013cq Associated with the Very Energetic GRB 130427A, ApJ, 776, 98. 2013

[316] Yakovlev, D. G., Kaminker, A. D., Gnedin, O. Y., & Haensel, P., Neutrino emission from neutron stars, Phys. Rep., 354, 1. 2001

[317] Yoon, S.-C., Podsiadlowski, P., & Rosswog, S., Remnant evolution after a carbon-oxygen white dwarf merger, MNRAS, 380, 933. 2007

[318] Young, P. A., Fryer, C. L., Hungerford, A., et al., Constraints on the Progenitor of Cassiopeia A, ApJ, 640, 891. 2006

[319] Zel'dovich, Y. B., Ivanova, L. N., & Nadezhin, D. K., Nonstationary Hydrodynamical Accretion onto a Neutron Star., Soviet Astronomy, 16, 209. 1972

[320] Zhang, B., Fan, Y. Z., Dyks, J., et al., Physical Processes Shaping Gamma-Ray

Burst X-Ray Afterglow Light Curves: Theoretical Implications from the Swift X-Ray Telescope Observations, ApJ, 642, 354. 2006

[321] Zhang, B., & Mészáros, P., Gamma-Ray Burst Afterglow with Continuous Energy Injection: Signature of a Highly Magnetized Millisecond Pulsar, ApJ, 552, L35. 2001

[322] Zhang, D., & Dai, Z. G., Hyperaccretion Disks around Neutron Stars, ApJ, 683, 329. 2008

[323] —, Hyperaccreting Neutron Star Disks and Neutrino Annihilation, ApJ, 703, 461. 2009

[324] Zhang, W., Woosley, S. E., & Heger, A., Fallback and Black Hole Production in Massive Stars, ApJ, 679, 639. 2008

[325] Zhu, C., Chang, P., van Kerkwijk, M. H., & Wadsley, J., A Parameter-space Study of Carbon-Oxygen White Dwarf Mergers, ApJ, 767, 164. 2013

[326] Zhu, C., Pakmor, R., van Kerkwijk, M. H., & Chang, P., Magnetized Moving Mesh Merger of a Carbon-Oxygen White Dwarf Binary, ApJ, 806, L1. 2015